# Histaminergic signaling underlies the early stages of color vision in the butterfly, *Papilio xuthus*

Pei-Ju CHEN

Doctor of Philosophy

Department of Evolutionary Studies of Biosystems
School of Advanced Sciences
The Graduate University for Advanced Studies,
SOKENDAI

# Histaminergic signaling underlies the early stages of color vision in the butterfly, *Papilio xuthus*

Pei-Ju CHEN

*Submitted in fulfilment of the requirements for the degree of Doctor of Philosophy*

Department of Evolutionary Studies of Biosystems, School of Advanced Sciences,
SOKENDAI (The Graduate University for Advanced Studies)

2019

# Abstract

Spectrally opponent responses, i.e. wavelength-dependent response-polarity inversions, have been observed at the level of photoreceptors quite frequently in butterflies. The opponent photoreceptors show fast-onset hyperpolarization when stimulated with specific wavelengths. Similar fast, on-transient hyperpolarizing responses that are found in the insect second-order visual neurons (lamina monopolar cells, LMCs), are mediated by histamine-gated chloride channels. In the lamina of *Papilio*, the photoreceptors are not only presynaptic to LMCs, but also pre- and post-synaptic to other photoreceptors. Thus, I hypothesized that histaminergic sign-inverting synapses exist between different spectral receptors as a mechanism for the spectral opponency in butterfly photoreceptors. I conducted immunolocalization on two candidates of histamine-gated chloride channels, PxHCLA and PxHCLB, in the visual system of the butterfly *Papilio xuthus*. The anti-PxHCLA labeling was associated with the plasma membrane of non-photoreceptor neurons that are postsynaptic to photoreceptors, suggesting that PxHCLA is located in the LMCs. The anti-PxHCLB labeling overlapped with photoreceptor axons, indicating the PxHCLB is expressed at the inter-photoreceptor synapses. I also analyzed physiological properties of these channels by whole-cell patch-clamp using those expressed in cultured cells. The patch-clamp experiments confirmed that both PxHCLA and PxHCLB are indeed activated by histamine and permeate chloride ions. Using sharp microelectrode recording in discontinuous single-electrode current-clamp mode, I have shown that the responses of both LMCs and spectrally opponent photoreceptors could be reversed when the membrane potential was close to the equilibrium potential of chloride ions. To understand how the histaminergic synapses mediate signal processing in the early visual system, I recorded responses of LMCs and photoreceptors in the *Papilio* lamina. Regarding the spectral properties, LMCs seem to integrate chromatic signals from the photoreceptors in the same ommatidium. It suggests that PxHCLA channels most likely implement the primary visual processing from photoreceptors to secondary neurons. On the other hand, several classes of spectrally opponent photoreceptors were recorded. The recorded opponent responses are well explained by the ommatidial type-specific inter-photoreceptor (sign-inverting) synaptic connections via PxHCLB. The findings in this thesis bring a closer view on the underlying neural circuits of color processing at the initial visual stage in *Papilio*.

# Acknowledgements

First and foremost, I would like to thank my wonderful advisor Dr. Kentaro Arikawa for his great supports throughout my PhD study. My scientific development is mainly attributed to his consistent supervision and our extensive discussion. Without him, I would not be able to enjoy this “crazy” but interesting project. I am also deeply grateful to my co-advisor Dr. Gregor Belušič for his encouragement, fruitful comments and suggestions on my research. I also wish to thank Dr. Atsuko Matsushita for her valuable advice, useful criticism and discussion. This thesis owes to their helpful guidance, patience, critical thinking and insight.

This thesis also would not have been possible without the contributions of several people. My sincere thanks to Drs. Hiroshi Akashi, Makoto Tominaga and Yasunori Takayama who supported the whole-cell patch-clamp technique for analyzing physiological properties of histaminergic channels at National Institute for Physiological Sciences, Japan. I am particularly grateful to Dr. Michiyo Kinoshita for her excellent technical assistance and taking good care of my life in Hayama. I deeply appreciate advices from Dr. Yohey Terai regarding the technological guidance for the immunoblot. I also wish to thank Drs. Akira Sasaki and Hisashi Ohtsuki and Mr. Ming Liu of Academia Sinica for their fruitful discussion about model simulation. Special thanks also go to Dr. Motohito Wakakuwa and Dr. Michael Perry of New York University who provided antisera for this work.

Many thanks as well to the rest of the members of laboratory and all of my fellow colleagues in SOKENDAI for their invaluable friendships and assistance. Especially Dr. Finlay Stewart for careful discussion and English editing and Dr. Hisaharu Koshitaka for helping to rear butterflies. A very big thank you goes through Drs. Nicolas Nagloo, Marko Ilić and Primož Pirih for stimulating discussion and making our work a joy. Another big thank you goes to the endless support and encouragement all the time from Drs. Anik Budhi Dharmayanthi, Quintin Lau and Wanjing Zheng, and also, other friends in Zushi including Ms. Aryanie Amellina, Ms. Megan Aplin, Mr. Helmy Prabowo, and our baby star Andra. Without them, I could not have fun both in the lab and for my life in Japan. Also thank you to Dr. Andrej Meglič and the members of Gregor’s lab for the care while I was staying at University of Ljubljana.

I would like to extend my gratitude to Dr. En-Cheng Yang of National Taiwan University, Dr. Chuan-Chin Chiao of National Tsing Hua University, Dr. Tsyr-Huei Chiou of National Cheng Kung University, and Ms. Jing-Wen Wang of University of Queensland for their valuable comments and interesting discussion in the conferences.

My sincere thanks also go to the financial support from Japan-Taiwan Exchange Association for the Interchange Association Scholarship and JSPS (Japan Society for the Promotion of Science) for Research Fellowships for Young Scientists (DC 1).

Lastly, I want to express my deepest gratitude to my friends in Taiwan who always have supported and encouraged me. Also deeply appreciate my doctors who tried their best to support me having good physical condition for study abroad. Most of all, I would like to thank my family ceaseless supports and all-out care. All achievements and glories attribute to them.

# Table of Contents

# List of Figures

# List of Tables

# Chapter 1

## General introduction

## 1.1 The complex color vision of butterflies

Vision is, for most animals, one of the important sensory modalities that allows to perceive the information about the surroundings. Color vision enhances animals' ability to find a good habitat, locate food sources, search for preys, detect predators, and to find mates (Neumeyer, 1991; Kelber, 2006). Like many other animals, insects use chromatic signals to sustain their lives in the world (Briscoe and Chittka, 2001). The habitats of insects are highly diverse with different visual conditions in terms of light intensity and spectral composition. Therefore, insects have been thought to have developed visual systems that were shaped by their evolutionary history and specifically adapted in response to ecological pressure. However, each taxonomic group of insects, in fact, has evolved its own distinctive set of photoreceptor classes with spectral sensitivities showing little variation within a group (Briscoe and Chittka, 2001; Lind et al., 2017). For example, a conserved set of spectral receptors have been revealed in 40 hymenopteran species including bees, wasps and sawflies (Peitsch et al., 1992). These species share very similar sets of UV-, blue- and green-sensitive photoreceptors, even though they occupy diverse ecological niches. In comparison, photoreceptors of butterflies are unusual for having a remarkable diversification and spectral tuning (Stavenga et al., 2001; Stavenga and Arikawa, 2006; Briscoe, 2008; Arikawa and Stavenga, 2014). The reasons why butterflies have a high diversity of spectral receptor classes are still unknown but may implicate recognition of valuable nectar sources as well as food plants for laying egg. Furthermore, many butterflies are decorated with colorful wings, which presumably tuned to the photoreceptor sensitivity spectra in conspecific individuals (Stavenga and Arikawa, 2006; Lind et al., 2017).

### *Color vision and spectral receptors*

Color vision is defined as the capability of discriminating visual stimuli based solely on the perception of the difference on spectral composition independent of the stimulus intensity (Menzel, 1979). The general rule is that each photoreceptor cell contains no more than one visual pigment. The absorption spectrum of a visual pigment can be read as the absorption probability with a photon with a certain energy (inversely related to its wavelength). This concept is in essence the Principle of Univariance (Naka and Rushton, 1966). Actually, a single photoreceptor cannot distinguish different light spectra. The necessary prerequisite that allows a visual system to discriminate colors is the coexistence of at least two photoreceptors with different spectral sensitivities (Mollon, 1989; Kelber, 2016).

The sensitivity of a photoreceptor to the light spectrum is determined by the absorption spectrum of the visual pigment (Menzel, 1974; Land and Nilsson, 2012). A visual pigment molecule is a G-protein-coupled receptor, which is composed of an opsin protein with seven-transmembrane domains and a light-sensitive retinoid chromophore (Seki and Vogt, 1998; Shichida and Imai, 1998). In humans and bees, it is retinal, derivative of vitamin A1; in Lepidoptera, it is 3-hydroxyretinal, derivative of vitamin A3 (Seki and Vogt, 1998; Briscoe and Chittka, 2001; Stavenga and Arikawa, 2006). When a photon is absorbed by the visual pigment, the energy of the photon will change the chromophore structure and activate G-protein that triggers the phototransduction cascade (Briscoe and Chittka, 2001; Kelber et al., 2003). Photoreceptors then convert light energy into electrical signal, forming neural information, which will be transmitted to further visual neuropils to establish the visual sensation (Menzel and Backhaus, 1989; Shichida and Imai, 1998).

The events of duplications and losses of opsin genes have occurred independently several times in insects during their evolutionary history (Terakita, 2005; Henze and Oakley, 2015; Feuda et al., 2016). Opsin gene duplication is an important force driving the expansion of spectral diversity in visual pigments, epitomized by over 20 opsins in dragonflies (Futahashi et al., 2015). Diversification of butterfly spectral receptors is attributed to recent lineage-specific gene duplications (Frentiu et al., 2007b; Briscoe, 2008; Arikawa and Stavenga, 2014). For example, UV-sensitive short-wavelength (SW) opsins are duplicated in *Heliconius* (Nymphalidae) (Briscoe et al., 2010). Duplicated blue-sensitive middle-wavelength (MW) opsins have diversified into blue- and violet-sensitive opsins in Pieridae (Arikawa et al., 2005; Awata et al., 2009; Ogawa et al., 2012) and into blue- and blue-green-sensitive opsins in the Lycaenidae (Sison-Mangus et al., 2006). Long-wavelength (LW) opsins are duplicated in *Helmeuptychia* (Nymphalidae), *Apodemia* (Riodinidae) (Frentiu et al., 2007a) and in the family Papilionidae (Kitamoto et al., 1998; Briscoe, 2000; Awata et al., 2010; Chen et al., 2016).

Despite the fact that the visual pigments are the primary factors in determination of spectral sensitivities of photoreceptors, there are various additional factors that may influence the final spectral outputs from the photoreceptors. For example, the screening effect of other photoreceptors in the same ommatidium could influence the action spectra of the photoreceptor (Menzel, 1974; Stavenga, 1992). The other case is one photoreceptor cell expressing multiple visual pigments, leading to a broader spectral sensitivity (Kitamoto et al., 1998; Arikawa et al., 2003; Ogawa et al., 2012; Chen et al., 2016).

In addition to visual pigments, clusters of screening pigments that are concentrated near the rhabdoms can narrow the spectral sensitivity by their absorption and scattering properties or act as long-pass filters (Carlson and Chi, 1979; Gribakin, 1988; Stavenga, 1992; Briscoe and Chittka, 2001; Kelber, 2006; Wakakuwa et al., 2007). The proximal photoreceptors of the small white butterfly, *Pieris rapae*, show a prominent example of spectra tuning towards red through the filtering effect by the perirhabdomal pigments (Qiu and Arikawa, 2003; Wakakuwa et al., 2004b). The green, red, and deep-red receptors express the same visual pigment, PrL (*Pieris rapae* Long-wavelength type). The pale-red and deep-red pigments around the rhabdom suppress the spectral sensitivity at the short wavelengths and lead to a shift to turn the PrL-expressing proximal photoreceptors into the red and deep-red receptors. The effect of perirhabdomal pigments resulting in a pronounced red-shifted has also been reported in other butterflies such as *Papilio xuthus* (Arikawa and Stavenga, 1997; Arikawa et al., 1999a), *Colias erate* (Ogawa et al., 2013), *Troides aeacus* (Chen et al., 2013), and *Graphium sarpedon* (Chen et al., 2016).

Another case of a filtering effect modifying the spectral sensitivity in short-wavelength range is achieved by the acquisition of UV-absorbing fluorescing pigments. The fluorescing material, 3-OH retinol, absorbs UV light (maximally around 330 nm) and strongly suppresses the sensitivity of the UV opsin-containing photoreceptors in the shorter wavelength region, shifting their peak sensitivity to 400 nm (Arikawa et al., 1999b; Kitamoto et al., 2000). Fluorescing ommatidia have been found in all papilionid species tested (Kitamoto et al., 2000; Matsushita et al., 2012; Chen et al., 2013; Chen et al., 2016). Among them, the eyes of the Common Bluebottle, *Graphium sarpedon*, even show a further diversification: their ommatidia are either strongly, weakly or non-fluorescent (Chen et al., 2016).

In addition to the filtering effects by the pigments, spectral sensitivity of the photoreceptors can also be modified and sharpened by electrical interactions between the photoreceptors. Electrical inhibition has been observed in the retina of the Australian orchard butterfly, *Papilio aegeus* (Horridge et al., 1983; Matić, 1983) and the golden birdwing butterfly, *Troides aeacus* (Chen et al., 2013).

Taken together, butterflies appear to use numerous mechanisms to modify and diversify their spectral types of photoreceptors. Different mechanisms can exist simultaneously in an individual photoreceptor. For example, in the strongly fluorescent ommatidia of *Graphium*, a broad-green receptor coexpresses three LW opsins resulting in a broad sensitivity in the long-

wavelength region but in a low UV sensitivity due to the suppression by the UV-absorbing fluorescent pigment (Chen et al., 2016). Combinations of different mechanisms provide a potential for spectral receptor multiplication in the eyes of butterflies.

***Studying color vision in butterflies***

Accumulated evidence indicates that flower-visiting insects including many species of bees and butterflies use their color vision to maximize success in foraging. About 100 years ago, von Frisch (1914) firstly demonstrated "true color vision" in insects by showing that honey bees can be trained to discriminate colors independent of the stimulus intensity (Menzel, 1979; Kelber et al., 2003). Honey bee has trichromatic vision with three spectral classes of photoreceptors peaking at the wavelengths of 340 nm (ultraviolet, UV), 440 nm (blue), and 550 nm (green) (Menzel and Blakers, 1976; Menzel and Backhaus, 1989).

Color vision studies in butterflies started after 1920s by the pioneer Ilse (Ilse, 1928; 1937; 1941), and, later, by Swihart (Swihart and Swihart, 1970; Swihart, 1971). And more studies came out from 20 years ago. Two studies were published almost simultaneously that established the presence of true color vision in the Japanese yellow swallowtail butterfly, *Papilio xuthus* (Kinoshita et al., 1999) and the Australian orchard butterfly, *P. aegeus* (Kelber and Pfaff, 1999). Further experiments have demonstrated that *P. xuthus* has tetrachromacy (Koshitaka et al., 2008) and some aspects of high-order color vision such as color constancy and simultaneous color contrast (Kinoshita and Arikawa, 2000; Kinoshita et al., 2008; Kinoshita and Arikawa, 2014).

The color vision system of butterflies appears to have evolved from an ancestral trichromatic system based on the UV-, blue- and green-sensitive photoreceptors (Menzel and Backhaus, 1989; Peitsch et al., 1992; Lin, 1993; Skorupski and Chittka, 2010; Blackiston et al., 2011). Over millions of years, probably due to their interaction with flowers, the color vision of flower-visiting butterflies has become richer by adding photoreceptors with various spectral sensitivities in a species-specific manner. For example, the nymphalid *Heliconius erato* has five classes of spectral receptors (McCulloch et al., 2016) while papilionid and pierid butterflies seem to be more diverse. The pierids *Pieris rapae* and *Colias erate* have eight (Stavenga and Arikawa, 2011) and nine classes of spectral receptors (Pirih et al., 2010; Ogawa et al., 2013), respectively. The papilionid *Papilio xuthus* has eight (Arikawa, 2003), *Troides aeacus* has nine (Chen et al., 2013) and the extreme case in *Graphium Sarpedon* with

fifteen distinct spectral classes of photoreceptors (Chen et al., 2016) (Figure 1-1). A high degree of variety of butterfly spectral receptors is attributed to several mechanisms, such as opsin gene duplications and various spectral filtering effects, as mentioned in the previous section.

Such photoreceptor variability raises a question of whether all spectral receptors contribute to color vision. This question has been answered by behavioral experiments in the foraging *Papilio xuthus* (Koshitaka et al., 2008). The butterflies were trained to detect the difference between two monochromatic lights of slightly different wavelengths. Then the receptor-noise limited color opponency model (Vorobyev and Osorio, 1998) was applied to predict how the butterfly would perform if various combinations of spectral receptors were used. While *Papilio* eyes contain eight classes of spectral receptors, their wavelength discrimination performance indicates that their color vision is tetrachromatic with UV, blue, green and red channels (Koshitaka et al., 2008). The excluded receptors, e.g. violet and broadband receptors, are probably used for some specific visual functions, such as for detecting particular signals or low intensity light. On the other hand, this experiment also showed that *Papilio* is able to detect lights with wavelength difference as small as 1 nm in three distinct wavelength regions: 430, 480 and 560 nm (Koshitaka et al., 2008). This is the smallest value so far found in any species. It seems that even though not all spectral receptors are involved in wavelength discrimination, the variety of spectral classes of photoreceptors may improve color discrimination system, at least in part, for butterflies seeing colorful world (Osorio and Vorobyev, 2008).

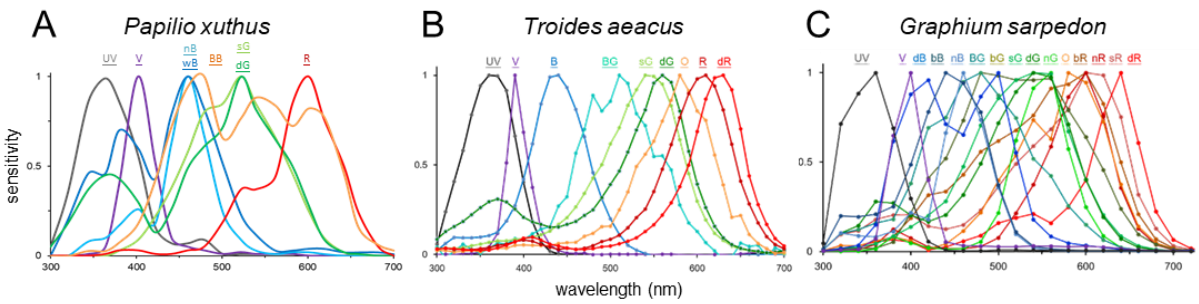


**Figure 1-1. Diversity of the spectral receptors in the eyes of Papilioninae butterflies. (A)** *Papilio xuthus*. Eight classes of photoreceptor were identified electrophysiologically (modified from Arikawa, 2003). **(B)** *Troides aeacus formosanus*. Nine spectral receptor classes were found (modified from Chen et al., 2013). **(C)** *Graphium sarpedon*. Fifteen spectrally distinct receptors were recorded (modified from Chen et al., 2016). *B*, blue; *bB*, broad blue; *wB*, wide blue; *BB*, broadband; *bG*, broad green; *BG*, blue-green; *bR*, broad red; *dB*, dual-peaked blue; *dG*, dual-peaked green; *dR*, deep red; *nB*, narrow blue; *nG*, narrow green; *nR*, narrow red; *O*, orange; *R*, red; *sG*, single-peaked green; *sR*, shouldered red; *UV*, ultraviolet; *V*, violet.

### *Spectral organization in the eye of* Papilio

The studies in butterfly eyes have considerably progresses recently. Among them, the Japanese yellow swallowtail butterfly, *Papilio xuthus*, is the most extensively studied species. The behavioral experiments have revealed its impressive color vision. Moreover, the spectral organization of its retina has also been studied thoroughly. Therefore, *Papilio* has become a powerful model for the study of color vision.

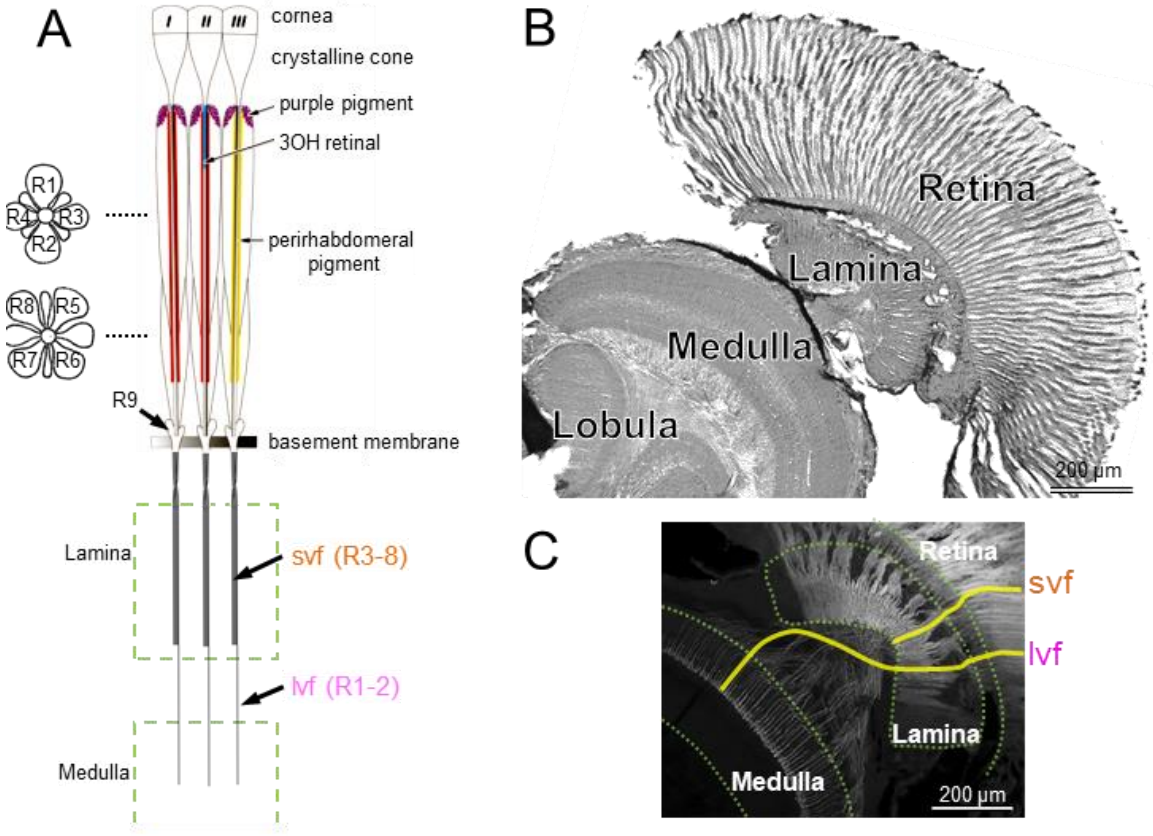


**Table 1-1. Summary of the spectral organization of the three types of ommatidia**

| | Type I | | Type II | | Type III | |
|---|---|---|---|---|---|---|
| Ratio | 50% | | 25% | | 25% | |
| Pigment | red | | red | | yellow | |
| Fluorescence | no | | yes | | no | |
| Photoreceptors | S(λ) | opsin | S(λ) | opsin | S(λ) | opsin |
| R1 | UV[1] | PxUV[1] | V | PxUV | wB | PxB |
| R2 | nB[1] | PxB[1] | | | | |
| R3-R4 | dG | PxL1, PxL2 | sG | PxL1, PxL2 | dG | PxL1, PxL2 |
| R5-R8 | R | PxL3 | BB | PxL2, PxL3 | dG | PxL2 |

**Figure 1-2. Spectral organization and photoreceptor axons in *Papilio* eye.** (**A**) Diagrammatic sketch of the three types of ommatidia. The rhabdomeres of the photoreceptors R1–R9 form together a fused rhabdom, which is surrounded by clusters of red (type I and II ommatidia) or yellow (type III) perirhabdomal pigments. Type II contains fluorescing pigment in the distal region of the rhabdom. (continued on the next page)

The compound eye of *Papilio xuthus* consists of about 12,000 units called ommatidia, each containing nine photoreceptors (R1–R9) (Figure 1-2A). Rhabdomeres of photoreceptors jointly constitute the fused rhabdom, and an obvious segregation to distal and proximal parts exists in the so-called tiered type of rhabdom, where R1–R4 are distal photoreceptors, R5–R8 are proximal photoreceptors and R9 is the basal photoreceptor (Bandai et al., 1992). R1 and R2 are long visual fibers (lvfs) that extend their axons to the medulla (the second optic ganglion in the optic lobe), while R3–R8 are short visual fibers (svfs) with their axons terminate in the lamina (the first optic ganglion) (Takemura et al., 2005) (Figure 1-2C). R9 is probably a svf (Matsushita et al., in preparation).

The ommatidia can be divided into three heterogeneous types based on characteristic pigmentation around the rhabdom (Figure 1-2A). Red pigment appears in proximal photoreceptors R5–R8 of type I and II ommatidia as four clusters, arranged in trapezoidal and square configurations, respectively, while type III ommatidia have four yellow spots instead. These perirhabdomal pigments can act as spectral filters for the proximal photoreceptors resulting in sensitivity spectra that are red-shifted (Arikawa et al., 1999a). On the other hand, about 25% ommatidia are the so-called fluorescing ommatidia because they emit strong, whitish fluorescence under UV epi-illumination. These fluorescing ommatidia contain a UV-absorbing fluorescent pigment, which is most likely 3-hydroxyretinol (3-OH retinol), in the distal portion of type II ommatidia (Arikawa et al., 1999b).

---

All ommatidia have purple pigment distally in the photoreceptor cell bodies. Photoreceptors send their axons to the optic lobe. Short visual fibers (svfs) terminate in the lamina while long visual fibers (lvfs) terminate in the medulla (modified from Arikawa and Stavenga, 2014). (**B**) Horizontal section through the compound eye including the retina and the optic lobe, stained with Azur II (Takemura et al., 2005). (**C**) Confocal image shows photoreceptor axons traced by Texas Red-conjugated dextran. Two yellow lines indicate the trace of a svf and a lvf that terminated in the lamina and medulla, respectively (Takemura et al., 2005). **Table 1-1.** Summary of the spectral organization of the three types of ommatidia, with the localization of five opsins (Arikawa, 2003). [1] R1 and R2 may be interchanged.

The ommatidial heterogeneity is also apparent based on specific sets of opsin expression (Table 1-1). Five opsins are expressed in *Papilio* eye, which are R360 (PxUV), R460 (PxB), R515 (PxL2), R545 (PxL1), and R575 (PxL3). *In situ* hybridization of five opsin mRNAs have revealed that PxUV and PxB mRNAs were expressed in the two distal photoreceptors, R1 and R2, in three combinations: one PxUV and another PxB (type I), both PxUV (type II), or both PxB mRNAs (type III) (Kitamoto et al., 2000). The other two distal photoreceptors, R3 and R4, coexpress PxL1 and PxL2 mRNAs in all ommatidial types. PxL2 mRNA is also detected in the proximal photoreceptors, R5–R8, of type III ommatidia while PxL3 mRNA exists in the proximal photoreceptors of type I ommatidia. The proximal photoreceptors of type II ommatidia coexpress PxL2 and PxL3 mRNAs (Kitamoto et al., 1998; Arikawa, 2003).

Due to the changes in the type and the coexpression of multiple visual pigments, along with lateral filtering effects, *Papilio* eye contains at least six classes of photoreceptors (Arikawa, 2003). Five of them peak in the UV (360 nm), violet (V, 400 nm), blue (B, 460 nm), green (G, 540 nm), and red (R, 600 nm) wavelength regions. The sixth, broadband receptor (BB), is an anomalous spectral type with a very large bandwidth (the half-bandwidth is approximately 220 nm) covering blue, green, and red wavelength range (420–640 nm). According to the sensitivity in the UV wavelength range, the B receptor class can be further divided into wide-band (wB) and narrow-band (nB); similarly, the G receptor class can be further divided into double-peaked (dG) and single-peaked (sG). Therefore, strictly speaking, eight spectral receptors with distinct spectral sensitivities are found in the eye of *Papilio*. By integrating the results of intracellular electrophysiology along with dye injection, the location of these spectral receptors has been identified: types I, II, and III ommatidia have four (UV, nB, dG, R), three (V, sG, BB), and two (wB, dG) receptor classes, respectively (Arikawa, 2003). Combining molecular results and electrophysiological recording, it can be concluded that the fluorescing pigments in type II ommatidia act as a UV-absorbing filter (Arikawa et al., 1999b) and the red and yellow perirhabdomal pigments in the proximal photoreceptors act as long-pass filter (Arikawa et al., 1999a). Table 1-1 summarizes the characteristics of the three types of ommatidia in the eye of *Papilio xuthus*.

## 1.2 Signal processing in the early visual system

After the light is transduced by the photoreceptors in insect eyes, visual information is further processed and transmitted towards the brain via the optic lobes, which include three neuropils: (from distal to proximal) the lamina, the medulla, and the lobula complex (Figure 1-2B). Photoreceptors produce a depolarizing, tonic response upon light stimulation through the activation of TRP and TRPL channels (Hardie and Franze, 2012). The photoreceptor potential is a graded function of light intensity. The potential spreads passively along the axon to its presynaptic terminal (Järvilehto and Zettler, 1973). Axons of photoreceptors from the same ommatidium are packed together, forming a module called cartridge with a few second-order visual neurons, lamina monopolar cells (LMCs), in the lamina (Ribi, 1987; Takemura and Arikawa, 2006) (Figure 1-3). The visual signal is transmitted from the photoreceptors to the LMCs through synaptic connections. Because the majority of this thesis discusses how the visual system extracts chromatic information at the first synapse, here I will briefly review what is already known about the corresponding neurotransmitter and ion channels.

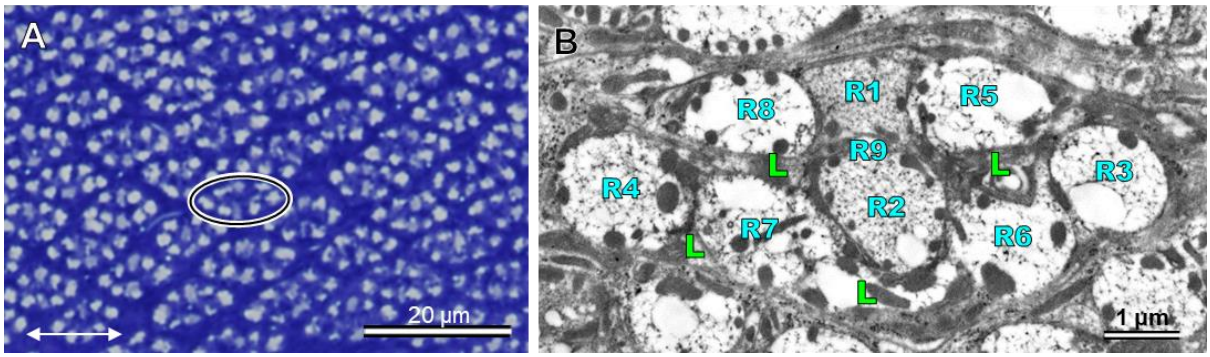


**Figure 1-3. Lamina cartridges of the *Papilio*.** (**A**) Cross section through the middle depth of lamina stained with Azur II, showing numerous compartments; each of them called a lamina cartridge (*oval*). A *double-headed arrow* indicates the dorso-ventral axis. (**B**) Electron micrograph of a lamina cartridge which contains nine photoreceptor axons (R1–R9) and four LMCs (L) (Takemura and Arikawa, 2006).

### *Histamine as a neurotransmitter*

In arthropods, photoreceptors depolarize in response to light and in turn release transmitter that leads to the hyperpolarization of postsynaptic interneurons. GABA had been thought to be the transmitter candidate, since it exists in insect optic lobes (Maxwell et al., 1978). Moreover, GABA can be synthesized and transported to the terminals of barnacle ocellar photoreceptors (Koike and Tsuda, 1980). It is also taken up by the glial cells in the lamina of flies (Campos-Ortega, 1974). However, in a latter experiment in the barnacle, GABA failed to mimic the photoreceptor's transmitter in recordings from postsynaptic cells (Timpe and Stuart, 1984).

The evidence gradually shifted to histamine as a transmitter. Some insects, e.g. cockroach, locust and moth, have high concentration of histamine in the retina and lamina (Elias and Evans, 1983). Hardie (1987) first suggested that histamine is a neurotransmitter in insect photoreceptors, based on his recordings from LMCs in the housefly, *Musca domestica*. The postsynaptic LMCs depolarized and hyperpolarized by applying GABA and histamine, respectively. The histamine-induced hyperpolarization successfully mimicked the natural response of LMCs to light. Furthermore, the antagonists can not only block the physiological response of LMCs to light but also inhibit the response of LMCs treated with histamine application (Hardie, 1988). Both light-induced and histamine-induced hyperpolarization showed similar sensitivities to antagonists. Subsequently, the role of histamine as a neurotransmitter was also confirmed in species from all three of the major groups of arthropods: Crustacea (e.g. barnacles), Chelicerata (e.g. horseshoe crab and spiders) and Uniramia (e.g. a variety of insects) (Morgan et al., 1999; Nässel, 1999; Schmid and Becherer, 1999; Stuart, 1999; Homberg, 2002; Hamanaka et al., 2012; Sombke and Harzsch, 2015). These studies again provided a support for the hypothesis that histamine is evolutionarily conserved as a neurotransmitter in arthropod photoreceptors. However, pharmacology of histamine differs among arthropods (reviewed by Stuart et al., 2007).

***Histamine-gated chloride channels***

After histamine was confirmed to act as the neurotransmitter in arthropod photoreceptors, the postsynaptic LMCs were therefore predicted to express histamine receptors. A major step in characterizing the histaminergic channel was taken when Hardie (1989) recorded the activity of single channels by patch-clamping dissociated LMCs of the blowfly, *Calliphora vicina*. A chloride current was observed in the LMC in response to histamine application, indicating that the channel-in-question is a histamine-gated chloride channel.

In 2002, four research groups independently identified and cloned two receptor subunits that coding histamine-gated chloride channels in *Drosophila*. Three groups performed a bioinformatics approach to search for the sequences that were homologous to known ligand-gated anion channels from the *Drosophila* genome (Gisselmann et al., 2002; Witte et al., 2002; Zheng et al., 2002). Gisselmann et al. (2002) and Zheng et al. (2002) also confirmed that the functional histamine-gated chloride channels could be successfully expressed in *Xenopus* oocytes from the identified cDNA clones. The fourth group took a genetic approach by cloning channels from a mutant fly having defective ERG (electroretinogram) responses to light in the

lamina (Gengs et al., 2002). Because of this history, several synonym names of the two channels were given (as listed in Table 1-2). In this thesis, I will use the terminology of Gengs et al. (2002) referring to the two genes as *hclA* and *hclB* and their protein as HCLA and HCLB, respectively.

**Table 1-2. Nomenclature and GenBank accession numbers of fly histamine-gated chloride channel genes**

| Research group | Gene encoded for HCLA | Gene encoded for HCLB | Accession # |
|---|---|---|---|
| Gengs et al., 2002 | *hclA* | *hclB* | AY049774 |
| Gisselmann et al., 2002 | DM-HisCl-α1 | DM-HisCl-α2 | AF435469 |
| Witte et al., 2002 | HA-Cl I | HA-Cl II | AF411340 |
| Zheng et al., 2002 | HisCl2 | HisCl1 | AF382403 |

The encoded proteins of two *Drosophila* histamine-gated chloride channels, HCLA and HCLB, share 60% amino acid identity with each other (Zheng et al., 2002). Both of them belong to the Cys-loop ligand-gated ion channel superfamily, and each functional receptor is pentameric (Thompson et al., 2010). Figure 1-4 shows their predicted topology of them (Witte et al., 2002). A large N-terminal extracellular domain acts as a key element in ligand recognition.

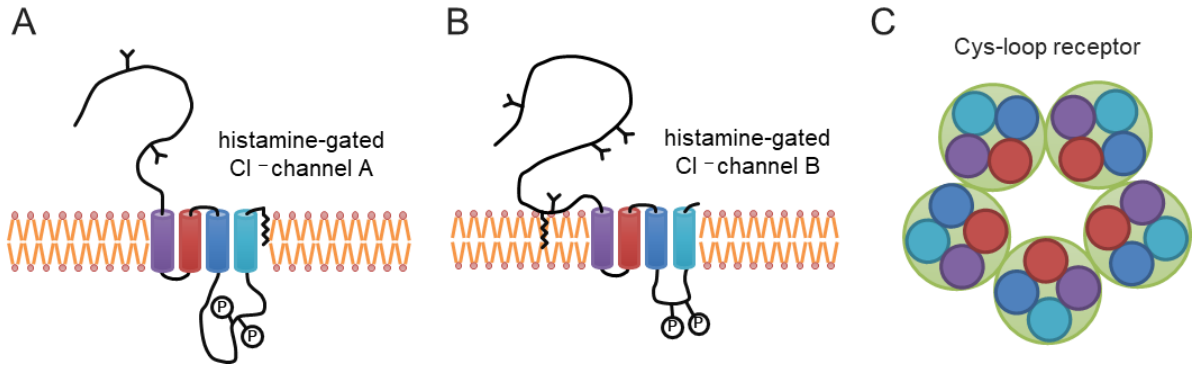


**Figure 1-4. Schematic diagram of the histamine-gated chloride channels in *Drosophila*.** (**A**–**B**) Predicted topology of protein subunits for the gene *hclA* (**A**) and *hclB* (**B**). Branched lines indicate potential N-linked glycosylation sites, circled Ps indicate consensus sequences for PKC phosphorylation. Cylinders are putative transmembrane regions (modified from Witte et al., 2002). (**C**) Schema showing the structure of a Cys-loop ligand-gated ion channel: each functional receptor is formed by five subunits.

Localizing the mRNA from the two *hcl* genes was not straightforward. Both genes were detected by RT-PCR, but *hclB* could not be detected by *in situ* hybridization (Gisselmann et al., 2002; Witte et al., 2002). In 2008, Pantazis et al. (2008) have successfully detected two genes in higher resolution by using a green fluorescent protein (GFP) reporter gene strategy and mRNA tagging technique in *Drosophila*. The *hclA* enhancer drove GFP expression in the LMC cell body layer along with their dendrites in the lamina (Figure 1-5A). In addition, the cell bodies of transmedullary cells at the medulla rind and medulla layers M1, M2, M3, and M5 were positive for GFP. Some axons of unknown cells, which are assumed to be the targets of photoreceptors, were also stained in the medulla and their terminals in the lobula. In contrast, the enhancer of *hclB* drove GFP expression in the lamina epithelial glia cells (Figure 1-5B). Gao et al. (2008) also obtained similar expression patterns for both histamine receptors in the eye of *Drosophila*. Further progress on the *hclB* localization was reported recently: Schnaitmann et al. (2018) have demonstrated in *Drosophila* that *hclB* drove GFP expression in the glial cells in the lamina as well as the axons of photoreceptors R7 and R8 in the medulla (Figure 1-5C).

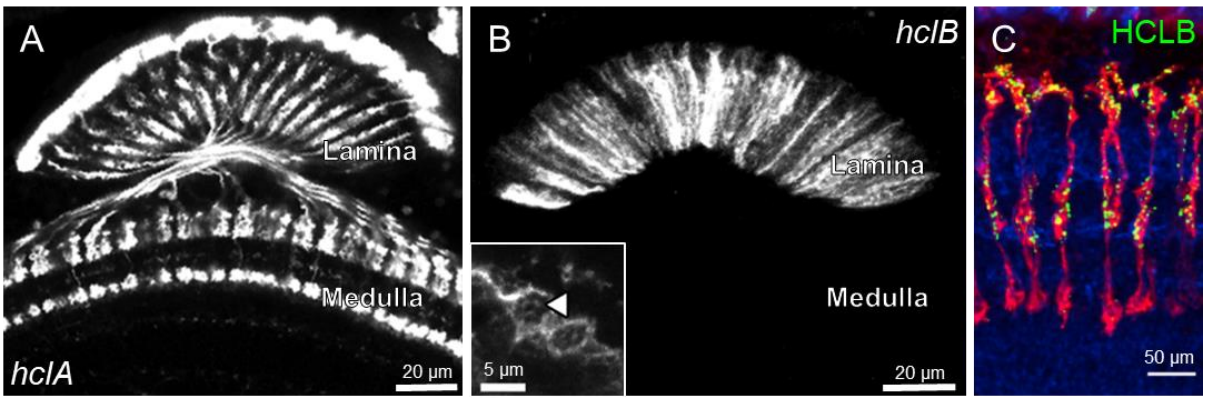


**Figure 1-5. Localization of the histamine-gated chloride channels in the eye of *Drosophila*.** (**A**–**B**) Enhancer analysis of the two histamine receptor genes: *hclA*-GAL4-driven expression of GFP (**A**) and *hclB*-GAL4-driven expression GFP (**B**). The *hclA* was detected in lamina monopolar cells L1–L3 and medulla cells. The *hclB* was detected in intrinsic cells in the lamina, but not in the monopolar cells. Inset in **B**: a cartridge cross-section reveals that the fibers are epithelial glia that surround the neuroommatidia. Figures taken from Pantazis et al. (2008). (**C**) A GFP-tagged *hclB* gene reveals HCLB expression (anti-GFP, *green*) in the terminals of R7 and R8 photoreceptors, which labeling with anti-DsRed (*red*), in medulla layers M1–M3. Figure taken from Schnaitmann et al. (2018).

Accumulated evidence have implicated that the HCLA is a subunit of the native histamine receptor in the LMCs postsynaptic to photoreceptors (Gengs et al., 2002) and is required for synaptic transmission at the photoreceptor-LMC synapse (Rister et al., 2007; Pantazis et al., 2008). Pantazis et al. (2008) performed patch clamp on *Drosophila* S2 cells that were transfected with *hclA* to check their electrophysiological properties, which were further compared with those reported previously in native channels on the LMCs by Skingsley et al. (1995). The dose-response experiment with histamine showed that not only the values of $EC_{50}$ (effective concentration for 50% of maximal response) but also cooperativity $n_H$ (slope of dose-response curve) were almost identical in the *hclA*-expressing cell ($EC_{50}$ = 25 µM, $n_H$ = 2.6) (Pantazis et al., 2008) (Figure 1-6A) and in the isolated *Drosophila* LMC ($EC_{50}$ = 24 µM, $n_H$ = 2.4) (Skingsley et al., 1995) (Table 1-3). Similarly, Kita et al. (2017) also demonstrated an exact match in histamine sensitivity between the housefly (*Musca domestica*) *hclA*-expressing cell ($EC_{50}$ = 33 µM) (Figure 1-6B) and the native receptor on the *Musca* LMCs ($EC_{50}$ = 34 µM) (Skingsley et al., 1995) (Table 1-3). Functional expression of the cloned *hclA* in *Drosophila* and *Musca* provided convincing evidence for the identity of the native receptor as *hclA* subunit in LMCs.

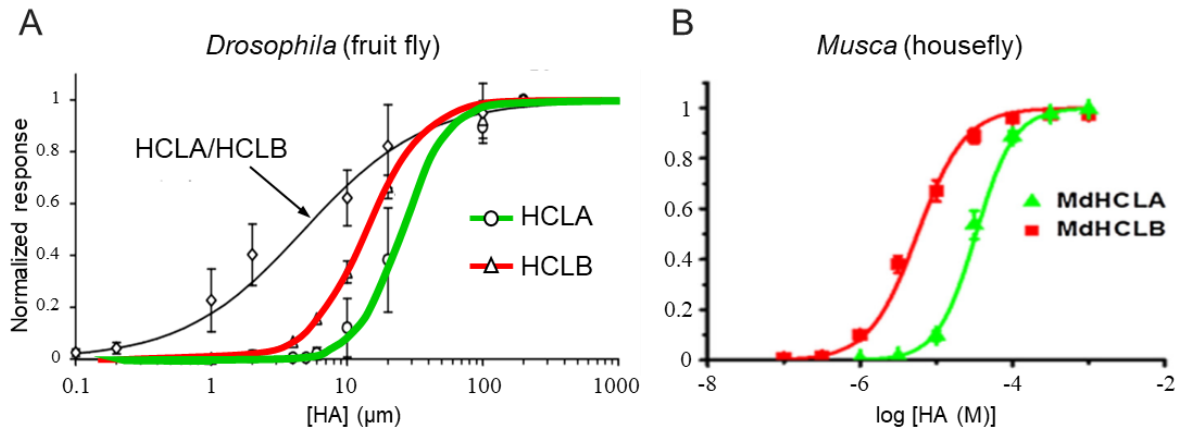


**Figure 1-6. Dose-response functions of fly HCLA and HCLB for histamine (HA).** (**A**) HCLA homomer (*circles*, *red line*), HCLB homomer (*triangles*, *green line*) and HCLA/HCLB heteromer (*diamonds*) of *Drosophila melanogaster*. Error bars represent ±1 SD. Figure taken from Pantazis et al. (2008). (**B**) MdHCLA (*circles*, *red line*) and MdHCLB(*triangles*, *green line*) channels of *Musca domestica*. The data are expressed as the mean ±SEM. Figure taken from Kita et al. (2017).

**Table 1-3. Histamine (HA) and GABA dose-response parameters**

| *Drosophila melanogaster* | | | | *Musca domestica* | | | |
|---|---|---|---|---|---|---|---|
| channel | agonist | $EC_{50}$ (μM) | $n_H$ | channel | agonist | $EC_{50}$ (μM) | $n_H$ |
| HCLA[1] | HA | 25.0 ± 8.8 | 2.6 ± 0.6 | MdHCLA[5] | HA | 33.1 ± 3.4 | 2.35 ± 0.16 |
| HCLB[1] | HA | 14.1 ± 1.7 | 2.0 ± 0.4 | MdHCLB[5] | HA | 6.28 ± 1.05 | 1.33 ± 0.09 |
| HCLB[2] | GABA | 1000 ± 100 | 1.5 ± 0.1 | MdHCLB[5] | GABA | 1110 ± 60 | 1.42 ±0 .06 |
| HCLA/HCLB[1] | HA | 4.8 ± 2.6 | 1.0 ± 0.2 | | | | |
| Native (*wt*)[3] | HA | 24 ± 8 | 2.5 ± 0.5 | Native[3] | HA | 34 ± 6 | 3.1 ± 1.3 |
| Native (*hclA*)[4] | HA | 190 ±77 | 3.1 ± 0.4 | | | | |

All fitted parameters are mean ± SE.
[1]Data from Pantazis et al. (2008)
[2]Data from Gisselmann et al. (2004)
[3]Data from Skingsley et al. (1995) ; in wild type LMC
[4]Data from Gengs et al. (2002); in *hclA* null mutant LMC
[5]Data from Kita et al. (2017)

The value of $EC_{50}$ for histamine in *hclA* null mutant of *Drosophila* was about 10-fold higher than in the wild type (Gengs et al., 2002) (Table 1-3), suggesting the contribution of HCLA in synaptic transmission. In flies, HCLA is a necessary component at synapses to convey the outputs from R1–R6 to L1–L3 LMCs (Rivera-Alba et al., 2011). The fly photoreceptors R1–R6 are thought to be responsible for motion detection because they all exhibit identical broad spectral sensitivity (Heisenberg and Buchner, 1977; Yamaguchi et al., 2008). Behavioral experiments in *hclA* null mutant of *Drosophila* revealed defective motion detection (Rister et al., 2007; Gao et al., 2008). Phylogenic examination demonstrated an extremely high conservation of HCLA receptor among different insect species (Iovchev et al., 2006). It is therefore tempting to speculate the HCLA channels of *Papilio xuthus* (PxHCLA) may function for signal transmission in the visual system similarly as in other insects.

On the other hand, electroretinogram (ERG) recordings also provided lines of evidence showing that the cloned *hclA* mediated photoreceptor synaptic transmission. In wild-type flies, the ERG is characterized by a corneal negative sustained photoreceptor component with brief positive “on” and negative “off” transients, which are primarily derived from the LMC response (Figure 1-7A). The *hclA* null mutant were found to lack “on” and “off” transients in the ERG (Gengs et al., 2002; Pantazis et al., 2008) (Figure 1-7B). In contrast, the ERG of *hclB* null mutation was similar to that of the wild type (Figure 1-7C). If anything, the amplitude of the positive “on” transient showed a two-fold increase in the *hclB* null mutants compared with the wild type (Pantazis et al., 2008). Taken together, the defective ERG implies that the HCLA receptor is required for synaptic transmission, while the role of HCLB is likely in shaping the postsynaptic response.

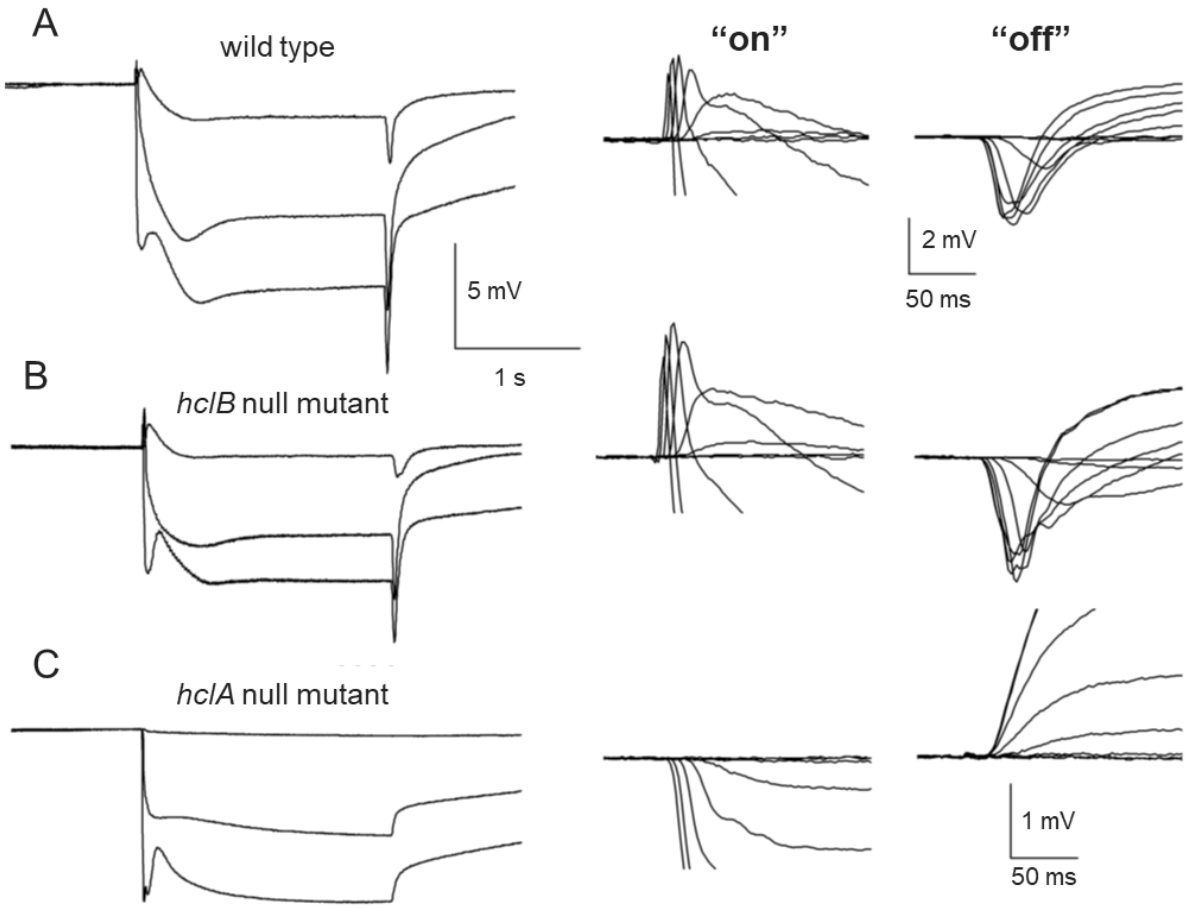


**Figure 1-7. ERG recordings from *hclA* and *hclB* null mutants.** ERGs recorded in response to 2 s light steps of increasing intensity (7 steps covering 6 log units of intensity). Examples of "on" (*left*) and "off" (*right*) transients in response to light stimuli are shown on the right on an expanded scale after aligning baselines immediately before light on or off. (**A**) Wild-type control. The conspicuous transients at light on (*left*) and off (*right*) represent the contribution of the LMCs in the lamina. (**B**) *hclB* null mutation. Transients were qualitatively similar in waveform to wild-type controls, but the "on" transients were approximately twofold larger. (**C**) *hclA* null mutation. Transients were completely eliminated. Figure taken from Pantazis et al. (2008).

*hclB* expression in *Drosophila* has been found exclusively in the lamina epithelial glia (Gao et al., 2008; Pantazis et al., 2008; Schnaitmann et al., 2018) (Figure 1-5B), which is assumed to take up histamine released from photoreceptors (Edwards and Meinertzhagen, 2010). Thus, the fly HCLB is also assumed to be involved in a histamine recycling pathway between photoreceptor terminals and the glial cells (Yusein et al., 2010). However, recently, the HCLB was found in the photoreceptor terminals in *Drosophila* medulla (Schnaitmann et al., 2018) (Figure 1-5C). The axons of photoreceptors R7 and R8 originating from the same ommatidium, directly inhibit each other at their axon terminals in the medulla via HCLB, resulting in antagonistic interactions. The fly photoreceptors R7 and R8 are spectrally heterogeneous and thus are thought to be involved in color processing (Morante and Desplan, 2004). The finding implies a novel role for HCLB in color opponent processing at the first

visual synapse (Schnaitmann et al., 2018). Anyhow, the function of HCLB remains less clearly determined since it has been found to be responsible for distinct roles in different types of cells.

***LMC responses***

The HCLA is a key element in the transmission of the visual signal from photoreceptors to LMCs. Photoreceptors respond to light with graded, tonic depolarization, which leads to a release of neurotransmitter at the photoreceptor synaptic terminals. Histamine, the only neurotransmitter identified so far in arthropod photoreceptors (Stuart et al., 2007), subsequently binds to HCLA on the membrane of the postsynaptic LMCs. LMCs elicit graded hyperpolarization in response to photoreceptor histaminergic signaling (Hardie, 1987). The typical LMC response starts with a fast hyperpolarizing on-transient, followed by a sustained plateau, and ends with a depolarizing off-transient (Figure 1-8A). The fast on-transient hyperpolarization is a phasic response and is assumed mainly due to an increase in the membrane chloride conductance through histamine-gated chloride channel (Hardie et al., 1989). Comparing the $V$-log $I$ function between the photoreceptor and the LMC, it becomes clear that the LMC is more sensitive to small changes in light intensity, showing a steeper slope and will saturate with small (< 10 mV) signals. It indicates that the photoreceptor signal is amplified at the photoreceptor-LMC synapse, which increases the signal-to-noise ratio and enhances contrast coding for downstream transmission. Ultimately, it maximizes the information capacity of the LMC (Laughlin, 1984).

At the end of the light stimulus, the depolarizing off-transient is observed in the LMC. Yet, the origin of this depolarization has not been understood well. The off-transient may be related to a decrease in histamine release from the photoreceptor. However, the “off” depolarization does not simply reflect the rate of repolarization of the photoreceptor. The postsynaptic depolarization in LMCs can be even faster than in the presynaptic cell (Oertel and Stuart, 1981). The amplitude of depolarization increases under light adaptation. In some cases, the depolarizing off-transient is characterized by the depolarizing spike (Järvilehto and Zettler, 1971; Zettler and Järvilehto, 1971; Hardie and Weckström, 1990; Rusanen and Weckström, 2016; Rusanen et al., 2017; Rusanen et al., 2018). In *Papilio xuthus*, two groups of LMCs have been reported based on the existence/absence of depolarizing off-spikes (Rusanen et al., 2018). Non-spiking LMCs (Figure 1-8A) with no or small “spikelets” terminate at the distal surface

of the medulla, and thus they are most likely L1/2, according to the previous description of LMC in *Papilio* (Ribi, 1987; Hamanaka et al., 2013). Spiking LMCs (Figure 1-8B) with prominent off-spikes have terminals slightly deeper in the medulla, and thus were classified as L3/4. These spikes are most likely mediated by voltage-gated $Na^+$ channels (Uusitalo et al., 1995). Whether and how the depolarizing off-transients and off-spikes are involved in information coding by LMCs is still unknown.

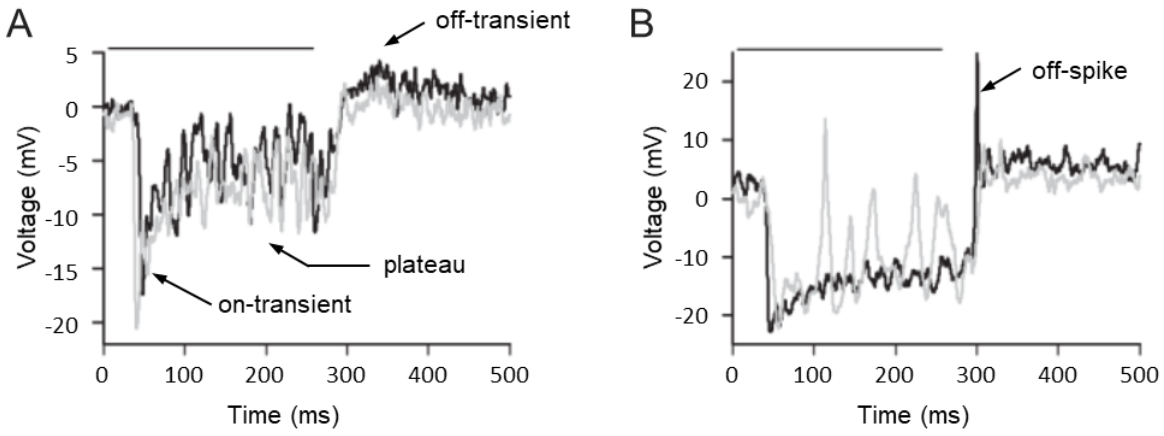


**Figure 1-8. Voltage responses of *Papilio* LMCs to light stimulation.** Voltage responses to 250 ms light pulses (*horizontal lines*). For each LMC, responses at two light intensities are presented: at an intensity where the LMC produced the highest amplitude off-spike (*black traces*), and at a ten-fold lower light level (*gray traces*). (**A**) Recordings from the L1/2 cell. (**B**) Recordings from the L3/4 cell showing a prominent off-spike. Figure modified from Rusanen et al. (2018).

The signal processing at the photoreceptor-LMC synapse is sign-reversing. The histamine acts as a kind of inhibitory neurotransmitter, hyperpolarizing the postsynaptic LMCs. Background light leads the photoreceptors to depolarize continuously and release histamine continuously (Hardie et al., 1989). Additional light stimulus can elicit additional histamine release. Suppose that the animal is viewing visual stimuli fluctuating around the mean intensity, which leads photoreceptor to depolarize continuously and release histamine continuously (Juusola et al., 1996). When the intensity slightly decreases, photoreceptors will repolarize, which reduces released histamine. Such “disinhibition” in the postsynaptic LMCs causes them to depolarize and in turn release excitatory neurotransmitter onto the third-order neurons, signaling that the light has dimmed (Stuart et al., 2007).

## 1.3 The motivation for this study

How does the nervous system process the chromatic information after the various spectral photoreceptors detect light? I have asked this question in butterflies. The high degree of diversity in their eyes provides a good basis from which it is possible to extract the common principles of how visual neurons evolved for processing chromatic information.

To analyze the spectral content of light, it is necessary to compare outputs from at least two different spectral receptors, in a process known as spectral opponency. Opponent responses, i.e. positive at some wavelengths and negative at others, provide a more accurate way of encoding wavelength information than the ratio of receptor responses (Buchsbaum and Gottschalk, 1983). In flies, the spectrally identical photoreceptors R1–R6 terminate in the lamina and thus are termed the short visual fibers (svfs), while the spectrally heterogeneous R7 and R8, which are thought to be essential for color vision (Morante and Desplan, 2004), project to the medulla and thus are termed the long visual fibers (lvfs) (Boschek, 1971; Strausfeld, 1971; Meinertzhagen and O'neil, 1991). Therefore, the medulla has been the most plausible candidate locus where the first stage of color processing takes place (Kelber, 2016). In line with this assumption, spectral opponency, a key feature in color processing, had been reported in the medulla and/or higher visual centers in several insect species: butterfly *Papilio troilus* (Swihart, 1970), honey bee *Apis mellifera* (Kien and Menzel, 1977; Yang et al., 2004), bumble bee *Bombus impatiens* (Paulk et al., 2008), locust *Locusta migratoria* (Osorio, 1986), cockroach *Periplaneta americana* (Kelly and Mote, 1990; Saari et al., 2018), and fruit fly *Drosophila melanogaster* (Schnaitmann et al., 2018).

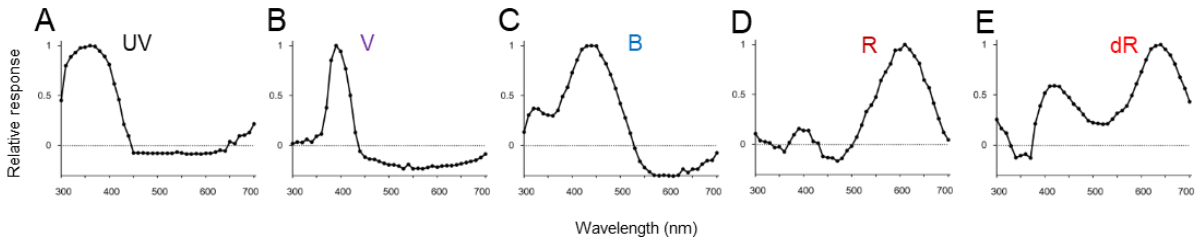


**Figure 1-9. Averaged spectral response curves of spectrally opponent photoreceptors in the retina of *Troides aeacus*.** In these photoreceptors, negative-going responses were observed when they were stimulated at certain wavelengths. (**A**) UV receptor. (**B**) Violet receptor. (**C**) Blue receptor. (**D**) Red receptor. (**E**) Deep-red receptor. Figure modified from Chen et al. (2013).

Rather unexpectedly, photoreceptors showing spectral opponency have also been found even at the level of the retina in butterflies (Horridge et al., 1983; Matić, 1983; Chen et al., 2013) (Figure 1-9). However, how and whether this phenomenon of early visual processing

is involved in butterfly color vision remains controversial, largely because the neural mechanisms underlying these antagonistic interactions are poorly understood.

Shaw (1975) first proposed that the extracellular return current passing through photoreceptor terminals as the mechanism for a similar phenomenon in locusts. Shaw's hypothesis has also been applied to the butterfly *Papilio aegeus* by Matić (1983), but this account fails to explain the case of *Troides* (Chen et al., 2013). The effect may be an artifact caused by simultaneous recording of the extracellular potential originating from neighboring photoreceptors (as in an ERG), or due to genuine synaptic interactions between photoreceptors. A recent study demonstrated in *Drosophila* that the terminals of photoreceptors R7 and R8 mutually inhibit in the medulla producing spectral opponency via histamine-gated chloride channels (Schnaitmann et al., 2018). It suggests that the *Drosophila* visual system extracts chromatic information already at the level of photoreceptors.

In terms of synaptic connections in the lamina of *Papilio xuthus*, not only the second-order neurons, LMCs, but presumably also the photoreceptors can be directly postsynaptic to photoreceptors (Takemura and Arikawa, 2006) (Figure 1-10). Histamine-gated chloride channels have been assumed to be involved in synaptic transmission and supposed to exist in the membrane of the postsynaptic cells (i.e. LMCs and photoreceptors) in *Papilio* lamina. If the channels indeed existed at putative synapses between different spectral receptors, the observed spectral opponency could be reasonably explained.

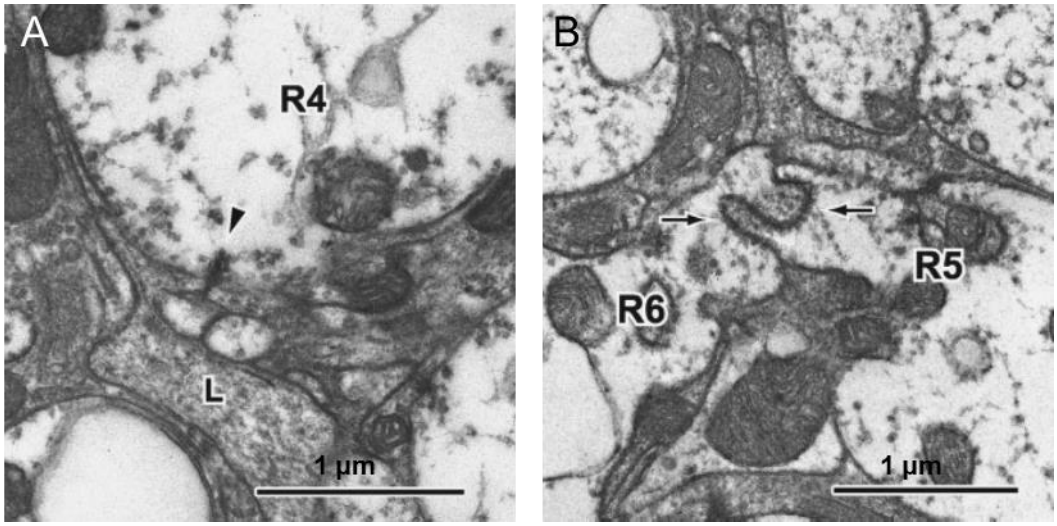


**Figure 1-10. Photoreceptor's synaptic connections in the *Papilio* lamina cartridges.** (**A**) Synapse-like contacts between the photoreceptors and LMCs (L). Photoreceptor R4 contains a contact site at the axon membrane (*arrowheads*), opposite to which is an electron-dense LMC profile. (**B**) Interphotoreceptor contacts between photoreceptors R5 and R6 (*arrows*). Figure taken from Takemura and Arikawa (2006).

The opponent photoreceptors exhibit fast-onset hyperpolarization, i.e. the time-to-peak of the hyperpolarizing responses is shorter than that of the depolarizing responses (Matić, 1983; Chen et al., 2013) (Figure 1-11). It is difficult to imagine how the extracellular return current from neighboring cells could generate a response faster than endogenous depolarization of the photoreceptor. On the other hand, this phenomenon could be explained by the action of histaminergic channels (Hardie et al., 1989). The time course of fast-onset hyperpolarization upon light stimulation that is observed in opponent photoreceptors resembles that of on-transient hyperpolarizing responses recorded in the LMCs, the second-order visual neurons of insects. The hyperpolarizing responses in LMCs are mediated by chloride channels that are activated by histamine released from depolarized photoreceptors (Hardie, 1989). Thus, I hypothesize that the putative inter-photoreceptor synapses represent a histaminergic sign-inverting mechanism between spectrally distinct receptors. This is the "histamine hypothesis" that I have proposed to account for the spectral opponency of butterfly photoreceptors (Chen et al., 2013). In fact, a similar mechanism was recently identified in the medulla of *Drosophila* (Schnaitmann et al., 2018).

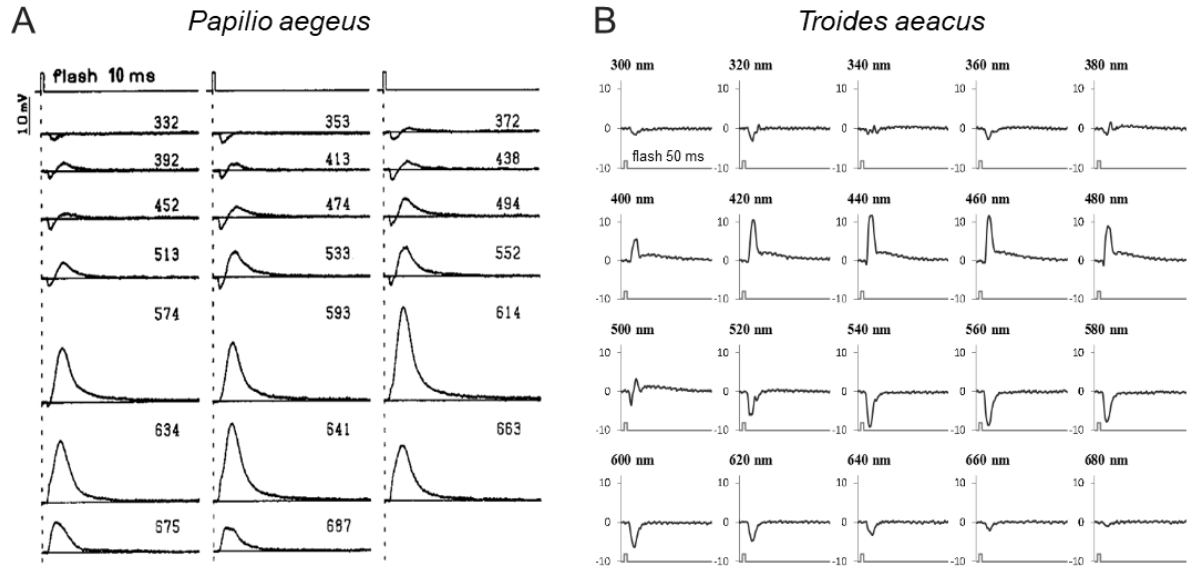


**Figure 1-11. Waveforms of spectrally opponent photoreceptors in the retina.** (**A**) Recording from *Papilio aeageus*. A red receptor shows fast-onset hyperpolarization that precedes any depolarization from 332 nm to 574 nm. Figure taken from Matić (1983). (**B**) Recording from *Troides aeacus*. A blue receptor shows fast-onset hyperpolarization between 320 nm and 380 nm as well as between 480 nm and 520 nm. Figure modified from Chen et al. (2013).

## 1.4 The significance of this project

Today's biology strongly focuses on a few "model" species, such as *Drosophila* and mice, to understand the "general" principles. This is somewhat contradictory because extensive comparison is crucial to extract such principles. The fly visual system is in fact peculiar in many aspects. For example, the projection pattern of photoreceptor axons is unique. In the lamina, eight photoreceptors originating from seven neighboring ommatidia are bundled together with five LMCs to form a lamina cartridge, in a connection scheme known as neural superposition (Hardie, 1985). Six of the eight photoreceptors R1–R6 are short visual fibers (svfs), which terminate in the lamina and are presynaptic to LMCs. The other two photoreceptors R7/R8 make no synaptic contacts in the lamina and instead send their long axons directly to the medulla, where they terminate on their postsynaptic targets; these photoreceptors are termed long visual fibers (lvfs) (Hardie, 1985). No photoreceptors have lateral processes extending into neighboring lamina cartridges in flies (Rivera-Alba et al., 2011), which also appears to be a characteristic unique to this insect order. In moths, bees and butterflies, for example, a single cartridge comprises photoreceptor axons from a single ommatidium, and these have long lateral processes penetrating into neighboring cartridges, where they form specific neuronal circuits (Ribi, 1976; Takemura and Arikawa, 2006; Stockl et al., 2016). Such variations in the lamina circuitry strongly suggest that the visual processing in the lamina is variable among species, probably reflecting differences in their visual ecology (Greiner et al., 2005) and evolutionary history.

On the other hand, *Drosophila* has a relatively incapable color vision, so this species is a rather poor choice as a model for the study of color vision. The Japanese yellow swallowtail butterfly, *Papilio xuthus*, is one of a few invertebrate species that have been studied sufficiently so that it can be concluded that they have true color vision (Kinoshita et al., 1999). They can discriminate wavelength differences of about 1 nm (Koshitaka et al., 2008), which is comparable to human performance (De Valois and Jacobs, 1968) and twenty times more sensitive than *Drosophila* (Schnaitmann et al., 2013).

Our knowledge of histamine receptors in insect visual systems is based mainly on studies of flies. This project provides the first comparative study of histamine-gated chloride channels in an insect visual system other than flies. Recent progress in the analysis of visual circuits of *Drosophila* is impressive (Wardill et al., 2012; Takemura et al., 2013; Schnaitmann et al., 2018), but studies on the more "colorful" eyes and brains of butterflies are necessary to

fully understand the neuronal basis of early color processing.

## 1.5 Aims and questions

Can the histamine hypothesis explain the recorded spectral opponency of butterfly photoreceptors? What are the roles of histaminergic channels at the early stage of color processing in the *Papilio* visual system? How and whether is the unique phenomenon of photoreceptor spectral opponency observed in butterflies involved in their color vision? This thesis attempts to answer these questions by examining the histamine-gated chloride channels, visual neurons and synaptic interactions at the initial stage of visual processing. I have performed immunohistochemistry and several electrophysiological experiments including patch clamp, single electrode switching clamp, and intracellular recording followed by dye injection to examine the following hypotheses:

- Do any histamine-gated chloride channels exist at the presumptive inter-photoreceptor synapses? (Chapter 2)
- Whether and what channel properties of histaminergic receptors are similar across species? (Chapter 3)
- How are the visual signals conveyed to the second-order visual neurons, LMCs, through histaminergic synapses in the *Papilio* lamina? (Chapter 4)
- Could the spectral responses of opponent photoreceptor be explained by inter-photoreceptor connections? (Chapter 5)
- How diverse are the spectrally opponent pathways in the early visual system of *Papilio*? (Chapter 5)

At the end of this thesis, I will discuss the evolutionary insights into neuronal principles underlying chromatic processing from a comparative point of view on differences in histaminergic channels in the visual systems of butterflies and flies.

# Chapter 2

## Immunolocalization of histamine-gated chloride channels in the *Papilio* visual system

This chapter is based on the following paper:

**Immunolocalization suggests a role of the histamine-gated chloride channel PxHCLB in spectral opponent processing in butterfly photoreceptors**

Pei-Ju Chen, Atsuko Matsushita, Motohiro Wakakuwa, Kentaro Arikawa (2018)

Journal of Comparative Neurology

doi: 10.1002/cne.24558

## 2.1 Abstract

Spectrally opponent responses, i.e. wavelength-dependent inversions of response polarity, have been observed at the level of photoreceptors in butterflies. Since anatomical inter-photoreceptor connections have been found in the butterfly *Papilio xuthus*, and histamine is the only neurotransmitter so far identified in insect photoreceptors, I hypothesize that histaminergic sign-inverting synapses exist in the lamina between different spectral receptors as a mechanism for spectral opponency as in the medulla of *Drosophila*. Here, I localized two histamine-gated chloride channels, PxHCLA (*Drosophila* HCLA homolog) and PxHCLB (*Drosophila* HCLB homolog), in the visual system of *Papilio xuthus* by using specific antisera. The anti-PxHCLA labeling was associated with the membrane of non-photoreceptor cells that are postsynaptic to photoreceptors, while the anti-PxHCLB labeling overlapped with photoreceptor axons, indicating that PxHCLB is expressed at inter-photoreceptor synapses: PxHCLB is likely involved in producing spectral opponency at the first visual synapses. Color processing in *Papilio* may appear earlier than previously hypothesized in insect visual systems.

Keywords: insect, compound eye, photoreceptor, lamina, medulla, histamine receptor

## 2.2 Introduction

The medulla has long been considered as the most plausible candidate where the processing of color information begins in insect visual systems (Kelber, 2016). However, I frequently encountered photoreceptors that exhibited spectral opponency in the retina of a butterfly *Troides aeacus* (Chen et al., 2013). In fact, such opponent responses seem rather common in butterflies (Horridge et al., 1983; Matić, 1983; Chen et al., 2013), but their origin remains unknown. Recently, Schnaitmann et al. (2018) convincingly demonstrated in *Drosophila* that the terminals of photoreceptors R7 and R8 mutually inhibit in the medulla producing spectral opponency via a histamine-gated chloride channel, HCLB. Histamine is the only neurotransmitter so far identified in insect photoreceptors (Hardie, 1987), so the same mechanism may underlie the spectral opponency in butterfly photoreceptors.

In the lamina of *Papilio xuthus*, numerous synapse-like structures have been found between photoreceptors, as they form characteristic inter-photoreceptor connections (Takemura and Arikawa, 2006). Upon light stimulation, photoreceptors depolarize and in turn release histamine which results in hyperpolarizing the postsynaptic target. Thus, I hypothesize that the putative inter-photoreceptor synapses represent a histaminergic sign-inverting mechanism between spectrally dissimilar receptors. This is the "histamine hypothesis" that I have proposed to account for the spectral opponency of butterfly photoreceptors (Chen et al., 2013).

Do any histamine-gated chloride channels exist at the presumptive inter-photoreceptor synapses in the *Papilio* lamina? To address the question, I used immunohistochemistry to localize two recently identified histamine-gated chloride channels, PxHCLA (*Drosophila* HCLA homolog) and PxHCLB (*Drosophila* HCLB homolog) (Akashi et al., 2018), at both the light microscopic (LM) and electron microscopic (EM) levels. Briefly, PxHCLA is expressed in lamina monopolar cells (LMCs) — second-order neurons postsynaptic to photoreceptors — as is the case in *Drosophila* (Gengs et al., 2002; Gao et al., 2008), whereas the PxHCLB expression is associated with photoreceptor axons. The expression of PxHCLB at inter-photoreceptor synapses is consistent with the recent study in the *Drosophila* medulla (Schnaitmann et al., 2018). However, the distribution of PxHCLB immunoreactivity in the lamina is dissimilar to that of HCLB in *Drosophila*, where the channel is exclusively found in glial cells (Pantazis et al., 2008). The differences in distribution of histamine receptors in the visual systems of butterflies and flies suggest that considerable variation exists between the neural circuits of these species.

## 2.3 Materials and Methods

### *Animals*

Adult Japanese yellow swallowtail butterflies, *Papilio xuthus* Linnaeus, of both sexes were obtained from a laboratory stock culture derived from eggs laid by females caught around the campus of Sokendai, Kanagawa, Japan. The hatched larvae were fed with fresh citrus leaves, and raised under a short light regime (light: dark = 10 h: 14 h) at 25°C in the laboratory. The pupae were stored at 4°C for at least 3 months and then allowed to emerge at 25°C.

### *Reverse transcription polymerase chain reaction*

Dr. Motohiro Wakakuwa extracted polyA-RNA separately from the distal portion (contained the distal retina) and the proximal portion (contained a part of the proximal retina and the lamina) of the compound eye (Wakakuwa et al., 2003) using QuickPrep micro mRNA purification kit (GE Healthcare, Uppsala, Sweden). I carried out RT-PCR using specific primers to amplify fragments of mRNAs encoding PxHCLA (forward primer, TACCCGCGAA CTATGAAGAC; reverse primer, TTAGATGTAT TGCGCAAATT GTAT) and PxHCLB (forward primer, ACGAGATGAG CATACCCAAC C; reverse primer, CTCTTGAAAG ATTCTTTCGC AAAC).

### *Antisera production*

Dr. Motohito Wakakuwa produced polyclonal antisera against PxHCLA in rabbit (RRID: AB_2737352) and rat (RRID: AB_2737353), and against PxHCLB in rabbit (RRID: AB_2737354) and purified to > 70% purity. For each antiserum production, I mixed two pairs of oligo peptides. Sequences used for PxHCLA were PEDPKLYDKMRPPKKNDQ and TSEYRLLDLDWLKHM; for PxHCLB were ASYQEMEIKSESSLS and KAKYYDKNRAPKLLG. On the other hand, the antiserum specific to the *P. xuthus* UV opsin, PxUV, made in guinea pig, was kindly provided by Dr. Michael Perry.

### *Immunoblot analysis*

The specificity of these antisera was confirmed by immunoblot analysis. The retina and optic lobe were collected from compound eyes for protein extraction. Tracheae were removed as far as possible. The samples were homogenized in extraction butter containing 50 mM HEPES, 0.75% CHAPS, 0.8 mg/mL L-α-Phosphatidylcholine, 140 mM NaCl, 1 mM DTT, 1 μg/mL

aprotinin, and 1 μg/mL leupeptin (pH 6.5). The homogenate was centrifuged at 15,000 g for 10 min at 4°C. The supernatant was collected and mixed with equal volume of the SDS-PAGE Laemmli's sample buffer (Laemmli, 1970). The extracts were boiled for 5 min before loaded onto a 10% SDS-PAGE gel with either 0.4% or 0.5% N,N'-methylene-bis-acrylamide. Dual color (161-0374, Bio-Rad, Hercules, CA) and unstained (161-0363, Bio-Rad, Hercules, CA) protein standards were used to monitor protein transfer and to estimate the molecular mass, respectively. After being separated by electrophoresis, the protein samples were blotted onto polyvinylidene difluoride (PVDF) membrane with a semi-dry blotter (Bio Craft, Tokyo, Japan). The blotted proteins were stained with Coomassie Brilliant Blue R-250 (0.025% in destaining solution) for 5 min, followed by two changes of a methanol/acetic acid/water (5:1:4) destaining solution. Columns on the membrane were visible, and each column was cut into two halves for further detection by the specific primary antisera and their corresponding pre-immune sera. After destaining in pure methanol, the PVDF membrane was thoroughly washed with 0.1% Tween 20 in phosphate-buffered saline (PBST, pH 7.4).

To block non-specific binding sites, the PVDF membranes were incubated with avidin blocking solution for 15 min, and, after washing, biotin blocking solution for 15 min (endogenous avidin/biotin blocking kit; Abcam, Cambridge, MA), followed by 1 h incubation with 10% normal goat serum (NGS) containing 1% bovine serum albumin (BSA) in PBST at room temperature. The PVDF membrane was then incubated overnight with specific primary antibody and with the corresponding pre-immune serum: rat antiserum against PxHCLA (1:500), or rabbit antiserum against either PxHCLA (1:1,000) or PxHCLB (1:1,000) in 1% BSA in PBST at 4°C. The antibodies were detected by using the avidin-biotin complex method followed by DAB (3,3'-diaminobenzidine). The membrane was incubated at room temperature sequentially in the biotinylated goat anti-rat or anti-rabbit IgG secondary antiserum (Vector Laboratories, Burlingame, CA) at a dilution of 1:200 in PBST for 30 min and a 1:50 dilution of the avidin-biotin-peroxidase complex (ABC Kit; Vector Laboratories, Burlingame, CA) in PBST for 30 min. After washing with PBST, the bound peroxidase was visualized by reaction in 0.05% DAB solution containing 0.04% nickel ammonium sulfate and 0.0015% hydrogen peroxide ($H_2O_2$) until adequate stain intensity was observed.

***Photoreceptor axon tracing***

For tracing photoreceptor axons, I injected fluorescence dyes in the retina. A 1–2 mm wide window was made in the lateral region of eye, and then a pair of forceps with crystals of Texas

Red (TR)-conjugated dextran (for immunofluorescence microscopy) or Lucifer Yellow (LY, for immunoelectron microscopy) on the tip was manually inserted into the distal tier of the retina under a dissecting microscope. The window was covered with the excised cuticle, and sealed with a drop of Vaseline. The dye-injected butterflies were left overnight at 4°C to allow the injected dye to be taken up by photoreceptors. The injected eyes were then prepared as follows.

***Immunofluorescence microscopy***

The TR-injected compound eyes were fixed in 4% paraformaldehyde in 0.1 M phosphate buffer (PB; pH 7.4) and then microwave-irradiated six times for 5 s each (total 30 s). After further incubation in the fixative for 1 h on ice with gentle shaking, the cornea was removed. The eyes were briefly washed with 0.1 M PB, dehydrated with a graded series of ethanol followed by 100% terpineol, and infiltrated with xylene. The eyes were embedded in Paraplast (Sigma, USA) and sectioned at 8 μm thickness. Serial sections mounted on hydrophilic-coated slides (Mas-coated slides, Matsunami Glass) were deparaffinized with xylene and rehydrated through an ethanol series. The slides were transferred to a glass jar filled with boiling 10 mM EDTA (pH 8.0) and heated by microwave irradiation at 500 W for 5 min, then left for 2 h in the warm buffer to cool down slowly to room temperature. After this microwave antigen retrieval step, the sections were washed briefly with PBST. Non-specific binding sites for antibodies were blocked by treating the sections with 10% NGS containing 1% BSA in PBST for 2 h at room temperature. The sections were then incubated with the primary antiserum against either PxHCLA or PxHCLB for 2–3 overnights at 4°C, at the dilution of 1:1,000 (in 1% BSA in PBST) for the rat anti-PxHCLA and 1:10,000 for both rabbit anti-PxHCLA and rabbit anti-PxHCLB. To identify the ommatidial types in the retina, some sections were incubated with guinea pig anti-PxUV (1:100). To visualize neuropil structures, sections were simultaneously incubated with a mouse monoclonal anti-synapsin (1:50, DSHB Cat# 3C11, RRID:AB_528479), a presynaptic marker.

After washing in PBST, the sections were incubated in corresponding secondary antibodies Alexa Fluor 488 (green fluorescence), Alexa Fluor 647 (red fluorescence), or Cy3 (red fluorescence) goat anti-rabbit, goat anti-rat, or goat anti-mouse IgG conjugates (1:200; Molecular Probes, Eugene, OR) in PBST for 1 h at room temperature. For double labeling of anti-PxHCLB and anti-PxUV, some sections were first incubated with biotinylated goat anti-guinea pig IgG (1:200) for anti-PxUV for 1h at room temperature and then with a mixture of anti-rabbit Cy3-conjugated IgG (1:200) and Alexa Fluor 405-conjugated streptavidin (1:200)

in TPBS for 1 h at room temperature.

For localization of cell bodies, some sections were then stained with NeuroTrace 435/455 (N-21479, Invitrogen) for Nissl staining (1:200) for 20 min at room temperature. After further PBST wash, sections were mounted in Vectashield (H-1000, Vector Laboratories, Burlingame, CA). All slides were stored in the dark at 4°C until examination. Fluorescent images were taken using a fluorescence microscope (BX-60, Olympus) and a confocal microscope (A1Rsi, Nikon, Japan). Images were adjusted for contrast and brightness using Adobe Photoshop CS (Adobe Systems, San Jose, CA) and their colors were converted from Red-Green-Blue (RGB) to the color-blind-friendly Magenta-Green-Blue using ImageJ.

***Immunoelectron microscopy***

The LY-injected eyes were isolated and prefixed in 4% paraformaldehyde and 0.05% glutaraldehyde in 0.1 M PB overnight at 4°C. The cornea was removed in advance. After a brief wash with 0.1 M PB, the eyes were treated for antigen retrieval as described above. After washing with 0.1 M PB, the eyes were embedded in 35% gelatin, and sections (30–50 μm thick for cross and 50–100 μm thick for horizontal sections of optic lobe) were cut with a vibratome (Leica VT1000S, Wetzlar, Germany). The sections were collected in cold 0.1M PB and briefly checked whether or not LY injection was successful under a fluorescence microscope. After removing gelatin, the sections were washed briefly with PBST. For pre-embedding labeling, the sections were blocked in 10% NGS containing 1% BSA in PBST overnight at 4°C. The sections were then incubated with the respective primary antibodies in 1% BSA in PBST for 3–4 overnights at 4°C at the dilution of 1:10,000 for rabbit anti-PxHCLA and 1:20,000 for rabbit anti-PxHCLB.

The sections were washed in PBST, and then incubated in the biotinylated goat anti-rabbit IgG secondary antiserum (Vector Laboratories, Burlingame, CA) at a dilution of 1:200 in PBST for 2 h. After a further wash in PBST, a peroxidase-based enzymatic detection system was applied to provide immunocomplex of biotinylated secondary antibody by reacting with the avidin-biotin-peroxidase complex (ABC Kit; Vector Laboratories, Burlingame, CA) at a dilution of 1:50 in PBST for 2 h. After washing in PBST followed by 0.1 M PB, the sections were pre-incubated in 0.05% DAB in 0.1 M PB containing 0.04% nickel ammonium sulfate for 10 min. The immunocomplex was subsequently visualized by adding 0.0015% $H_2O_2$ to DAB solution. When adequate stain intensity was obtained, the reaction was stopped immediately by a quick wash and incubation in 0.1 M PB. The vibratome sections were then postfixed in 1%

osmium tetroxide ($OsO_4$) in 0.1 M PB for 1 h at room temperature. After washing and dehydration in ethanol series, sections were infiltrated with propylene oxide, embedded in Quetol 812 resin (Nisshin EM, Tokyo Japan), and polymerized overnight at 60°C.

Ultrathin sections, cut with a diamond knife, were mounted on nickel grids. For post-embedding labeling of LY-filled photoreceptors, the sections were briefly washed in 0.25% fish gelatin in sodium phosphate buffer (PBSG, pH 7.4) and then blocked with 4% BSA in PBSG for 1 h. Subsequently, the sections were incubated with rabbit anti-LY polyclonal antibody (1:400, Sigma-Aldrich Cat# L9163, RRID:AB_260435) for 3 overnights at 4°C. Note that anti-LY was raised in rabbit which was same to pre-embedding primary antibodies of PxHCLs. According to previous studies (Chan et al., 1990; Marcos et al., 1997), DAB immunoreaction products mask the epitopes of the reagents of the first sequence and thus prevent interaction with the reagents of the following sequence. I therefore carried out the post-embedding with goat anti-rabbit IgG conjugated to 15 nm gold particles (1:50 in PBSG; British BioCell, Cardiff, UK) on DAB-treated sections for 1 h at room temperature. After washing with PBSG followed by distilled water, the sections were examined and photographed with a transmission electron microscope (H7650, Hitachi, Tokyo) equipped with a digital camera (Quemesa, Olympus, Münster, Germany).

## 2.4 Results

### *Production and characterization of anti-PxHCL antisera*

I obtained antisera against the *Papilio xuthus* homologs of (*Drosophila*) histamine-gated chloride channels, PxHCLA and PxHCLB, for immunohistochemistry. The specificity of these antisera has been confirmed by immunoblot analysis (Figure 2-1). The results include control labeling using pre-immune antisera of the corresponding animals.

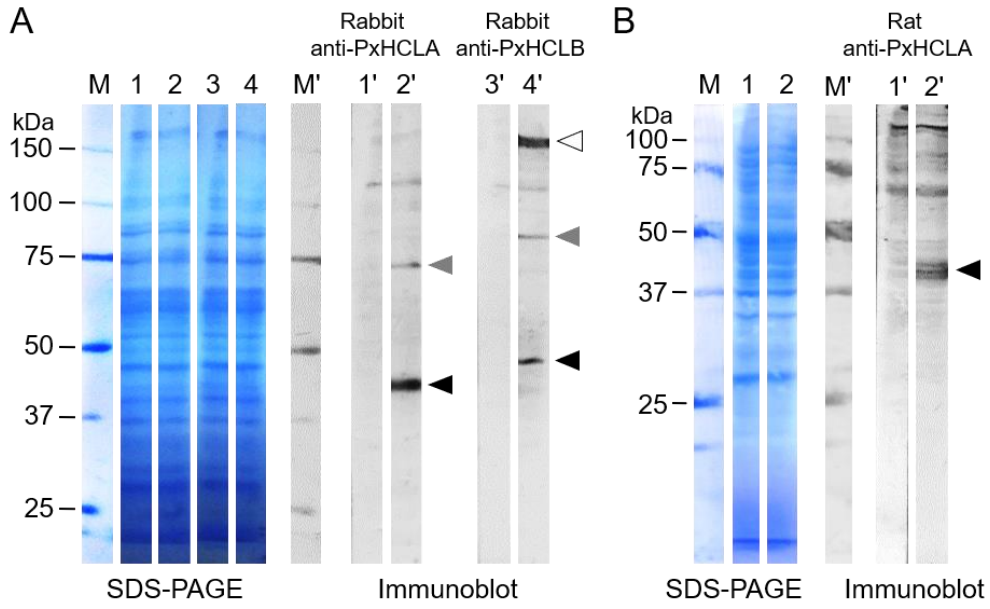


**Figure 2-1. SDS-PAGE profile and immunoblot analysis of the anti-PxHCL antisera.** Immunoblotting was performed using PxHCL antisera produced in a rabbit (**A**) and a rat (**B**). *Black*, *gray*, and *white arrowheads* indicate bands corresponding to monomer, dimer, and trimer, respectively. M and M': molecular mass markers. (**A**) Lane 1–4: SDS-PAGE (with 0.4% N,N'-methylene-bis-acrylamide) profile of proteins solubilized from *Papilio* compound eye. Lane 1'–4': immunoblots detected by the rabbit antiserum against PxHCLA (2') and its pre-immune serum (1'), as well as PxHCLB (4') and its pre-immune serum (3'). The rabbit anti-PxHCLA antiserum detects 43.6 kDa and 81.2 kDa protein bands, while the rabbit anti-PxHCLB antiserum detects 47.9 kDa, 94.1 kDa and 156.8 kDa protein bands. (**B**) Lane 1–2: SDS-PAGE (with 0.5% N,N'-methylene-bis-acrylamide) profile of proteins solubilized from *Papilio* compound eye. Lane 1'–2': immunoblotting detected by rat antiserum against PxHCLA (2') and its pre-immune serum (1'). The rat anti-PxHCLA antiserum detects a 43.9 kDa protein band.

The rabbit pre-immune sera showed a nonspecific band at a molecular mass of ~120 kDa (Figure 2-1A) and the rat pre-immune serum showed some nonspecific bands between 65 kDa and 120 kDa (Figure 2-1B). Excluding these nonspecific backgrounds, the rabbit anti-PxHCLA labeled a band at approximately 43.6 kDa and the rat anti-PxHCLA at 43.9 kDa. These are consistent with the molecular mass of PxHCLA monomer deduced from its amino acid sequence: 43.8 kDa. The rabbit anti-PxHCLA labeled another band at about 81.2 kDa, which is almost double the deduced mass and thus may represent a dimer of PxHCLA.

The rabbit anti-PxHCLB labeled three bands at molecular masses of approximately 47.9 kDa, 94.1 kDa, and 156.8 kDa. As the deduced molecular mass of PxHCLB monomer is 47.7 kDa, these are likely monomer, dimer, and trimer, respectively. The histamine-gated chloride channels belong to the Cys-loop receptor family (Thompson et al., 2010), and each functional receptor is formed by five subunits (see Figure 1-3). The appearance of PxHCL dimer and trimer on the immunoblot is probably attributable to incomplete solubilization of aggregated PxHCL subunits.

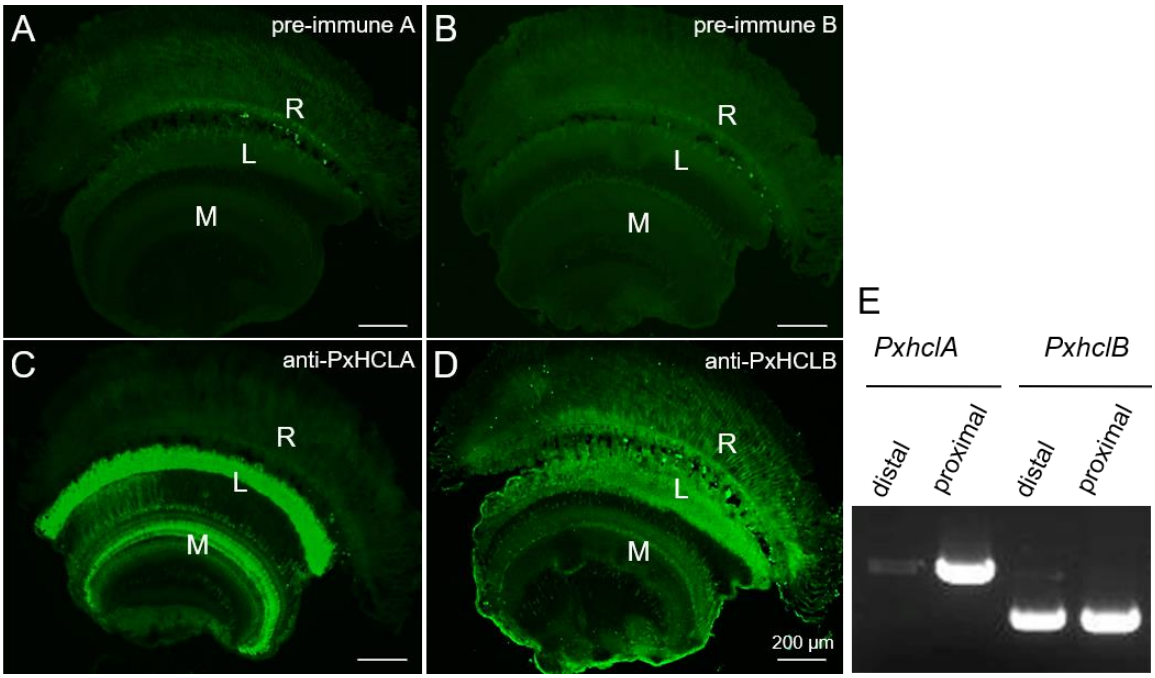


**Figure 2-2. Characterization of the anti-PxHCL antisera in the *Papilio* eye.** (**A**–**D**) Serial horizontal sections through the *Papilio* optic lobe were exposed to the rabbit anti-PxHCLA (**C**) and its pre-immune serum (**A**), as well as the rabbit anti-PxHCLB (**D**) and its pre-immune serum (**B**), visualized with a Cy3-conjugated secondary antibody. R, retina; L, lamina; M, medulla. The anti-PxHCLA labeled the lamina and some distinct layers of the medulla. The anti-PxHCLB labeled the proximal retina, the lamina, and a thin layer of the medulla. (**E**) The expression of *PxhclA* and *PxhclB* mRNA in the *Papilio* eye. The eyes were separated into distal and proximal portions. The former contained the distal retina only, while the latter contained a part of the proximal retina and the lamina. The *PxhclB* mRNA was detectable in both distal and proximal portions of retina, whereas the *PxhclA* mRNA was detected only in the proximal portion.

In immunohistochemical experiments, I simultaneously ran controls using pre-immune sera to exclude non-specific binding signals. The control labeling produced weak background fluorescence (Figure 2-2A,B). Both PxHCLA and PxHCLB antisera labeled the lamina and the medulla (Figure 2-2C,D), while the anti-PxHCLB labeled the retina as well (Figure 2-2D). The anti-PxHCLB immunolabeling was weaker than that of anti-PxHCLA. A similar phenomenon of limited HCLB labeling has also been reported in *Drosophila* (Gisselmann et al., 2002; Witte et al., 2002; Gao et al., 2008; Pantazis et al., 2008). This may

be due to a lower expression level of PxHCLB and/or the antisera being of non-optimal binding efficiency. Nevertheless, I could detect a characteristic distribution of PxHCLB in this study.

The RT-PCR revealed distinct distribution of mRNAs encoding PxHCLA and PxHCLB in the retina (Figure 2-2E). Both were expressed in the "proximal" sample (including a part of the proximal retina and the lamina, see Figure 7A of Wakakuwa et al. (2003)), while the "distal" sample (containing the distal retina) expressed only PxHCLB mRNA, not PxHCLA (Figure 2-2E). These results suggest that PxHCLB is somehow associated with photoreceptors.

***Localization of PxHCLs around the lamina***

Figure 2-3A–D are horizontal sections showing the basal part of retina, the fenestrated layer, which is fenestrated (= windowed) due to tracheae between which bundles of photoreceptor axons pass through, and the lamina. Both antisera intensely labeled around the lamina, but with different patterns. Anti-PxHCLA labeled the whole lamina (Figure 2-3A), while anti-PxHCLB labeled the proximal retina, fenestrated layer, as well as lamina (Figure 2-3C). I also localized cell bodies by Nissl staining (*magenta* in Figure 2-3B,D) after immunohistochemistry. The large cell bodies immediately proximal to the basement membrane are those of tracheal cells (Wakakuwa et al., 2004a). Medium-sized cell bodies within the lamina may be those of glial cells, but they have not been properly identified. Cell bodies of LMCs are densely packed between the proximal portion of the fenestrated layer and the distal border of the lamina (Figure 3b,d, arrowheads; Takemura et al., 2005; Hamanaka et al., 2012). The anti-PxHCLA labeling surrounded the cell bodies in the distal region of the lamina, while no labeling was detected in the fenestrated layer (Figure 2-3B). In contrast, anti-PxHCLB labeled the fenestrated layer, with no labeling around cell bodies of LMCs (Figure 2-3D).

I performed double labeling with anti-PxHCLA and anti-PxHCLB in cross sections through the lamina where photoreceptor axons were pre-labeled with TR-conjugated dextran (Figure 2-3E–J) to determine the relationship of photoreceptors and the channel candidates. Figure 2-3F shows an array of modules called lamina cartridges (*dotted oval*). Each cartridge contains nine photoreceptor axons originating from a single ommatidium and at least four LMCs (Ribi, 1987; Takemura and Arikawa, 2006). Eight photoreceptors R1–R8 (Figure 2-3F, *asterisks*) are visible; the axon of R9 is too small to be identified at the LM level. The anti-PxHCLA immunolabeling exhibited a web-like pattern (Figure 2-3E) appearing between photoreceptor axons within each lamina cartridge whilst being absent from its center (Figure 2-3H). I sometimes observed thin PxHCLA-positive processes surrounding the cartridges (Figure

2-4A–E, *arrows*). These processes may contain those of not only neurons but glial cells, but I have no direct evidence for this so far. In contrast, PxHCLB immunoreactivity was detected in each cartridge overlapping with photoreceptor axons (Figure 2-3J). The merged view of anti-PxHCLA and anti-PxHCLB labeling reveals little overlap (Figure 2-3I). Most likely, PxHCLA and PxHCLB exist in LMCs and photoreceptors, respectively.

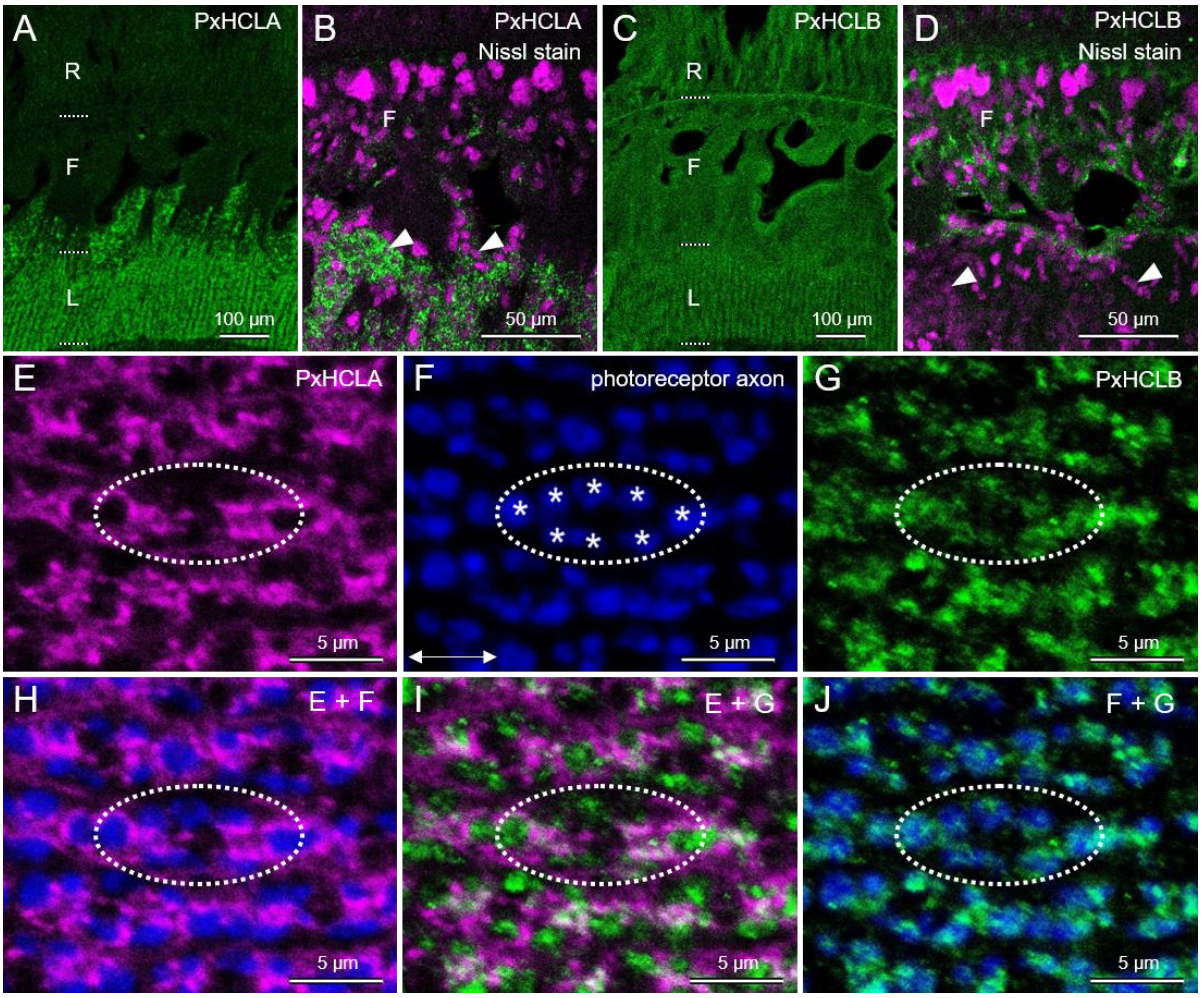


**Figure 2-3. Immunofluorescence localization of PxHCLA and PxHCLB around the *Papilio* lamina.** (**A**–**D**) Horizontal sections of the eye showing from the basal region of the retina (R) to the proximal end of the lamina (L) at lower magnification (**A,C**) and at higher magnification (**B,D**), double labeled with either anti-PxHCLA (*green* in **A,B**) or -PxHCLB (*green* in **C,D**) and Nissl stain (*magenta* in **B,D**). (**A**) Strong labeling of anti-PxHCLA was found throughout the lamina but not in other regions. (**B**) The fenestrated layer (F) represents the path of the photoreceptor axons, and cell bodies of LMCs (*arrowheads*) are packed in the proximal fenestrated layer. Anti-PxHCLA labeling was detected around cell bodies but not in the fenestrated layer. (**C,D**) Anti-PxHCLB labeling was detected in the proximal retina, fenestrated layer and lamina, while no labeling was observed around cell bodies (*arrowheads*). (**E**–**J**) A cross section through the lamina, double labeled with rat anti-PxHCLA (*magenta* in **E,H,I**) and rabbit anti-PxHCLB (*green* in **G,I,J**), along with TR-injected photoreceptor axons (*blue* in **F,H,J**). PxHCLA immunoreactivity was found between photoreceptor axons within cartridges. In contrast, PxHCLB immunoreactivity largely overlapped with photoreceptor axons. *Dotted ovals* in **E**–**J** indicate the same single cartridge. *Asterisks* in **F** indicate axons of R1–R8. A *double-headed arrow* in **F** indicates dorso-ventral axis.

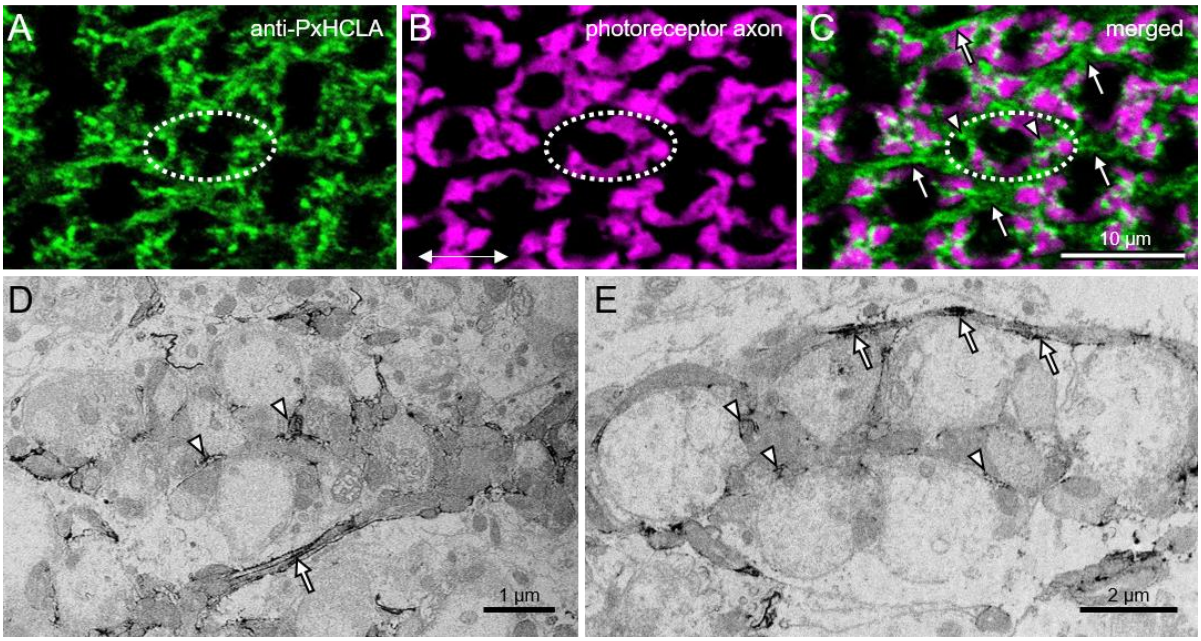


**Figure 2-4. The PxHCLA-positive processes surrounding lamina cartridges in the *Papilio* lamina.** (**A**–**C**) A cross section through the lamina, labeled with ranti-PxHCLA (*green* in **A,C)**. TR was injected in the photoreceptors (*magenta* in **B,C**). The anti-PxHCLA immunolabeling was detected within (*arrowheads*) and around (*arrows*) the lamina cartridges. (**D,E**) The PxHCLA-immunopositive processes within (*arrowheads*) and around (*arrows*) cartridges were found also in immunoelectron microscopy with DAB staining. A *double-headed arrow* in **B** indicates dorso-ventral axis.

My double labeling immunoelectron microscopy further revealed subcellular distribution of these channel candidates. I visualized the labeling with anti-PxHCLA or anti-PxHCLB with pre-embedding DAB staining, while I identified photoreceptors by injecting Lucifer Yellow (LY) detected by post-embedding immunogold labeling using rabbit anti-LY. First, I performed control labeling ensuring that the secondary antibody did not interact with the epitopes of anti-PxHCLs: no gold particles were observed in the DAB-treated sections when the anti-LY was omitted from the post-embedding experiment (data not shown). Furthermore, the immunogold labeling of anti-LY did not overlap with DAB reaction for anti-PxHCLs, indicating the negative cross-reactivity of anti-rabbit colloidal gold secondary antibody in double labeling even if two antibodies were produced in the same animal species. This method was established previously and has been applied to other systems (Chan et al., 1990; Marcos et al., 1997).

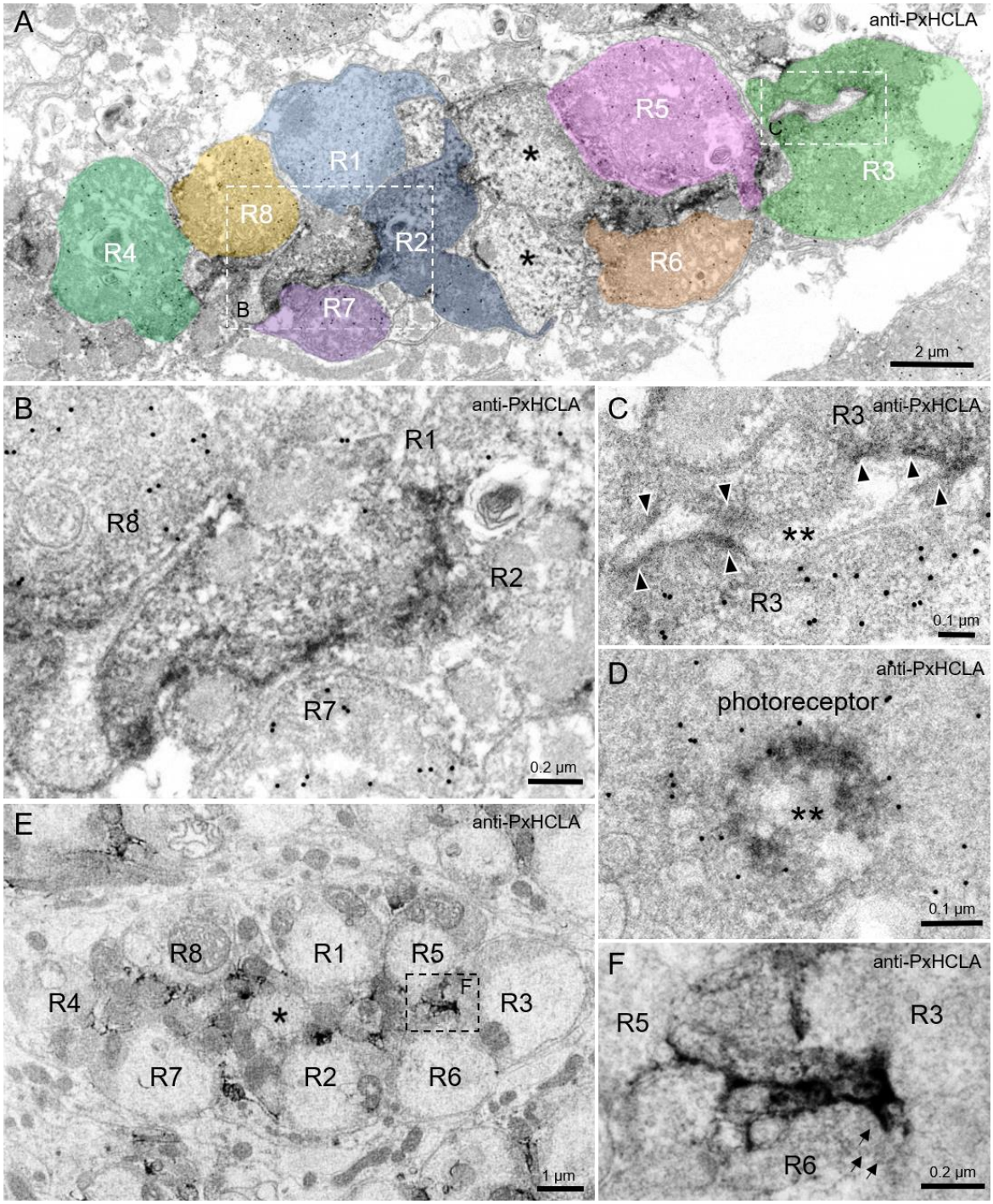


**Figure 2-5. Immunoelectron microscopic localization of PxHCLA in the *Papilio* lamina.** Cross sections through lamina cartridge at a middle depth of the lamina, labeling with anti-PxHCLA visualized by pre-embedding DAB staining. (**A,E**)The anti-PxHCLA immunoreactivity was detected outside of photoreceptors, indicating PxHCLA exists in the non-photoreceptor cells. Colored patches in *a* indicate LY-injected photoreceptor cells (R1–R8), identified by post-embedding anti-LY immunogold labeling. *Asterisks* in **A** and **E** indicate PxHCLA-immunonegative non-photoreceptor cells in the central region of the cartridge. (**B,F**) The anti-PxHCLA immunoreactivity was associated with the plasma membrane of non-photoreceptor cells that contact to photoreceptors. *Arrows* in **F** denote presumed synaptic vesicles in the photoreceptor cytoplasm near the membrane facing the PxHCLA-positive cell. (**C,D**) Some anti-PxHCLA immunolabeling was found on the membrane of non-photoreceptor cell (*double asterisks*) processes penetrating into photoreceptors. *Arrowheads* in **C** denote DAB labeled membrane structures.

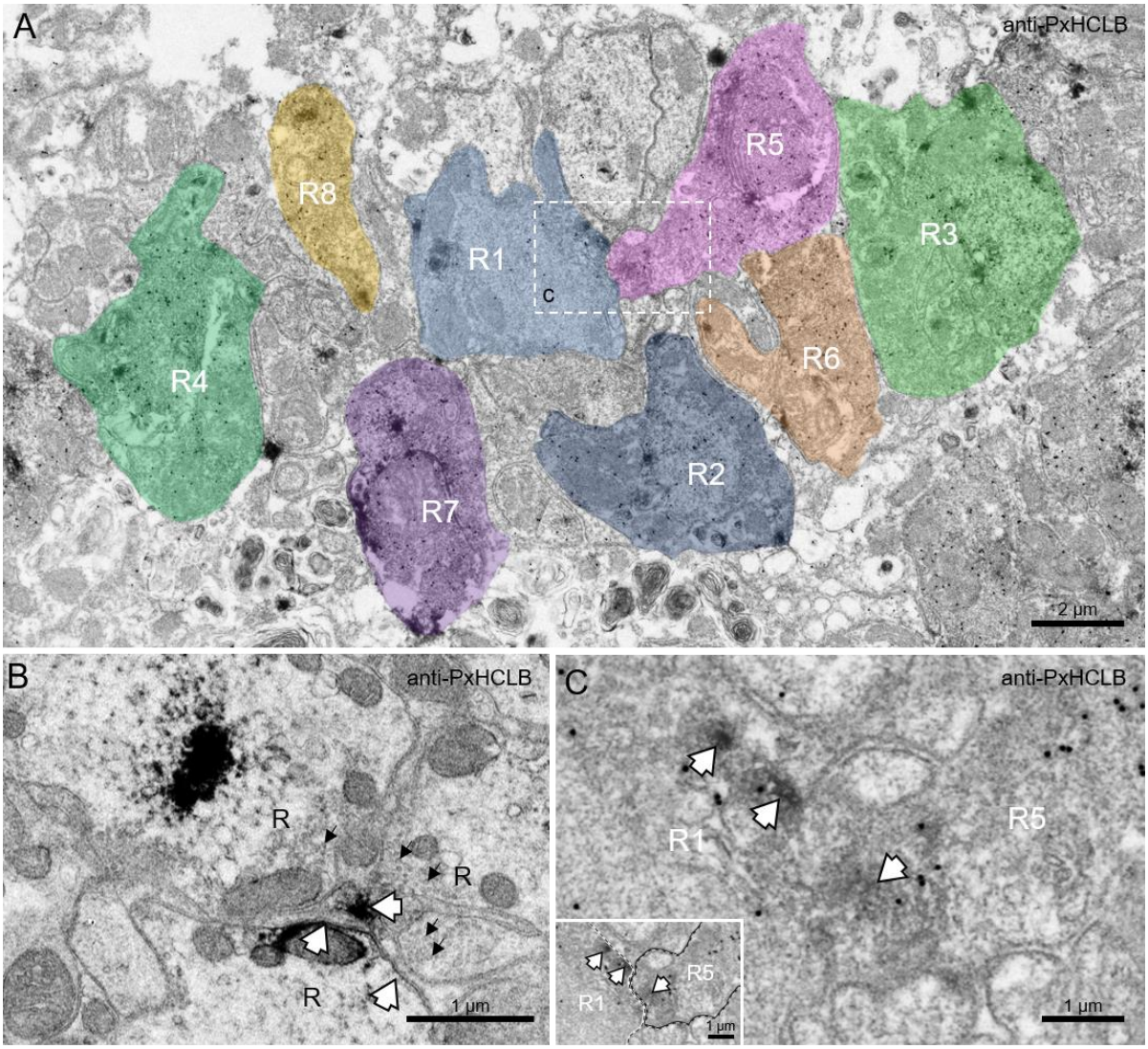


**Figure 2-6. Immunoelectron microscopic localization of PxHCLB in the *Papilio* lamina.** Cross sections through a lamina cartridge labeled with anti-PxHCLB, visualized by pre-embedding DAB staining. (**A**) The LY-injected photoreceptor cells (R1–R8) were identified by post-embedding anti-LY immunogold labeling. The anti-PxHCLB immunoreactivity was associated with photoreceptors. (**B**) The anti-PxHCLB immunolabeling was detected within photoreceptor axons as well as on photoreceptor membranes facing to adjacent photoreceptors which contained a dense region of synaptic vesicle-like structures (*small arrows*). (**C**) The immunoreactive profiles of anti-PxHCLB lie around the membrane of photoreceptors (*white arrows*), indicating possible inter-photoreceptor synaptic contacts between R1 and R5. *Dashed lines* in inset denote membrane borders of photoreceptors R1 and R5.

Photoreceptors R1–R8 were distinguishable based on the immunogold labeling of anti-LY. The DAB immunoreaction products of anti-PxHCLA (Figure 2-5A,E) showed the immunoreactivity in regions between photoreceptors and absent from the cartridge center as observed at the LM level (Figure 2-3E,H). This unlabeled central region contains non-photoreceptor cells (Figure 2-5A,E, *asterisks*), which most likely correspond to the main trunks of LMCs. Figure 2-5B and 5F show that the anti-PxHCLA labeling is associated with the

plasma membrane of non-photoreceptor cells. Inside photoreceptor cells, I observed a collection of synaptic vesicle-like structures of ca. 30 nm in diameter, clustered adjacent to the DAB-labeled cells (Figure 2-5F, *arrows*); these PxHCLA-expressing cells are most likely LMCs. On the other hand, the labeling was found in the photoreceptor region as well (Figure 2-5C,D). There were distinctive membrane structures (Figure 2-5C, *arrowheads*) between the immunogold-positive region and immunogold-negative region (*double asterisks*), suggesting the labeled compartments are processes of LMCs penetrating into the photoreceptor (Takemura and Arikawa, 2006). These labeling characteristics indicate that the PxHCLA channels are mainly expressed on the lateral processes of LMCs, rather than their main trunks.

The anti-PxHCLB showed a distinct labeling pattern from anti-PxHCLA. A number of immunoreactive profiles of anti-PxHCLB were detected around the membranes of adjacent photoreceptors (Figure 2-6B,C, *white arrows*), suggesting a functional role of PxHCLB at inter-photoreceptor synapses. Notably, those located on the plasma membrane are presumably functional histamine receptors. Some of the labeling lies within photoreceptor cytoplasm far from the membrane, which probably indicates immature PxHCLB peptides.

***Localization of PxHCLs in the medulla***

I carried out double immunofluorescence labeling using anti-PxHCLs (either anti-PxHCLA or anti-PxHCLB) and anti-synapsin in the medulla where photoreceptors were pre-injected with TR-conjugated dextran (Figure 2-7A–F). I thus determined the possible distribution of PxHCLs as well as their relationship with the long visual fiber (lvf) terminals. The medulla exhibits eight layers based on the anti-synapsin labeling pattern (Hamanaka et al., 2012). The anti-PxHCLA labeled the medulla layers 2, 4, 5a and proximal layers 6-8 (Figure 2-7A). The strongest labeling appears in columns spanning layer 4. In the distal part of layer 4 (4a), separation can be seen between the columnar structures. A bundle of dextran-injected photoreceptor axons appears to be running through each of the columns (Figure 2-7C). In the proximal part of layer 4 (4b), where lvfs terminate (Figure 2-7B), the columnar structures seem to have swollen terminals wide enough to contact each other. A similar diffuse blebby pattern was observed in the labeling with anti-PxHCLB in the same layer (Figure 2-7D).

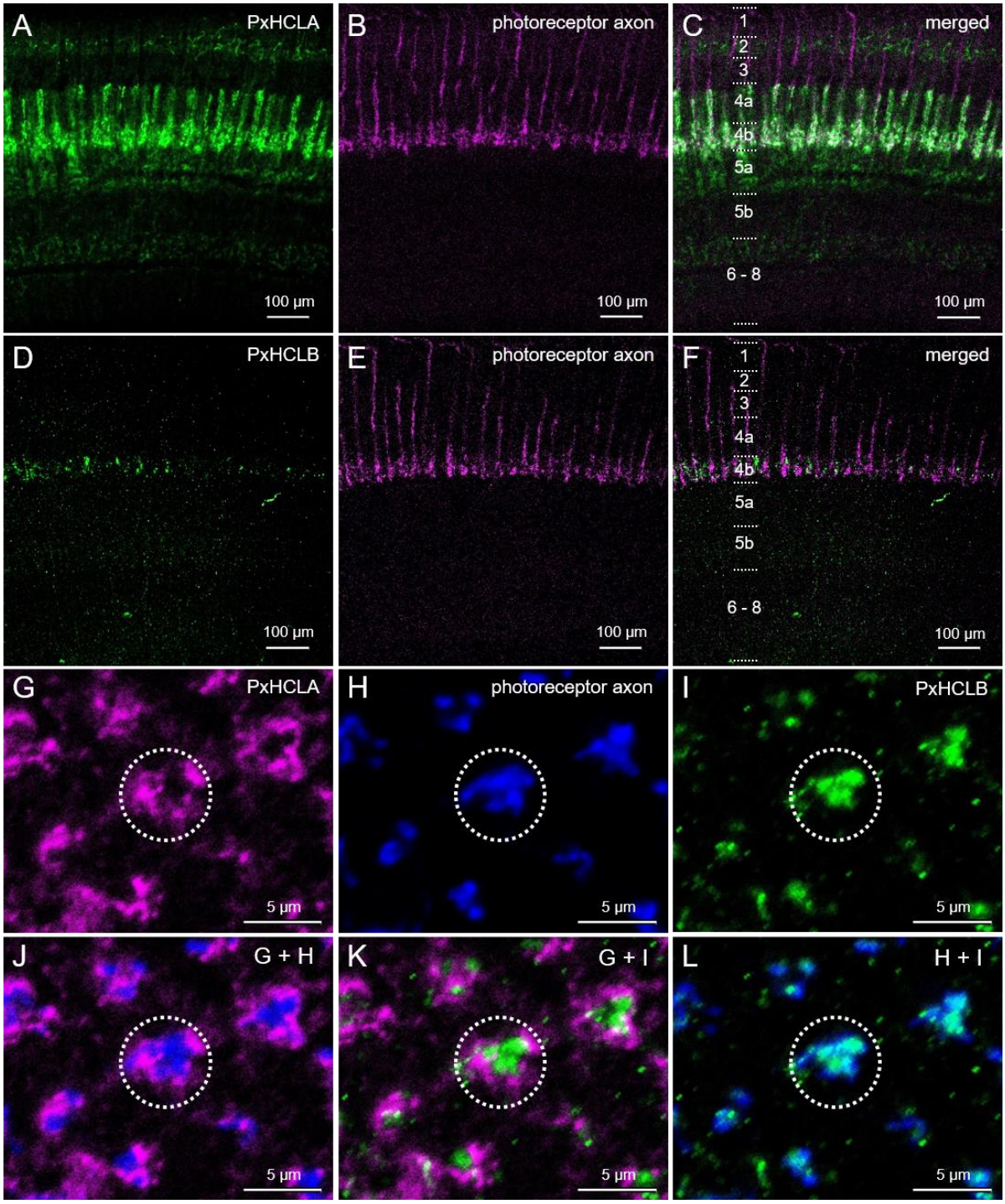


**Figure 2-7. Immunofluorescence localization of PxHCLA and PxHCLB in the *Papilio* medulla.** (**A**–**F**) Horizontal sections showing the medulla layers, double labeled with either anti-PxHCLA (*green* in **A,C**) or anti-PxHCLB (*green* in **D,F**) and photoreceptor axons (lvfs, *magenta* in **B,C,E,F**). The numbers in (**C,F**) indicate medulla layers. The anti-PxHCLA labeled the medulla layers 2, 4, 5a and partially 6–8 (**A**), while the anti-PxHCLB labeled 4b (**D**). Axons of lvfs terminate in layer 4b (**B,E**). (**G**–**L**) A cross section through the medulla layer 4b, double labeled with anti-PxHCLA (*magenta* in **G,J,K**) and anti-PxHCLB (*green* in **I,K,L**), along with TR-injected photoreceptor axons (*blue* in **H,J,L**). The ring-like pattern of anti-PxHCLA labeling (**G**) encircled lvfs (**J**), while the clustered pattern of anti-PxHCLB labeling (**I**) overlapped with the lvf axons (**L**). *Dotted circles* in **G**–**L** indicate the profile of a single medulla module.

The immunofluorescence labeling of both anti-PxHCLA and anti-PxHCLB colocalized with photoreceptor axon terminals. I thus double-labeled the cross sections through the medulla layer 4b with anti-PxHCLA and anti-PxHCLB in samples where lvf axons were pre-labeled with dextran (Figure 2-7G–L). The anti-PxHCLA labeling forms ring-like patterns (Figure 2-7G) encircling lvf axons (Figure 2-7J). This labeling pattern suggests that the columns seen in longitudinal sections (Figure 2-7C) are in fact cylinder-like structures through which the lvfs run. On the other hand, the anti-PxHCLB labeling forms clusters (Figure 7I), which overlap with lvf axons (Figure 2-7L). The labeling with anti-PxHCLA and anti-PxHCLB shows little overlap, suggesting these two channels have distinct distributions (Figure 2-7K). On the other hand, at lower magnification, I found that the medulla modules, each includes lvfs from the same ommatidia, were not equally stained by the anti-PxHCLB (Figure 2-8B). The ratio of strongly (*solid circles*) and weakly (*dotted circles*) stained medulla modules is about half (125 among 247 modules in total) and half (122 among 247 modules).

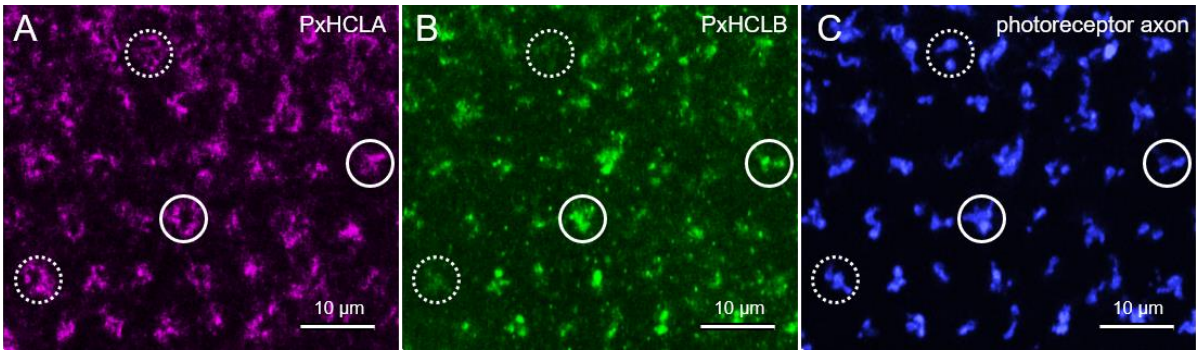


**Figure 2-8. Different expression levels of PxHCLB in the *Papilio* medulla.** (**A**–**C**) A cross section through the medulla layer 4b, double labeled with rat anti-PxHCLA (*magenta* in **A**) and rabbit anti-PxHCLB (*green* in **B**), along with TR-injected photoreceptor axons (*blue* in **C**). Some medulla modules were strongly stained by anti-PxHCLB (*solid circles*) while some of them were stained weakly (*dotted circles*).

The EM cross sections through the medulla layer 4b reveal several modules containing at least two photoreceptor axons (Figure 2-9A, *asterisks*), which are most likely lvfs R1 and R2 (Takemura et al., 2005). The PxHCLA-positive cells surround the lvf axons (Figure 2-9B–D). Such a labeling profile corresponds to the ring-like pattern of anti-PxHCLA at LM level (Figure 2-7G). The DAB immunoreaction products of anti-PxHCLA are localized on the membrane of non-photoreceptor cells at the sites where they face photoreceptor axons. Concomitantly, some vesicles (Figure 2-9C, *arrows* in inset) are observed in the cytoplasm of photoreceptor axons near the membrane facing the PxHCLA-positive cells, suggesting that these regions are actually synapses. The PxHCLA-positive cells are most likely secondary

neurons in the medulla receiving inputs from the lvfs. On the other hand, anti-PxHCLB labeling colocalizes with photoreceptor axons (Figure 2-9E,F). The DAB immunoreaction products appear on the plasma membrane of photoreceptors (Figure 2-9E,F, *arrows*) and within the cytoplasm of lvfs. The former distribution of anti-PxHCLB at least suggests synaptic interaction between photoreceptors.

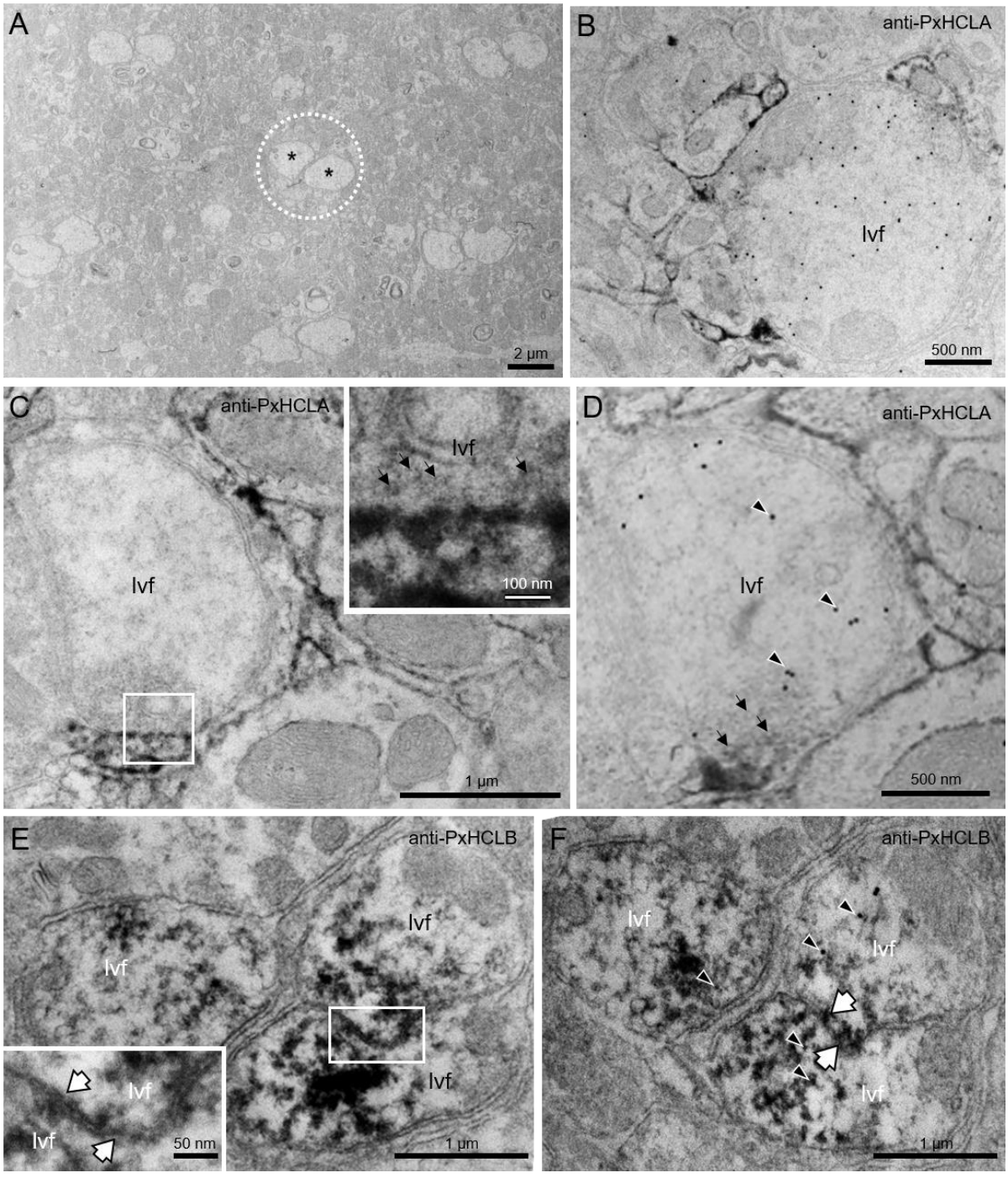


**Figure 2-9. Immunoelectron microscopic localization of PxHCLA and PxHCLB in the *Papilio* medulla.** (**A**) A cross section through medulla layer 4b at lower magnification. A *dotted circle* encloses a module including photoreceptor axons (lvfs, *asterisks*) from a single ommatidium. (continued on the next page)

***Localization of PxHCLB in the retina***

In addition to the lamina and the medulla, the retina is immunopositive to anti-PxHCLB. Horizontal sections through retina revealed that the anti-PxHCLB immunoreactivity was restricted to about one-third proximal region of the photoreceptor layer (Figure 2-10A). To determine the position of anti-PxHCLB, I then prepared serial cross sections through the proximal tier of retina. Two characteristics were found. First, intense immunolabeling was observed around the rhabdom region (Figure 2-10C). Second, some ommatidia were free of anti-PxHCLB labeling.

In *Papilio*, three types of ommatidia are distinguished by the expression pattern of UV opsin in the photoreceptors R1 and R2 (Kitamoto et al., 2000): type I (50%) with one labeled cell (*solid circle* in Figure 2-10B), type II (25%) with two (*dotted circle*), and type III (25%) without (*dashed circle*). Therefore, the antibody against PxUV opsin was used to correlate the anti-PxHCLB labeling with ommatidial types. The ratio of PxHCLB-positive ommatidia depended on the depth of the cross-section. The total length of the rhabdom, from the tip to the end of the basal photoreceptor R9, reaches to about 450 μm. At a depth of about 300 μm from the tip, about 50% ommatidia (30 of 60 ommatidia in total), which correspond to type I ommatidia, initially showed anti-PxHCLB labeling (data not shown). As the depth progressed to about 330 μm, anti-PxHCLB labeling was then detected in type II ommatidia as well; as a result, about three-fourth ommatidia (45 of 60 ommatidia) were PxHCLB-positive (Figure 2-10C). In other words, the labeling region of anti-PxHCLB in type II ommatidia was slightly shorter than in type I.

(**B**–**F**) Cross sections through medulla layer 4b double labeled with either anti-PxHCLA (**B**–**D**) or anti-PxHCLB (**E,F**) visualized with DAB reaction, while photoreceptor axons were detected with anti-LY immunogold labeling (**B,D,F**). (**C,D**) Two pictures of a module in the medulla layer 4b, labeled with anti-PxHCLA. The LY-injected lvf axon, labeled by gold particles (*arrowheads* in **D**), contained a dense region of synaptic vesicle-like structures (*small arrows* in **C** inset and **D**) near the membrane facing to the DAB-labeled cell. The PxHCLA-labeled cells were not lvfs, confirmed by anti-LY immunogold labeling (*arrowheads* in **D**). (**E,F**) Two pictures of a module in the medulla layer 4b, labeled with anti-PxHCLB. The LY-injected lvf axons were identified by anti-LY immunogold labeling (*arrowheads* in **F**). The anti-PxHCLB immunolabeling distributed within photoreceptors. Some labeling was associated with the photoreceptor membrane facing to other photoreceptors (*white arrows*), indicating possible inter-photoreceptor synaptic contacts between lvf axons.

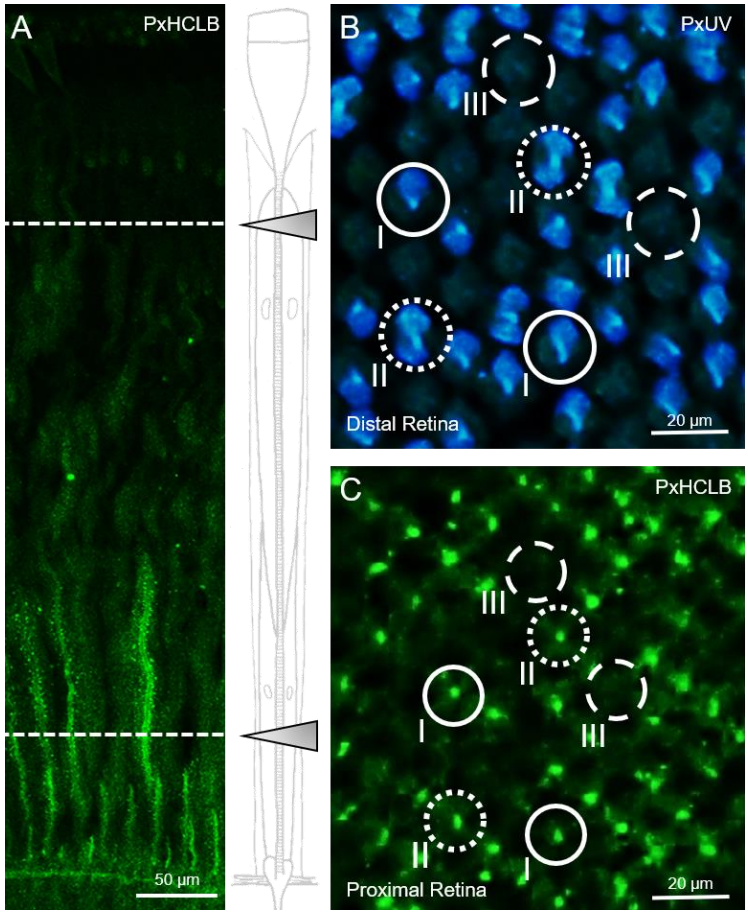


**Figure 2-10. Correlated anti-PxHCLB labeling with ommatidial types in the *Papilio* retina.** (**A**) Horizontal sections of the eye showing from the cornea to the basal region of the retina, labeled with anti-PxHCLB (*left*). Diagrammatic longitudinal of an ommatidium (r*ight*). Anti-PxHCLB labeling was detected in the one-third proximal region of the photoreceptor layer. (**B**–**C**) Cross sections of retina, double-labeled with anit-PxUV opsin (**B**) in the distal tier (50 µm from the tip of rhabdom) and anti-PxHCLB (**C**) in the proximal tier (350 µm from the rhabdom tip). (**A**) Three types of ommatidia, I (*solid circles*), II (*dotted circles*), and III (*dashed circles*), are identified by the localization of UV opsin in photoreceptors R1 and R2. (**B**) Immunoreactivity of anti-PxHCLB was detected in type I and II ommatidia.

Analysis of the DAB reaction in the proximal retina at the EM level revealed that PxHCLB-positive ommatidia had intense labeling in the immediate proximity of the rhabdom within proximal photoreceptors R5–R8 (Figure 2-11). The ommatidia with rectangular rhabdom (Figure 2-11E) are free of anti-PxHCLB labeling and thus may correspond to type III ommatidia. The ommatidia with square (Figure 2-11C) and trapezoidal (Figure 2-11D) rhabdom, which probably correspond to either type I or type II ommatidia, are PxHCLB-immunopositive. To identify what organelles were stained, I referred to pre-immune EM sections at the corresponding sites and found unique patches containing numerous vesicles of ca. 60 nm in diameter (Figure 2-11B). These organelles resembled trophospongium-like structures that reported previously in the distal region of the *Papilio* proximal photoreceptors R5–R8 (Eguchi and Meyer-Rochow, 1983; Miyako-Shimazaki et al., 1997).

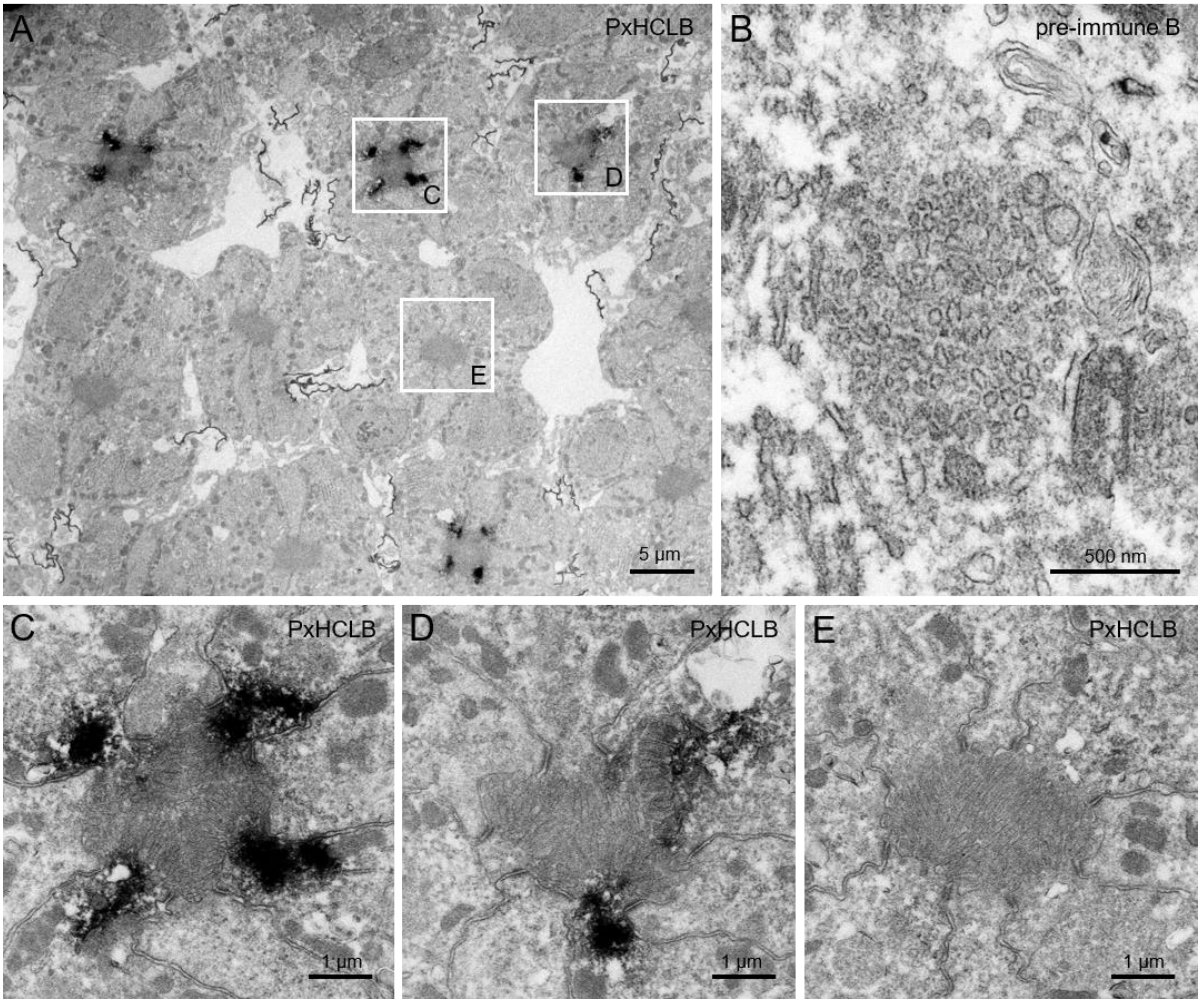


**Figure 2-11. Immunoelectron microscopic localization of PxHCLB in the *Papilio* retina.** A cross section through the proximal retina at a depth of ca. 340 µm from the tip of the rhabdom, labeled with anti-PxHCLB and visualized by DAB reaction (**A**). Three types of ommatidia are identified according to the shape of the rhabdom: square (**C**), trapezoidal (**D**) and rectangular (**E**); the former two ommatidial types were PxHCLB-immunopositive while the last type was PxHCLB-immunonegative. (**B**) A cross section showing the corresponding site of anti-PxHCLB labeling, exposed to the pre-immune serum of PxHCLB; trophospongium-like structures can be observed.

## 2.5 Discussion

Histamine is the only neurotransmitter identified so far in arthropod photoreceptors (Stuart et al., 2007). The synapse-like structures in the lamina of *Papilio* indicate that both LMCs and photoreceptors can be postsynaptic to photoreceptors (Takemura and Arikawa, 2006). Histamine-gated chloride channels have therefore been assumed to exist in the membranes of these postsynaptic cells. In the present study, I demonstrate the following. First, PxHCLA exists in the second-order neurons, which are postsynaptic to svfs and lvfs in the lamina as well as to lvfs in the medulla. Second, the PxHCLB-positive membranes in both the lamina and medulla are most likely those of photoreceptors, and thus PxHCLB may be expressed at the presumptive inter-photoreceptor synapses. Possible contribution of glial cells has not yet been analyzed. My results provide the first comparative anatomy of histamine-gated chloride channels in an insect visual system other than flies and, perhaps more importantly, I achieved a higher resolution of localization than has been previously obtained.

***Photoreceptor synaptic transmission to second-order neurons via PxHCLA***

The area strongly labeled with anti-PxHCLA (Figure 2-3A) corresponds to the lamina synaptic region in *Papilio* as in *Drosophila*. A similar expression pattern where LMCs and possible amacrine cells express HCLA has been reported for *Drosophila* (Witte et al., 2002; Gao et al., 2008; Pantazis et al., 2008; Jagadish et al., 2014). The DAB labeling of anti-PxHCLA provides much higher resolution and suggests synaptic interaction between the photoreceptors and the LMCs. The serial block face-scanning electron microscopy (SBF-SEM) analysis of the *Papilio* lamina reveals that a cartridge contains four LMCs of different morphology, three receiving numerous inputs from the photoreceptors, while one receives inputs mainly from one LMC (Matsushita et al., in preparation), similar as the L4-type LMC of *Drosophila* (Rivera-Alba et al., 2011). It is in fact difficult to identify the type of LMC in our present EM pictures, but the PxHCLA-expressing cells are most likely the LMCs those receiving inputs from photoreceptors. The similarities in distribution and amino acid sequences of HCLA channels (Iovchev et al., 2006) suggest that they serve similar functions among insects. The channels are most likely involved in the synaptic interaction between photoreceptors and LMCs in the lamina.

The LM and EM immunolabeling in the medulla provides compelling evidence that PxHCLA is expressed in the second-order neurons that are postsynaptic to lvfs R1 and R2. However, the connectivity between lvf terminals and their targets in the *Papilio* medulla is still unknown. In flies, photoreceptors R7 terminate in the medulla layer M6, where they make

connections with transmedullary Tm5 neurons and/or medulla intrinsic Dm8 neurons. Photoreceptors R8 connect to Tm9 and Tm20 in layer M3 (Gao et al., 2008). The PxHCLA-expressing cells in layer 4b are perhaps *Papilio* counterparts of these *Drosophila* medulla neurons.

It is also possible that LMCs receive lvf inputs at their medulla terminals via HCLA. In *Drosophila*, HCLA expression is detected in the medulla layers M1, M2, M3, and M5 (Pantazis et al., 2008; Schnaitmann et al., 2018), where LMCs terminate (L1 terminates at M1 and M5, L2 at M2 and L3 at M3). There L1 receives inputs from R8, while L2 and L3 receive inputs from R7 (Takemura et al., 2013). These lvf-LMC synapses can be histaminergic mediated by HCLA. Situation is similar in *Papilio*, where PxHCLA immunoreactivity is found in the medulla layers 2, 4, 5a and 6-8 (Figure 2-7A,C). The layer 4 contains histamine-containing lvf terminals (Hamanaka et al., 2012) as well as terminals of some LMCs (Ribi, 1987; Rusanen et al., 2018). Therefore, those PxHCLA-positive cells may be LMCs. While histamine is detected in other medulla layers as well (Hamanaka et al., 2012), I cannot exclude the possibility that neurons other than LMCs and even glial cells express PxHCLA.

***Local antagonistic interactions between photoreceptors via PxHCLB***

The overlap of PxHCLB immunoreactivity with photoreceptor axons (Figures 2-3J, 2-6, 2-7L) is not consistent with HCLB expression in the glial cells in *Drosophila* lamina (Gao et al., 2008; Pantazis et al., 2008). The glial cell HCLB in flies may be involved in a putative histamine recycling pathway (Edwards and Meinertzhagen, 2010; Yusein et al., 2010) or may contribute to shaping the LMC responses (Pantazis et al., 2008; Rivera-Alba et al., 2011). It may be not the case in *Papilio* because PxHCLB has only been found in the photoreceptors. However, whether or not PxHCLB is expressed in presumptive glial cells in the *Papilio* lamina still needs to be confirmed carefully.

The anti-PxHCLB labeling in the medulla is restricted to layer 4b where lvfs R1 and R2 terminate (Figure 2-7D–F) with axon collaterals (Takemura et al., 2005) and, thus, synaptic contacts between lvfs (Figure 2-9E,F). Similarly, photoreceptors are PxHCLB-positive at the membranes abutting other photoreceptors in the lamina (Figure 2-6B,C), indicating possible inter-photoreceptor synaptic contacts between multiple svfs as well as between svfs and lvfs (Figure 6-1). The expression of PxHCLB between photoreceptors is consistent with HCLB expression in the *Drosophila* medulla, where HCLB is involved in direct synaptic interactions between lvfs R7/R8 (Schnaitmann et al., 2018). Accordingly, the *Papilio* photoreceptors may

also implement direct antagonistic interactions via PxHCLB; in the case where the photoreceptors belong to different spectral classes, the interaction implies spectral opponency.

Most interestingly, the terminals of lvfs in the medulla show different expression levels of PxHCLB (Figure 2-8B). About one-half of medulla modules were strongly stained by PxHCLB (*solid circles*), and the other half were weakly or none stained (*dotted circles*). Each medulla module contains two lvfs R1 and R2 (Takemura et al., 2005), which are either one UV and one blue-sensitive receptor, or two violet-sensitive receptors, or two blue-sensitive receptors in type I (50%), II (25%) and III (25%) ommatidia, respectively (Arikawa, 2003). Although in the present study I could not identify the ommatidial type, the fact that about half of medulla modules were PxHCLB-immunopositive suggests that they most likely belong to type I ommatidia. As I predicted, PxHCLB is involved in antagonistic interactions between spectrally distinct photoreceptors, which only occur in the retinotopic projections of type I ommatidia in the medulla. Thus, PxHCLB are probably crucial in the medullar cartridges of type I ommatidia, conveying UV-blue spectral opponency.

On the other hand, the PxHCLB labeling was also detected in the proximal region of the retina (Figure 2-10) where photoreceptor cell bodies are located. Correlated with ommatidial types, the PxHCLB is expressed in type I and II ommatidia but not in type III (Figure 2-10C). Moreover, the labeling length of anti-PxHCLB in type I ommatidia is slightly longer than in type II. I expect that type III ommatidia may be PxHCLB-positive in a more proximal region because no cartridge was free of anti-PxHCLB immunolabeling in the lamina (Figure 2-3F). A previous study has indicated that the *Papilio* photoreceptors are mutually connected in ommatidial type-specific manner (Takemura and Arikawa, 2006). Types I, II, and III have four (UV, blue, green, red), three (violet, green, broadband), and two (blue, green) receptor classes, respectively (Arikawa, 2003). In comparison, type III ommatidia have less variety than the other two ommatidial types in terms of the spectral classes. Whether the expression levels of PxHCLB in different ommatidial types in the retina as well as in the medulla corresponds to the degree of varieties of spectrally heterogeneous receptors is in question that awaits further testing.

Another question is why anti-PxHCLB labeled particularly the trophospongium-like organelles in the proximal retina (Figure 2-11)? The functional histaminergic channels may exist at the synaptic sites that are assumed to be around the photoreceptor terminals. In the present study, however, anti-PxHCLB labeling was detected within photoreceptor cytoplasm

not only in the retina but also in the lamina and the medulla. The labeling is most likely on immature PxHCLB peptides. A previous study has observed that, in the *Papilio* proximal photoreceptors, the place where the trophospongium-like structures were located is frequently close to the rough and smooth endoplasmic reticulum (Miyako-Shimazaki et al., 1997). At present, I cannot state with certainty whether those PxHCLB-positive trophospongium-like organelles are involved in the process of PxHCLB protein synthesis or synaptic interaction between photoreceptors. However, labeling patterns suggested that PxHCLB was exclusively associated with the photoreceptors.

***Mechanisms for spectrally opponent neurons in early visual processing***

The spectrally opponent neurons so far reported in insects are the spiking neurons in the medulla and the lobula (Kien and Menzel, 1977; Osorio, 1986; Kelly and Mote, 1990; Yang et al., 2004; Paulk et al., 2008). Consequently, color processing had long been generally considered to start in the medulla. However, spectral opponency has occasionally been detected even in the retina (i.e. photoreceptors) of butterflies (Horridge et al., 1983; Matić, 1983; Chen et al., 2013). Findings of the histaminergic sign-inverting synapses between the photoreceptors in *Papilio* in this study and in *Drosophila* (Schnaitmann et al., 2018) indicate a possible neuronal circuit for insect color vision: the spectral opponency potentially occurs at the level of the photoreceptors. My electrophysiological recordings in *Papilio* suggest that the photoreceptor spectral opponency can be seen more clearly in the lamina, where inter-photoreceptor synapses exist, than in the retina (see Chapter 5). The immunolocalization of PxHCLB at the inter-photoreceptor synapses suggests the possibility of spectral opponent processing existing in the lamina, while in *Drosophila* a photoreceptor-level opponency only emerges in the medulla (Schnaitmann et al., 2018).

The direct antagonistic interaction between the photoreceptors via HCLB in insects is simpler than the functionally analogous circuit in the vertebrate retina, where cones receive feedback signals from spectrally distinct cones via horizontal cells (Demb and Singer, 2015). Although it seems that in insects no interneurons are necessarily involved in spectrally opponent processing at the first synapses, Schnaitmann et al. (2018) has shown in *Drosophila* that HCLA in some interneurons also involves indirectly in the R7/R8 antagonistic interactions. Similar mechanism may exist in *Papilio*, but presently I have no evidence for such a mechanism in the butterflies.

# Chapter 3

## Physiological characterization of histamine-gated chloride channels from the butterfly *Papilio xuthus*

This chapter is based on the following paper:

**Physiological responses of ionotropic histamine receptors, PxHCLA and PxHCLB, to neurotransmitter candidates in a butterfly, *Papilio xuthus***

Hiroshi D. Akashi[1], Pei-Ju Chen[1], Tokiho Akiyama[1], Yohey Terai[1], Motohiro Wakakuwa[1], Yasunori Takayama[2,3], Makoto Tominaga[2,3], Kentaro Arikawa[1] (2018)

Journal of Experimental Biology 221: jeb183129

doi: 10.1242/jeb.183129

[1]Department of Evolutionary Studies of Biosystems, SOKENDAI (The Graduate University for Advanced Studies), Hayama, Kanagawa 240-0193, Japan.

[2]Division of Cell Signaling, Okazaki Institute for Integrative Bioscience (National Institute for Physiological Sciences), National Institutes of Natural Sciences, 5-1 Higashiyama, Myodaiji, Okazaki, Aichi, 444-8787, Japan.

[3]Department of Physiological Sciences, SOKENDAI (The Graduate University for Advanced Studies), 5-1 Higashiyama, Myodaiji, Okazaki, Aichi, 444-8787, Japan.

Declaration by author

Despite not being first author, I have made significant contribution to this original manuscript, and in this chapter have only included content of which I was leading the research in. This includes physiological properties of histaminergic channels. I have not included the content made by co-authors, Hiroshi D. Akashi, Tokiho Akiyama and Yohey Terai, including sequence analysis and molecular phylogeny. Please refer to original manuscript for more details regarding study contributions by the lead author.

## 3.1 Abstract

Histamine is the only known neurotransmitter released by arthropod photoreceptors. Synaptic transmission from photoreceptors to second order neurons is mediated by the activation of histamine-gated chloride channels (HCLs). These histaminergic synapses have been assumed to be conserved among insect visual systems. However, our understanding of the channels in question has thus far been based on studies in flies. In the butterfly *Papilio xuthus*, we have identified two candidate histamine-gated chloride channels, PxHCLA and PxHCLB, and studied their physiological properties using a whole-cell patch-clamp technique. We studied the responses of channels expressed in cultured cells to histamine as well as to other neurotransmitter candidates, namely GABA, tyramine, serotonin, D-/L- glutamate, and glycine. We found that histamine and GABA activated both PxHCLA and PxHCLB, while the other molecules did not. The sensitivity to histamine and GABA was consistently higher in PxHCLB than in PxHCLA. Interestingly, simultaneous application of histamine and GABA activated both PxHCLA and PxHCLB more strongly than either neurotansmitter individually; histamine and GABA may have synergistic effects on PxHCLs in the regions where they colocalize. Our results suggest that the physiological properties of the histamine receptors are basically conserved among insects, but that the response to GABA differs between butterflies and flies, implying variation in early visual processing among species.

Keywords: histamine, GABA, chloride channel, visual processing, butterfly

## 3.2 Introduction

In the previous chapter, I performed immunohistochemistry to localize two histamine-gated chloride channels, PxHCLA and PxHCLB, in the visual system of *Papilio xuthus*. The antibodies for immunohistochemistry were produced against peptides of the gene products possibly encoding the histamine receptors in *Papilio*. In this chapter, I would like to confirm whether these molecules were really histamine-gated chloride channels and whether channel properties of histaminergic receptors are similar across species.

Considerable studies have accumulated for the physiological properties of histaminergic channels and their functional roles in visual processing in flies. Since the channel belongs to the superfamily of Cys-loop receptors that are pentameric ligand-gated channels (Thompson et al., 2010), forming homomeric (i.e. HCLA homomer and HCLB homomer) or heteromeric (i.e. HCLA/B heteromer) receptors are possible. In flies, HCLA and HCLB subunits appear to form a heteromer in co-transfected cells, but it is unclear whether this occurs naturally in the visual system (Gisselmann et al., 2004; Pantazis et al., 2008). In contrast, the expression of HCLA and HCLB homomers has been confirmed in the *Drosophila* visual system. Electrophysiological analysis has demonstrated that HCLA homomers expressed on cultured cells exhibit similar channel properties to the histamine-gated chloride channels on isolated lamina monopolar cells (LMCs) (Skingsley et al., 1995; Pantazis et al., 2008). Furthermore, electroretinography has revealed that *hclA* null mutants fail to produce fast transient components derived from the LMCs (Pantazis et al., 2008). These studies suggest that the channels on the LMCs are HCLA homomers and may be crucial for synaptic transmission.

The role of HCLB is less decisive since it has been found in different types of cells: in glial cells in the *Drosophila* lamina (Pantazis et al., 2008) and in the region of the medulla where the long axons of some photoreceptors terminate (Schnaitmann et al., 2018). At any rate, several differences in physiological properties between HCLA and HCLB have been reported. In the case of *Drosophila melanogaster* and housefly *Musca domestica*, their HCLB homomers show higher sensitivity to histamine than the HCLA homomers (Gisselmann et al., 2004; Kita et al., 2017). Furthermore, GABA, once a neurotransmitter candidate for arthropod photoreceptors, can act as an agonist of the HCLB, while the HCLA is insensitive to GABA (Gisselmann et al., 2004; Kita et al., 2017). Although the HCLB channel can be activated only by a very high concentration of GABA (about 100-fold higher than that of histamine), GABA can co-localize with histamine in fly visual systems (Meinertzhagen and O'neil, 1991; Nässel,

1991).

In the present study, I focused on the physiological function of HCL channels in *Papilio xuthus*. The PxHCLA and PxHCLB subunits were transfected to cultured cells and analyzed for their ion channel properties by whole-cell patch-clamp. Since several neurotransmitter candidates have been detected in the lamina of *Papilio* (Hamanaka et al., 2012) and other insects (Nässel, 1991; Sinakevitch and Strausfeld, 2004; Kolodziejczyk et al., 2008) in addition to histamine, I therefore studied the HCLs' responses to these molecules, namely, GABA, tyramine, serotonin, D-/L- glutamate, and glycin. The recordings have been carried out under collaboration with Drs. Hiroshi Akashi, Yasunori Takayama, and Prof. Makoto Tominaga at the National Institute for Physiological Sciences (NIPS), Japan.

## 3.3 Materials and Methods

### *Animals*

I used spring-form adult Japanese yellow swallowtail butterflies, *Papilio xuthus* Linnaeus, of both sexes. The butterflies were taken from a laboratory culture derived from eggs laid by females caught around the SOKENDAI campus in Hayama, Kanagawa, Japan.

### *Identification of PxhclA and PxhclB cDNA sequences*

The whole head tissues were dissected and preserved in RNA*later* solution (Thermo Fisher Scientific, MA, USA). Total RNAs were extracted from the heads of *Papilio* using TRIzol reagent (Thermo Fisher Scientific), and used for first-strand cDNA synthesis by PrimeScript II 1st Strand Synthesis Kit (TaKaRa, Shiga, Japan). The *Papilio PxhclA* and *PxhclB* predicted cDNA sequences were retrieved from GenBank (http://www.ncbi.nlm.nih.gov/genbank/) by BLASTN search (Altschul et al., 1990) using the *Drosophila melanogaster hclA* and *hclB* as query sequences: *PxhclA*: XM_013313248 and *PxhclB*: XM_013319237, respectively. The 5'- and 3'-untranslated region (UTR) sequences of these homolog sequences were then retrieved from PapilioBase (http://papilio.bio.titech.ac.jp/papilio.html) (Nishikawa et al., 2015). Primers for polymerase chain reaction (PCR) on both UTR sequences were designed as follows: *PxhclA*_F1 (5'-taaggcaaaaaacttcccgcgaac-3') and *PxhclA*_R1 (5'-tgctaaatcgagactggaagag-3'), and *PxhclB*_F1 (5'-cttgtgtgcgcgattgtacagtgac-3') and *PxhclB*_R1 (5'-gttccacgagtattggttttcatc-3'). These primer pairs were used to amplify the *PxhclA* and *PxhclB* full-length cDNAs by PCR using Ex Taq HS polymerase (TaKaRa). Reactions for the cDNA amplifications were carried out in Mastercycler (Eppendorf, Hamburg, Germany) using the following protocol: an initial denaturing step at 93°C for 3 min, 30 cycles of denaturation at 93°C for 1 min, annealing at 60°C for 1 min, extension at 72°C for 1 min 35 sec, and a final extension step at 72°C for 1 min. DNA sequencing was performed for the purified PCR products using BigDye Terminator v3.1 Cycle Sequencing Kit (Applied Biosystems, Foster City, CA, USA) with the PCR primers or inner primers: *PxhclA*_seqF1 (5'-gacattttcttcgcccaaacgtg-3') and *PxhclA*_seqR1 (5'-caggacatgatgacgatgagac-3'), and *PxhclB*_seqF1 (5'-actttccacgagatgagcatacc-3') and *PxhclB*_seqR1 (5'-ccaaagtaagcaacgatgtgac-3'). The sequences were analyzed in ABI3130xl DNA Sequencer (Applied Biosystems). The *PxhclA* and *PxhclB* sequences determined in this study were deposited in the international nucleotide sequence database DDBJ/EMBL/GenBank (accession numbers LC373508 and LC373509, respectively).

***Vector construction***

We designed primers *PxhclA*_F1_IF (5'-taccgagctcggatctaaggcaaaaaacttcccgcgaac-3') and *PxhclA*_R1_IF (5'-cacactggactagtgtgctaaatcgagactggaagag-3'), and *PxhclB*_F1_IF (5'-taccgagctcggatccttgtgtgcgcgattgtacagtgac-3') and *PxhclB*_R1_IF (5'-cacactggactagtggttccacgagtattggttttcatc-3'). The 15 bases at 5' end of these primers were overlapped with the ends of the cloning site of the linearized vector for cloning. These primers were used to amplify the cDNAs containing the entire coding region of *PxhclA* or *PxhclB* by PCR using PrimeSTAR Max DNA polymerase (TaKaRa). Reactions for the cDNA amplifications were carried out in Mastercycler (Eppendorf) using the following protocol: an initial denaturing step at 98°C for 3 min, 30 cycles of denaturation at 98°C for 10 s, annealing at 55°C for 15 s, extension at 72°C for 2 min, and a final extension step at 72°C for 1 min. After purification of the PCR products, each of *PxhclA* and *PxhclB* cDNAs was cloned independently into pcDNA3.1(+) vector (Invitrogen, Carlsbad, CA, USA) using In-Fusion HD Cloning Kit (TaKaRa). The plasmids were transformed into *ECOS* competent *E. coli* DH5α cells (Nippon Gene, Tokyo, Japan). Each *E. coli* cell with plasmid clone was grown in 2 mL of LB medium supplemented with ampicillin overnight. The plasmid DNAs were purified from the culture using QIAprep Spin Miniprep Kit (Qiagen, Germantown, MD, USA). The target insert sequences were confirmed by PCR and sequencing.

***Cell transfection***

We transfected HEK293T cells with a vector of pGL1 (0.1 μg) and the pcDNA3.1(+)-*PxhclA* vector (1 μg) or the pcDNA3.1(+)-*PxhclB* vector (1 μg) or both (0.5 μg each) or none (as the control) in OPTI-MEM medium (Life Technologies) using Lipofectamine Plus reagents (Life Technologies). After three hours of incubation at 37˚C, we substituted the OPTI-MEM medium for D-MEM medium (Life Technologies), and the cells were settled and cultured on 12 mm-diameter coverslips at 37˚C. Four types of cells expressing PxHCLA homomer, PxHCLB homomer, the combination of the two, i.e. PxHCLA/B, or neither of them were obtained. We carried out more than thirty independent transfections throughout the study.

***Electrophysiological recordings***

Methods of whole-cell patch-clamp recordings were as described previously (Takayama et al., 2017). A coverslip with cultured cells on the top was placed in the chamber mounted on a Nikon Eclipse TE2000-S inverted microscope. Standard bath solution for the whole-cell patch-clamp

recording contained (in mM) 140 NaCl, 5 KCl, 2 $CaCl_2$, 2 $MgCl_2$, 10 glucose, and 10 HEPES. This solution was also used as a vehicle for chemicals (histamine, GABA, tyramine, serotonin, L-/D-glutamate, and glycine) tested in the following experiments. The bath solutions were maintained at about 26°C, and perfused through silicone tubes by gravity. The solution in the pipette used for the whole-cell patch-clamp recording contained (in mM) 140 KCl, 5 EGTA, and 10 HEPES. The pH of all solutions was adjusted to 7.4 by NaOH. The whole-cell recording data were collected at a sampling frequency of 10 kHz and lowpass filtered with a cutoff of 5 kHz for analysis (Axopatch 200B Amplifier, Molecular Devices), which was performed using pCLAMP 10.4 software (Molecular Devices). For the experiments analyzing the responses of PxHCLs to agonists, the voltage ramp-pulses (300 ms duration) from -100 to +100 mV were applied every 5 s to the patch-clamped cell otherwise held at 0 mV. To test the current stability during 300 ms of the voltage ramp-pulses, voltage-step pulses (300 ms) from -100 mV to +100 mV with an increment of 20 mV were applied to the patch-clamped cell held at 0 mV every 60 s to obtain a stable baseline. Whole-cell patch-clamp recordings were performed 16-22 hours after transfection of HEK293 cells. All of the patch-clamp methods were performed at a room temperature.

***Statistical analysis***

The current responses were obtained at -60 mV in the voltage ramp-pulses for analysis. To analyze histamine and GABA dose dependency of PxHCLs, the current responses were normalized to the maximal current response. The normalized currents, $I/I_{max}$, were used to draw dose-response curves by fitting the data using the simple Hill function:

$$\frac{I}{I_{max}} = \frac{1}{1+\left(\frac{EC_{50}}{[agonist]}\right)^{n_H}} \quad (3.1)$$

where $EC_{50}$ represents the concentrations of histamine or GABA required to elicit 50% of $I_{max}$, agonist is either histamine or GABA, and $n_H$ represents the Hill coefficient. To analyze the effects of histamine and GABA mixtures on PxHCLs, the current responses elicited by the initial histamine application were used to normalize the following current responses. We avoided using the saturating concentration of histamine to reduce the risks of cell damage for the following chemical applications. Statistical significance was evaluated using Student's paired *t*-test at a value of $p < 0.05$. Data in figures are presented as mean ± standard error (SE).

## 3.4 Results

During the period 16–22 hours after transfection, the cells transfected with *PxhclA*, *PxhclB*, *PxhclA/PxhclB* or none were used to study physiological properties by whole-cell patch-clamp recording. Different neurotransmitter candidates (i.e. histamine, GABA, tyramine, serotonin, D-/L- glutamate, and glycine) were applied to cultured cells. The application of histamine and GABA activated the transfected cells expressing PxHCLA homomer (Figure 3-1A), PxHCLB homomer (Figure 3-1B), and PxHCLA/B heteromer, while other chemicals did not. As examples shown in Figure 3-1, when applying histamine, the negative slow deflection of the baseline current was observed, indicating the flow of chloride inward current. On the other hand, the ramp pulses became larger due to the reduction of membrane resistance suggesting the opening of ion channels by histamine. In control cells, no responses were recorded in any chemicals including histamine and GABA.

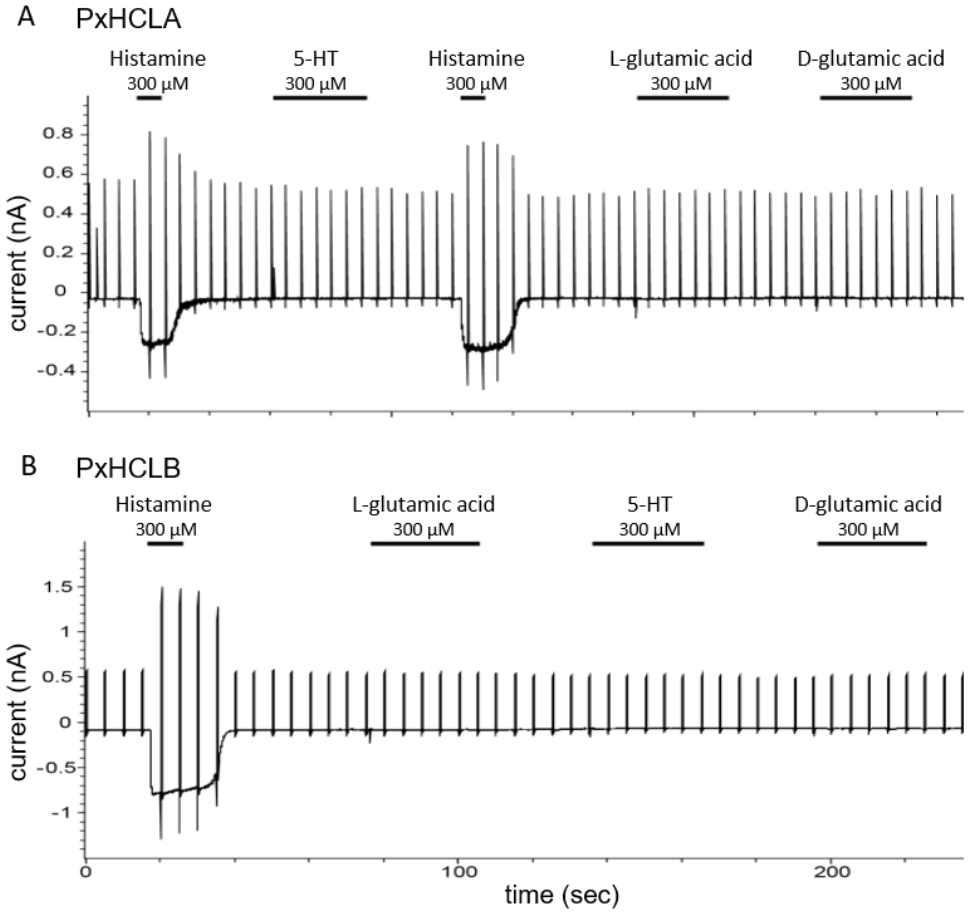


**Figure 3-1. Examples of current traces of humoristic PxHCLA** (A) **and PxHCLB** (B) **subunits expressed in HEK293 cell applying to different neurotransmitter candidates.** Bars indicate the duration of chemical applications. Both PxHCLA and PxHCLB only responded to histamine and showed no response to 5-HT (serotonin), L-glutamic acid, and D-glutamic acid. The recording was performed by Dr. Yasunori Takayama.

Figure 3-2A and 3-2B show representative traces recorded from *PxhclA*-transfected cells under histamine and GABA applications, respectively. Figure 3-2C and 3-2D show the current-voltage (I-V) relationship of *PxhclA*-transfected cells under the application of histamine and GABA, respectively. The I-V relationship was basically linear at higher concentrations, but weak outward rectification was observed at lower concentrations. Since the intra- and extracellular concentrations of chloride ions were approximately equal in our experiments, this implies a reversal potential for chloride ions of around 0 mV, which was consistent with our results (Figure 3-2C,D). The voltage step-pulses produced histamine and GABA-induced currents that were stable over a 300 ms interval (Figure 3-2E,F).

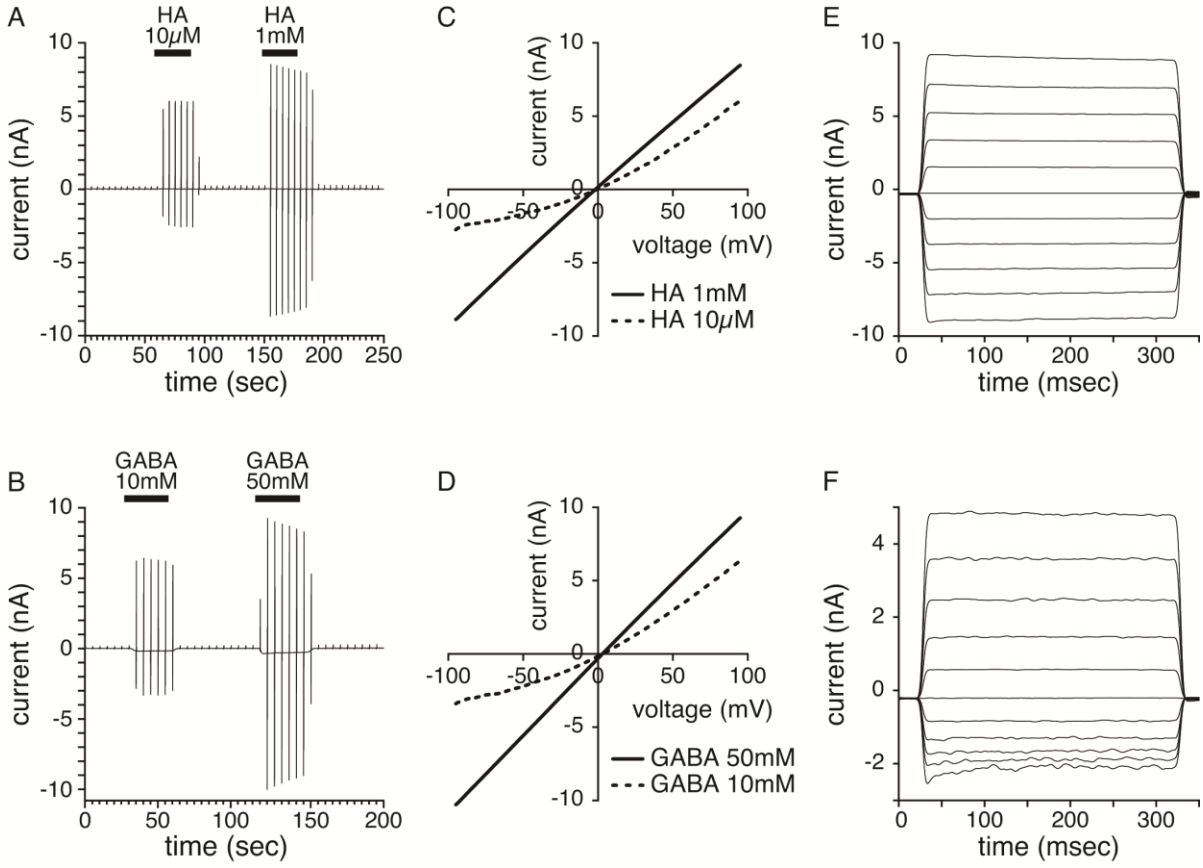


**Figure 3-2. Representative current traces of PxHCLA expressed in HEK293 cell under histamine and GABA applications.** (**A,B**) Representative traces of PxHCLA, showing its activation by histamine (HA) (**A**) and GABA (**B**) in a dose-dependent manner. Bars indicate the duration of chemical applications. (**C,D**) Current-voltage relationship of PxHCLA at two HA (**C**) and GABA (**D**) concentrations. A linear relationship exists at high concentrations but weak rectification is observed at low histamine and GABA concentrations. (**E,F**) Representative traces of current through PxHCLA recorded under HA (**E**) and GABA (**F**) during 300 ms voltage steps between −100 mV and +100 mV with an increment of 20 mV. The applied histamine and GABA concentrations were 20 μM and 10 mM, respectively. Currents were more or less stable over 300 ms at all voltages.

Figure 3-3 shows the results obtained from the analysis on *PxhclB*-transfected cells under histamine and GABA applications, in the same format as Figure 3-2 for *PxhclA*-transfected cells. While I observed dose-dependent responses in *PxhclB*-transfected cells as well as in *PxhclA*-transfected cells, the maximal current responses were generally smaller in the former than in the latter (see scales of Figures 3-2 and 3-3). *PxhclB*-transfected cells showed a linear I-V relationship at high agonist concentrations but weak outward rectifications at low concentrations (Figure 3-3C,D). Histamine and GABA-induced currents were stable over 300 msec (Figure 3-3E,F).

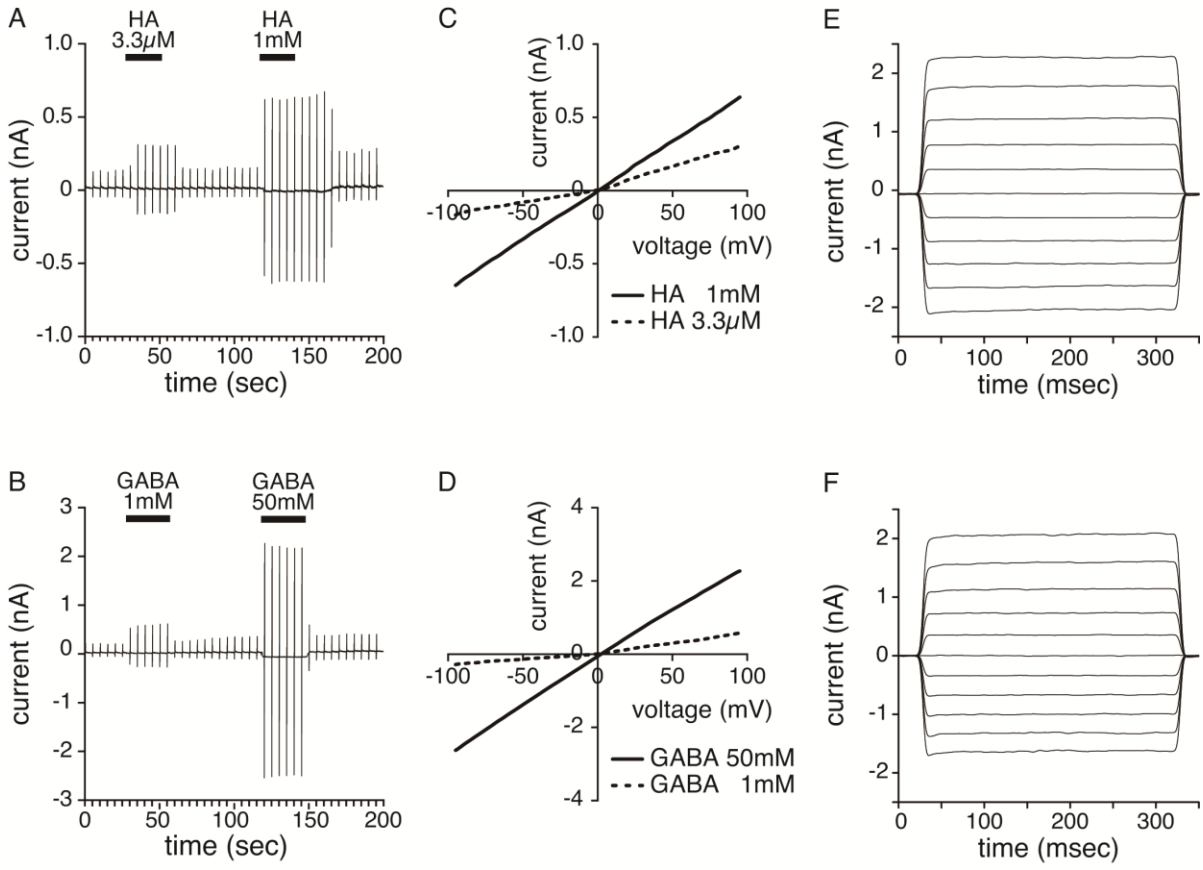


**Figure 3-3. Representative current traces of PxHCLB expressed in HEK293 cell under histamine and GABA applications.** (**A,B**) Representative traces of PxHCLB, showing its activation by histamine (HA) (**A**) and GABA (**B**) in a dose-dependent manner. Bars indicate the duration of chemical applications. (**C,D**) Current-voltage relationship of PxHCLB at two HA (**C**) and GABA (**D**) concentrations. A linear relationship exists at high concentrations but weak rectification is observed at low histamine and GABA concentrations. (**E,F**) Representative traces of current through PxHCLB recorded under HA (**E**) and GABA (**F**) during 300 ms voltage steps between −100 mV and +100 mV with an increment of 20 mV. The applied histamine and GABA concentrations were 6.6 μM and 2.5 mM, respectively. Currents were stable over 300 ms at all voltages.

Figure 3-4 shows histamine and GABA dose dependency fitted with the simple Hill function for cells transfected by *PxhclA*, *PxhclB*, or both. The fitted parameters of $EC_{50}$ and the slope, $n_H$, are summarized in Table 3-1 *PxhclB*-transfected cells showed the highest sensitivity to both histamine and GABA. For both histamine and GABA, the slope of the dose-response curves was shallowest for *PxhclA/PxhclB*-cotransfected cells, while the slopes were similar between *PxhclA*- and *PxhclB*-transfected cells. I used 1 mM histamine and 50 mM GABA across all three transfections to obtain their maximal current responses for each agonist. However, the currents recorded from those cells reached their maxima at slightly lower agonist concentrations. According to the dose-response curves, the saturating concentrations of histamine were, in fact, approximately 300 μM and 30 μM for *PxhclA*- and *PxhclB*-transfected cells, respectively, and that of GABA was 10 mM for *PxhclB*-transfected cells (Figure 3-4).

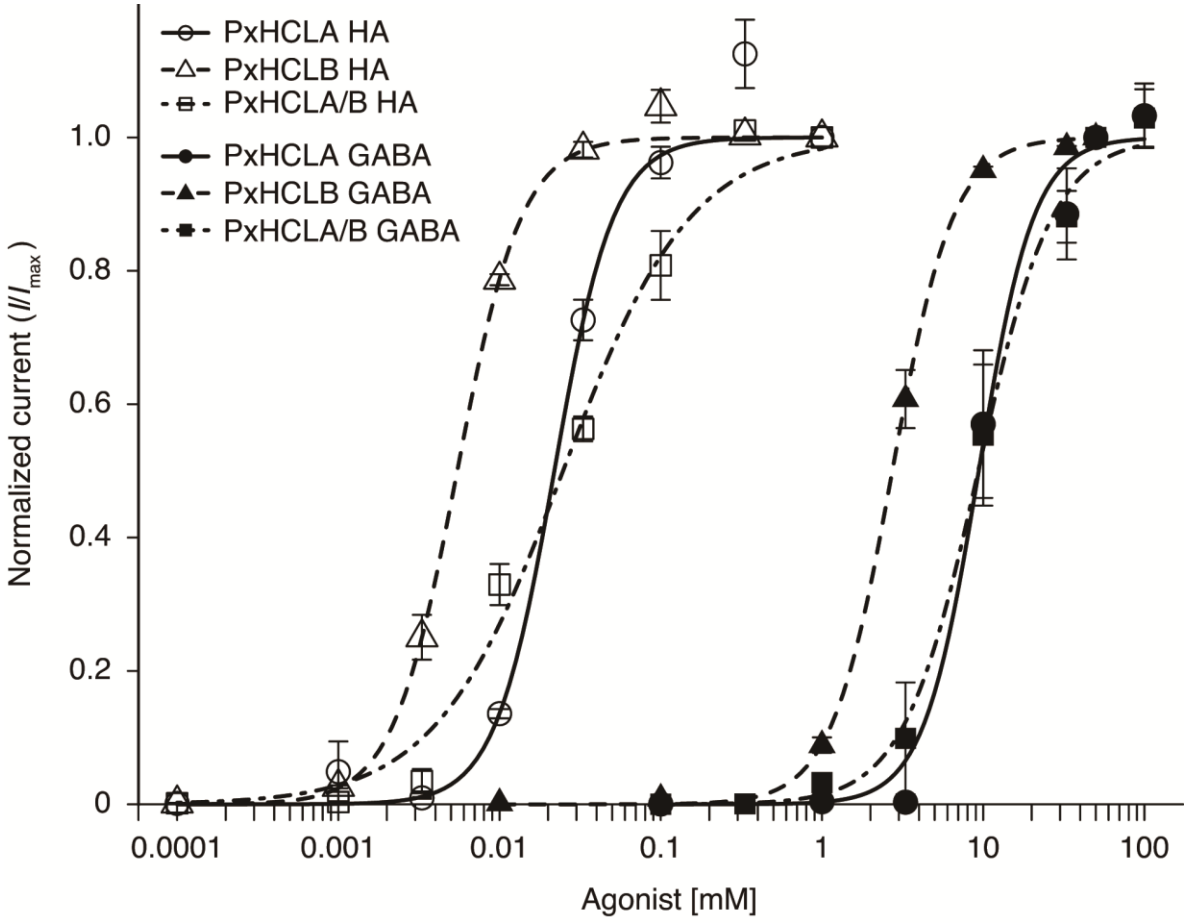


**Figure 3-4. Dose-response curves of PxHCLA, PxHCLB, and PxHCLA/B for histamine (HA) and GABA.** Current amplitudes were normalized by the current at 1 mM for histamine and 50 mM for GABA. Each point is based on the measurement from at least three separate cells taken from six independent transfection sessions in total. The curves were drawn by Simple Hill fittings (equation (3.1)).

**Table 3-1. Histamine and GABA dose-response parameters of PxHCLs**

| Receptor type | Histamine | | GABA | |
|---|---|---|---|---|
| | $EC_{50}$ (μM) | $n_H$ | $EC_{50}$ (mM) | $n_H$ |
| PxHCLA homomer | 21.9 ± 1.6 | 2.4 ± 0.3 | 9.4 ± 0.8 | 2.5 ± 0.7 |
| PxHCLB homomer | 5.5 ± 0.2 | 2.2 ± 0.1 | 2.7 ± 0.1 | 2.3 ± 0.2 |
| PxHCLA/B heteromer | 24.8 ± 2.9 | 1.1 ± 0.1 | 9.3 ± 0.9 | 1.9 ± 0.3 |

All fitted parameters are mean ± SE.

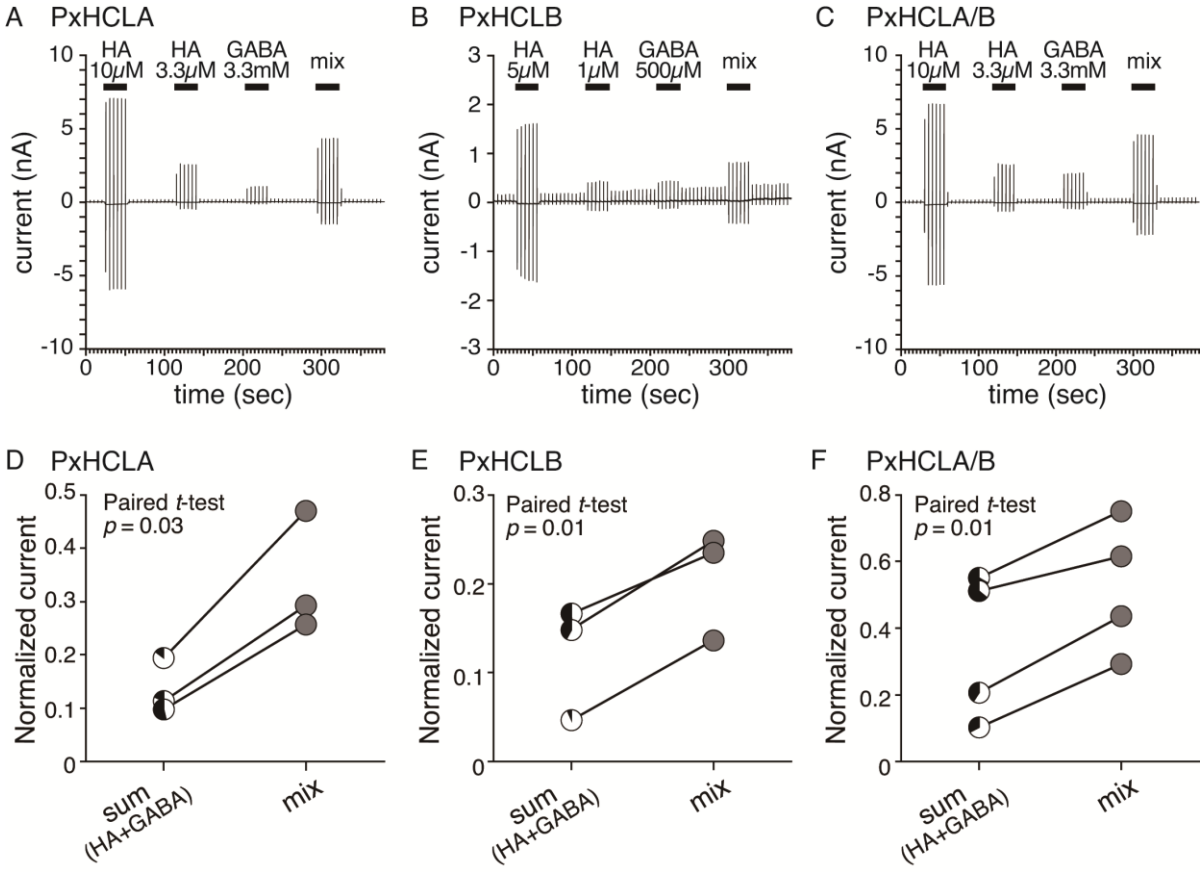


**Figure 3-5. Possible synergistic effects of histamine and GABA on PxHCLs.** (**A**–**C**) Representative traces from HEK293 cell expressing PxHCLA (**A**), PxHCLB (**B**), and PxHCLA/B (**C**), showing the synergistic effects observed under histamine (HA) and GABA applications. Bars indicate chemical applications. Mix indicates the simultaneous application of histamine and GABA at concentrations equal to their concentrations on the second and third applications in the trial, respectively. (**D**–**F**) Synergistic effects of histamine and GABA on PxHCLA (**D**), PxHCLB (**E**), and PxHCLA/B (**F**). The lines connect the responses recorded from the same cell. Sum (HA+GABA) indicates the sum of the currents recorded from the second and third chemical applications. Pie charts indicate the ratio of histamine (*white*) and GABA (*black*) induced currents. Mix indicates the currents recorded from the applications of histamine and GABA mixtures (*gray*). Both sum and mix were normalized to the currents recorded from the first application of histamine.

Simultaneous application of histamine and GABA elicited synergistic effects. Figure 3-5A–C show representative response traces of *PxhclA*-transfected, *PxhclB*-transfected, and *PxhclA/PxhclB*-cotransfected cells, respectively. The sum of the current responses elicited from individual applications of histamine and GABA were significantly smaller than the current responses elicited from histamine and GABA mixtures in all transfection cases (Figure 3-5D–F).

Note that this study used HEK293T cells to express the molecules. Physiological responses of ectopically-expressed HCLs of *Drosophila melanogaster* and *Musca domestica* were analyzed using insect S2 cells (Pantazis et al., 2008) and *Xenopus* oocyte (Kita et al., 2017), respectively. All of these studies including the present one have revealed similar characteristics, indicating that the effect of using different expression system would be minimal.

## 3.5 Discussion

Electrophysiological studies on HCLs in *Drosophila melanogaster* and *Musca domestica* have shown that the $EC_{50}$ values of native channels on the LMCs for histamine (24 µM and 34 µM, respectively) are similar to that of *in vitro*-expressed HCLA homomers for histamine (25 µM and 33 µM, respectively) (Skingsley et al., 1995; Pantazis et al., 2008; Kita et al., 2017). As PxHCLA homomers have an $EC_{50}$ for histamine (21.87 µM) similar to that of *Drosophila*, PxHCLA homomers most likely have a similar biological function, i.e. synaptic transmission from photoreceptors to LMCs. In fact, PxHCLA is expressed in neurons postsynaptic to photoreceptors both in the lamina and the medulla of *Papilio* (Chen et al., 2019).

PxHCLB homomers have a much lower $EC_{50}$ for histamine than PxHCLA homomers. Histamine at the concentration of the PxHCLB homomer $EC_{50}$ barely activates PxHCLA, reaching only around 5% of its maximum current (Figure 3-4). The lower $EC_{50}$ for histamine in the HCLB homomer than in HCLA is consistent with previous reports in flies (Gisselmann et al., 2004; Kita et al., 2017); however, its significance remains unclear. I have found by immunohistochemistry that PxHCLA channels are expressed at the photoreceptor-LMC synapses whereas PxHCLB channels are expressed at the inter-photoreceptor synapses (Chen et al., 2019). The lower $EC_{50}$ in PxHCLB might reflect the fact that the inter-photoreceptor synapses the color opponent synapses are smaller and less work-intensive than the photoreceptor-LMC synapses. Therefore, the inter-photoreceptor synapse may be activated by lower numbers of vesicles. Additionally, the PxHCLB channels with lower $EC_{50}$ could response to histamine earlier than PxHCLA channels. It would allow photoreceptors to pre-process mutual signals via PxHCLB before they activate higher-order neurons via PxHCLA. The functional implication of this physiological characteristics underlying visual signal processing is discussed in the general discussion chapter (Chapter 6) together with the roles of PxHCLB channels in the early visual systems.

For cotransfected cells, there were partly discrepant results between *Papilio* and *Drosophila*. In *Drosophila*, *hclA*/*hclB*-cotransfectants show the lowest $EC_{50}$ for histamine among the three cell types (Gisselmann et al., 2004; Pantazis et al., 2008). In contrast, *PxhclA*/*PxhclB*-cotransfectants have an $EC_{50}$ for histamine similar to that of *PxhclA*-transfected cells (Table 3-1). The $EC_{50}$ of GABA in *PxhclA*/*PxhclB*-cotransfectants is also similar to *PxhclA*-transfectants. On the other hand, $n_H$, the slope of the histamine dose-response curve, was smaller in *PxhclA*/*PxhclB*-cotransfectants than those of *PxhclA* and *PxhclB* transfectants,

although the curve for GABA was close to that of *PxhclA*-transfectants. We would have to carefully consider any possibilities of heteromeric channels and/or mixed expression of *PxhclA* and *PxhclB* homomers in the cotransfected cells in varying proportions. In fact, a shallower slope of the histamine dose-response curve has also been observed in the fly *hclA/hclB*-cotransfectant (Pantazis et al., 2008); however, the underlying mechanism remains unclear. While HCLA has been localized in LMCs and medulla neurons, HCLB has been localized in lamina glial cells and lvfs R7 and R8 in *Drosophila* (Pantazis et al., 2008; Schnaitmann et al., 2018). Therefore, HCLA/B heteromers seem unlikely to exist *in vivo*, at least in the visual system.

In several experiments, histamine and GABA were applied simultaneously. Interestingly, the increase in current occurred upon coapplication in all three transfectants (Figure 3-5). This indicates a possibility that histamine and GABA might have synergistic effects on PxHCLs (Figure 3-5), while simultaneous application of histamine and GABA affect HCLB of housefly only in an additive manner (Kita et al., 2017). The high sequence similarity between PxHCLs and fly HCLB, particularly in the putative agonist binding sites, imply that a small number of amino acid substitutions are responsible for the functional divergence if any. The activation of PxHCLA or PxHCLB homomers by histamine and GABA might be functionally significant. In *Papilio*, for instance, a subset of LMCs are GABAergic (Hamanaka et al., 2012). They terminate in the distal region of the medulla along with the lvfs, which release histamine upon light stimulation. Thus, the possible synergistic effects of histamine and GABA could modulate synaptic transmission in this region.

The variability in the response to GABA between HCLA and PxHCLA may reflect differences in the underlying visual circuits between flies and butterflies. In flies, LMCs are postsynaptic to svfs R1–R6, which all have identical spectral sensitivity (Rivera-Alba et al., 2011), and they are assumed to be responsible mainly for motion vision. In contrast, the spectrally heterogeneous lvfs R7 and R8, which are thought to be essential for color vision, have no synaptic interactions with photoreceptors or LMCs in the lamina. Unlike in flies, the *Papilio* lvfs have a number of lateral processes in the lamina, making local contacts with both svfs and LMCs (Takemura and Arikawa, 2006). As a result, the medulla neurons expressing PxHCLA in *Papilio* receive not only chromatic inputs from histaminergic lvfs but also mixed chromatic and motion signals from LMCs, including the GABAergic ones (Hamanaka et al., 2012). On the other hand, the medulla neurons expressing HCLA in flies only receive chromatic signals from histaminergic lvfs because their HCLAs are insensitive to GABA. Therefore, I

propose that flies have evolved an optimal achromatic motion vision system primarily dependent on R1–R6 broadband photoreceptors (Hardie, 1985), while in butterflies pathways for color and motion vision are less segregated at the early stages of visual processing (Stewart et al., 2015). The sensitivity of PxHCLs to GABA is about 500-fold less than that of histamine. Whether or not this is physiologically relevant has to be confirmed, for example by direct measurement of neurotransmitter concentrations at the synaptic sites.

Skingsley et al. (1995) conducted whole-cell patch-clamp recordings on isolated LMCs in five dipteran species with diverse visual ecologies, in order to study the physiological characteristics of HCLA channels. The dose response functions of LMCs in fast-flying diurnal species exhibit lower sensitivity (higher $EC_{50}$ value) and a narrower dynamic range (larger $n_H$ ) than those in slow-flying crepuscular species. Under the histamine concentration that elicits 10 % of $I_{max}$ in each species, single channel analyses of HCLAs have revealed similar properties among species. Therefore, the observed species differences should be attributed mainly to synaptic gain and perhaps also to absolute sensitivity of single channels (Skingsley et al., 1995). To better understand the evolution of early visual processing in insects, it would be worthwhile to compare the LMC membrane response properties as well as single channel properties, for example, between butterflies whose flight speeds greatly differ (Dudley and Srygley, 1994).

# Chapter 4

## Electrophysiological characteristics of lamina monopolar cells in the *Papilio* lamina

## 4.1 Abstract

The eye of the butterfly, *Papilio xuthus*, contains eight spectrally heterogeneous photoreceptors. In the lamina, nine photoreceptors are bundled with four second-order neurons, lamina monopolar cells (LMCs), forming a cartridge. There the photoreceptors relay information to LMCs via histamine-gated chloride channel PxHCLA. To understand how the histaminergic synapses mediate signal processing in the early visual system, I recorded the spectral responses of single LMCs in the *Papilio* lamina. The recorded LMCs can be divided into non-spectral opponent and spectral opponent cells. I found that the non-opponent type of LMCs can be further divided into three spectrally heterogeneous classes, which respectively resemble the sums of photoreceptor spectral sensitivities in the three ommatidial types. The LMCs seem to integrate spectral signals mainly from the photoreceptors in the same ommatidium. The records of spectrally opponent LMCs provide a clue that *Papilio* LMCs do perform the processing of chromatic information. I propose that both spectrally opponent and non-opponent LMCs feed signals into motion detection circuitry and in parallel into the spectral opponent circuitry. Some LMCs were stained to correlate the LMC spectral class to the LMC morphological class. In addition, other electrophysiological characteristics such as spiking properties, response-intensity functions, polarization sensitivities, and current injection effects in different spectral LMC classes were examined.

Keywords: lamina monopolar cell (LMC), spectral sensitivity, opponency, color vision, signal processing, intracellular recording

## 4.2 Introduction

The eyes of the butterfly, *Papilio xuthus*, bear three spectrally heterogeneous types of ommatidia each housing nine photoreceptor cells R1–R9 (Arikawa, 2003). These photoreceptors are bundled with four second-order neurons, lamina monopolar cells (LMCs), forming a cartridge in the lamina (Takemura and Arikawa, 2006). Observing the synaptic connections there, I found by immunohistochemistry that LMCs express PxHCLA (*Papilio xuthus* histamine-gated chloride channels A) postsynaptic to photoreceptors (Chen et al., 2019). To investigate the spectral coding of LMCs through PxHCLA, I studied the spectral properties of the *Papilio* LMCs in the lamina.

In flies, the short visual fibers (svfs) R1–R6, that terminate in the lamina and make synapses to LMCs, share a common spectral sensitivity covering a broad spectrum (Hardie, 1985; 1986; Rivera-Alba et al., 2011). The color signal processing is thought to be dependent on the spectrally heterogeneous long visual fibers (lvfs) R7 and R8 that terminate in the medulla (Heisenberg and Buchner, 1977; Morante and Desplan, 2004; Yamaguchi et al., 2008). Unlike in flies, the *Papilio* LMCs receive inputs from all receptors with variable spectral sensitivities in the lamina (Takemura and Arikawa, 2006). Furthermore, behavioral experiments have demonstrated that green and red receptors, which are svfs contacting with LMCs, are involved in *Papilio* color discrimination (Kinoshita et al., 2008; Stewart et al., 2015). The chromatic information from green and red svfs must pass through the LMCs, which implies that the *Papilio* LMCs may exhibit variable spectral sensitivities.

Rusanen et al. (2018) have conducted a preliminary study on the spectral sensitivity of *Papilio* LMCs. Most LMCs they recorded showed broad spectral sensitivities probably receiving inputs from different spectral photoreceptors. These LMCs are suitable for motion detection. However, no clear sign of distinctive spectral classes could be found in their experiments. Therefore, it is worthwhile to reexamine the spectral properties of the *Papilio* LMCs to establish their role in chromatic processing.

In the present study, I found that the LMCs are either spectrally opponent or non-opponent. Both respond to broad spectrum of light, but the former one includes three spectrally heterogeneous classes, which are ommatidial type-dependent. The opponent group implies that the LMCs are probably involved not only in achromatic but also in chromatic signaling circuitries. I also correlated the different LMC spectral classes with other electrophysiological properties such as polarization sensitivities.

## 4.3 Materials and Methods

### *Animals*

Adult Japanese yellow swallowtail butterflies, *Papilio xuthus* Linnaeus, of both sexes were obtained from a laboratory stock culture derived from eggs laid by females caught around the campus of Sokendai, Kanagawa, Japan. The hatched larvae were fed with fresh citrus leaves and raised under a short light regime (light: dark = 10 h: 14 h) at 25°C in the laboratory. After emergence, the butterflies were fed with sucrose solution and kept in the 10°C or 4°C incubator before being used for experiments.

### *Light stimulation*

The stimulus light was provided from a 500 W xenon arc lamp through a series of 23 narrow-band interference filters (IF) with 20 nm interval from 300 to 740 nm. The duration of each flash was fixed to 30 ms with 1 s interval. The light was guided through a quartz optical fiber providing a point light source of about 1.56° in diameter for the animal. Light intensity was controlled by a set of neutral density (ND) filters. The exit of the fiber was mounted on the perimeter device and accurately positioned at the optical axis of the ommatidium containing the cell being penetrated. The quantum flux of each monochromatic light was measured by a radiometer (model 470D; Sanso, Tokyo, Japan), and adjusted maximally to $5.0 \times 10^{11}$ photons · $cm^{-2}$ · $sec^{-1}$ (~$2.5 \cdot 10^6$ photons · $facet^{-1}$ · $sec^{-1}$, with a facet diameter of 25 μm) at the corneal surface using an optical wedge, i.e., motorized, continuously graded neutral density filter.

A newly developed LED array device was also used (Belušič et al., 2016). The device was equipped with 21 narrow-band light-emitting diodes (LEDs) with peak wavelengths 365, 375, 390, 403, 422,435, 451, 471, 495, 514, 525, 540, 560, 577, 590, 595, 620, 630, 657, 673, and 686 nm. The quantum flux was controlled using 12-bit pulse width modulation at 1 kHz and a set of ND filters. The duration of each flash was fixed to 10 ms with 50 ms, 100 ms, or 150 ms interval. The light was accurately directed into the optical axis of a single ommatidium by using the beam at minimal aperture (~2°).

### *Intracellular electrophysiology*

A butterfly whose wings and legs were amputated was mounted on a stage. In order to yield the longest electrode excursion for cell penetration in the lamina, the animal's head was rotated about 20° right from its dorso-ventral axis. A silver chloride wire was inserted into the stump

of an antenna serving as the reference electrode. The eye was positioned at the center of the Cardan arm perimeter device, which was set in a Faraday cage.

Microelectrodes were pulled from borosilicate glass capillaries (1 mm/0.5 mm outer/inner diameter) with a P-2000 laser micropipette puller (Sutter, Novato, CA, USA), and filled with 2M potassium acetate. The resistance of the electrode was about 80–120 MΩ. For inserting a glass microelectrode, a small hole covering about 10–20 facets was made in the dorsal region of the eye. A glass microelectrode was advanced into the lamina or medulla through the retina, basement membrane, and the fenestrated layer.

The signal was amplified with a SEC-05X or SEC-10LX amplifier (Npi electronic, Tamm, Germany), conditioned with a Cyber Amp 320 (Axon Instruments, Union City, CA, USA) and digitized with a Micro 1401 (CED, Cambridge, UK) analog-digital (A/D) converter. WinWCP (Strathclyde Electrophysiology Software, Version 4.0.5) and AcqKnowledge (BioPac Systems) packages were used for data acquisition and further analysis.

Spectral responses of photoreceptors were recorded by applying a series of equiquantal monochromatic flashes from short to long wavelength and in the reverse direction. Polarization responses were recorded at the given wavelength by rotating a UV-capable polarization filter OUV2500 (Knight Optical, UK) in front of the exit pupil of the optical fiber: 0˚ was defined as the vertical direction. For recording the angular responses, the Cardan arm was moved at 0.2° intervals through the center of a receptive field between dorsal (+5°) and ventral (-5°) position. The response-light intensity ($V$-log $I$) function was recorded over 4 log unit-intensity range at the given wavelength. The recorded $V$-log $I$ data were fitted to the Naka-Rushton function: $V/V_{max} = I^n/(I^n + K^n)$, where $I$ is the stimulus intensity, $V$ is the response amplitude, $V_{max}$ is the maximum response amplitude, $K$ is the stimulus intensity eliciting 50% of $V_{max}$, and $n$ is the exponential slope. The $V$-log $I$ function was used to convert the $V$ values into photon numbers required to elicit the responses. The normalized reciprocal of the relative photon numbers then yielded the spectral, polarization and angular sensitivities.

***Staining and anatomy***

Following the intracellular recording, some recorded LMCs were marked by injecting 10mM Alexa Fluor 568 solution in 200 mM KCl (A10441, Molecular Probes, Eugene, OR) (resistance 140–160 MΩ) or 3% Neurobiotin tracer (Vector Laboratories, Burlingame, CA) in 2M potassium acetate (resistance 100–120 MΩ). I injected Alexa Fluor 568 into the cells by

applying 150 ms negative current pulses of 3 nA with 3.3 Hz frequency for 10 min, and for the Neurobiotin tracer, I applied 150 ms positive current pulses of 2 nA with 3.3 Hz frequency for 10 min.

After the injection, the eyes, with the optic lobe and cornea still attached, were isolated and fixed in 4.0% paraformaldehyde in 0.1 M phosphate buffer (PB; pH 7.4) overnight at 4°C. I removed the cornea from the compound eye before the tissues were embedded in gelatin/albumin mixture, which subsequently were post-fixed in 8 % paraformaldehyde in PB overnight at 4°C. Horizontal sections at a thickness of 50 μm were cut with a vibratome (Leica VT1000S, Weizlar, Germany), then washed in PB, and incubated with Alexa Fluor 488-conjugated streptavidin (1:200; Invitrogen, Carlsbad, CA, USA) in 0.1M phosphate-buffered saline containing 0.5% Triton X (PBST, pH 7.4) overnight at 4°C. After further PB wash, sections were set on the gelatin-coated slide glass, dehydrated in an ethanol series, cleared in xylene and mounted in Mount-Quick (Daido Sangyo, Tokyo, Japan) beneath a cover slip. All slides were stored in the dark at 4°C until examination. Fluorescent images were taken using a fluorescence microscope (BX-60, Olympus) and a confocal laser scanning microscope (A1Rsi, Nikon, Japan). Confocal images were acquired at an interval of 0.1–0.6 μm. If the stained LMC distributed in different sections, the images were taken separately and then merged into a single image using NIS-Elements software (Nikon, UK).

## 4.4 Results

To record LMC responses in the lamina, I made a hole on the cornea, through which a sharp electrode was inserted and advanced through the retina to lamina. In most of cases, after the electrode was inserted about 400–500 μm depth, the fenestrated layer full of trachea was encountered before reaching the lamina. I specifically focused my attention on the hyperpolarizing cells because the LMC has been known to elicit graded hyperpolarization upon light stimulation by the opening chloride channels (Hardie, 1987; 1989).

***Light response properties***

Figure 4-1 illustrates some units that hyperpolarized to bright white light stimuli in the *Papilio* lamina. The typical LMCs exhibit an initial fast hyperpolarizing on-transient, followed by a sustained plateau, and ending with a depolarizing off-transient after the offset of light (Figure 4-1D). Their characteristic responses are distinguishable from the extracellular potential which also displays hyperpolarization to lights, but lacks a repolarized plateau and a depolarizing off-transient (Figure 4-1F). In addition to the typical LMC, another type of cells showed a very similar waveform of the response with a hyperpolarizing on-transient, a sustained plateau and a depolarizing off-transient (Figure 4-1E). However, this cell type has longer latency (the time required for the membrane potential to reach to the peak) than that of the typical LMCs (Figure 4-1G). I therefore tentatively call this type of response as a “slow LMC-like unit”.

**LMCs and slow LMC-like units**

The slow LMC-like unit can be distinguished from the typical LMC by at least four characteristics in terms of membrane potential, hyperpolarizing on-transient, response-light intensity ($V$-log $I$) function, and angular sensitivity. Based on these characteristics, I recognized 84.2% recorded cells as typical LMCs (130 among 196 cells in total). The remaining 13.8% recorded cells were slow LMC-like units (27 among 196 cells in total) and most of them were recorded in the distal lamina immediately after the electrodes passed the fenestrated layer.

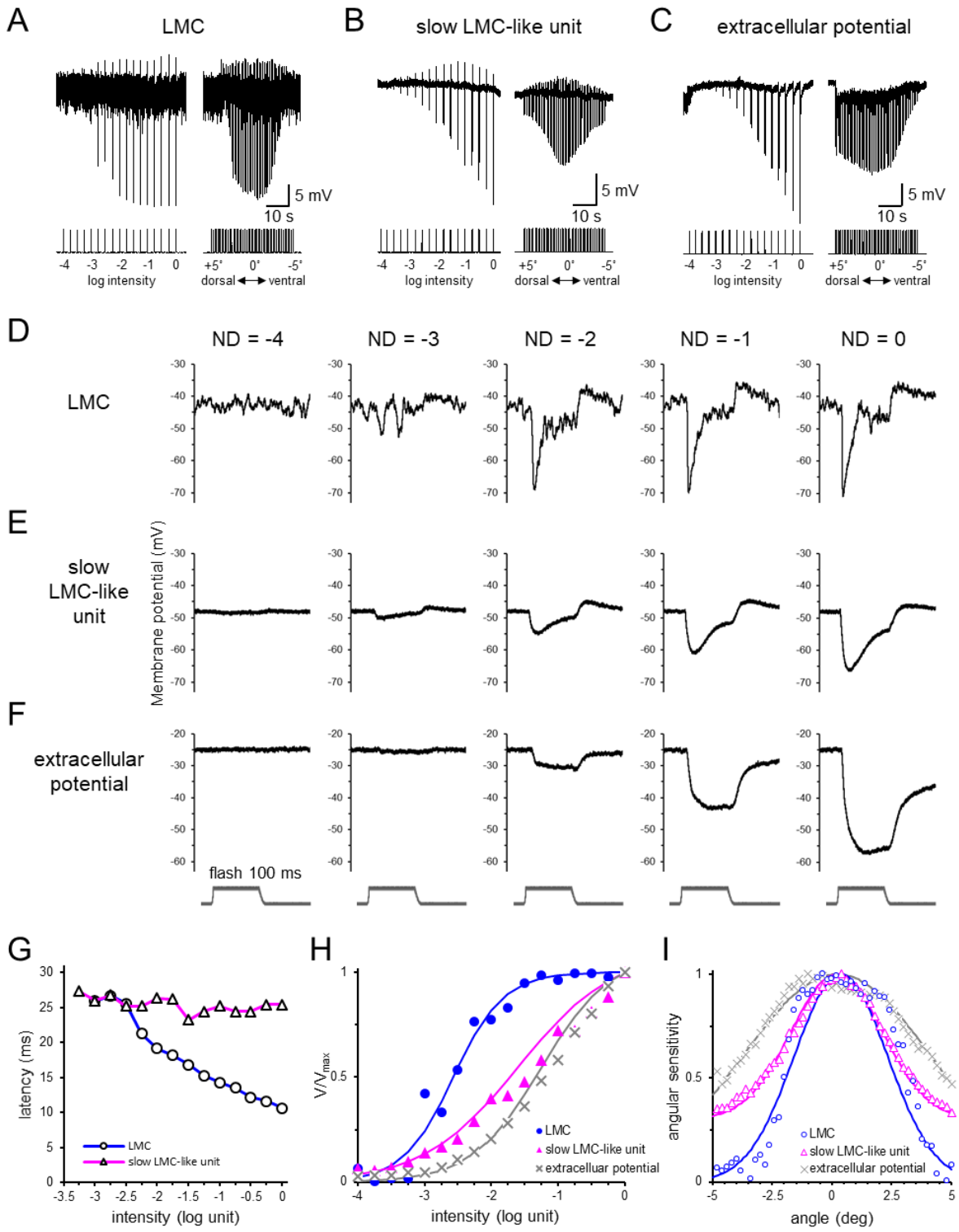


**Figure 4-1. Light responses of hyperpolarizing units in the *Papilio* lamina.** (**A**–**C**) Membrane potential traces of a typical LMC (**A**), a slow LMC-like unit (**B**) and extracellular potential (**C**) showing their response-light intensity (*V*-log *I*) functions graded in 0.25 log intensity steps at 540 nm upon 100 ms pulses (*left*) and angular responses measured with angular steps of 0.2° over 10° (dorsal (+5°) to ventral (-5°)) with 30 ms pulses at 540 nm (*right*). (**D**–**F**) Waveforms of the *V*-log *I* recorded in **A**–**C** at five light intensities, (from left to right) each 10-fold brighter than the last by a neutral density (ND) series. (**G**) The latencies (the time required for the membrane potential to reach to the peak) of hyperpolarizing on-transients under different light intensity levels derived from a typical LMC shown in **A** and a slow LMC-like unit shown in **B.** (continued on the next page)

Comparing the recording traces in Figure 4-1A and Figure 4-1B, I found that the membrane potential of the typical LMC contains pronounced oscillations (Figure 4-1D) as the LMC potential in flies (Van Hateren, 1987), while it is less noisy in the slow LMC-like unit (Figure 4-1E).

Second, the typical LMC shows an extremely fast hyperpolarizing on-transient at the onset of light stimulus, followed by a rapid repolarization before forming a sustained plateau (Figure 4-1D). In contrast, the slow LMC-like unit has long lasting hyperpolarizing on-transient along with a slow repolarization (Figure 4-1E). The hyperpolarizing response latency of the slow LMC-like unit is about 25–30 ms and it is consistent under different light intensities (Figure 4-1G). The typical LMC shows a response latency of 25 ms in dim light which decreases to 10–15 ms in bright light (Figure 4-1G). In other words, the latency of the typical LMC significantly decreases as the light intensity increases while in the slow LMC-like unit it does not.

Third, response amplitude of the typical LMC saturates at a considerably lower light intensity (Figure 4-1A), which is very different to those of the slow LMC-like unit (Figure 4-1B). The slope, $n$, of the $V$-log $I$ curve is much steeper for the typical LMC (usually $n$ is over 1), while the slopes are similar between the slow LMC unit and the extracellular potential ($n$ are less than 1) (Figure 4-1H).

**(H)** Normalized $V/V_{max}$ curves of hyperpolarizing responses to different light intensities from the recording in **A**–**C**. The *lines* are the best fits of the Naka-Rushton function for a typical LMC with the exponential slope $n$ of 1.14 and the stimulus intensity eliciting 50% $V_{max}$ (log$K$) of -2.57, a slow LMC-like unit with $n$ of 0.61 and log$K$ of -1.57, and extracellular potential with $n$ of 0.84 and log$K$ of -1.25. (**I**) The angular sensitivities of a typical LMC, a slow LMC-like unit and extracellular potential derived from the angular response records in **A**, **B** and **C**, respectively. The *lines* are the best fits of the Gaussian function for each unit.

I also measured the angular responses of the typical LMC (Figure 4-1A), slow LMC-like unit (Figure 4-1B) and extracellular potential (Figure 4-1C). Figure 4-1I indicates that the angular sensitivity profiles among them varied considerably in shape. The acceptance angle is defined as the angular width of the visual field at 50% of maximum sensitivity (Washizu et al., 1964; Snyder, 1979). The extracellular potential had the largest receptive field with an acceptance angle of 9.3°. The typical LMC and the slow LMC-like unit possessed narrower receptive fields of width at the half-sensitivity level: approximately 5.2° and 6°, respectively (Figure 4-1I). The receptive fields are much wider than the electrophysiologically determined acceptance angle of a *Papilio* ommatidium, which is about 1.9° (Shibasaki et al., 2006). It implies that both typical LMCs and slow LMC-like units receive inputs not only from its own cartridge but probably also from the six neighboring cartridges.

Noteworthily, while the typical LMC had a slightly narrower acceptance angle than the slow LMC-like unit, if based on the 80% sensitivity level, the typical LMC had a wider receptive field than the slow LMC-like unit instead. On the other hand, if sensitivities below 50% were included, then the area from which light was able to contribute to the responsiveness of the slow LMC-like unit was significantly greater. The typical LMC nearly lost its angular sensitivity function over 10° while a receptive field of the slow LMC-like unit was more extensive with 35% sensitivity at the same angle.

**Spiking LMCs and non-spiking LMCs**

Previously, Rusanen et al. (2018) reported that some *Papilio* LMCs present a depolarizing off-spike immediately after the termination of a light stimulus (Figure 1-8B). Accordingly, LMCs can be further divided into two types: spiking LMC and non-spiking LMC. I have also encountered a number of spiking LMCs. Figure 4-2A shows voltage responses of a spiking LMC to 1 s light pulses at seven intensities. The off-spikes were detectable in bright light (ND = -1.5 to 0). The amplitudes of the hyperpolarizing on-transient, sustained plateau and depolarizing off-spike increase as light intensities increase. The *V*-log *I* curves of the hyperpolarizing on-transient (Figure 4-2B) and sustained plateau (Figure 4-2C) are similar. Their amplitudes saturated at relatively lower light intensities. In contrast, the depolarizing off-spike (Figure 4-2D) has a relatively shallower *V*-log *I* curve. In fact, off-spike responses exhibit high variability from recording to recording even in the same cell.

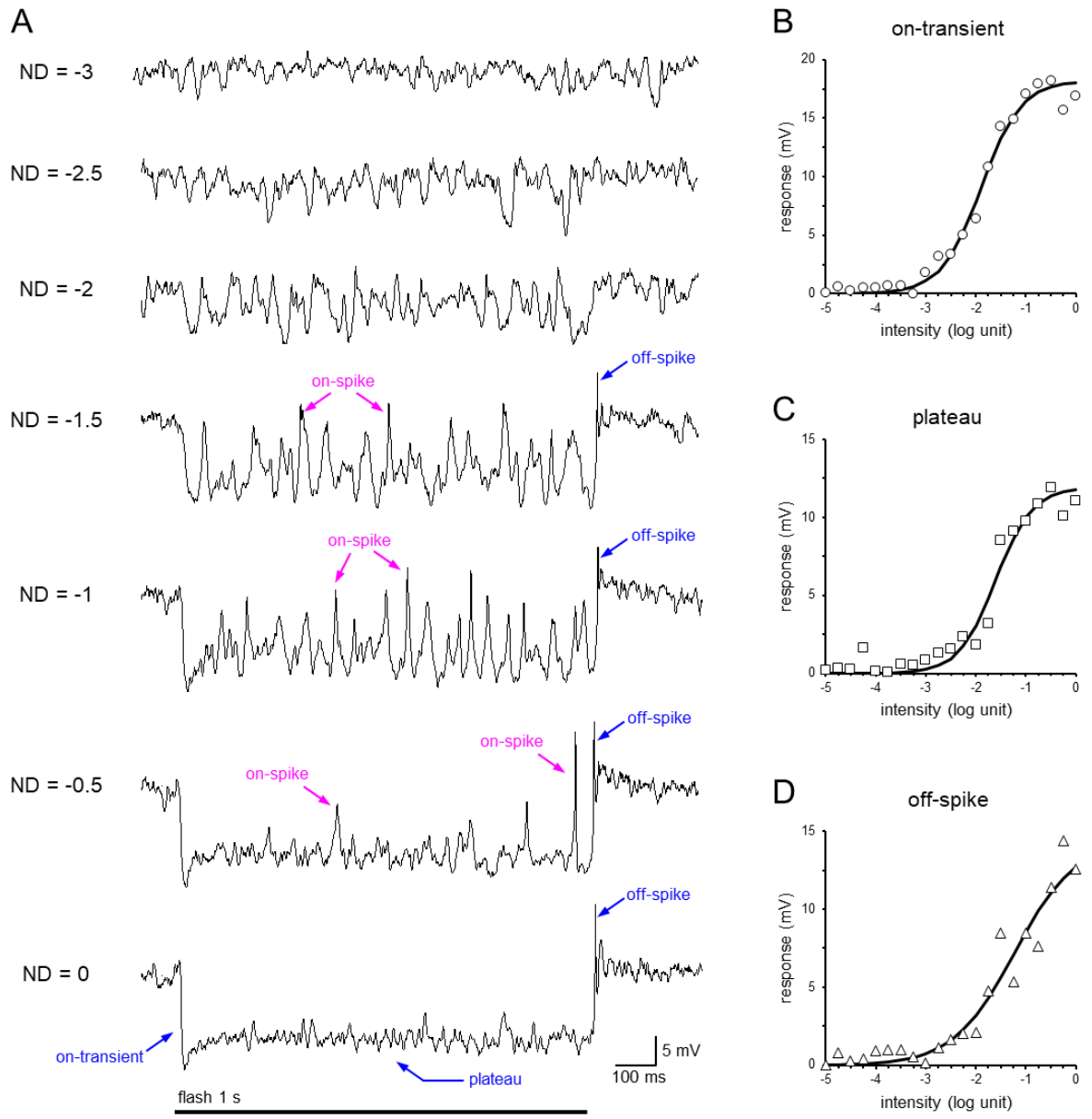


**Figure 4-2. Light responses of a spiking LMC at different light intensity levels.** (**A**) Spiking LMC responses to 1 s flashes (*horizontal bars*) at 540 nm, graded in 0.5 log intensity steps. (**B**–**D**) A set of *V*-log *I* functions of a hyperpolarizing on-transient (**B**), a sustained plateau (**C**) and a depolarizing off-spike (**D**) recorded from a spiking LMC in **A**, with the best fits of the Naka-Rushton function. The exponential slope *n* and the stimulus intensity eliciting 50% $V_{max}$ (log*K*) are as follows: 1.08 and -1.89 for an on-transient, 1.19 and -1.61 for the plateau, and 0.71 and -1.24 for an off-spike, respectively.

Apart from off-spikes, I also observed the so-called on-spikes during the light stimulus. These depolarizing on-spikes appeared randomly and were more evident in dim light (e.g., ND = -1.5 and -1 in Figure 4-2A). Their spiking rate and amplitudes decreased in bright light (e.g., ND = -1 and 0 in Figure 4-2A). Previously, Rusanen et al. (2018) have reported and discussed the same phenomenon of the spiking rate decreasing with light intensity in the *Papilio* spiking LMCs.

In general, my recordings in spiking LMCs share similar characters as previously reported by Rusanen et al. (2018), except the occurrence ratios of spiking and non-spiking LMCs. Rusanen et al. (2018) demonstrated that 41 out of 67 recorded LMCs (61.2%) displayed off-spikes in their recording. In my case, I only recorded 15.4% (26 among 169 cells in total) of typical LMCs producing off-spikes after the offset of light. The reason for this is unknown. However, I have noticed a tendency that I could not observe off-spikes in newly emerged animals. To support this observation, I compared the occurrence ratio of spiking LMCs with the days after adult eclosion. Figure 4-3 indicates that the off-spikes were barely recorded in fresh butterflies and only appeared in older individuals. The occurrence ratio of spiking LMCs increases to 23.9% (26 out of 109 LMCs) in the butterflies over the age of 10-days old, and, more than 50% recorded cells were spiking LMCs in those over 23-days old. However, the age demonstrated here may not represent their real age because I kept the emerged adults at 10°C or 4°C. At any rate, the off-spike generation might be related to the time after adult eclosion. On the other hand, off-spikes have only been overserved in the typical LMCs while the slow LMC-like units never displayed off-spikes in my recordings.

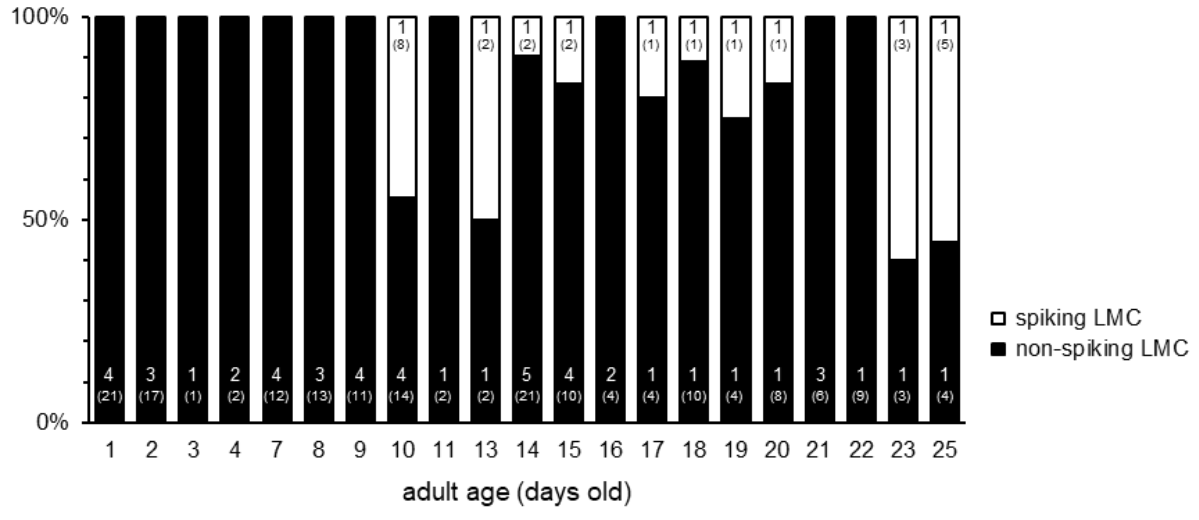


**Figure 4-3. The occurrence ratios of spiking LMCs and non-spiking LMCs in different ages of experimental butterflies.** The age bins display the ratios in recording numbers of cells. The numbers in each bin indicate the numbers of butterflies (49 individuals in total) and the numbers in bracket are the cell numbers (109 cells in total). The off-spikes were observed only in 10-days old or older individuals.

### *Spectral properties*

To investigate how is the chromatic information conveyed to the second-order LMCs through histaminergic synapses, I measured the spectral sensitivities of typical LMCs and also of the slow LMC-like units in the *Papilio* lamina. In the previous section, I divided typical LMCs into spiking and non-spiking LMCs based on the presence of a depolarizing off-spike. However, I found that these off-spikes were not reliable for classifying the spectral types of LMCs due to two main reasons. One is, as mentioned, that the off-spikes only occur in older animals. Another one is that the generation of off-spikes seems to be unrelated to wavelength. Figure 4-4 illustrates a spiking LMC responding to three runs of spectral scans from UV to red wavelengths. While the spectral responses of hyperpolarizing on-transients were consistent among recordings, the off-spikes appeared randomly with wavelengths. For example, there was no prominent off-spike after the stimulation at the UV wavelength range in the first spectral scan. However, an off-spike was observed after a light stimulation at 375 nm in the second scan and more obvious in the third spectral scan where off-spikes also appeared at 365 nm and 390 nm. Table 4-1 also indicates that the spiking LMCs can be found in different spectral types. Accordingly, in this section, I ignored off-spikes for the classification of LMC spectral classes.

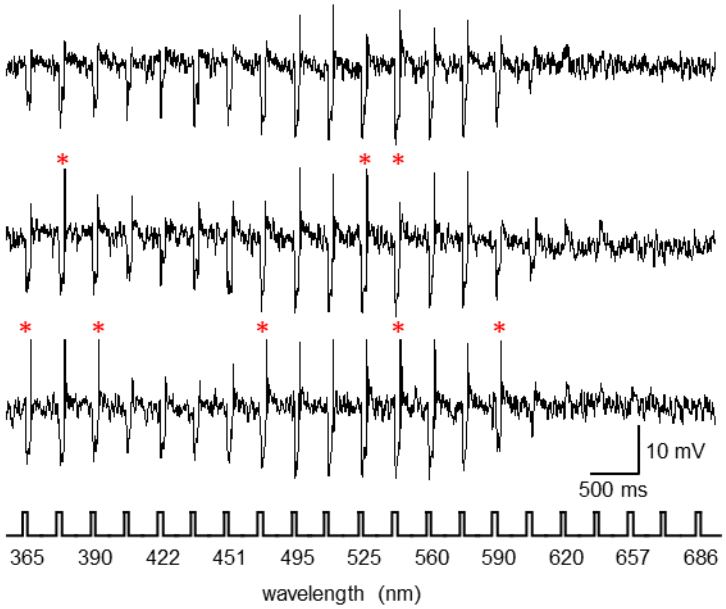


**Figure 4-4. Spectral responses of a spiking LMC.** Membrane potential traces of a spiking LMC upon three continuous runs of isoquantal spectral stimulation with 50 ms pulses from the LED array. *Asterisks* indicate the variation in the presence of off-spikes from previous records upon the same wavelength stimulation.

Based on the spectrally opponent responses, i.e. ones that are positive at some wavelengths and negative at others, I first divided the typical LMCs into two types: non-spectrally opponent and spectrally opponent. LMCs were then grouped into different spectral classes regarding their spectral sensitivities (Table 4-1). On the other hand, all recorded slow LMC-like units share a consistent and unique spectral sensitivity which can be distinguished from those of typical LMCs. Further details of each spectral class are described below.

**Table 4-1. The recording numbers of LMC types, spectral classes and spiking properties**

| LMC type | opponency | spectral class | | non-spiking | spiking |
|---|---|---|---|---|---|
| LMC *N*=169 (84.2%) | non-opponent *N*=130 (76.9%) | I | *N*=57 (43.8%) | *N*=46 | *N*=11 |
| | | II | *N*=17 (13.1%) | *N*=14 | *N*=3 |
| | | III | *N*=55 (42.3%) | *N*=54 | *N*=1 |
| | | others | *N*=1 (0.8%) | *N*=1 | *N*=0 |
| | opponent *N*=39 (23.1%) | SW | *N*=7 (17.9%) | *N*=6 | *N*=1 |
| | | MW | *N*=4 (10.3%) | *N*=3 | *N*=1 |
| | | LW | *N*=23 (59.0%) | *N*=10 | *N*=8 |
| | | others | *N*=5 (12.8%) | *N*=5 | *N*=0 |
| slow LMC-like unit *N*=27 (13.8%) | non-opponent *N*=27 (100%) | | | *N*=27 | *N*=0 |

**Spectral sensitivity of slow LMC-like units**

I recorded slow LMC-like units by using the LED array (13 units) and the IF series (14 units), yielding very similar spectral response profiles (Figure 4-5). All of them contained maximal hyperpolarization at 480 nm to 520 nm along with an evident UV-peak. Their sensitivities gradually decrease with increasing wavelengths from green to red spectral ranges, having <20% sensitivity over 640 nm. Most of them displayed a prominent depolarizing off-transient at all wavelength ranges.

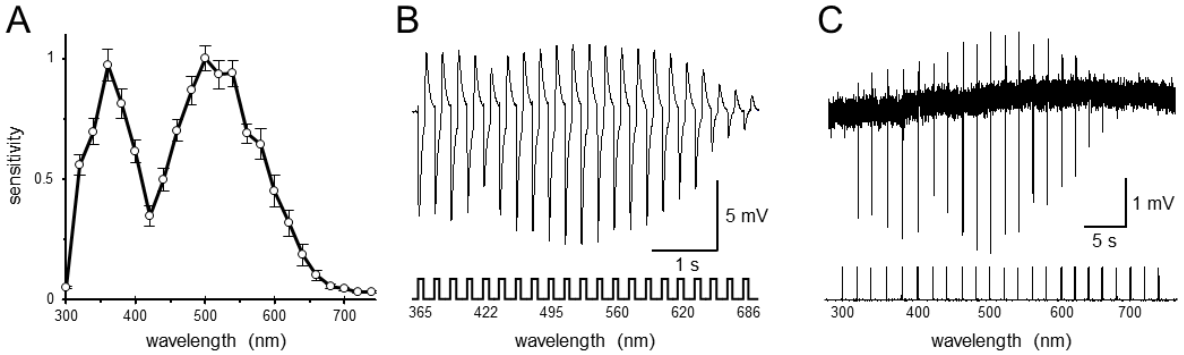


**Figure 4-5. The spectral sensitivity of the slow LMC-like unit.** (**A**) An average spectral sensitivity (mean ± SEM) of slow LMC-like units (*N*=14). (**B**–**C**) Membrane potential traces of slow LMC-like units upon isoquantal spectral stimulation with 100 ms pulses from the LED array (**B**) and with 30 ms pulses from the IF series (**C**).

### Non-opponent LMCs

I successfully recorded the spectral properties in 130 non-opponent type of LMCs in the *Papilio* lamina. All of them responded to a broad spectrum of light. Regarding the spectral responses, they can be divided into 3 spectrally heterogeneous classes based on sensitivities at UV (360 nm) and red (620 nm) wavelengths. The first class includes LMCs with high UV/high red sensitivities (Figure 4-6A): their response amplitudes at 360 nm and 620 nm were over 60% relative to the maximal hyperpolarization. LMCs in this class had maximal hyperpolarization at 580 to 620 nm. The second class includes LMCs with low UV/high red sensitivities (Figure 4-6B): their response amplitudes at 360 nm were less than 30% and at 620 nm were over 60% relative to the maximal hyperpolarization which peaked at 480 to 560 nm. The third class includes LMCs with high UV/low red sensitivities (Figure 4-6C): their response amplitudes at 360 nm were more than 70% and at 620 nm were less than 30% relative to the maximal hyperpolarization which peaked at 460 to 540 nm.

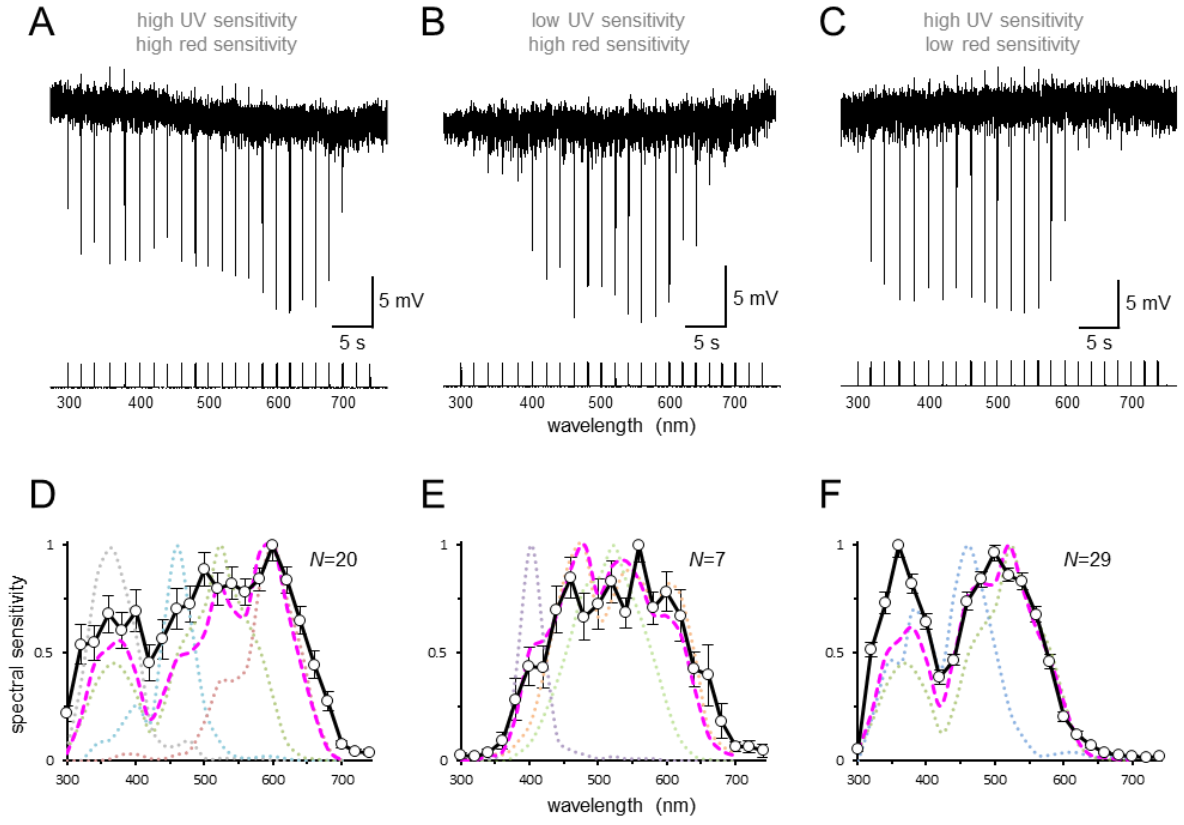


**Figure 4-6. Spectral sensitivities of non-opponent LMCs.** (**A**–**C**) Membrane potential traces of three spectral classes of non-opponent LMCs upon isoquantal spectral stimulation with 30 ms pulses from the IF series. (**D**–**F**) Average spectral sensitivities (mean ± SEM; *thick solid lines*) of three spectral classes correspond to the weighted linear sum (*magenta dashed lines*) of receptor sensitivities (*thin dotted lines*) of the three ommatidial types. *N*, sample number.

*Thick solid lines* in Figure 4-6D–F represent average spectral sensitivities of each class from 56 LMCs whose recordings included spectral responses and *V*-log *I* functions for the spectral sensitivity conversion. I then compared them with the weighted linear sum of receptor spectral sensitivity $S(\lambda)$ in *Papilio* three types of ommatidia, which is given by normalizing the summation of receptor spectral sensitivities multiplied by the occupation ratio of receptors in each ommatidium:

$$S(\lambda) = \sum R_i\,(\lambda)$$

Where $R_i(\lambda)$ is the spectral sensitivity of photoreceptor $i$ ($i$ = 1–8) in each ommatidium (Arikawa et al., 2003).

*Magenta dashed lines* in Figure 4-6D, Figure 4-6E and Figure 4-6F respectively indicate the weighted linear sum of photoreceptor spectral sensitivities (*colored dotted lines* in Figure 4-6D–F) in type I, type II and type III ommatidia. The spectral sensitivities of three spectral classes of non-opponent LMCs resemble to the sum of receptor sensitivities in three ommatidial types, suggesting that a majority of LMCs receive numerous inputs from different photoreceptors within the same cartridge. Accordingly, I termed the non-opponent LMCs in the spectral classes with high UV/high red sensitivities as type I LMC, low UV/high red sensitivities as type II LMC, and high UV/low red sensitivities as type III LMC. In addition, I also encountered one LMC with low UV/low red sensitivities, which I could not classify it into any of the three main spectral classes. Table 4-1 summarized the ratios of each spectral class in my recording.

On the other hand, the off-transient exhibited a high variability from cell to cell. All LMC examples shown in Figure 4-6 did not display clear off-transients at any wavelength. However, some LMCs had evident off-transients at all wavelength rangs (e.g., Figure 4-11E), while in some other LMCs the off-transients only appeared at some wavelengths (e.g., Figure 4-11C). Contrary to the off-spikes, the presence of off-transients at certain wavelengths was consistent in the recorded cells.

**Spectrally opponent LMCs**

I have encountered 39 LMCs exhibiting spectral opponency (Figures 4-7, 4-8). Figure 4-7 illustrates the three main classes of spectrally opponent LMCs with depolarization at either UV (Figure 4-7D), blue-violet (Figure 4-7E), or red (Figure 4-7F) wavelengths. They are thus respectively termed as short wavelength (SW)-opponent LMCs (Figure 4-7A; 7 units), middle wavelength (MW)-opponent LMCs (Figure 4-7B; 4 units) and long wavelength (LW) -opponent LMCs (Figure 4-7C; 23 units).

The SW-opponent LMCs had hyperpolarization peaked at 480 to 540 nm and depolarizing spectrally opponent responses in the wavelength region below 380 nm where their hyperpolarization was absent (Figure 4-7A). The MW-opponent LMCs had hyperpolarization covering from UV to red wavelengths and their depolarization was limited in the wavelength region between 400 nm to 450 nm (Figure 4-7B). The LW-opponent LMCs showed depolarization in the wavelength region above 630 nm. The amplitudes of hyperpolarizing responses in this class significantly decreased above 600 nm (Figure 4-7C).

In addition to the main opponent classes, which contain more than three records in each, I also encountered five opponent LMCs showing unique spectral responses (Figure 4-8). The depolarizing opponent responses in a UV+/B+/G+/R- opponent LMC covered a broad spectrum range from UV to red and the hyperpolarization only appeared in the red wavelength (Figure 4-8A). In contrast, the response polarities at UV and red wavelengths were opposite in a UV-/B+/G+/R+ opponent LMC shown in Figure 4-8D. This cell only hyperpolarized to UV light and depolarized to the wavelength above 450 nm. The response profile of a UV+/B+/G-/R+ opponent LMC looks quite complicated (Figure 4-8B). This cell had hyperpolarizing on-transients in the UV to green wavelength ranges, but its plateau depolarized in UV, blue and red wavelengths. In the end, the cell only hyperpolarized in the green wavelength range. Figure 4-8E illustrates a UV-/B+/G+/R- opponent LMC that had depolarizing opponent responses in the blue and green wavelengths. A UV+/B-/G+/R- opponent LMC shown in Figure 4-8C illustrates a further complexity with four changing phases.

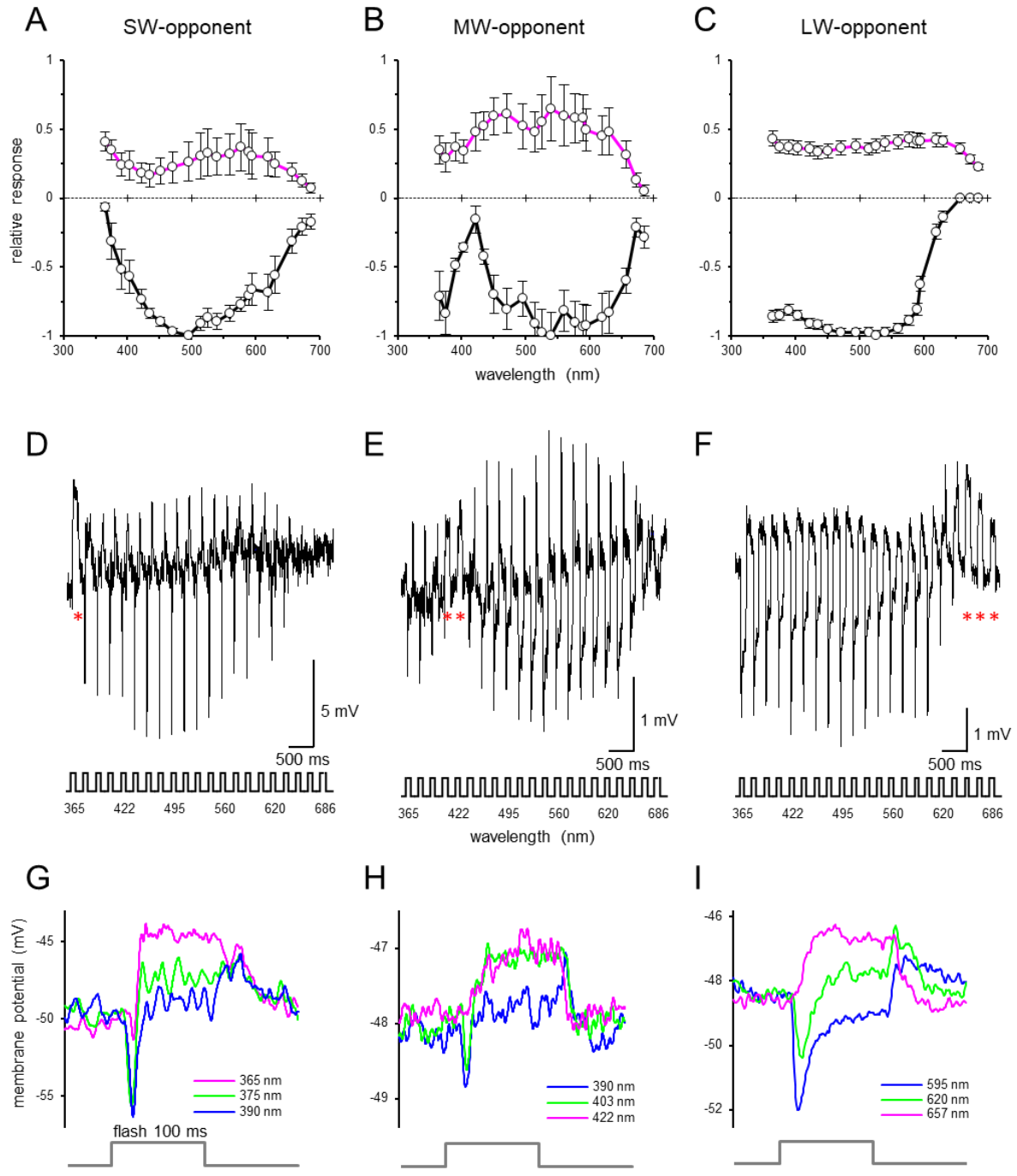


**Figure 4-7. Spectral responses of spectrally opponent LMCs.** (**A**–**C**) Averaged spectral response curves (mean ± SEM) of short wavelength (SW)-opponent LMCs (**A**; *N*=7), middle wavelength (MW)-opponent LMCs (**B**; *N*=4) and long wavelength (LW) -opponent LMCs (**C**; *N*=23). The *black curves* and *magenta curves* in **A**–**C** indicate the averaged amplitudes of hyperpolarizing and depolarizing responses, respectively. (**D**–**F**) Membrane potential traces of a SW-opponent LMC (**D**), a MW-opponent LMC (**E**) and a LW-opponent LMC (**F**) upon isoquantal spectral stimulation with 100 ms pulses from the LED array. *Asterisks* indicate the depolarizing spectrally opponent responses. (**G**–**I**) Expended time scale shows some waveforms of the recording in **D**–**F** at the wavelengths producing hyperpolarizing (*blue line*), intermediate (*green line*) and opponent depolarizing responses (*magenta line*). (**G**) Waveforms of the SW-opponent LMC in **D**. (**H**) Waveforms of the MW-opponent LMC in **E**. (**I**) Waveforms of the LW-opponent LMC in **F**.

Regarding waveforms of responses, the opponent responses is marked by the lack of the hyperpolarizing on-transient. The onset time of depolarization is slightly later than that of the hyperpolarizing on-transients (Figure 4-7G – I). Moreover, the depolarization appears within the duration of the light stimulus. Therefore, the depolarizing opponent responses cannot be confused with the depolarizing off-transient. I propose that the depolarization in spectrally opponent LMCs is mainly composed of the depolarizing plateau. However, the origin of the depolarizing opponent responses remains uncertain.

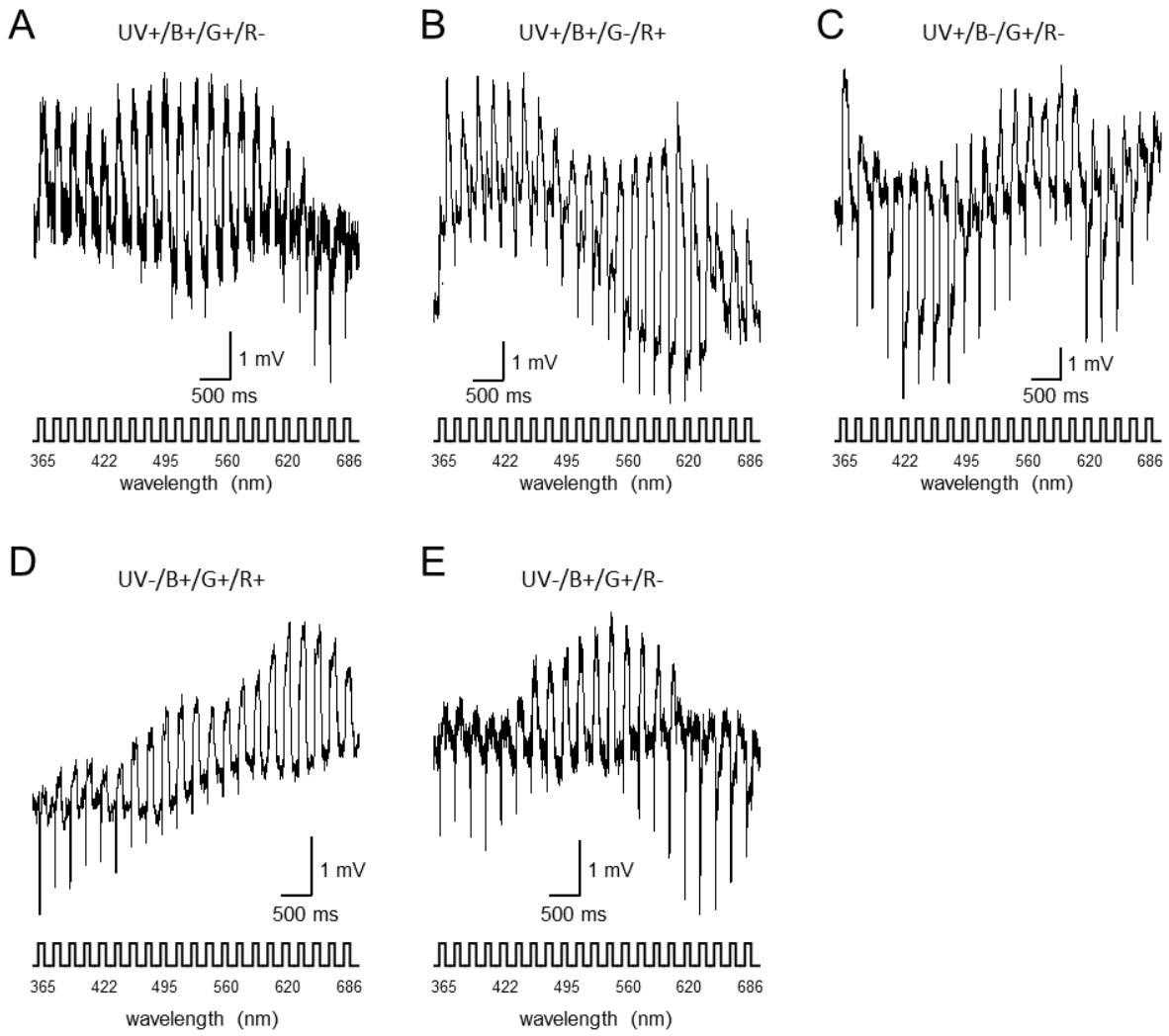


**Figure 4-8. Spectral responses of other spectrally opponent LMCs.** Membrane potential traces of a UV+/B+/G+/R- opponent LMC (**A**), a UV+/B+/G-/R+ opponent LMC (**B**), a UV+/B-/G+/R- opponent LMC (**C**), a UV-/B+/G+/R+ opponent LMC (**D**), and a UV-/B+/G+/R- opponent LMC (**E**) upon isoquantal spectral stimulation with 100 ms pulses from the LED array.

**Effects of stimulus size in spectral responses**

The spectral responses for determining spectral classes in the above section were recorded with a point source (closed aperture; ~2°). Figure 4-1I reveals that the receptive field of both the typical LMC and the slow LMC-like unit are larger than an ommatidium. Are the spectral sensitivities modified by possible interaction with neighboring cartridges? To address this question, I compared the spectral responses to different sizes of light source by changing the size of an aperture that was placed between the light source and the eye, behind the objective lens of the stimulating apparatus. The aperture of the stimulating beam could be varied between 2° and 15°. Some examples are shown in Figure 4-9.

All slow LMC-like units increased the response amplitudes including hyperpolarizing on-transient, sustained plateau and depolarizing off-transient (Figure 4-9A). The extended source stimulation (open aperture; ~15°) brings a proportional increase in response amplitudes at all wavelengths and thus their spectral sensitivities were same to those recorded with a point source.

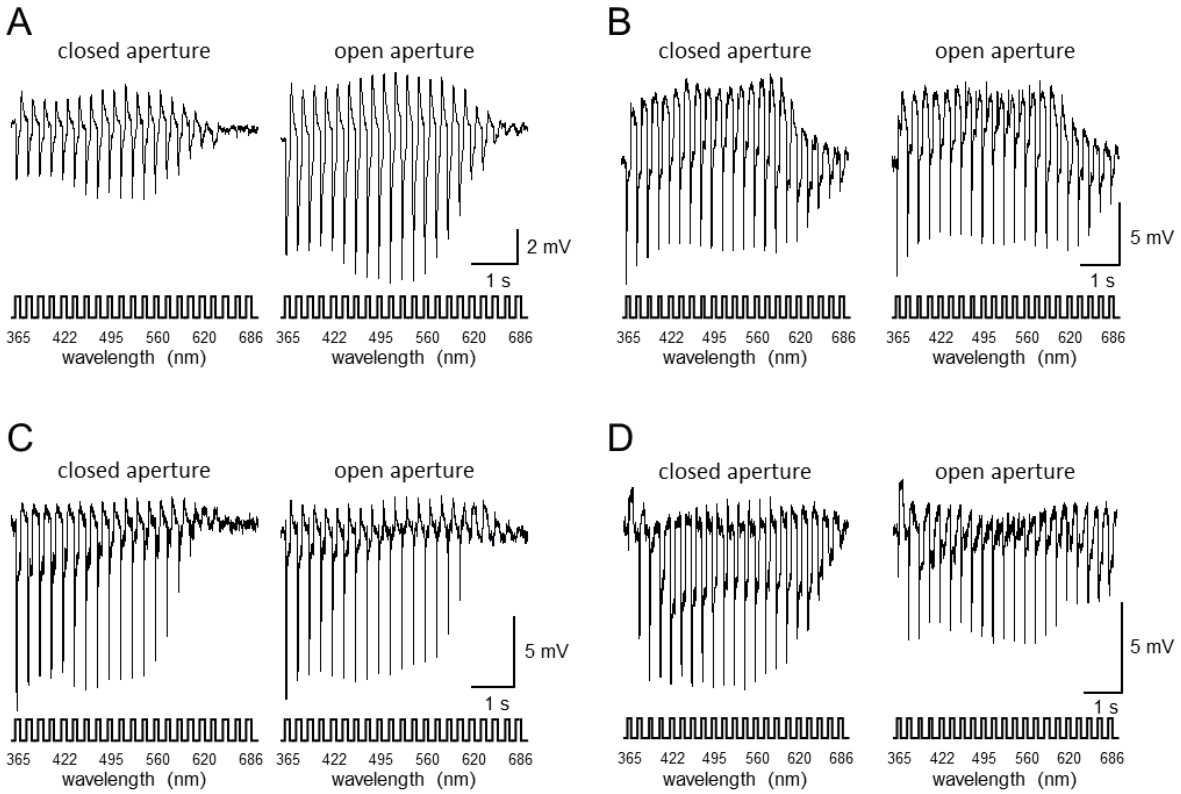


**Figure 4-9. Spectral response curves of LMCs toward a point source (*left)* with a closed aperture and an extended source with a fully open aperture (*right*).** Membrane potential traces of a slow LMC-like unit (**A**), a non-opponent type I LMC (**B**), a LW-opponent LMC (**C**), and a SW-opponent LMC (**D**) upon isoquantal spectral stimulation with 100 ms pulses from the LED array.

In contrast to the slow LMC-like units, no significant change has been found in the amplitude of hyperpolarizing on-transient in most typical LMCs (e.g., Figure 4-9B, C). However, the changes were found in the plateau and off-transient. Figure 4-9B illustrates a non-opponent type I LMC. The amplitudes of hyperpolarization were almost identical between the point source stimulus and the extended source, while those of the plateau became smaller. Furthermore, small off-spikes appeared in the green wavelength range by opening the aperture. A LW-opponent LMC shown in Figure 4-9C demonstrates similar phenomena in decreasing plateau response amplitudes and increasing depolarizing off-transient with the extended source. In addition, the depolarizing opponent responses in the red wavelength range were more evident with the extended source. The cases in Figure 4-9B and Figure 4-9C, the spectral sensitivities did not change with the stimulus size. Taken together, opening the aperture seems to decrease the plateau amplitude but increase the presence of off-transient or off-spikes while producing no significant effect in spectral sensitivities.

However, I also observed the change in spectral sensitivities in some LMCs such as in a SW-opponent LMC shown in Figure 4-9D. The amplitude of hyperpolarizing on-transient increased in the UV and deep-red wavelength ranges but it decreased in other wavelengths when using the extended source. Moreover, the plateau amplitude decreased in the UV and green but increased in red. As a result, the hyperpolarizing peak shifted from 540 nm to 580 nm. This LMC might have strong interactions with neighboring cartridges.

**Effects of light intensities on spectral sensitivities**

Figure 4-10A demonstrates the *V*-log *I* functions of a non-opponent type III LMC at UV (360 nm), blue (480 nm), green (540 nm), and red (600 nm) wavelengths. The *V*-log *I* curves are parallel irrespective of the stimulating wavelength (Figure 4-10B). The exponential slope *n* and the stimulus intensity eliciting 50% $V_{max}$ (log*K*) of each *V*-log *I* curve are given in Table 4-2. All *V*-log *I* curves contained high *n* values of around 1.20, and thus resulted in relatively narrow dynamic range in all wavelengths. The narrow dynamic range affects the spectral sensitivity. Figure 4-11 illustrates spectral responses and sensitivities of three spectral classes of non-opponent LMCs at different light intensity levels. The spectral responses changed dramatically with the stimulus intensity.

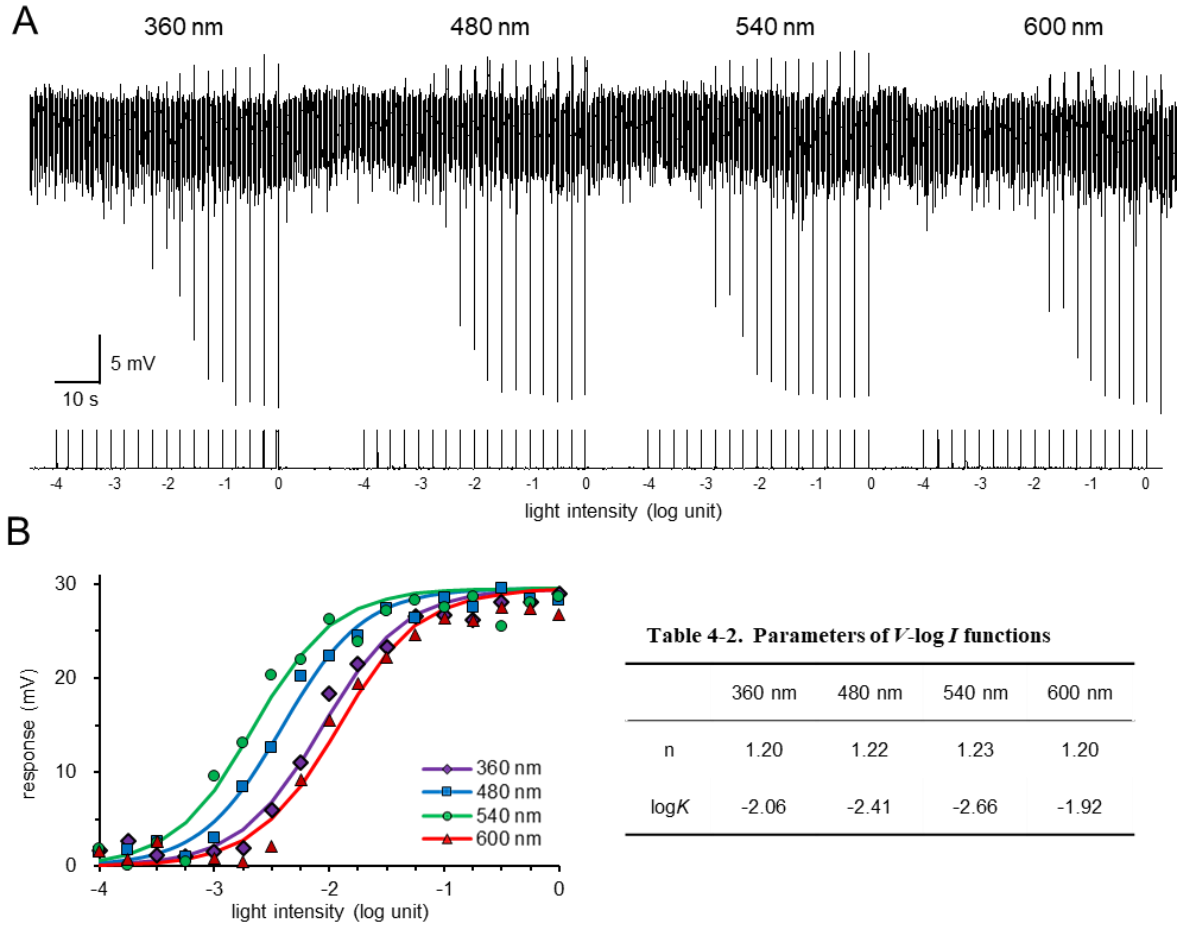


**Table 4-2. Parameters of *V*-log *I* functions**

| | 360 nm | 480 nm | 540 nm | 600 nm |
|---|---|---|---|---|
| n | 1.20 | 1.22 | 1.23 | 1.20 |
| log*K* | -2.06 | -2.41 | -2.66 | -1.92 |

**Figure 4-10. *V*-log *I* functions of a type III LMC at different stimulation wavelengths.** (**A**) A membrane potential trace of the cell upon 30 ms pulses at four wavelengths (from left to right) 360, 480, 540, and 600 nm, graded in 0.25 log intensity steps. (**B**) Four *V*-log *I* curves of hyperpolarizing responses from the recording in **A** measured at wavelengths at (from left to right) 540, 480, 360, and 600 nm. The *lines* are the best fits of the Naka-Rushton function through each curve. The exponential slope *n* and the stimulus intensity eliciting 50% $V_{max}$ (log*K*) of each *V*-log *I* curve are shown in **Table 4-2**.

Figure 4-11E shows the spectral responses of the type III LMC whose *V*-log *I* function is illustrated in Figure 4-10. Its spectral responses were barely detectable at the lowest illumination level (ND = -4). At a brighter light intensity (ND = -3), the spectral responses of hyperpolarization showed two peaks at 360 nm and 520 nm. Such spectral sensitivity (*blue line* in Figure 4-11F) resembles that of dual-peaked green (dG) receptors. Figure 4-10B has demonstrated that the cell was most sensitive to green light; this cell might be receiving inputs mainly from the dG receptors in type III ommatidia. The spectral responses became very broad covering from UV to green wavelengths at the highest intensity level (ND = -2), corresponding to the *V*-log *I* functions as shown in Figure 4-10B. The most significant change of spectral sensitivities between two illuminations were found in the blue and red wavelengths. The sensitivities increased by 40% at 420 nm, 600 nm and 620 nm (*magenta line* in Figure 4-11F).

Similar effects were also found in type I LMCs (Figure 4-11A – D). Such effects would influence the reliability of the determination of LMC spectral classes. For example, note the case of a type I LMC shown in Figure 4-11A. At the dimmer illumination (ND = -2), the cell showed high UV/low red sensitivities, which resembles to the type III LMC. However, the high red sensitivity was observed at the brighter illumination (ND = -1) and thus the cell is recognized as the type I LMC. Since the majority of LMCs saturated at relatively low intensity levels, I usually did not use very bright illuminations for measuring spectral sensitivities. It could have led the classification of LMC spectral classes misleading.

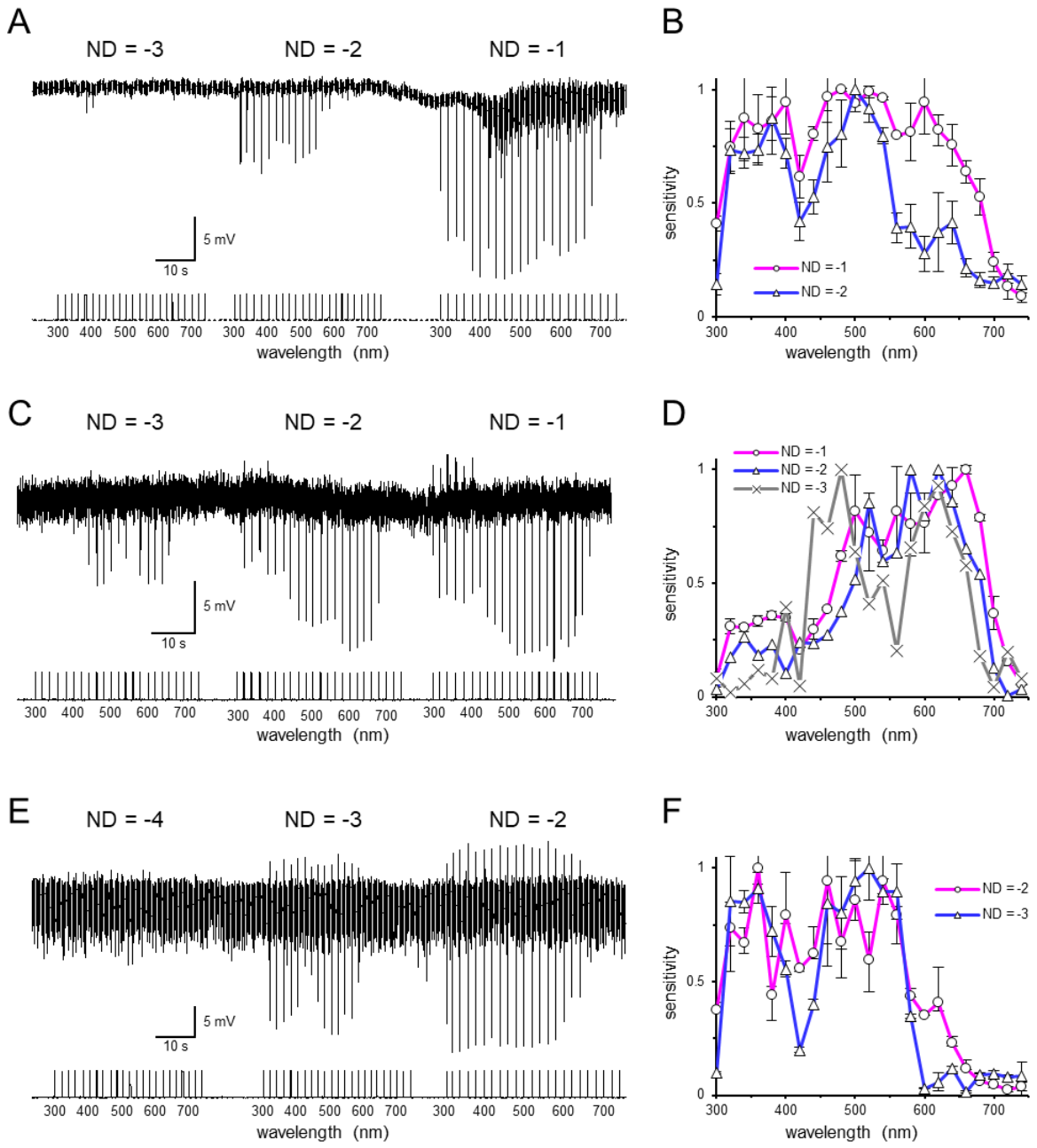


**Figure 4-11. The spectral responses and sensitivities of non-opponent LMCs at different light intensity levels.** (**A,C,E**) Membrane potential traces of two type I LMCs (**A,C**) and a type III LMC (**E**) upon 30 ms isoquantal spectral pulses from 300 to 740 nm at three illumination levels. (**B,D,F**) Average spectral sensitivities (mean ± SEM; each curve is the average of two recordings) of type I LMCs (**B,D**) and a type III LMC (**F**) at different light intensities from the recording in **A,C,E,** respectively.

***LMC morphology***

Previously, Ribi (1987) classified four morphological types of LMCs (L1–L4) in the Australian Orchard butterfly, *Papilio aegeus*. Hamanaka et al. (2013) also proposed that LMCs of *Papilio xuthus* might have four morphological types. The recent progress in the serial block face-scanning electron microscopy (SBF-SEM) analysis of the *Papilio xuthus* LMCs suggested that each cartridge contains four morphological distinct LMCs (Matsushita et al., in preparation). Regarding the branching patterns in the lamina, L1 bear the dendritic processes within its own cartridge, while the dendritic processes of L2–L4 extend into the neighboring cartridges in addition to its own. On the other hand, Rusanen et al. (2018) have stained two groups of LMCs showing different morphology in the medulla terminal: L1/L2 and L3/L4. The cells of L1/L2 have roundish terminals which terminate at the distal surface of the medulla, whereas the cells of L3/L4 have elongated terminals that terminate in a slightly deeper layer. These two morphological groups were correlated to spiking properties: only L3/L4 displayed prominent off-spikes (Rusanen et al., 2018).

In this study, I further correlated the LMC morphological types with spectral properties. Spectral responses of LMCs were first recorded by intracellular recording to identify the spectral type. Then, I injected the dye into the recorded cell to identify its morphological types. So far, I have successfully stained some non-opponent LMCs (Figures 4-12,4-13,4-14). Based on the presence of dendritic processes and positions of axon terminals in the medulla along with the presence and absence of long lateral processes in the lamina, I temporarily grouped four stained LMCs into three distinct morphological types.

Figure 4-12 shows a neurobiotin-injected LMC whose spectral sensitivities are illustrated in Figure 4-11B. According to its spectral sensitivity spanning from UV to red, this LMC is most likely a type I LMC located in the cartridge of a type I ommatidium. The cell body of the stained LMC was found in the region outside of the distal lamina (Figure 4-12A). A thin neurite connecting the cell body extended toward the lamina. The axon in the lamina was densely covered with radially arranged dendritic processes along its entire length (Figure 4-12B). These short side branches extend almost horizontally, and they seemed to swell to form blebby endings. The 90˚ rotated confocal image indicates that these processes were limited within its own cartridge (Figure 4-12B'). The axon projected from the anterior lamina to the posterior medulla via the first optic chiasma (Figure 4-12A). The cell terminated in the proximal border of medulla layer 2 (Figure 4-12A) and furcated into two thick branches (Figure 4-12C).

The bushy-like structures with numerous side branches were observed in the layer 1 and the proximal layer 2 of the medulla.

Since the stained LMC terminated in the shallower layer of medulla, the cell most likely belongs to the L1/L2 group according to the morphological description of LMCs by Rusanen et al. (2018). The intracellular recording of the stained LMC demonstrated that the cell did not produce off-spikes (Figure 4-11A), which is consistent with the physiological characteristics of L1/L2 as well (Rusanen et al., 2018). Furthermore, the SBF-SEM analysis of the *Papilio xuthus* LMCs indicates that the lateral processes of L1 are restricted to its own cartridge while those of L2 extend into the neighboring cartridges (Matsushita et al., in preparation). The stained LMC with short lateral processes may be L1. Taken together, I conclude that the stained LMC is most likely a type I-L1.

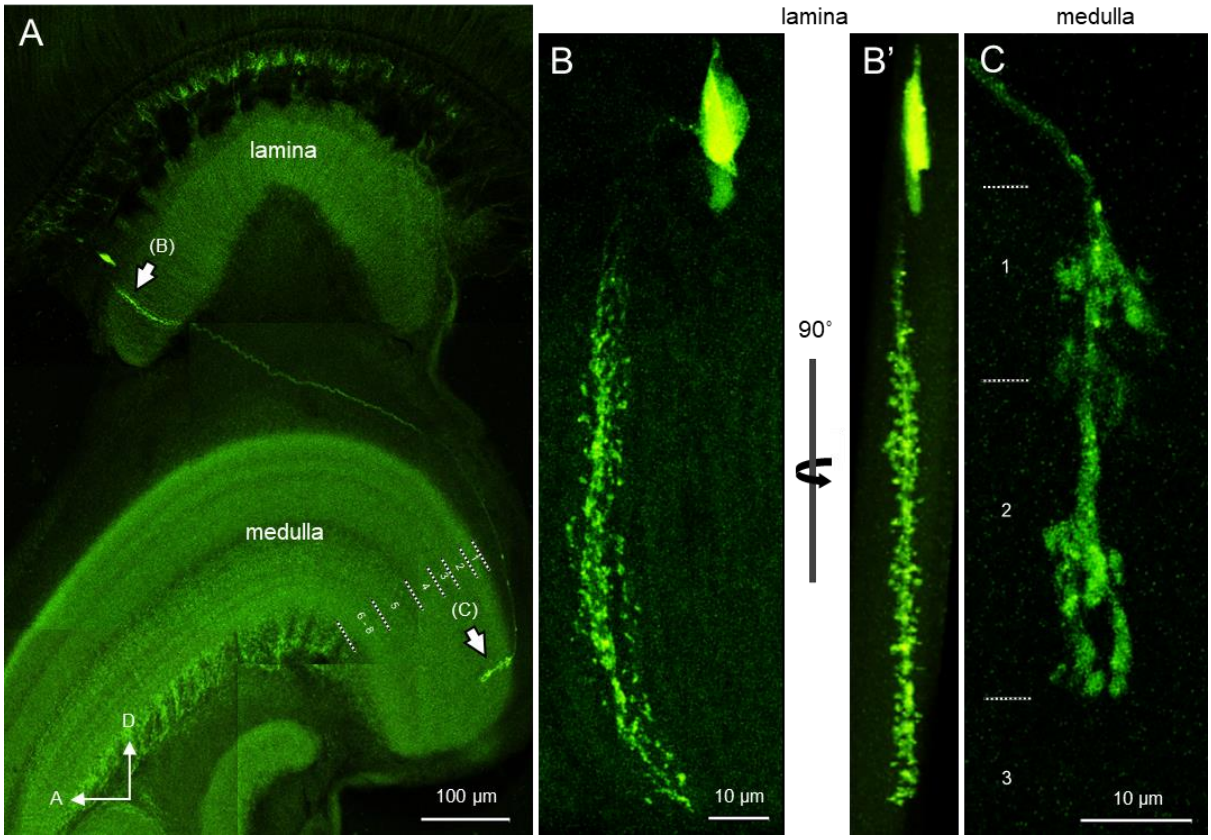


**Figure 4-12. Morphology of a neurobiotin-injected type I LMC with a terminal in the distal medulla.** (**A**) The stained cell projected it axon from the anterior lamina to the posterior medulla (*arrows*). The cell body was located outside of the proximal lamina and the axon terminated in the medulla layer 2. *A*, anterior; *D*, distal. (**B**) Confocal images in the lamina show that the stained LMC bore many dendritic processes within a cartridge. **B'** represents a 90˚ rotated view of **B**. (**C**) Confocal image in the medulla shows the stained LMC bearing several bushy-like structures in medulla layers 1 and 2. The numbers in **A** and **C** indicate medulla layers.

Figure 4-13 shows a stained LMC with the spectral sensitivities illustrated in Figure 4-11F. This LMC had low sensitivity in the red part of the spectrum, and thus this is most likely a type III LMC in the cartridge of the type III ommatidia. Though the cell body could not be visualized, a single axon, stained by Alexa Fluor 568 fluorescing dye, was detected in the lamina and the medulla (Figure 4-13A). The cell was first observed under a fluorescence microscope; however, the staining was not strong enough for the subsequent confocal microscopy. After crossing through the first optical chiasma, the stained LMC terminated in the medulla layer 2 (Figure 4-13C). Furthermore, no off-spike was observed in this cell (Figure 4-11E). The cell may belong to L1/L2 morphological group. The magnification of fluorescence microscope was not high enough to illustrate the pattern of dendritic processes in the lamina in detail for the further classification (Figure 4-13B). At any rate, I propose that this LMC is a type III-L1/L2, based on its terminal position in the medulla and a lack of off-spikes to light stimulation. Additionally, the cell had swollen structures in the medulla layer 1 and the proximal layer 2 (Figure 4-13C), indicating these positions were probably bearing side branches, though it is difficult to conclude by the low resolution. In fact, comparing the first stained LMC (Figure 4-12) and the second stained LMC (Figure 4-13), they show a high similarity in the morphological pattern of the axon in the medulla and the terminal position (Figures4-12C,4-13C). They probably belong to the same morphological type of L1.

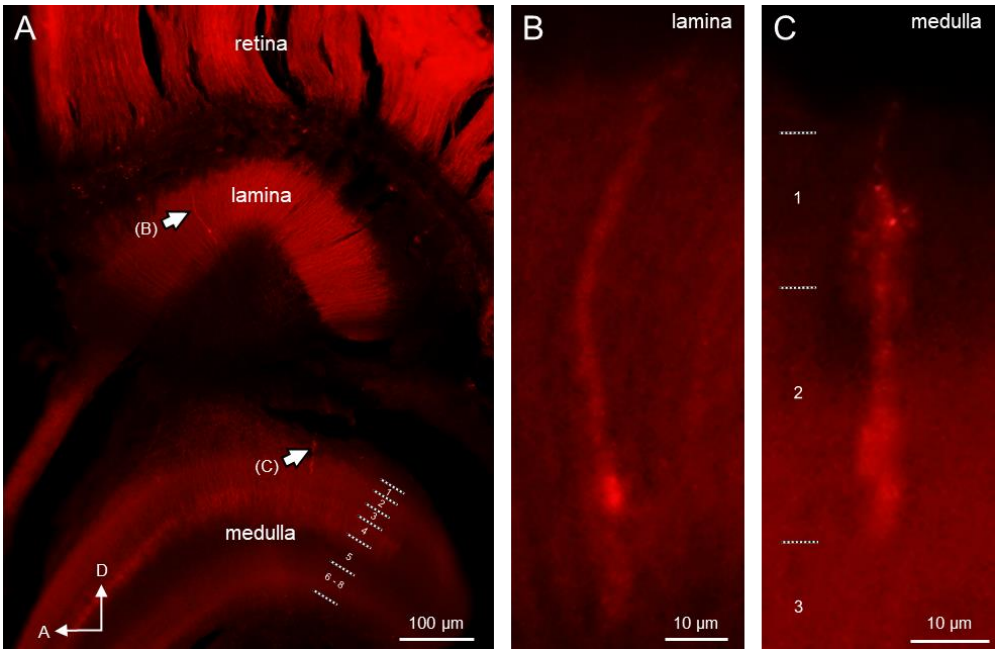


**Figure 4-13. Morphology of an Alexa Fluor 568-injected type III LMC with a terminal in the distal medulla.** (**A**) The stained cell projected it axon from the anterior lamina to the posterior medulla (*arrows*). The axon terminated in the medulla layer 2. *A*, anterior; *D*, distal. (**B**) Morphology of the stained LMC in the lamina. (**C**) Micrograph shows the stained LMC bore several bushy-like structures in the medulla. The numbers in **A** and **C** indicate medulla layers.

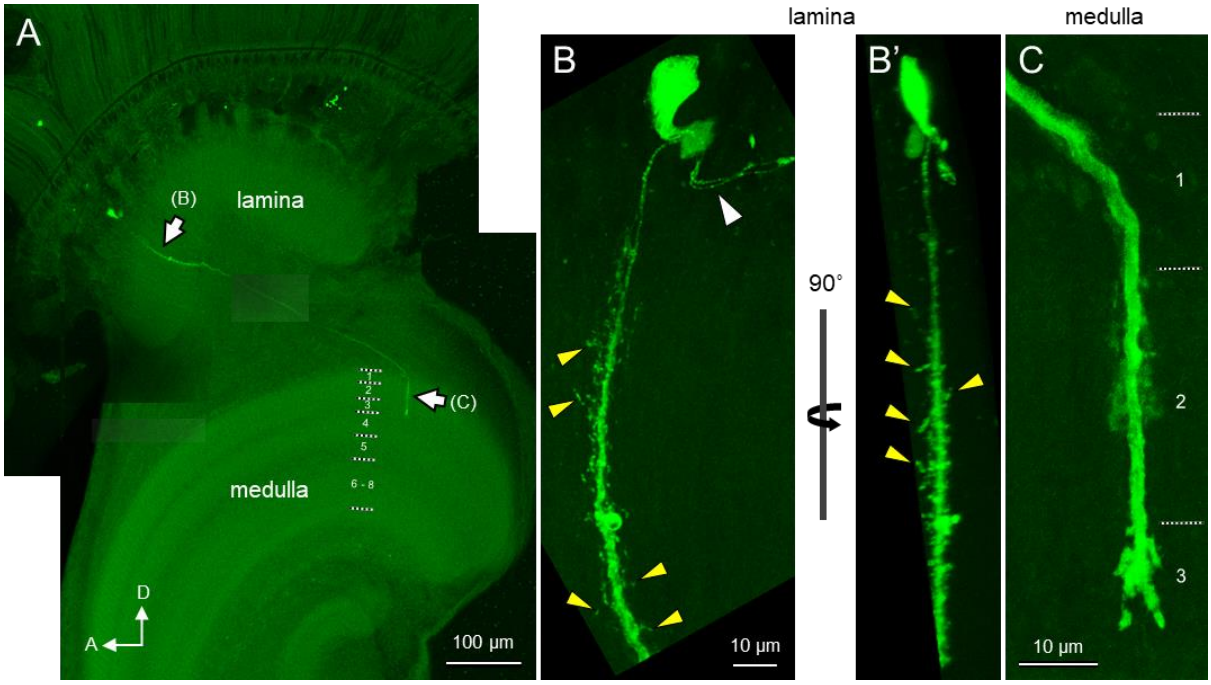


**Figure 4-14. Morphology of a neurobiotin-injected type III LMC with a terminal in the distal medulla.** (**A**) The stained cell projected it axon from the anterior lamina to the posterior medulla (*arrows*). The cell body was located outside of the proximal lamina and the axon terminated in the medulla layer 3. *A*, anterior; *D*, distal. (**B**) Confocal images in the lamina show that the stained LMC bore some short and long dendritic processes. *Yellow arrowheads* indicate long lateral processes. *A white arrowhead* indicates the thin neurite that formed a horizontal ring outside of the distal lamina. **B'** represents a 90˚ rotated view of **B**. (**C**) Confocal image in the medulla shows the stained LMC bore bushy branches in medulla layers 2 and 3. The numbers in **A** and **C** indicate medulla layers.

Figure 4-14 shows another type III LMC that injected by neurobiotin and visualized by Alexa Fluor 488. The results of electrophysiological recording in the recorded cell are presented in the Supplementary Figure 4-S1. This LMC had no red sensitivity and thus it may be a type III LMC in the cartridge of a type III ommatidium. The cell body of the stained LMC was found in the region outside of the distal lamina (Figure 4-14A). A thin neurite extended from the cell body and formed a horizontal oval ring (Figure 4-14B; *white arrowhead*) between the basement membrane and the distal border of the lamina before penetrating the lamina. The diameter of the axon increased as it passed its way through the lamina. The axon in the lamina possessed not only short side branches that stay within the cartridge but also long ones (Figure 4-14B; *yellow arrowheads*). The long dendritic processes can be seen more clearly in the 90˚ rotated confocal image (Figure 4-14B'). These wide horizontal processes have the potential to contact neighboring cartridges which corresponds to a wide acceptance angle (~5°) of the cell (Supplementary Figure 4-S1C). The axon left the anterior lamina through the first optic chiasma to its ending in the posterior medulla (Figure 4-14A). The cell ended as a dense arborization in the layer 3 and two thick branches were observed at the end (Figure 4-14C). The bushy-like structures which probably are side branches existed in the distal layer 2 of the medulla.

No off-spike was observed in the stained LMC during the recording (Supplementary Figure 4-S1), the cell most likely belongs to the L1/L2 group according to the spiking properties of LMCs by Rusanen et al. (2018). Comparing to the previous examples of the stained L1 (Figures 4-12,4-13), this LMC (Figure 4-14) terminated in the deeper layers of the medulla. The bushy arborizations were observed immediately after the axons entered the medulla, i.e. the medulla layer 1, in the stained L1 (Figures 4-12C,4-13C). In contrast, this LMC had bushy arborizations began from the layer 2 and no side branches were observed in the medulla layer 1 (Figure 4-14C). Therefore, the stained cell may belong to different morphological types from the L1 and is most likely a L2. In fact, similar to the description of *Papilio aegeus* L2 (Ribi, 1987) and the *Papilio xuthus* L2 that examined by SBF-SEM (Matsushita et al., in preparation), this stained LMC possessed some long thin side branches that could extend to neighboring cartridges in the lamina. I therefore assumed that the stained LMC that terminated in the medulla 3 with long lateral processes in the lamina is a type III-L2.

Combining electrophysiology along with dye injection, LMC spectral types and morphological types can be correlated. Three example of non-opponent LMCs were shown here including a type I LMC and two type III LMCs. One of type I LMC (Figure 4-12) and one of type III LMC (Figure 4-13) terminated in the medulla layer 2 and thus they were identified as L1. Another type III LMC (Figure 4-14) terminated in the medulla layer 3 and thus it was identified as L2. All these cells terminated in the shallower medulla and did not show off-spikes which were corresponded with previous observation of the *Papilio xuthus* LMCs by (Rusanen et al., 2018). Although the branching patters of these stained cells were consistent with the description of LMCs in *Papilio aegeus* by Ribi (1987), the terminal positions were not. According to the previous description of LMCs in *Papilio aegeus* by Ribi (1987), L1, L2 and L3 terminate in medulla layers 1, 2 and 3, respectively. It indicates that the LMCs of *Papilio aegeus and Papilio xuthus* terminate in different layers of the medulla. Alternatively, the medulla layers 1, 2 and 3 described by Ribi (1987) in *Papilio aegeus* in fact correspond to the layers 2, 3 and 4 in *Papilio xuthus*, respectively. More stained cells are necessary to approach the conclusion.

***Polarization properties***

I found that about 44.4% slow LMC-like units had polarization sensitivities at 90˚ and 43.5% typical LMCs (27 among 62 cells in total) had polarization sensitivities at either 0˚, 45˚ /135˚ or 90˚. Here I show some recordings in both slow LMC-like units (Figure 4-15) and typical LMCs (Figures 4-16,4-17,4-18,4-19) and their dependence of polarization properties on wavelength and light intensity.

All slow LMC-like units (*N*=8), excluding those which had little or no polarization sensitivities, contained the same polarization sensitivity peaking at 90˚ (Figure 4-15C). Their polarization responses were generally small but significant and were independent of wavelength (Figure 4-15D; except at 360 nm).

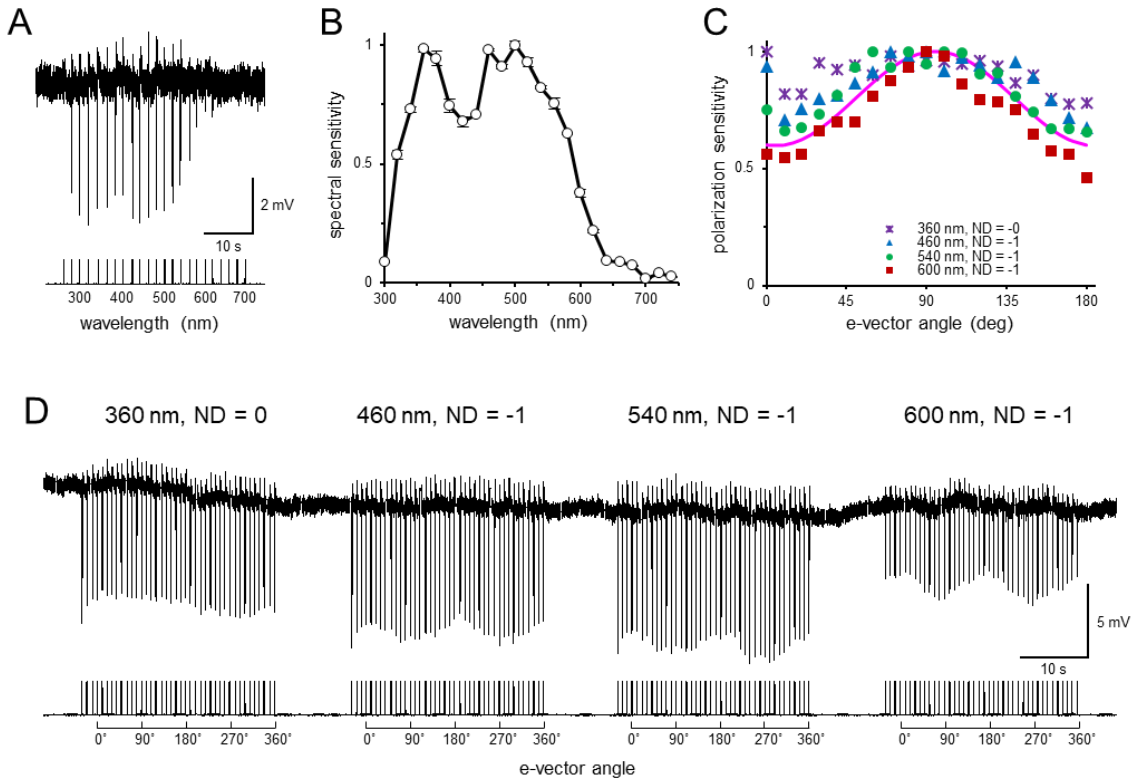


**Figure 4-15. A slow LMC-like unit with moderate polarization sensitivity and maximum at 90˚.** (**A**) Membrane potential trace of the cell upon 30 ms isoquantal spectral pulses from 300 to 740 nm. (**B**) Averaged spectral sensitivity of the recorded cell (mean ± standard errors). (**C**) Polarization sensitivities of the recording in **D**. *Magenta line* is the best-fit sinusoidal curve with the peak angle at 90° and PS~1.8. (**D**) Membrane potential trace of the cell upon 30 ms pulses through a rotating polarizer with different light intensities and different color stimulation by interference filters.

I also recorded many typical LMCs showing polarization sensitivities peaking at 90˚ in different spectral LMC types. For example, Figure 4-16 and Figure 4-17 are respectively a type III LMC and a type I LMC with the polarization sensitivity peaking at 90˚. I measured

their polarization sensitivities with different wavelengths and intensities. In both cells the polarization responses depended only upon intensities but not upon wavelengths.

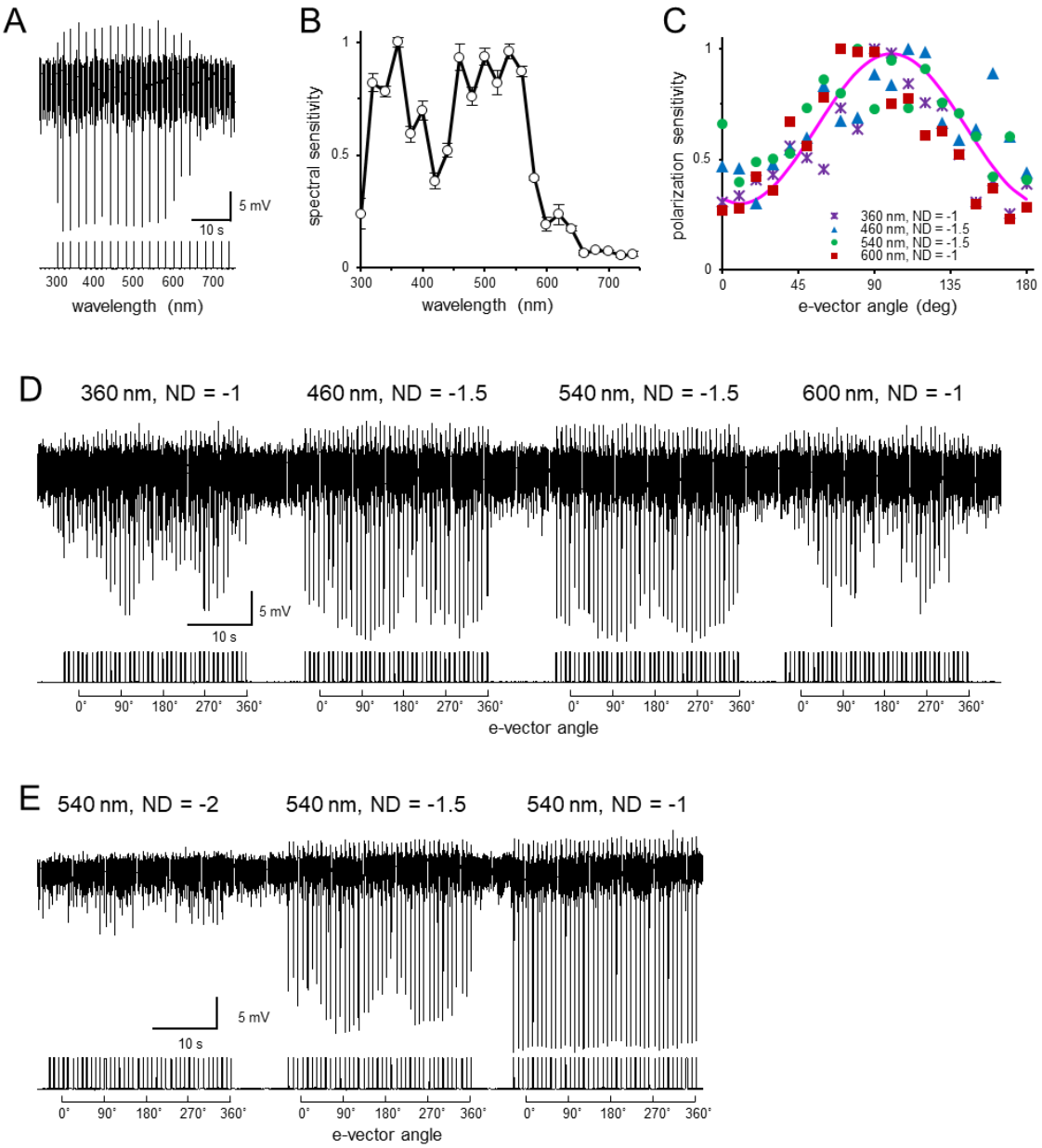


**Figure 4-16. A type III LMC with a high polarization sensitivity and maximum at 90˚.** (**A**) Membrane potential trace of the cell upon 30 ms isoquantal spectral pulses from 300 to 740 nm. (**B**) Averaged spectral sensitivity of the recorded cell (mean ± standard errors). (**C**) Polarization sensitivities of the recording in **D**. *Magenta line* is the best-fit sinusoidal curve with the peak angle at 90° and PS~2.7. (**D**–**E**) Membrane potential trace of the cell upon 30 ms pulses through a rotating polarizer with different light intensities and different color stimulation by interference filters.

The polarization responses shown in Figure 4-16D reveals the recorded type III LMC had a consistent polarization sensitivity over all wavelengths. Figure 4-16E further demonstrates that its polarization sensitivities were undetectable in dim light (ND = -2) and in bright light (ND= -1) because responses were too small and saturated, respectively.

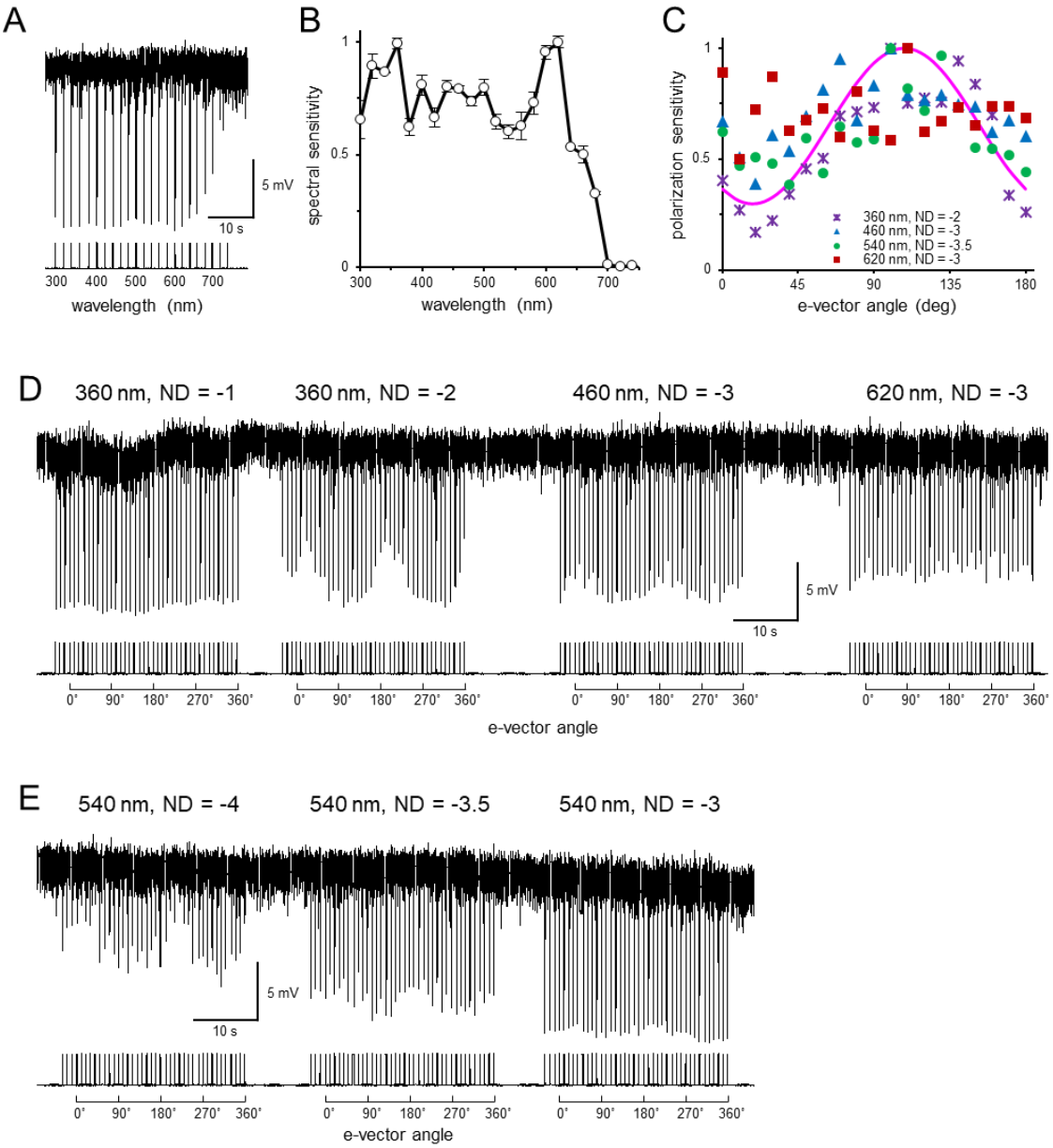


**Figure 4-17. A type I LMC with a high polarization sensitivity and maximum sensitivity at 90˚.** (**A**) Membrane potential trace of the cell upon 30 ms isoquantal spectral pulses from 300 to 740 nm. (**B**) Averaged spectral sensitivity of the recorded cell (mean ± standard errors). (**C**) Polarization sensitivities of the recording in **D** and **E**. *Magenta line* is the best-fit sinusoidal curve with the peak angle at 90° and PS~3. (**D**–**E**) Membrane potential trace of the cell upon 30 ms pulses through a rotating polarizer with different light intensities and different color stimulation by interference filters.

Similarly, Figure 4-17 illustrates the polarization sensitivities were consistent peaking at 90˚ to stimulus at different wavelengths in a type I LMC. Its polarization sensitivities were barely detectable in bright illumination (e.g., 360 nm, ND = -1, Figure 4-17D; 540 nm, ND = -3, Figure 4-17E).

In addition to the polarization sensitivity peaking at 90˚, I also recorded cells with the polarization sensitivity with maximum at 0˚ (e.g., Figure 4-18) and at 45˚/135˚ (e.g., Figure 4-19). Table 4-3 summarizes the recording numbers of each LMC polarization sensitivity class among the different spectral types of LMCs.

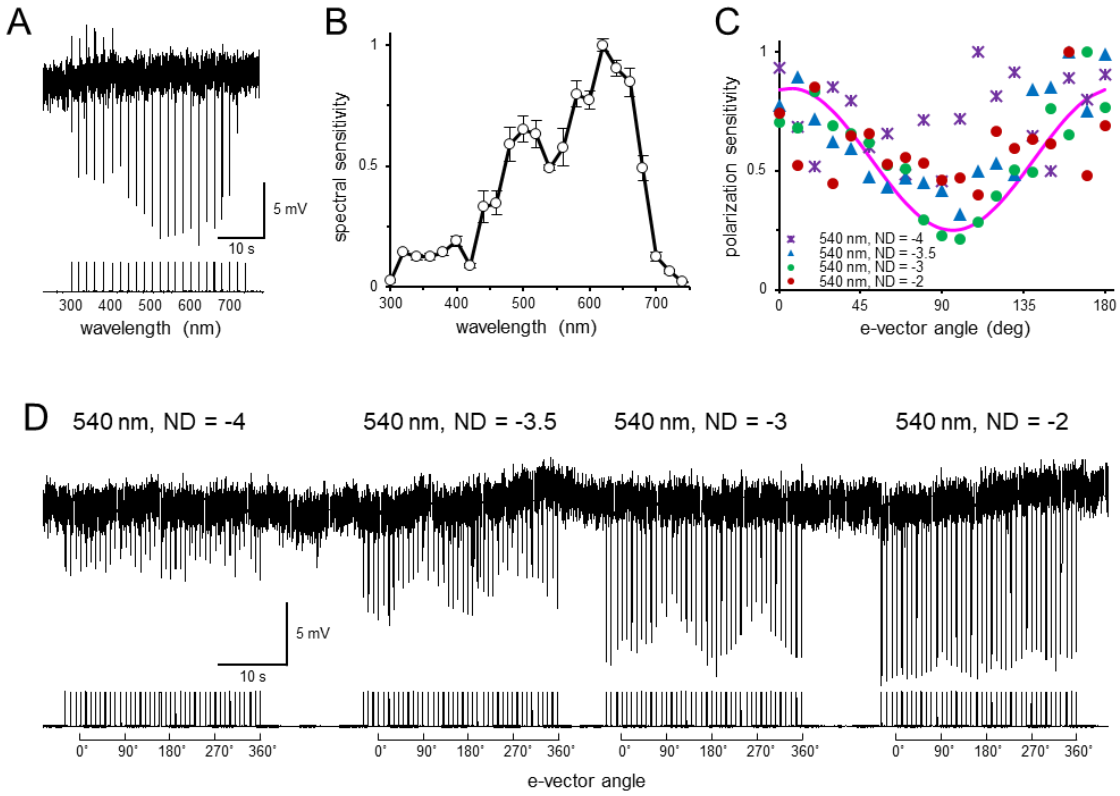


**Figure 4-18. A type I LMC with a high polarization sensitivity and maximum sensitivity at 0˚.** (**A**) Membrane potential trace of the cell upon 30 ms isoquantal spectral pulses from 300 to 740 nm. (**B**) Averaged spectral sensitivity of the recorded cell (mean ± standard errors). (**C**) Polarization sensitivities of the recording in **D**. *Magenta line* is the best-fit sinusoidal curve with the peak angle at 0° and PS~4. (**D**) Membrane potential trace of the cell upon 30 ms pulses at 540 nm through a rotating polarizer with different light intensities.

**Table 4-3. Summary of LMC spectral types and polarization sensitivities (PS)**

| | LMC | | | | slow LMC-like |
|---|---|---|---|---|---|
| PS | total | type I | type II | type III | unit |
| 0˚ | *N*=4 (6.4%) | *N*=2 | *N*=1 | *N*=1 | *N*=0 |
| 45˚/135˚ | *N*=7 (11.3%) | *N*=1 | *N*=1 | *N*=5 | *N*=0 |
| 90˚ | *N*=16 (25.8%) | *N*=4 | *N*=1 | *N*=11 | *N*=8 (44.4%) |
| none | *N*=35 (56.5%) | *N*=14 | *N*=3 | *N*=18 | *N*=10 (55.6%) |

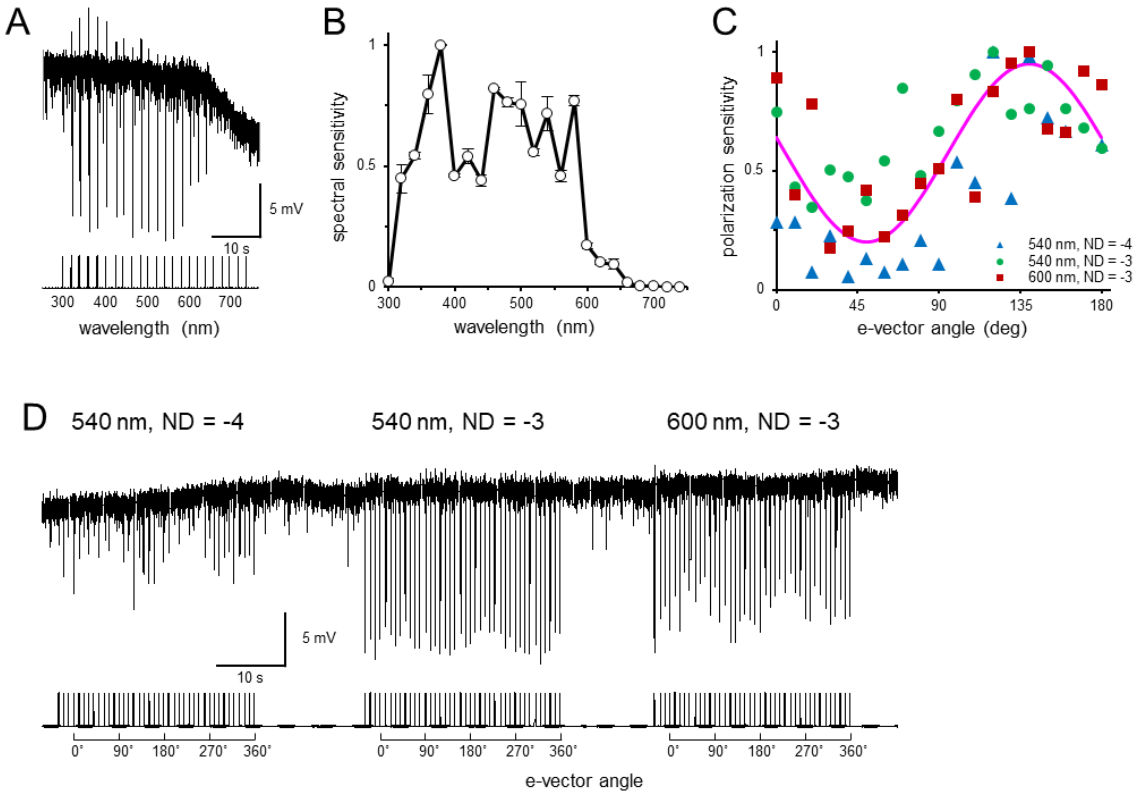


**Figure 4-19. A type III LMC with a high polarization sensitivity and maximum sensitivity at 135°.** (**A**) Membrane potential trace of the cell upon 30 ms isoquantal spectral pulses from 300 to 740 nm. (**B**) Averaged spectral sensitivity of the recorded cell (mean ± standard errors). (**C**) Polarization sensitivities of the recording in **D**. *Magenta line* is the best-fit sinusoidal curve with the peak angle at 135° and PS~4. (**D**) Membrane potential trace of the cell upon 30 ms pulses through a rotating polarizer with different light intensities and different color stimulation by interference filters.

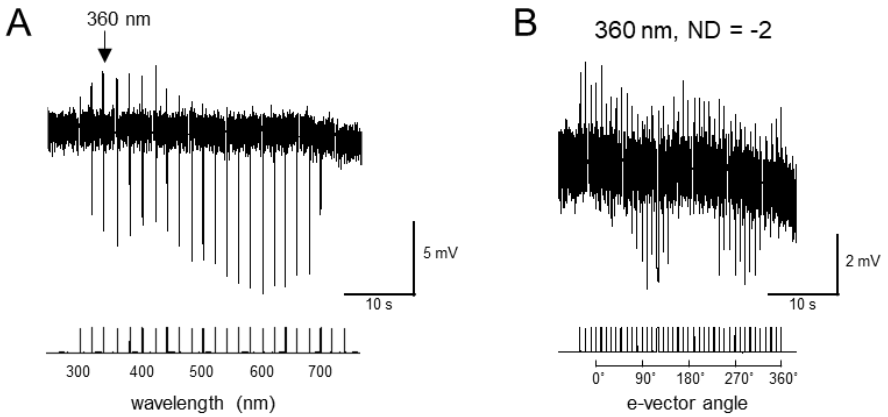


**Figure 4-20. A type I LMC showed polarization opponency.** (**A**–**B**) Membrane potential traces of the cell upon 30 ms isoquantal spectral pulses from 300 to 740 nm (**A**) and a sequence of polarization pulses at 360 nm through a rotating polarizer (**B**).

On the other hand, I have obtained a type I LMC showing polarization opponency (Figure 4-20). The cell had clear depolarizing off-transients only in the UV (Figure 4-20A). The opponent polarization responses were observed when I measured the polarization sensitivity at 360 nm in dim light (ND = -2) (Figure 4-20B). The response amplitudes of both hyperpolarizing on-transients and depolarizing off-transients changed with polarization angles. As a result, the cell had a maximal depolarizing peak at 0˚ and a maximal hyperpolarizing peak at 90˚, which would enhance contrast in polarization signals.

***Current injection***

The hyperpolarizing on-transient of LMCs is probably mainly due to an increase in the membrane chloride conductance through histamine-gated chloride channel (Hardie et al., 1989). Therefore, the chloride current amplitude and direction can be altered by the injection of current with affects the membrane potential and hence the electromotive driving force. To test whether the LMC responses are due to current through histaminergic channels, I performed current clamp analyses. Furthermore, as this thesis aims to identify the spectral properties of the *Papilio* LMCs under different conditions, I recorded their spectral responses along with positive (depolarizing) and negative (hyperpolarizing) current injections. I have successfully clamped different spectral types of LMCs, whose responses that could be changed with current injections (Figure 4-21).

Figure 4-21A shows the typical responses of LMCs upon current injections. This type I LMC lacked off-spikes before any current injection (Figure 4-21A, -43 mV trace). When I injected negative currents to the cell and brought the membrane hyperpolarized about 10 mV below its original resting potential (from -43 mV to -53 mV by injecting -0.4 nA current), the components of hyperpolarizing on-transients and sustained plateau were virtually disappeared but depolarizing instead (Figure 4-21A, -53 mV trace). This indicated that at -53mV, the cell was close to equilibrium potential of the ion, causing the hyperpolarization. This value rough matches the $Cl^-$ equilibrium potential (Asmild and Willumsen, 2000; Uusitalo and Weckström, 2000). The on-transients and sustained plateau were reversed and amplified when the membrane was further hyperpolarized (Figure 4-21A, -72 mV trace).

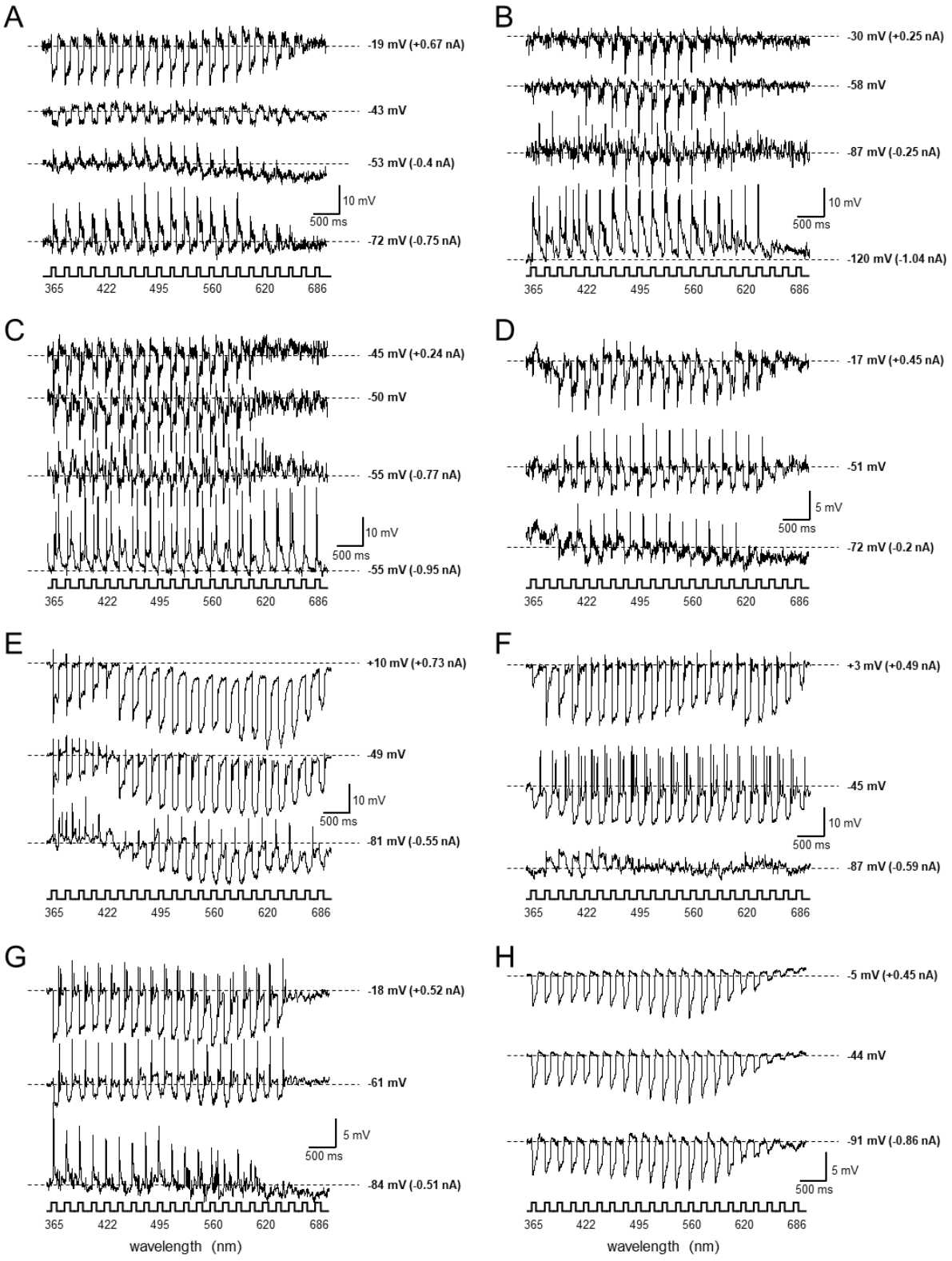


**Figure 4-21. Responses of LMCs and a slow LMC-like unit to spectral sweeps and current injection.** The cells were stimulated with 100 ms isoquantal spectral pulses along with positive (top trace), none (middle trace), and negative (bottom trace) injection. The numbers at the right side of each panel indicate the resting potential and the numbers in bracket are the injected current. (**A**) A non-spiking type I LMC. (**B**) A non-spiking type II LMC. (**C**) A non-spiking type III LMC. (**D**) A spiking SW-opponent LMC. (**E**) A spiking type I LMC. (**F**) A spiking type I LMC. (**G**) A spiking type III LMC. (**H**) A slow LMC-like unit.

On the other hand, the amplitudes of hyperpolarizing on-transient and sustained plateau increased proportionally in all wavelength ranges when I injected positive currents to the cell and brought the membrane depolarized about 25 mV above its resting potential (Figure 4-21A, -19 mV trace). Membrane depolarization to values above the equilibrium potential (~-53 mV) increased the electromotive driving force of the ion flowing through the LMC channels. Current clamp experiments strongly suggest that LMC signaling is mediated by histaminergic $Cl^-$ channels.

Similar response patterns were also observed in a type II LMC (Figure 4-21B). This LMC also lacked off-spikes at its original resting potential (Figure 4-21B, -58 mV trace). The response amplitudes of hyperpolarizing components decreased with the decreasing membrane potential by injecting negative current (Figure 4-21B, -87 mV trace). At this potential, the cell displayed depolarizing off-spikes in the wavelengths from UV to green. These off-spikes appeared mainly in the UV wavelength at much more negative membrane potential (Figure 4-21B, -120 mV trace), while on-transients reversed from hyperpolarizing to depolarizing and appeared in the wavelengths from UV to red along with large depolarizing plateau. Noteworthily, the cell was insensitive to UV and red, but depolarizing spikes were induced in these wavelengths. On the other hand, the injection of positive currents did not lead to a significant change in responses (Figure 4-21B, -30 mV trace). This suggests that the current injection altered the potential only within a certain postsynaptic region of the LMC and affected only a limited range of the ionic currents in the immediate vicinity of the electrode tip, overall indicating space clamp limitations.

Figure 4-21C illustrates a type III LMC having similar response patterns with current injection as the cell shown in Figure 4-21B. The cell's responses also did not change with the positive current injection (Figure 4-21C, -45 mV trace), while the negative current injection changed the cell properties from non-spiking (Figure 4-21C, -50 mV trace) to a spiking LMC (Figure 4-21C, -55 mV traces). When I injected more negative currents from -0.77 nA to -0.95 nA, the membrane potential did not decrease proportionally with the injected amount of negative currents; however, the waveform of responses changed dramatically. The polarity of on-transients reversed from hyperpolarizing to depolarizing and the cell displayed much evident depolarizing off-spikes along with large depolarizing plateau under a higher amount negative current injection (Figure 4-21C, the lowest trace). The depolarizing plateau and on-transients appeared at the wavelengths from UV to red, while the off-spikes were limited at the wavelengths from UV to green and did not appear at the red wavelength to which the cell was

insensitive. This indicates that the histaminergic channels which cause the non-spiking LMC response were remote from the electrode tip and thus poorly clamped, while the channels that cause the spiking were located next to the electrode tip and responded to the clamp with altered spike frequency and amplitude.

Figure 4-21D illustrates an example of a SW-opponent LMC which displayed large off-spikes (Figure 4-21D, -51 mV trace). When I injected negative currents, the response amplitudes of hyperpolarizing on-transients and sustained plateau decreased (Figure 4-21D, -72 mV trace) as other LMCs shown previously, while the change in the amplitudes of depolarizing off-spikes was undetectable. These off-spikes had reduced amplitude during positive current injections (Figure 4-21D, -17 mV trace). Instead, the amplitudes of hyperpolarizing on-transients and hyperpolarizing plateau increased when I further depolarized the membrane potential.

Figure 4-21E reveals a type I LMC, which displayed small off-spikes before the current injection (Figure 4-21E, -49 mV trace). The off-spikes became larger when the membrane potential was more hyperpolarized by injecting negative currents (Figure 4-21E, -81 mV trace). Negative current injection decreased the hyperpolarizing responses to green and red flashes while responses to UV and blue flashes were annihilated or even reversed. The positive current injections resulted in slightly increased hyperpolarizing responses especially in the UV and red wavelengths (Figure 4-21E, +10 mV trace) whereas the off-spikes were suppressed. This means that the electrode tip was located near the LMC site postsynaptic to UV and blue photoreceptors and near the spike initiating zone, but remotely from the sites postsynaptic to LW receptors.

Figure 4-21F shows another type I LMC, which displayed prominent multiple off-spikes before the current injection (Figure 4-21F, -48 mV trace). These off-spikes disappeared when I injected whether positive (Figure 4-21F, +3 mV trace) or negative currents (Figure 4-21F, -87 mV trace). The amplitudes of hyperpolarizing on-transients and sustained plateau were either increased or decreased when I brought the membrane potentials to more positive values (Figure 4-21F, +3 mV trace) or negative values (Figure 4-21F, -87 mV trace), respectively. Similar as the cell shown in Figure 4-21E (-81 mV trace), but stronger, the hyperpolarizing components nearly disappeared in the green and red and their polarity was reversed from hyperpolarizing to depolarizing in the UV and blue wavelengths (Figure 4-21F, -87 mV trace). Again, the electrode was probably located postsynaptically to UV and blue photoreceptors.

Figure 4-21G illustrates an opposite case in a type III LMC, which displayed large depolarizing off-spikes (Figure 4-21G, -61 mV trace). In the cases of spiking LMCs shown in Figure 4-21D (-17 mV trace), Figure 4-21E (+10 mV trace) and Figure 4-21F (+3 mV trace), the positive current injections led to the suppression of the off-spikes. However, this LMC displayed multiple off-spikes when I injected positive currents (Figure 4-21G, -18 mV trace). Moreover, the negative current injection substituted the depolarizing off-spikes with large depolarizing on-transients (Figure 4-21G, -84 mV trace). This indicates that the hyperpolarizing currents and LMC response polarity were reversed, thereby triggering the spikes at the rising edges at the onset of light flashes. Similar to other LMCs, the response amplitudes of hyperpolarizing plateau significantly increased and decreased to positive and negative current injections, respectively.

I also tried to clamp slow LMC-like units. The example shown in Figure 4-21H shows that here the current injections failed to evoke any significant differences in responses to light flashes. The failure in clamping the hyperpolarization implies that the synaptic sites of slow LMC-like units were far away and electrically decoupled from the recording site.

## 4.5 Discussion

The aim of this thesis is to understand the histaminergic signaling underlying the neural circuits of color processing at the initial visual stage. In this study, I carried out intracellular electrophysiology in the secondary visual neurons, LMCs. The major findings are the classification of three spectral types of non-opponent LMCs and the discovery of spectrally opponent LMCs.

***Slow LMC-like units***

The second-order LMCs process the visual information to the medulla with sign-inverting voltage responses (Hardie, 1989). Accumulated studies have implicated that the histamine-gated chloride channel (HCLA) is required for synaptic transmission at the photoreceptor-LMC synapse (Skingsley et al., 1995; Rister et al., 2007; Pantazis et al., 2008). Through the opening of the histaminergic channels, LMCs respond to light with a graded, intensity-dependent hyperpolarizing on-transient, a sustained plateau and a depolarizing off-transient (Hardie et al., 1989). In the *Papilio* lamina, I have observed two distinct units producing responses bearing all three above mentioned components upon light stimulation. A major part of the impaled cells displayed a fast hyperpolarizing on-transient (Figure 4-1D) and were most likely the LMCs. In these units, the responses operated within a narrow dynamic range and could be saturated at relatively low light levels (Figure 4-1H), similar to LMCs reported previously in *Papilio xuthus* (Rusanen et al., 2018) and other insects (Järvilehto and Zettler, 1973; Laughlin, 1973; Van Hateren, 1987; de Souza et al., 1992). Furthermore, negative current injection could clamp the fast on-transient hyperpolarization (Figure 4-21A – G), which is attributed to the chloride conductance through histamine-gated chloride channel (Hardie et al., 1989). A minor part of the injected cells had longer latency and thus I termed them as slow LMC-like units (Figure 4-1E). In these units, clamping of the membrane responses was nearly impossible (Figure 4-21H). They have also showed many characteristics dissimilar to the formerly described LMCs and thus I doubt that this type of unit is the LMC. The failure in clamping the slow LMC-like units could be because the recording sites were far from the synaptic sites, in the cell soma which is connected to the active zones with a very thin neurite (Figures 4-12B,4-14B). Alternatively, these units could have actually been the extracellular responses, recorded within lamina cartridges.

The slow LMC-like unit share several common features with those of the extracellular potential. While in LMC cells the latency of hyperpolarization decreased with increase light

intensities, the latency of slow LMC-like unit was rather constant at different illumination intensities (Figure 4-1G). Both the slow LMC-like unit and the extracellular unit had shallow *V*-log *I* functions (Figure 4-1H) and did not reach response saturation even at the brightest light stimulation (ND = 0). Similarly, as the extracellular potential, the response amplitudes of the slow LMC-like unit increased with the change from a point stimulus to an extended source (Figure 4-9A).

The angular sensitivities between the slow LMC-like unit and the extracellular potential were rather different (Figure 4-1I). The slow LMC-like unit had a narrower acceptance angle than the extracellular potential. Although both had very wide receptive visual fields below the 35% sensitivity level, the receptive field of the slow LMC-like unit was much narrower than that of the extracellular potential. Furthermore, the waveform of the slow LMC-like units which had a depolarizing off-transient (Figure 4-1E) is distinct to that of the extracellular potential, which repolarized to the resting potential slowly after the offset of light (Figure 4-1F). These differences suggest the slow LMC-like units could be recorded from interneurons with long lateral processes or a cell body of the LMC. I usually encountered slow LMC-like units after the electrodes passed the fenestrated layer. They seemed to be more abundant near the border of the fenestrate layer and the distal lamina. Such place is close to the location of cell bodies of LMCs (Takemura et al., 2005; Hamanaka et al., 2012). The less noisy membrane potential of the slow LMC-like unit is probably due to the integration of numerous signals from its own lateral processes. My immunolocalization revealed that the PxHCLA histamine-gated chloride channels, which are responsible for signaling at photoreceptor-LMC synapses, are mainly expressed on the lateral processes of LMCs, rather than on their main trunks (Chen et al., 2019). If the slow LMC-like unit is due to the recording site at the cell body of the LMC, the long distance far from the synaptic site would explain why the slow LMC-like unit had a longer latency and why its responses could not be voltage or current-clamped.

All slow LMC-like units had the same spectral sensitivities (Figure 4-5A) and polarization sensitivities (Figure 4-15C), while those of the typical LMCs were rather variable. The anatomical analysis (Matsushita et al., in preparation), along with the present electrophysiological results, indicate that a majority of LMCs receive inputs from photoreceptors mainly within the same cartridge. Thus, I expected that the slow LMC-like units could be differentiated to three spectral classes corresponding to the three ommatidial types. Their identical spectral sensitivities are unexpected and hard to interpret. More anatomical work with dye injection is necessary for the identification of the slow LMC-like units.

***Spiking LMCs***

Occasionally, LMCs produce depolarizing fast transients as spikes after light-induced hyperpolarization, which have been observed in several insects (Järvilehto and Zettler, 1971; Zettler and Järvilehto, 1971; Hardie and Weckström, 1990; Rusanen and Weckström, 2016; Rusanen et al., 2017) including *Papilio xuthus* (Rusanen et al., 2018). These off-spikes are assumed to be mediated by voltage-gated $Na^+$ channels (Uusitalo et al., 1995). Based on the spiking property, Rusanen et al. (2018) divided the *Papilio* LMCs into two types: spiking and non-spiking. To investigate whether spikes are involved in the visual signal processing, they performed detailed experiments to examine the spiking properties in spiking LMCs. They proposed that the signaling strategies of spiking LMCs change with illumination intensity. In this study, I successfully recorded both spiking and non-spiking LMCs in the *Papilio* lamina and I also observed the similar characteristics reported by Rusanen et al. (2018). Below, I focus on the new findings in the *Papilio* spiking LMC.

I proposed that spectral processing is absent or very limited in off-spiking units. The spiking LMCs are not spectral type-specific (Table 4-1). Furthermore, the off-spikes were not wavelength dependent as an example shown in Figure 4-4. The off-spikes would be useless for chromatic signal processing but probably they are important for signaling in achromatic vision.

In addition, I found that the fraction of spiking LMCs encountered during recording was related to the age of animals (Figure 4-3), indicating that the developmental stage could affect the off-spike generation. The off-spikes were virtually absent in very young individuals. This implies that the voltage-gated $Na^+$ channels in the spiking LMCs are incorporated and functional after a limited period of maturation. Additionally, the fraction of spiking LMCs was not proportional to the animal's age, indication that the off-spikes are LMC type-specific, occurring in a limited population of cells which were not impaled at every day of postnatal development. With this observation in mind, the animal age is necessary to be considered if spiking properties are used as indicators for the LMC classification in future studies. The postnatal development of spiking units should influence certain aspects of butterfly behavior as well, perhaps the performance of achromatic vision.

***Spectral types of LMCs***

The *Papilio* eyes bear three spectrally heterogeneous types of ommatidia each comprised of a different set of spectral receptors: types I, II, and III have four (UV, blue, green, red), three

(violet, green, broadband), and two (blue, green) receptor classes, respectively (Table 1-1) (Arikawa, 2003). I found that the non-opponent type of LMCs can be divided into three spectrally heterogeneous classes (Figure 4-6): high UV/high red sensitivities (type I), low UV/high red sensitivities (type II) and high UV/low red sensitivities (type III), which are respectively resemble the weighted sum of photoreceptor spectral sensitivities in three ommatidial types. Accordingly, the LMCs seem to integrate the spectral signals mainly from the photoreceptors in the same ommatidium. These results are well consistent with the anatomical analysis of synaptic connections showing that a majority of LMCs receive numerous inputs from different photoreceptors within the same cartridge (Matsushita et al., in preparation).

I also encountered a number of spectrally opponent LMCs (Figures 4-7,4-8), which had depolarizing plateau at some wavelengths, as reported in the honey bee (de Souza et al., 1992). Regarding the occurrence of depolarization in different parts of the spectrum, I divided these opponent LMCs into three main classes ($N$>3 in each class; Figure 4-7) and five other classes ($N$=1 in each class; Figure 4-8). The main classes include the short wavelength (SW)-opponent LMCs (Figure 4-7A), middle wavelength (MW)-opponent LMCs (Figure 4-7B) and long wavelength (LW)-opponent LMCs (Figure 4-7C) according to their depolarization below 380 nm, between 400 nm to 450 nm or above 630 nm, respectively. They are probably the subtype of the type II LMC with a considerably low UV sensitivity, type I LMC with a relatively low sensitivity at 420 nm and type III LMC with a considerably low red sensitivity, respectively. A question arises whether the spectrally opponent LMCs and non-opponent LMCs are in fact belonging to different LMC morphological types. For example, I have stained three non-opponent LMCs, which morphologically corresponded to the L1 (Figures 4-12,4-13) and L2 (Figure 4-14) morphological types (Ribi, 1987). The spectrally opponent LMCs are probably L3-type and/or L4-type LMCs. If so, the origin of spectral opponency in LMCs may be related to off-spikes. According to the previous description by Rusanen et al. (2018), the *Papilio xuthus* LMCs L3/L4 displayed prominent off-spikes. Notably, based on the SBF-SEM analysis in the synaptic connection, the L4-type LMC is most likely a third-order neuron that received inputs from the other three LMCs in addition to photoreceptors (Matsushita et al., in preparation). If depolarizing responses in opponent LMCs were attributed to the inputs from LMCs, the spectral opponency could be unique for the L4-type LMC.

Firm determination of the LMC spectral type has proven to be quite difficult. The spectral sensitivities of LMCs strongly depended on illumination intensities (Figure 4-11). In other words, response amplitudes of LMCs at different wavelengths show different light

intensity dependences. This seems to be an unavoidable consequence of the integration numerous inputs from different spectral classes of photoreceptors. The effect could lead to a misclassification of LMC spectral classes. In my recordings, I recognized 57 non-opponent cells as type I LMCs and 55 non-opponent cells as type III LMCs (Table 4-1). Theoretically, the ratio of type I LMCs should be two times more than type III LMCs based on the ommatidial ratio in the *Papilio* eye (Arikawa, 2003). Therefore, I here have to note that some LMCs that I classified as type III LMCs can be type I LMCs in fact.

On the other hand, the ratio of type II LMCs is lower than what is expected from the ommatidial ratio in the *Papilio* eye (Arikawa, 2003). It could be due to the recording position. The suppression of the UV sensitivity in the *Papilio* type II ommatidia is attributed to UV-absorbing fluorescing pigments which are only present in the ventral eye region (Arikawa et al., 1999b). Therefore, the low UV sensitivity in type II LMCs could only be found in the ventral eye region while type II LMCs in the dorsal region might have higher UV sensitivity. Thus, the spectral sensitivities of type II LMCs in the dorsal region might resemble to those of type I LMCs. I penetrated LMCs in both dorsal and ventral eye regions. Hence, some type II LMCs recorded in the dorsal eye region could have been classified into wrong spectral classes.

One possible way to confirm the LMC spectral type is to check the morphology of photoreceptors R1 and R2 in the same cartridge of the recorded LMC. The *Papilio* ommatidial types can be distinguished by the combination of UV and blue receptors: type I with one UV and one blue, type II with two UV and type III with two blue (Table 1-1) (Arikawa, 2003). A thorough anatomy at the EM level reveals that the axons of UV and blue receptors have distinct patterns of lateral processes in the *Papilio* lamina (Matsushita et al., in preparation). To determine the LMC spectral type properly, further anatomical analysis in cartridges of stained LMCs at the EM level is necessary.

***LMCs involve in spectral processing***

The opponent interactions among photoreceptor signals provide the basis for color vision (Kelber, 2016). LMCs are one of the candidate cells which could perform the spectral opponency at the initial stage of visual processing. However, most LMCs reported so far are non-spectrally opponent with broad and uniform spectral sensitivities (Laughlin, 1976; Laughlin and Hardie, 1978; Moring, 1978). Other authors have found cases of LMCs which had narrow spectral sensitivity functions and thus were thought to be involved in the spectral

processing, but have not reported any opponent responses for these cells (Meinertzhagen et al., 1983; Horridge et al., 1984; Yang and Osorio, 1991). Spectral opponent LMCs have only been reported once in one cell of the worker honey bee (de Souza et al., 1992). The finding of several types of spectrally opponent LMCs in the present study provides a further cue that LMCs feed signals into spectral signaling circuitry in addition to motion detection circuitry.

The broad spectral sensitivities of all non-opponent LMCs, suggest that they could be mainly involved in motion detection. However, inputs from at least two different spectral types of units are sufficient to achieve spectral opponent processing in downstream interneurons. Therefore, there is no reason to exclude the possibility that the three spectral types of non-opponent LMCs contribute to spectral processing. For example, the difference between the spectral sensitivities in long wavelength ranges among three types are rather dramatic, especially above 620 nm (Figure 4-6). The type I LMC peaks at 600 nm, type II LMC peaks at 560 nm and type III LMC peaks at 500 nm. Spectral processing might be achieved by feeding their signals into opponent interneurons, which could in turn process wavelengths above ~500 nm. Of course, the same task could be even better performed by the spectrally opponent LMCs. Taken together, I propose that all LMCs feed signals into motion detection circuitry and in parallel into spectral opponent circuitry. The main three spectral types of opponent LMCs provide spectral opponent processing in short, middle and long wavelengths. Furthermore, the spectral processing in the long wavelength above 500 nm could be mediated and enhanced by comparing the incoming signals from the non-opponent LMCs as well.

***Current injection***

In the current injection experiments, I showed that the responses of the typical LMCs in the *Papilio* lamina could be changed with current injections. As results demonstrated in Figure 4-21, these LMCs showed high variability in terms of response amplitudes, polarity reversion and spiking properties from cell to cell. Here I summarize two common characteristics among them.

First, the components of the hyperpolarizing on-transient and sustained plateau were abolished when the membrane potential was close to the assumed equilibrium potential of chloride ions. In some cases, the polarity of the hyperpolarizing on-transient reversed from hyperpolarization to depolarization if more negative currents were injected. The decrease in response amplitude with negative current injection is attributed to the inhibition of chloride conductance. If the membrane potential below the equilibrium potential of chloride ions, the

ions move out the cell and result in polarity reversion. The reversal potential in *Papilio* LMCs which is similar to that in blowfly LMCs (Laughlin, 1981; Hardie et al., 1989). The results suggest that the chloride channels are the key players in the LMC signaling.

Second, the response amplitudes of the hyperpolarizing on-transient and sustained plateau were increased with positive currents increased. I found that a high amount of positive currents is necessary to observe this phenomenon. The increase in the hyperpolarizing response amplitudes is also due to the currents through histamine-gated chloride channels in the LMCs. Depolarization due to positive current injection has brought the membrane potential depolarized further away from the equilibrium potential of chloride ions and lead to stronger electrical driving force for the chloride anions.

The changes in response amplitudes and polarity of hyperpolarizing on-transient and sustained plateau with current injections were constant among cells, suggesting that these components are most likely derived from activation of chloride conductance. In contrast, the change in off-spikes with current injections seemed to be different from cell to cell. Previously, Rusanen et al. (2018) reported that off-spikes of spiking LMCs increased in amplitude with increased background hyperpolarization. I also observed some LMCs exhibiting similar characteristics as a case shown in Figure 4-21E (bottom trace). However, I found off-spikes in some spiking LMCs, such as the cases shown in Figure 4-21F (bottom trace) and Figure 4-21G (bottom trace), disappeared when I injected negative currents. The further variation between them was observed by injecting positive currents: the off-spikes became smaller in the former one (Figure 4-21F; top trace) but they were more prominent in the latter one (Figure 4-21G; top trace). In addition, some non-spiking LMCs displayed off-spikes when a high amount of negative currents was injected as the case shown in Figure 4-21B (off-spikes appeared in UV; bottom trace) and Figure 4-21C (off-spikes appeared in UV to green; bottom trace). The high variability of off-spikes with current injections make their origin in question. In addition to the putative voltage-gated $Na^+$ channels (Rusanen et al., 2018), it is possible that there have other mechanisms mediated LMCs off-spikes.

The current injection experiments showed significant space-clamp limitations. Current injections affected only a limited set of currents in the impaled cell, most likely those that were originating from postsynaptic channels or voltage-gated channels, close to the fine electrode tip. The phenomenon somehow reflects my immunohistochemical localization that the PxHCLA channels are mainly expressed on the LMC lateral processes (Chen et al., 2019).

This reveals the putative anatomical feature: synapses lamina cartridges could be layered depends on the spectral identity of the presynaptic cells. Furthermore, the high spatial order could be important for the spatiotemporal aspect of opponent processing. In fact, I have observed some LMCs showed "double opponency" which involves spatial antagonism of spectrally opponent mechanisms.

On the other hand, the change in membrane potentials by current injections could be analogous to the change of background illuminations. Under light adaptation, the steady background illumination leads the photoreceptors to continuously release histamine which in turn opens histamine-gated chloride channels in the second-order LMCs and result in the steady hyperpolarization. Injecting different amounts of negative currents might have mimicked light adaptation. I observed that the extended source stimulation brought a decrease in response amplitudes of the hyperpolarizing plateau in the typical LMCs (Figure 4-9B – D). Similarly, the response amplitudes of hyperpolarizing components decreased with increased background hyperpolarization by injecting negative currents. The results derived from the current injection experiments may provide cues for the situation of adaptation to bright light, which is important because *Papilio* is a diurnal animal. The reversed polarity of hyperpolarizing components by negative current injections is a common feature in the typical LMCs. In this line, I expect that the spectrally opponent LMCs may be more dominant under light adaptation. This conclusion of course awaits the further experiments by comparing the spectral sensitivities of LMCs under dark-adapted and light-adapted conditions.

***Polarization sensitivity***

The anatomical studies (Takemura and Arikawa, 2006; Matsushita et al., in preparation), along with the present electrophysiological results, suggest that *Papilio* LMCs receive inputs from numerous photoreceptors, which have their microvilli arranged radially (Bandai et al., 1992). As one would expect, my recordings revealed that more than half of typical LMCs (56.5%) and slow LMC-like units (55.6%) had virtually no polarization sensitivity due to the mutual offset after the convergence of numerous inputs from different photoreceptors. Others showed polarization sensitivities at either 0˚, 45˚ /135˚ or 90˚ among different spectral LMC types (Table 4-3).

The fraction of the typical LMCs that had a polarization sensitivity peak at 90˚ (25.8%) is much higher than those with peaks at 0˚ (6.4%) and 45˚/135˚ (11.3%). Moreover, all slow

LMC-like unit had polarization sensitivities, if any, peaking at 90˚ (Figure 4-15). The 90˚ polarization sensitivity is most likely attributed to the photoreceptors R3 and R4, which have their microvilli arranged horizontally (Bandai et al., 1992). It suggests that a majority of LMCs receive stronger inputs from the R3–R4 green receptors. I could not detect polarization sensitivities in more than half of LMCs. However, as the current results indicate, the light intensity level is very critical for the determination of polarization sensitivity. Therefore, there could be more LMCs exhibiting polarization sensitivity if they were measured at proper intensity. Furthermore, Table 4-3 indicates that the polarization sensitivity is independent of the LMC spectral type. Whether it is related to LMC morphological types still awaits further electrophysiology followed by dye injection.

## 4.6 Supplementary Materials

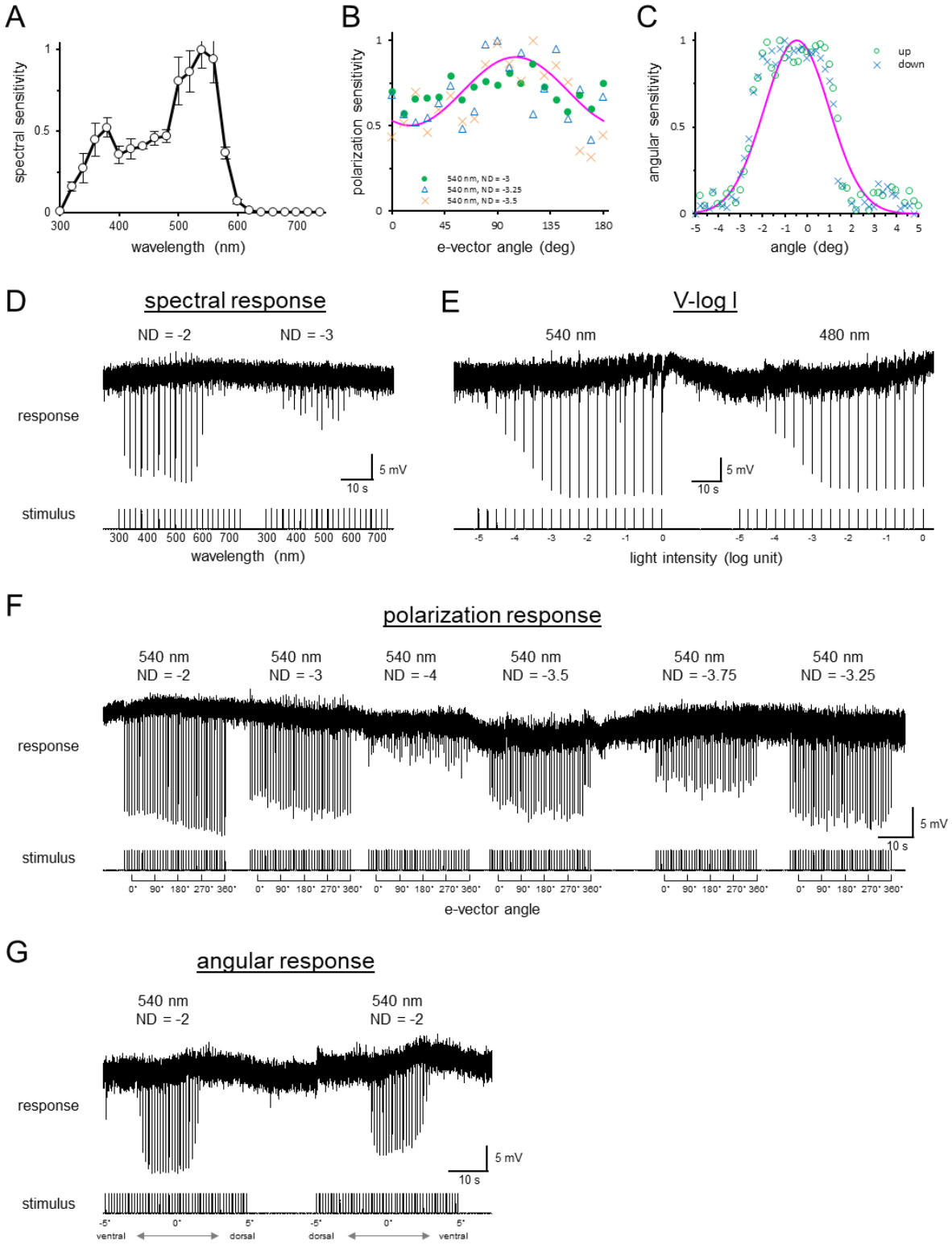

**Supplementary Figure 4-S1. Electrophysiological recording in a neurobiotin-stained type III-L2 LMC.** (**A**) Averaged spectral sensitivity of the recorded cell (mean ± standard errors). (**B**) Polarization sensitivities of the recording in **F**. *Magenta line* is the best-fit sinusoidal curve with the peak angle at 105° and PS~2. (**C**) Angular sensitivity of the recording in **G**. *Magenta line* is the best-fit of the Gaussian function. *Up*, ventral (-5°) to dorsal (+5°). *Down*, dorsal (+5°) to ventral (-5°) (**D**) Spectral responses. Membrane potential trace of the cell upon 30 ms isoquantal spectral pulses from 300 to 740 nm at two illumination levels. (**E**) Response-light intensity (V-log I) functions. Membrane potential trace of the cell upon 100 ms pulses at 540 nm and 480 nm graded in 0.25 log intensity steps. (**F**) Polarization responses. Membrane potential trace of the cell upon 30 ms pulses at 540 nm through a rotating polarizer with different light intensities. (**G**) Angular responses. Membrane potential trace of the cell upon 30 ms pulses at 540 nm with angular steps of 0.2° over 10°: ventral (-5°) to dorsal (+5°) and dorsal (+5°) to ventral (-5°).

# Chapter 5

## Electrophysiological characteristics of spectrally opponent photoreceptors in the *Papilio* lamina and medulla

## 5.1 Abstract

Spectrally opponent responses, i.e. wavelength-dependent response-polarity inversions, have been observed at the level of photoreceptors quite frequently in butterflies. The origin of the inhibition in these butterflies can be due to extracellular return currents, real synaptic transmission or by both. If the inhibition is synaptic, which spectral classes of photoreceptors are involved and how are their spectral sensitivities modified? To address these questions, I performed intracellular recording to record spectral responses of photoreceptor axons in the lamina and the medulla of *Papilio xuthus*. Previously, I found by immunohistochemistry that one of histamine-gated chloride channels, PxHCLB, is expressed at the inter-photoreceptor synapses in the *Papilio* lamina and medulla, where the short visual fibers (svfs) and the long visual fibers (lvfs) terminate, respectively. My intracellular recordings revealed that the *Papilio* lamina contains photoreceptors exhibiting spectral opponency of at least eight distinct spectrally opponent pathways. The recorded spectrally opponent responses can be well explained by the ommatidial type-specific inter-photoreceptor (sign-inverting) synaptic connections via PxHCLB. On the other hand, all recordings in lvfs in the medulla exhibited spectral opponency, corresponding to the three spectral classes of lvfs. By injecting currents, I have shown that the responses of spectrally opponent photoreceptor could be reversed when the membrane potential was close to the equilibrium potential of chloride. The results indicate that chloride channels are involved in the antagonistic interactions between photoreceptors at the initial stage of chromatic processing.

Keywords: antagonistic interaction, inter-photoreceptor synapse, histamine-gated chloride channel, spectral opponency, color vision, intracellular recording

## 5.2 Introduction

I have observed the photoreceptors of several butterflies (*Damora sagana, Graphium sarpedon, Papilio xuthus, Troides aeacus*) exhibiting spectral opponency. Opponent responses in photoreceptors had often been dismissed as artifacts caused by extracellular return current as in the case of flies (Weckström and Laughlin, 2010), rather than as a postsynaptic hyperpolarization of the photoreceptors in question.

With respect to the synaptic connections in the lamina of *Papilio xuthus*, it is important to note that the photoreceptors feed information to the second-order visual neurons, lamina monopolar cells (LMCs), but are also mutually connected by synapses in an ommatidial type-specific manner (Takemura and Arikawa, 2006). My immunohistochemical results showed that *Papilio* LMCs and photoreceptors express PxHCLA and PxHCLB (*Papilio xuthus* histamine-gated chloride channels A and B), respectively (Chen et al., 2019), which mediate the chloride current, potentially leading the post-synaptic elements to hyperpolarize. In fact, the opponent photoreceptors exhibit "fast on-set hyperpolarization" when stimulated with particular wavelengths (Matić, 1983; Chen et al., 2013) (Figure 1-11). Its time course resembles that of on-transient hyperpolarization recorded in the LMCs (Hardie, 1989). Accordingly, I have proposed the "histamine hypothesis", where histaminergic sign-inverting mechanism is involved in the direct synaptic interactions between photoreceptors (Chen et al., 2013). The expression of PxHCLB at the inter-photoreceptor synapses provides a set of anatomical evidence to support the hypothesis: in the case where photoreceptors are spectrally heterogeneous, the interaction could produce spectral opponency. Recently, a similar mechanism has been identified in the *Drosophila* medulla (Schnaitmann et al., 2018).

I have localized PxHCLB at the inter-photoreceptor synapses in the *Papilio* lamina and medulla (Chen et al., 2019), where short visual fibers (svfs) and long visual fibers (lvfs) terminate, respectively (Takemura et al., 2005). I thus carried out intracellular recording to record spectral responses of photoreceptor axons in both the lamina and the medulla. Interestingly, the recorded spectrally opponent responses can be well explained by the ommatidial type-specific inter-photoreceptor (sign-inverting) synaptic connections via PxHCLB. The present results indicate the antagonistic interactions between photoreceptors at the initial stage of chromatic processing.

## 5.3 Materials and Methods

### *Animals*

Adult Japanese yellow swallowtail butterflies, *Papilio xuthus* Linnaeus, of both sexes were obtained from a laboratory stock culture derived from eggs laid by females caught around the campus of Sokendai, Kanagawa, Japan. The hatched larvae were fed with fresh citrus leaves and raised under a short light regime (light: dark = 10 h: 14 h) at 25°C in the laboratory. After emergence, the butterflies were fed with sucrose solution and kept in the 10°C or 4°C incubator before being used for experiments.

### *Light stimulation*

The stimulus light was provided from a 500 W xenon arc lamp through a series of 23 narrow-band interference filters (IF) with 20 nm interval from 300 to 740 nm. The duration of each flash was fixed to 30 ms with 1 s interval. The light was guided through a quartz optical fiber providing a point light source of about 1.56° in diameter for the animal. The light intensity was controlled by a set of neutral density (ND) filters. The exit of the fiber was mounted on the perimeter device and accurately positioned at the optical axis of the ommatidium containing the cell being penetrated. The quantum flux of each monochromatic light was measured by a radiometer (model 470D; Sanso, Tokyo, Japan), and adjusted maximally to $5.0 \times 10^{11}$ photons・$cm^{-2}$・$sec^{-1}$ (~$2.5 \cdot 10^6$ photons・$facet^{-1}$・$sec^{-1}$, with a facet diameter of 25 μm) at the corneal surface using another optical wedge.

Newly developed LED array device was also used (Belušič et al., 2016). The device was equipped with 21 narrow-band light-emitting diodes (LEDs) with peak wavelengths of 365, 375, 390, 403, 422,435, 451, 471, 495, 514, 525, 540, 560, 577, 590, 595, 620, 630, 657, 673, and 686 nm. The quantum flux was controlled using 12-bit pulse width modulation at 1 kHz and a set of ND filters. The duration of each flash was fixed to 10 ms with 50 ms interval or 100 ms with 150 ms interval. The light was accurately directed into the optical axis of a single ommatidium by using the beam at minimal aperture (~2°).

### *Intracellular electrophysiology*

A butterfly whose wings and legs were amputated was mounted on a stage. In order to yield the longest electrode excursion for cell penetration in the lamina, the animal's head was rotated about 20° right from its dorso-ventral axis. A silver chloride wire was inserted into the stump

of an antenna serving as the reference electrode. The eye was positioned at the center of the Cardan arm perimeter device, which was set in a Faraday cage.

Microelectrodes were pulled from borosilicate glass capillaries (1 mm/0.5 mm outer/inner diameter) with a P-2000 laser micropipette puller (Sutter, Novato, CA, USA), and filled with 2M potassium acetate with resistance about 80–120 MΩ. For inserting a glass microelectrode, a small hole covering about 10–20 facets was made in the dorsal region of the eye. A glass microelectrode was advanced into the lamina or medulla through the retina, basement membrane, and fenestrated layer.

The signal was amplified with a SEC-05X or SEC-10LX amplifier (Npi electronic, Tamm, Germany), conditioned with a Cyber Amp 320 (Axon Instruments, Union City, CA, USA) and digitised with a Micro 1401 (CED, Cambridge, UK) analog-digital (A/D) converter. WinWCP (Strathclyde Electrophysiology Software, Version 4.0.5) and AcqKnowledge (BioPac Systems) packages were used for data acquisition and further analysis.

Spectral responses of photoreceptors were recorded by applying a series of equiquantal monochromatic flashes from short to long wavelength and in the reverse direction. The response-light intensity ($V$-log $I$) function was recorded over 4 log unit-intensity range at the given wavelength. Polarization responses were recorded at the given wavelength by rotating a UV-capable polarization filter OUV2500 (Knight Optical, UK) in front of the exit pupil of the optical fiber: 0˚ was defined as the vertical direction. For recording the angular responses, the Cardan arm was moved at 0.2° intervals through the center of a receptive field between dorsal (+5°) and ventral (-5°) position. I note that all recordings in this study could not be converted to sensitivity values due to their positive and negative polarity.

## 5.4 Results

### *Spectrally opponent photoreceptors in the lamina*

A sharp electrode was inserted from the cornea through the retina to the lamina. The location of recording in the lamina was revealed by frequent penetrations of LMCs. About one-fourth of photoreceptors in the lamina showed negative-going responses at specific wavelengths, whereas other three-fourth of photoreceptors showed purely depolarization in all wavelengths. Since it was difficult to exclude the possibility that the slower hyperpolarization could be an artifact caused by simultaneous recording of the extracellular potential originating from neighboring cells (as in an ERG), I only recorded from the cells showing the so-called "fast on-set hyperpolarization". Figure 5-1 shows an example of a B+/R- opponent receptor, with a positive response peaking at 460 nm and a negative response peaking at 600 nm. At the intermediate wavelength (540 nm), the response exhibits both depolarization and hyperpolarization. Importantly, its hyperpolarization preceded depolarization (Figure 5-1B). The latency (the time required for the membrane potential to reach to the peak) of the hyperpolarizing response is shorter than that of the depolarizing response (Figure 5-1C).

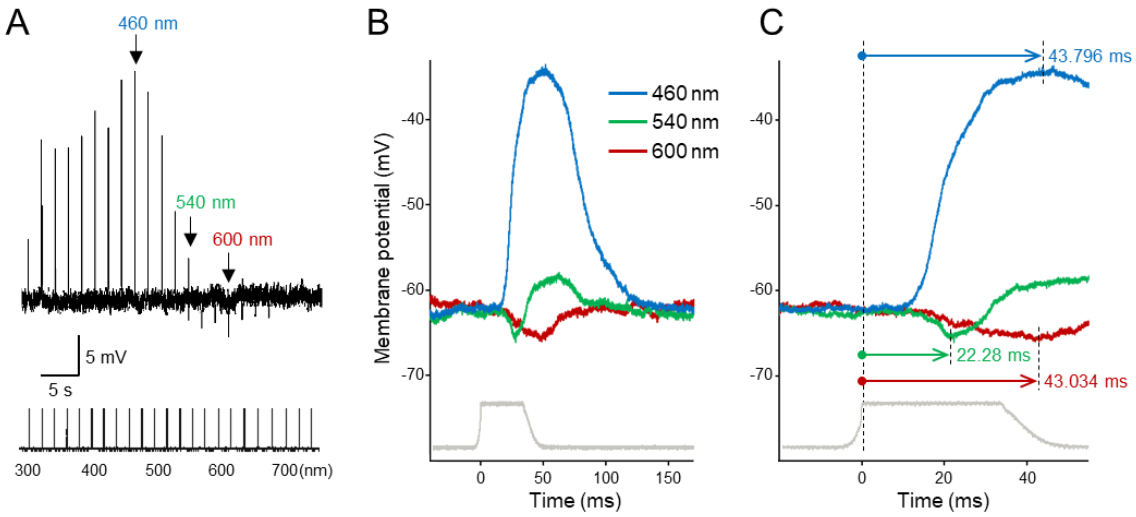


**Figure 5-1. Response profiles of a B+/R- receptor upon isoquantal spectral stimulation with 30 ms pulses with different color lights by interference filters.** (**A**) Membrane potential trace of the cell upon 30 ms pulses with different color lights from 300 nm to 740 nm (with 20 nm interval) by interference filters. (**B**) Waveforms of the recording in **A** at the positive peak (460 nm, *blue line*), intermediate (540 nm, *green line*) and negative peak (600 nm, *red line*) wavelengths. (**C**) Same waveforms from **B** with an expanded time scale. The bars and numbers indicate the response latencies.

Six primary classes of spectral receptor have already been distinguished in the retina of *Papilio xuthus*, which are the ultraviolet (UV), violet (V), blue (B), green (G), red (R), and broadband (BB) class (Arikawa, 2003). Following this receptor classification, in the lamina, I obtained more than 60 recordings of spectrally opponent photoreceptors, which I first categorized into six classes based on the positive peak wavelengths and then divided into distinct subclasses according to the hyperpolarization at different wavelength ranges. The recording numbers of spectrally opponent photoreceptor in the lamina, recorded by two different light simulated devices (i.e. LED array and IF series; see Materials and Methods), in distinct spectrally opponent classes are given in Table 5-1.

**Table 5-1. The recording number in each spectral class of opponent photoreceptors in the lamina**

| spectral classes | | ratio | light stimulation | |
|---|---|---|---|---|
| | | | LED array | IF series |
| UV | UV+/G- | *N*=7 (10.3%) | *N*=6 | *N*=1 |
| | UV+/G-/R+ | *N*=2 (2.9%) | *N*=2 | *N*=0 |
| Violet | V+/G- | *N*=7 (10.3%) | *N*=4 | *N*=3 |
| Blue | B+/R- | *N*=17 (25.0%) | *N*=13 | *N*=4 |
| | B+/G-/R+ | *N*=4 (5.9%) | *N*=4 | *N*=0 |
| | B+/G- | *N*=7 (10.3%) | *N*=5 | *N*=2 |
| Green | dG+/R- | *N*=3 (4.4%) | *N*=2 | *N*=1 |
| | UV-/sG- | *N*=1 (1.5%) | *N*=0 | *N*=1 |
| Red | B-/R+ | *N*=6 (8.8%) | *N*=5 | *N*=1 |
| Broadband | UV-/BB+ | *N*=14 (20.6%) | *N*=8 | *N*=6 |

**UV-positive opponent receptors**

The cells with maximal depolarization at 365 nm were grouped as UV-positive opponent receptors (9 units; Figure 5-2). They were recorded by the LED array (6 units) and the IF series (1 units), yielding very similar spectral response profiles (Figure 5-6A). All cells in this class depolarized mainly below 450 nm and hyperpolarized in the green wavelength range. According to the difference in the polarity of responses in the red wavelength range, the UV-positive opponent receptors can be further divided into two subclasses: UV+/G- (7 units) and UV+/G-/R+ (2 units). The UV+/G- receptors had a negative peak between 510 to 540 nm, while the negative peak of UV+/G-/R+ receptors was located in shorter wavelength range of 480–520 nm. The origin of depolarization in red wavelength in UV+/G-/R+ receptors is unknown yet, since the absorption spectrum of the *Papilio* rhodopsin R360 (PxUV) has little sensitivity beyond 450 nm.

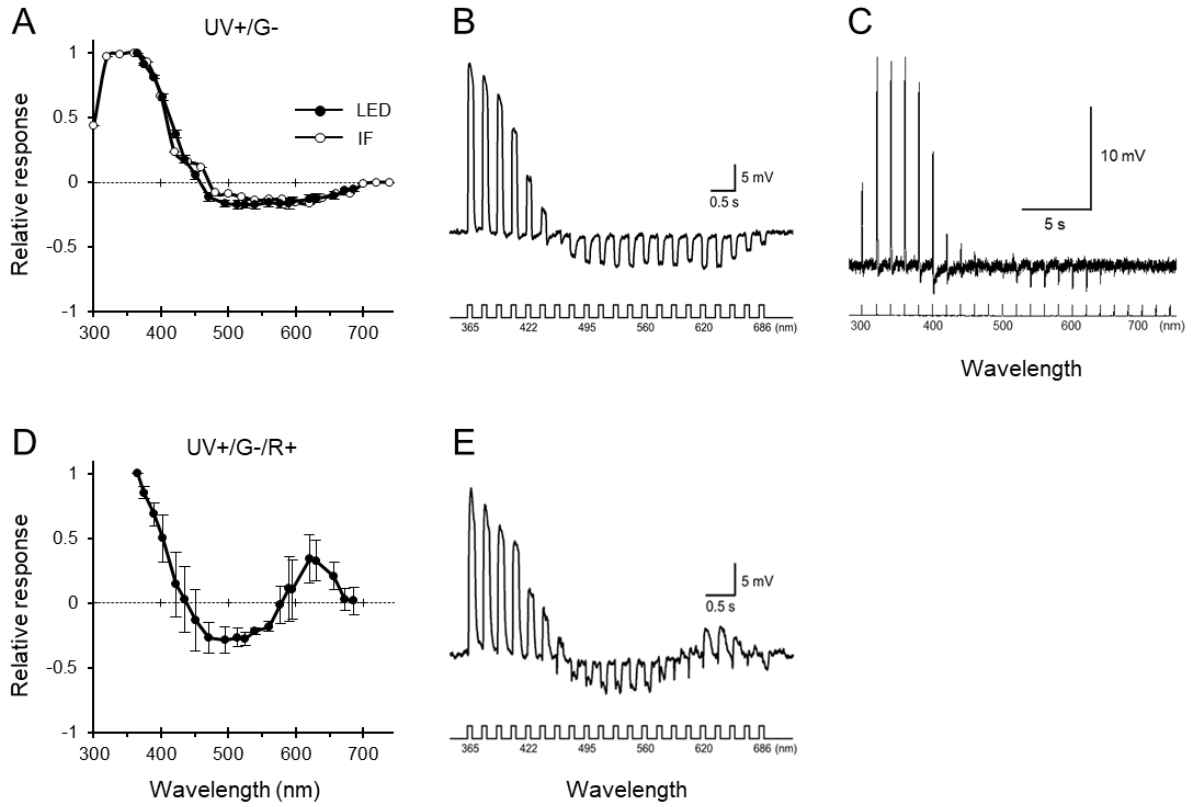


**Figure 5-2. Spectral responses of UV-positive opponent photoreceptors in the lamina.** (**A**) Averaged spectral response curves (mean ± SEM) of UV+/G- receptors measured by the LED array (LED, *solid circles*; $\lambda_{max,positive}$ = 365 nm, $\lambda_{max,negative}$ = 514 nm; *N*=6) and with the IF series (IF, *open circles*; $\lambda_{max,positive}$ = 360 nm, $\lambda_{max,negative}$ = 540 nm; *N*=1). Membrane potential traces of a UV+/G- receptor upon isoquantal spectral stimulation with 100 ms pulses from the LED array (**B**) and with 30 ms pulses from the IF series (**C**). (**D**) Averaged spectral response curves (mean ± SEM) of UV+/G-/R+ receptors ($\lambda_{max,positive}$ = 365 nm, $\lambda_{max,negative}$ = 495 nm; *N*=2). (**E**) Membrane potential trace of a UV+/G-/R+ receptor upon isoquantal spectral stimulation with 100 ms pulses from the LED array.

I performed the following tests to further check the origin of antagonistic interactions. First, to check whether the inhibition was simply happening within a single ommatidium, I changed the size of light source by an aperture placed between the light source and the eye. The spectral responses of a UV+/G-/R+ receptor that was stimulated with a point source (closed aperture; ~2°) and two different extended stimuli (half or fully open aperture, ~7°, 15°) were compared (Figure 5-3). To get a point source, I made the aperture as small as possible while the response was still present, thereby stimulating a single ommatidium. When increasing the aperture size, the response amplitude of depolarization did not change significantly both in UV and red wavelength ranges; however, those of hyperpolarization were strongly affected. The extended source stimulation brought an increase in hyperpolarization, indicating that the antagonistic interactions with neighboring ommatidia may be involved.

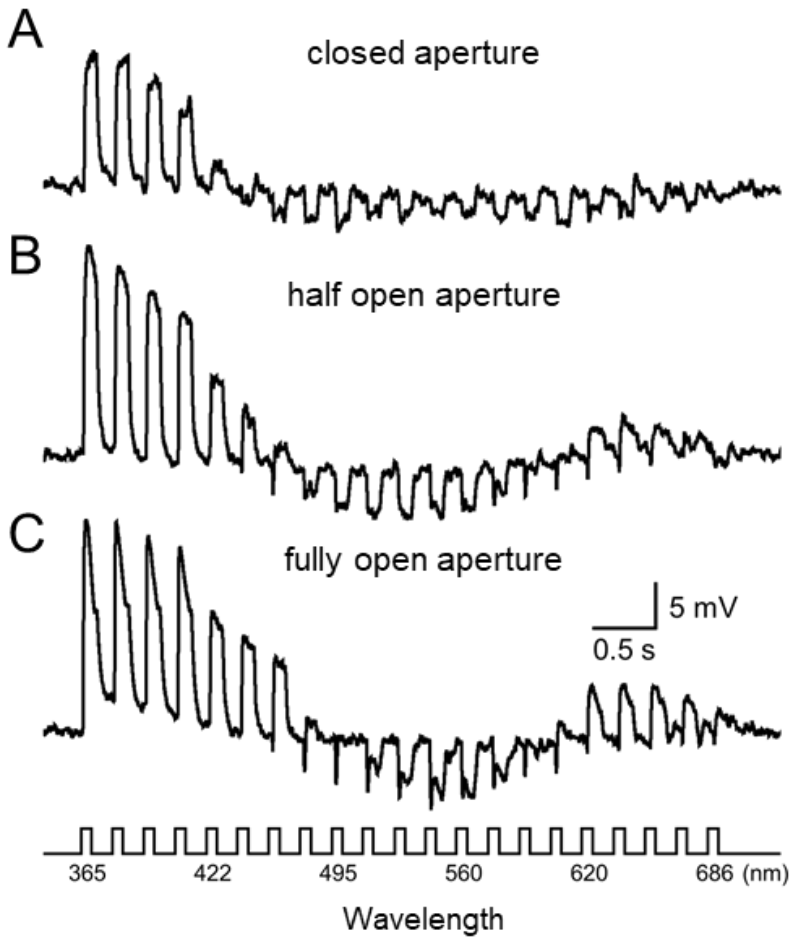


**Figure 5-3. Spectral response curves of a UV+/G-/R+ receptor toward a point source (A) and an extended source with half open aperture (B) and an extended source with fully open aperture (C)**. Membrane potential traces upon isoquantal spectral stimulation with 100 ms pulses from the LED array.

Further comparing the differences between the stimulation with half (Figure 5-3B) and fully (Figure 5-3C) open aperture, there was no significant change in terms of response amplitudes for both depolarization and hyperpolarization, but the response profiles were modulated. For instance, the suppression on the falling phase of depolarized responses was obvious when an aperture was fully open. It seemed that the suppression was slightly delayed and therefore the peak response amplitude was not strongly affected. Moreover, the suppression increased proportionally with increasing the degree of extended source. Accordingly, such suppression effect may be due to the extracellular potential. Apart from the ERG-like component, the fast on-set hyperpolarization, which can be seen clearly when responded to stimuli between 471 nm to 590 nm (Figure 5-3C), did not show significant changes upon the change of the aperture size from half to fully open as that from closed to half open. It is most likely that the interommatidial antagonism between photoreceptors across the cartridges is mainly contributed from the six surrounding ommatidia.

Second, to check which spectral receptor classes were involved in antagonistic interactions of the UV+/G-/R+ receptor, I performed selective adaptation experiments. The cell was first dark-adapted, and its spectral response was determined by spectral scans from 365–686 nm using the LED array. The spectral responses were then determined under a monochromatic background light at UV (360 nm), blue (450 nm), green (540 nm), and red (600, 650, and 700 nm) wavelengths (Figure 5-4). Light adaptation to UV and blue slightly reduced its depolarized responses at UV and blue wavelengths, respectively. This was due to the desensitization within the UV receptor, as expected. The hyperpolarizing responses at the blue wavelengths were slightly reduced by light adaptation to green. This indicated that the green receptors may be attributed to the antagonism at the blue wavelengths, at least partially. Light adaptation to red (600 and 650 nm) significantly reduced hyperpolarizing response from blue to red wavelengths, indicating that the red receptors may be attributed to the antagonism in these wavelengths. The failure in canceling the hyperpolarization in the green suggested that these slow hyperpolarizing responses probably came from the green receptors or other shorter wavelength-sensitive receptors. While the fast on-set hyperpolarization was not strongly influenced by green adaptation, it was strongly suppressed by red adaptation. Therefore, antagonistic interactions were likely coming from all other classes of spectral receptors, but most of them were from red receptors. On the other hand, while response amplitudes of the fast on-set hyperpolarization at red wavelengths were reduced evidently, those of depolarization were increased by red light adaptation instead. It is reasonable to expect that the reduction of

antagonistic inhibition would result in the increase of depolarization amplitudes. However, the origin of depolarization in the red wavelength could not be simply interpreted. It is unlikely that the depolarization is generated by double recording with another red receptor or positive electrical coupling.

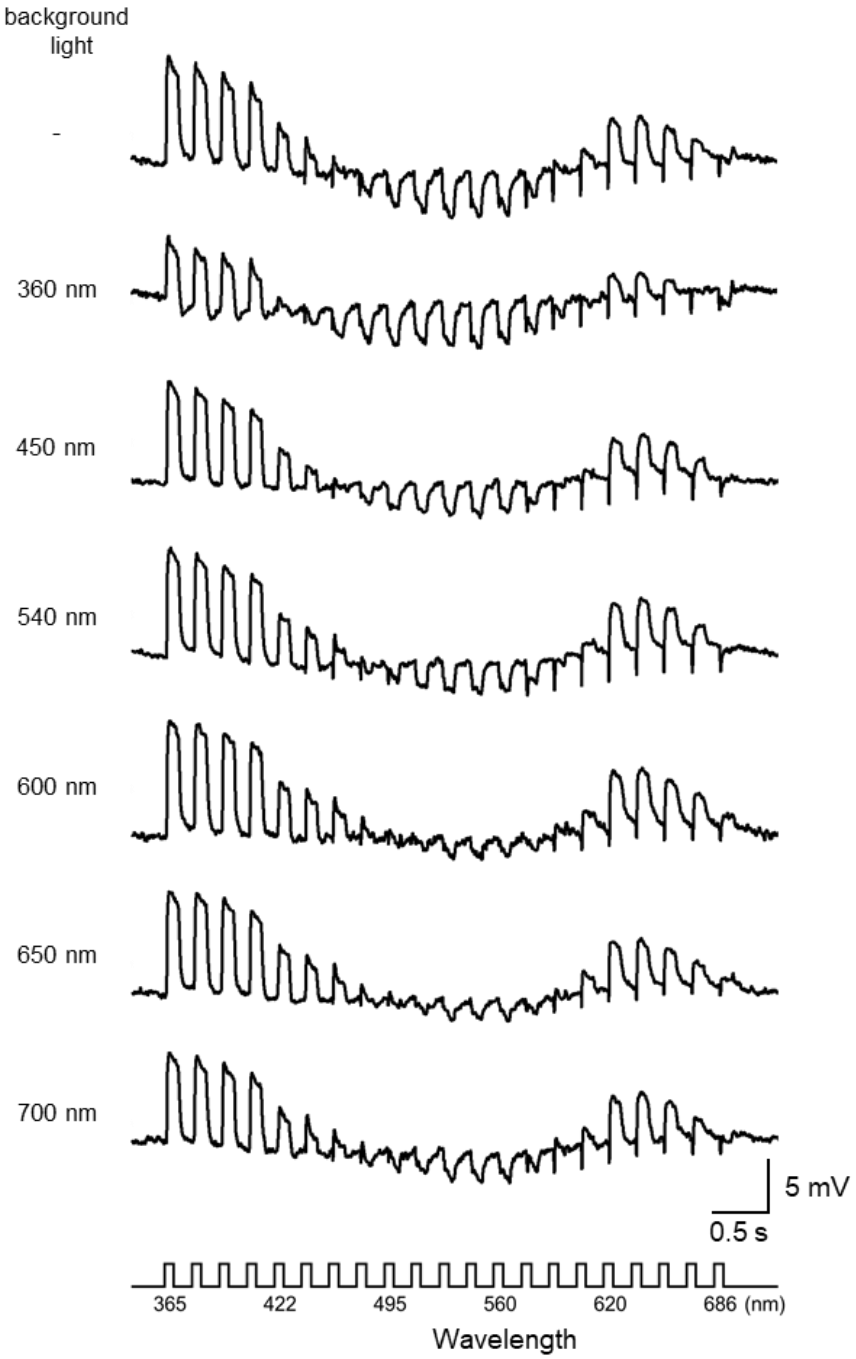


**Figure 5-4. Spectral responses of a UV+/G-/R+ receptor at different background lights**. The cell was stimulated with 100 ms isoquantal spectral pulses from the LED array. The first trace was recorded without background light, all other membrane potential traces were recorded with simultaneous background lights from a monochromator at wavelengths (from top to bottom) 360, 450, 540, 600, 650, and 700 nm.

Third, to test whether the antagonistic interaction is due to synaptic connections through neighboring photoreceptors, I recorded the spectral responses along with positive (depolarizing) and negative (hyperpolarizing) current injections. When I injected negative currents to an UV+/G-/R+ receptor and brought the membrane hyperpolarized about 30 mV below its resting potential, the amplitudes of hyperpolarizing light-responses were significantly reduced (Figure 5-5). The polarity could even be reversed to depolarization at blue and red wavelengths (*asterisks*). It indicated that the equilibrium potential of the ion causing the antagonistic hyperpolarization is already reached at this potential, which is close to the expected equilibrium potential of $Cl^-$, suggesting that $Cl^-$ channels mediate the opponent processing. While the amplitudes of hyperpolarizing light-responses were suppressed by injecting negative currents, those of depolarizing light-responses significantly increased, e.g. responses in UV and red wavelengths. The TRP channels are responsible for the depolarization of insect photoreceptors in response to light (Hardie and Franze, 2012). They allow $Na^+$ and $Ca^{2+}$ to enter the cell and give rise to depolarization. The equilibrium potentials of these cations ($Na^+$ and $Ca^{2+}$) are more positive than the resting potential. When the membrane was brought to be more negative, the electrical driving force of the ions increased; as a result, the amplitudes of depolarizing light-response increased.

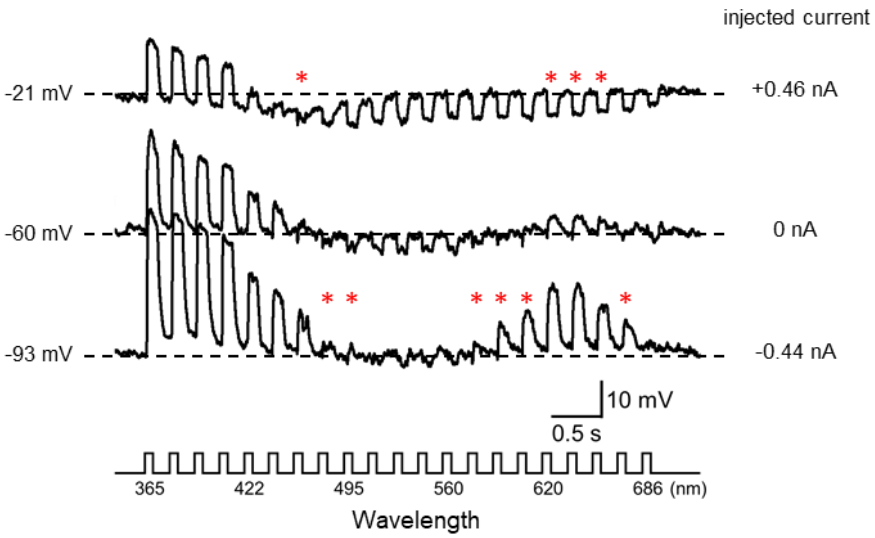


**Figure 5-5. Responses of a UV+/G-/R+ receptor to current injection.** The cell was stimulated with 100 ms isoquantal spectral pulses along with +0.46 nA (top trace), none (middle trace), and -0.44 nA (bottom trace) injection. *Asterisks* indicate the polarity of responses was reversed during depolarizing or hyperpolarizing current injection.

On the other hand, when I injected positive currents to the cell and brought the membrane depolarized about 40 mV beyond its resting potential, the amplitudes of

hyperpolarizing light-responses increased in the wavelength range from blue to red. The greater hyperpolarization can be explained by the stronger driving force of $Cl^-$ since the membrane was depolarized far from the equilibrium potential of $Cl^-$. The hyperpolarizing effect to responses in green wavelengths was relatively weaker than other wavelengths. It is probably because the recording site was far from the synapses, and thus the photoreceptor could not be clamped. In contrast, the reverse of polarity was observed in blue and red wavelengths (*asterisks*). Noteworthily, the polarity of original depolarizing responses to red stimulation was completely reversed to hyperpolarizing responses by injecting positive currents. The effect can be attributed to the reduction in intrinsical photoreceptor depolarization along with the increase in antagonistic hyperpolarization through $Cl^-$ channels. The clamp seems to be fine, and thus the origin of depolarization at red wavelength is still in question. At any rate, the results suggest that the antagonistic hyperpolarization may be attributed to $Cl^-$ channels, not to the extracellular return currents.

**Violet-positive opponent receptors**

I had recorded violet-positive opponent receptors (V+/G-) by using the LED array (4 units) and the IF series (3 units), yielding very similar spectral response profiles (Figure 5-6). All cells in this class depolarized mainly within the spectral range of 360–450 nm and had a narrow peak around 390 nm. On the other hand, they had hyperpolarizing responses at longer wavelengths (460–620 nm), and, either had a sharp cut-off (3 units) or hyperpolarization (4 units) at shorter wavelengths below 360 nm.

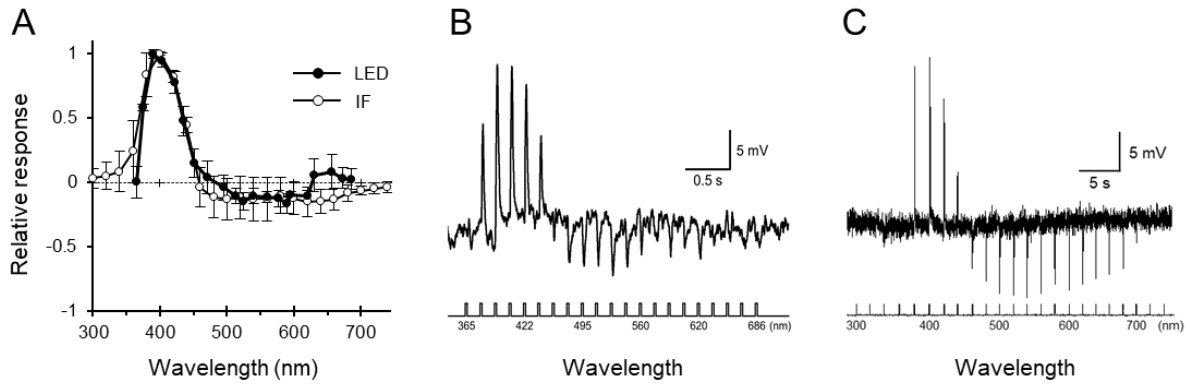


**Figure 5-6. Spectral responses of violet-positive opponent photoreceptors in the lamina.** (**A**) Averaged spectral response curves (mean ± SEM) of V+/G- receptors measured by the LED array (LED, *solid circles*; $\lambda_{max,positive}$ = 390 nm, $\lambda_{max,negative}$ = 590 nm; *N*=4) and with the IF series (IF, *open circles*; $\lambda_{max,positive}$ = 400 nm, $\lambda_{max,negative}$ = 620 nm; *N*=3). Membrane potential traces of a V+/G- receptor upon isoquantal spectral stimulation with 10 ms pulses from the LED array (**B**) and with 30 ms pulses from the IF series (**C**).

I also recorded the angular responses of a violet-positive opponent receptor at the peak wavelengths of depolarization and hyperpolarization (Figure 5-7A). The acceptance angles predicted from the angular responses (half maximum of the angular response function) were almost the same among the different wavelengths (Figure 5-7B). This suggests that the observed antagonistic inhibition was basically due to inter-photoreceptor interactions within a single ommatidium.

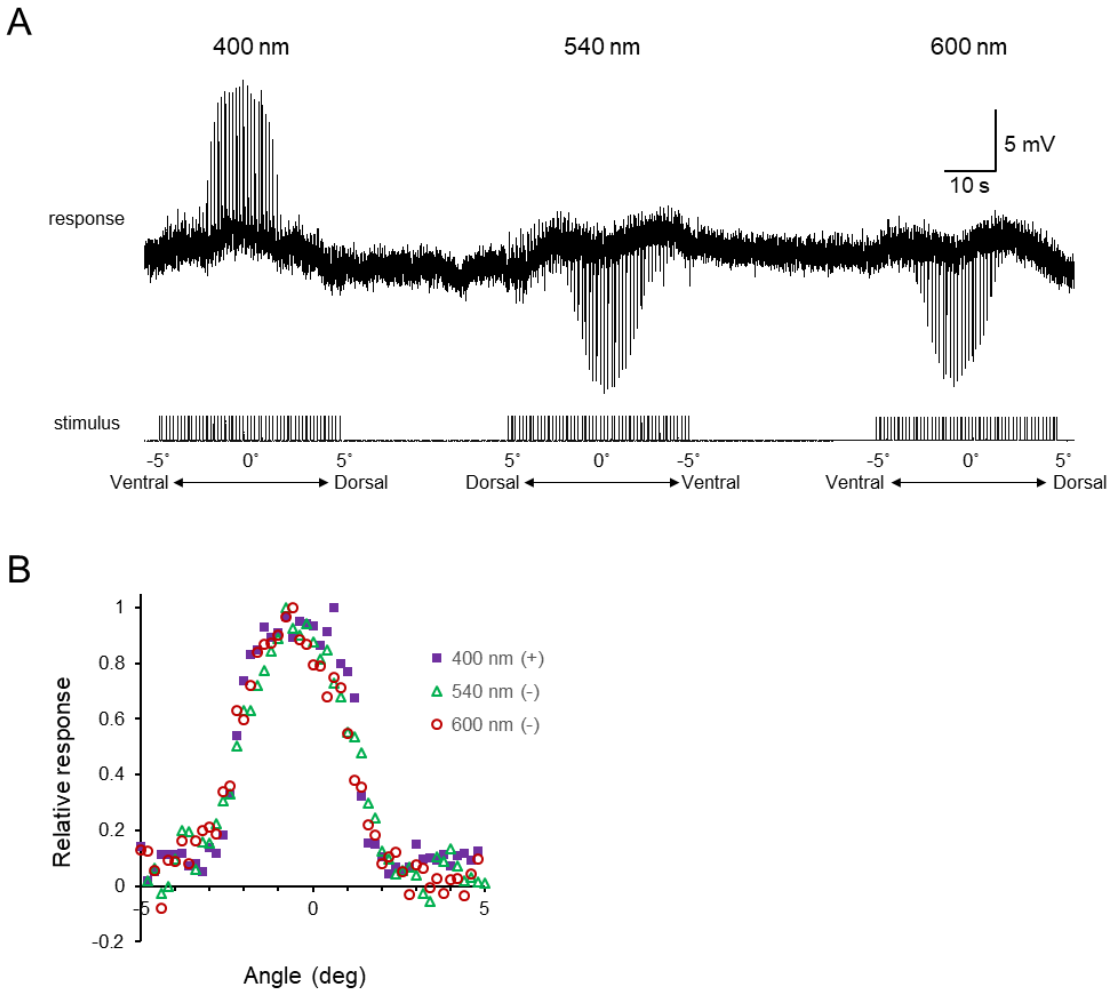


**Figure 5-7. Angular responses of a V+/G- receptor.** (**A**) Membrane potential trace of the cell measured with angular steps of 0.2° over 10° (dorsal (+5°) to ventral (-5°)) with 30 ms pulses at three wavelengths (from left to right) 400, 540 and 600 nm. (**B**) Relative angular responses of the recording in **A**. The cell has similar acceptance angles among the three wavelengths irrespective of response polarity.

**Blue-positive opponent receptors**

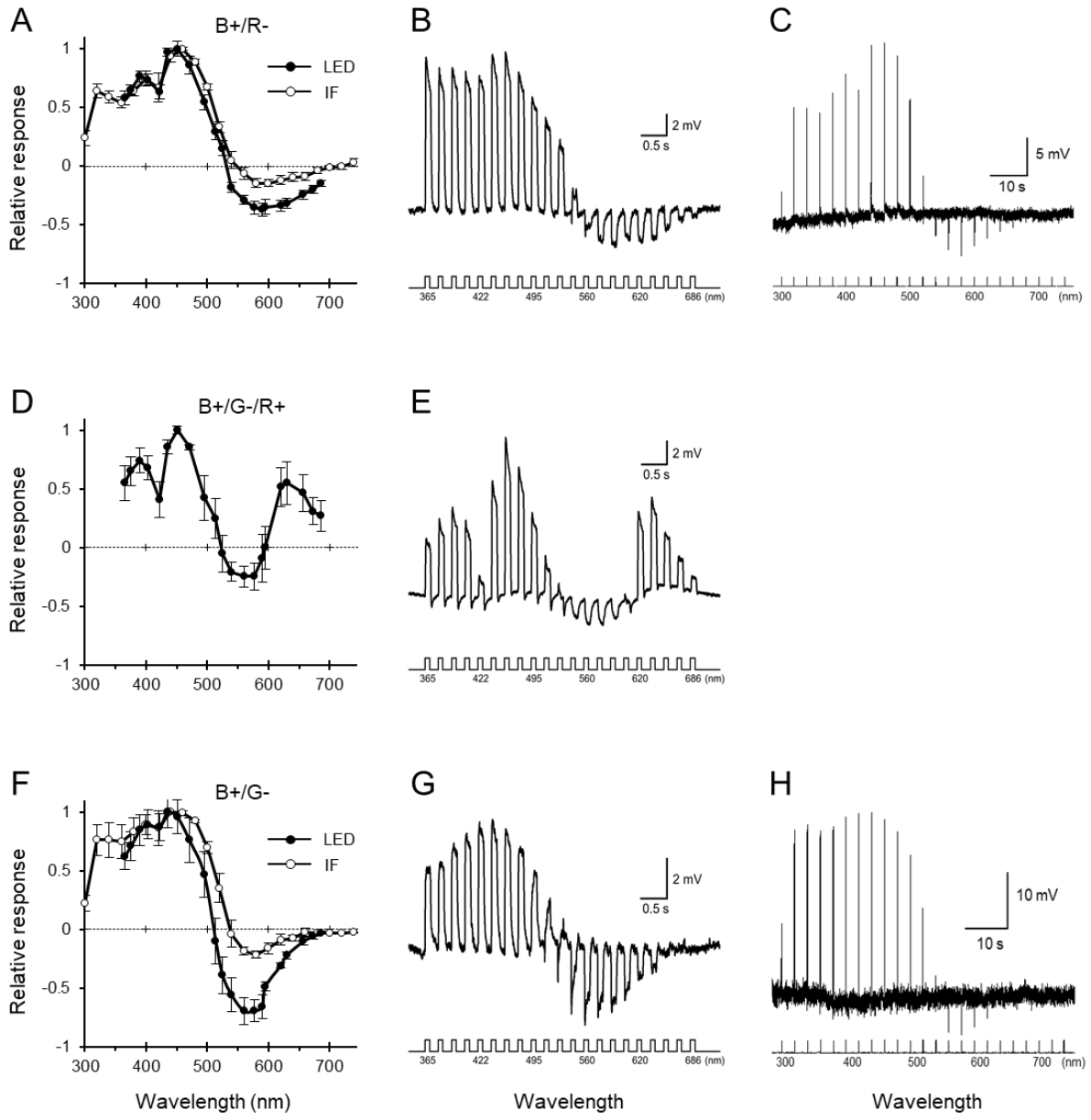


**Figure 5-8. Spectral responses of blue-positive opponent photoreceptors in the lamina.** (**A**) Averaged spectral response curves (mean ± SEM) of B+/R- receptors measured by the LED array (LED, *solid circles*; $\lambda_{max,positive}$ = 451 nm, $\lambda_{max,negative}$ = 590 nm; *N*=13) and with the IF series (IF, *open circles*; $\lambda_{max,positive}$ = 460 nm, $\lambda_{max,negative}$ = 580 nm; *N*=5). Membrane potential traces of a B+/R- receptor upon isoquantal spectral stimulation with 100 ms pulses from the LED array (**B**) and with 30 ms pulses from the IF series (**C**). (**D**) Averaged spectral response curves (mean ± SEM) of B+/G-/R+ receptors ($\lambda_{max,positive}$ = 451 nm, $\lambda_{max,negative}$ = 560 nm; *N*=4). (**E**) Membrane potential traces of a B+/G-/R+ receptor upon isoquantal spectral stimulation with 100 ms pulses from the LED array. (**F**) Averaged spectral response curves (mean ± SEM) of B+/G- receptors measured by the LED array (LED, *solid circles*; $\lambda_{max,positive}$ = 435 nm, $\lambda_{max,negative}$ = 560 nm; *N*=5) and with the IF series (IF, *open circles*; $\lambda_{max,positive}$ = 440 nm, $\lambda_{max,negative}$ = 580 nm; *N*=2). Membrane potential traces of a B+/R- receptor upon isoquantal spectral stimulation with 100 ms pulses from the LED array (**G**) and with 30 ms pulses from the IF series (**H**).

Among all spectrally opponent receptors in the *Papilio* lamina, cells with maximal depolarization at 440 to 460 nm with hyperpolarization in long wavelength, were the most frequently encountered (Table 5-1). The blue-positive opponent receptors can be further divided into three subclasses (Figure 5-8) according to response characteristics in the red; red negative (B+/R-; 18 units), red positive (B+/G-/R+; 4 units), or undetectable (B+/G-; 7 units). The B+/R- and B+/G- receptors have maximal hyperpolarization at 580–590 nm and 540–577 nm, respectively. The B+/G-/R+ receptors hyperpolarized at 525–600 nm and depolarized beyond 600 nm. Such depolarization in the red is similar to that seen in UV+/G-/R+ receptors.

I had recorded the B+/R- receptors by using the LED array (13 units) and the IF series (5 units). The former gave hyperpolarization beyond 540 nm, while the latter produced hyperpolarization only beyond 560 nm (Figure 5-8A–C). It is also the similar case for the B+/G- receptors that recorded by the LED array (5 units) and the IF series (2 units) (Figure 5-8F). The former gave hyperpolarization beyond 514 nm, while the latter produced hyperpolarization only beyond 540 nm. At any rate, the profiles of spectral responses were not significantly different between two stimulating methods.

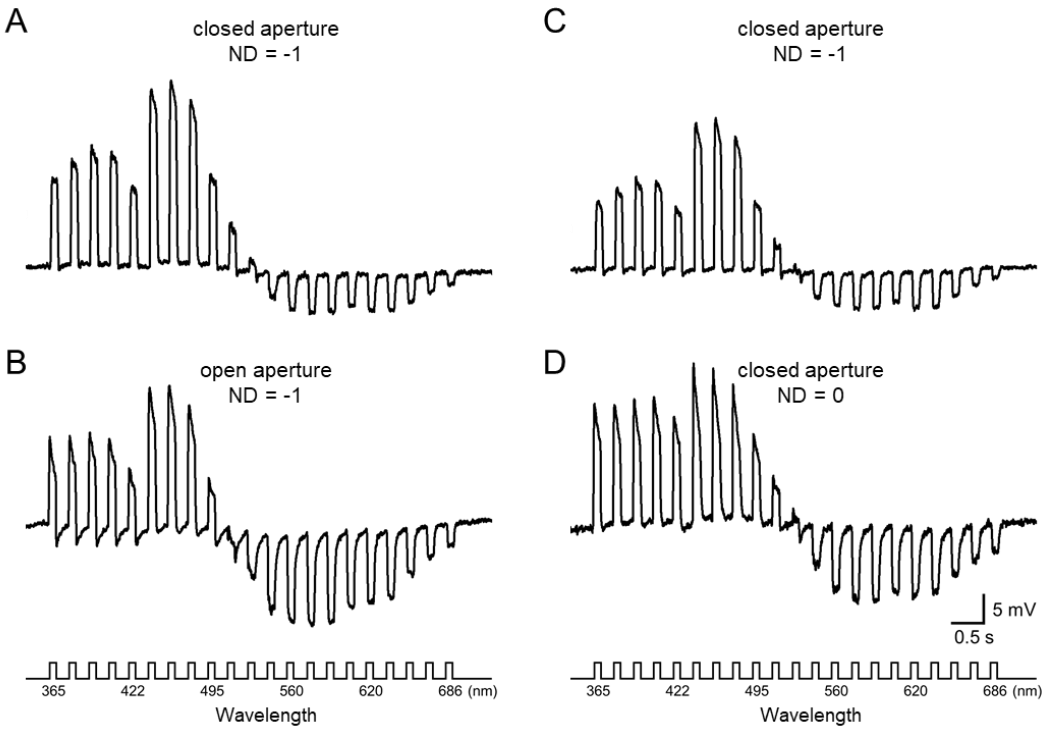


**Figure 5-9. Spectral response curves of B+/R- receptors at different stimulating conditions.** Membrane potential traces upon isoquantal spectral stimulation with 100 ms pulses from the LED array. Spectral response curves of a B+/R- receptor recorded with a point (**A**) and an extended source (**B**). Spectral response curves of another B+/R- receptor recorded with a point source at lower (**C**) and higher (**D**, 10-fold brighter) light intensities.

To check the origin of the antagonism, I stimulated a B+/R- receptor with a point source (closed aperture) and an extended source (open aperture). The amplitude of hyperpolarization from green to red wavelengths was rather constant when a single ommatidium was stimulated (Figure 5-9A). However, the amplitudes of hyperpolarizing responses in the green became larger when the extended stimulus was used (Figure 5-9B). It is different to the change of hyperpolarizing responses to a point source with 10-fold brighter intensity (Figure 5-9D): response amplitudes of the hyperpolarization increased proportionally at long wavelength range. I thus supposed that the antagonistic hyperpolarization of B+/R- receptors was mainly coming from red receptors within the same ommatidium, while the inhibition in the green may be coming from neighboring cartridges.

Measuring V-log I functions with a point source at different wavelengths provided more comprehensive descriptions of the antagonistic interactions in the opponent photoreceptors. Figure 5-10A shows a B+/R- receptor responding to a graded series of intensities at six wavelengths. The cell depolarized at its main peak wavelength (440 nm). The responses at adjacent wavelengths (360, 520, and 560 nm) contain a negative component. Taking a closer look at their waveforms (Figure 5-10B), the negative component preceded the depolarization. The fast hyperpolarization suggests that the cell receives antagonistic inputs from UV and green receptors within the same ommatidium. The cell purely hyperpolarized to the stimulation at 600 and 640 nm and produced similar V-log I curves (Figure 5-10A), however, with different waveforms (Figure 5-10B). The cell exhibited the fast on-set hyperpolarization at high intensities with 600 nm lights, suggesting the existence of antagonistic interactions. The weak and slow depolarization might be from the blue receptor itself. The fast and strong hyperpolarization was most likely due to the input from the red receptors within the same ommatidium. The phenomenon of fast on-set hyperpolarization was absent in waveforms that were evoked by stimulation at 640 nm; instead, smooth hyperpolarization was observed. The antagonistic interaction does not seem to exist beyond 640 nm.

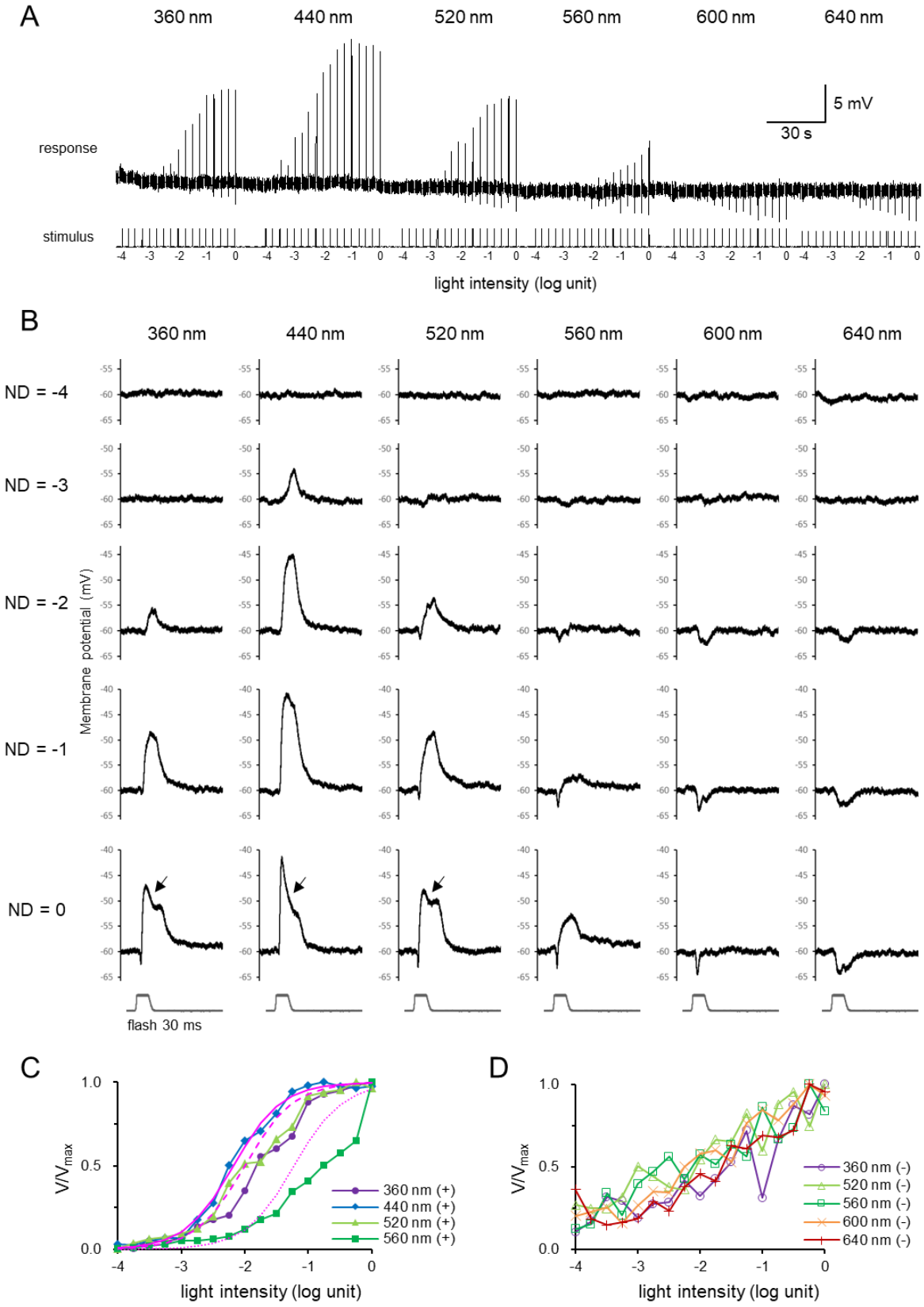


**Figure 5-10. Responses of a B+/R- receptor to 30 ms pulses presented with different interference filters at a graded series of illumination levels.** (**A**) Membrane potential trace of the cell was measured at six wavelengths (from left to right) 360, 440, 520, 560, 600, and 640 nm, graded in 0.25 log intensity steps.

(continued on the next page)

The $V/V_{max}$ curves of the recorded B+/R- receptor (Figure 5-10C) provide another support to the antagonistic interaction. The *solid line* is the Naka-Rushton function, fitted to the measurement at 440 nm. The *dashe*d and *dotted lines* were obtained by fitting the same function to the measurement at 520 and 560 nm. The three curves are essentially parallel and shifted along the abscissa. The $V/V_{max}$ curve of 360 nm was pretty similar to 520 nm and thus I compared them as the same group to the *dashed* fitted curve. The discrepancy between the *dashed* curve and the measured points at medium light intensities, e.g. ND = -2 to -1, suggests suppression, presumably coming from dual-peaked green receptors and fading away at high light intensities when the antagonistic hyperpolarization saturated. Similar effect was observed in the 560 nm $V/V_{max}$ curve as well. The source of suppression probably originated from the two green receptors and four red receptors within the same ommatidium. In contrast, the normalized $V/V_{max}$ curves of antagonistic hyperpolarization showed no significant difference among five wavelengths (Figure 5-10D). This suggests that the blue receptor received inputs at all measured wavelengths evenly except for its main peak wavelength at 440 nm. On the other hand, the waveforms of hyperpolarization from 360 to 520 nm exhibit a notch at brighter illuminations (ND = 0) on the falling phase after reaching the peak (Figure 5-10B; *arrows*). This indicates the existence of the inhibition in the slower hyperpolarization, which is most likely the extracellular return current in very bright light.

I also measured the polarization sensitivities of a B+/R- receptor at different wavelengths (Figure 5-11A). The cell depolarized at its peak wavelength (460 nm) and hyperpolarized at longer wavelength range, e.g. green (540 nm) and orange (580 nm). At the intermediate wavelength (540 nm), when increasing light intensity, the cell produced a mixture of the two polarities in responses as polarization opponency.

(**B**) Waveforms of the recording in **A** for six wavelengths at five light intensities, (from top to bottom) each 10-fold brighter than the last. *Arrows* indicate the notch on the falling phase after reaching the peak (**C**) Four $V/V_{max}$ curves of depolarizing responses from the recording in **A** measuring with wavelengths at (from left to right) 440, 520, 360, and 560 nm. The *solid line* was fitted through the curve measured using 440 nm and shifted parallel to fit points measured with 520 and 360 nm lights (*dashed line*) and 560 nm light (*dotted line*). (**D**) Five $V/V_{max}$ curves of hyperpolarizing responses from the recording in **A** measuring with wavelengths at 360, 560, 600, and 640 nm.

I then analyzed their depolarizing and hyperpolarizing polarization responses in different conditions. The responses were normalized and fitted to the sinusoidal curve with the peak angle value of depolarization (*solid* curve) and hyperpolarization (*dashed* curve) (Figure 5-11B). Except for the polarization response that were recoded with dimmer green (540 nm, ND = -1) light, all other normalized responses of both polarities at different wavelengths fit well to their own groups. The maximal polarization response of depolarization peaked at 20°. As we have known in *Papilio*, the blue receptor has microvilli aligned parallel to the dorso-ventral axis with polarization sensitivity peaking at 0° (Bandai et al., 1992). In order to insert electrodes into the lamina, the head of the animal was rotated about 20° from its dorso-ventral axis. This might lead to 20° deviation in polarization sensitivity, when the recorded cell was derived from the ommatidia directed to the front.

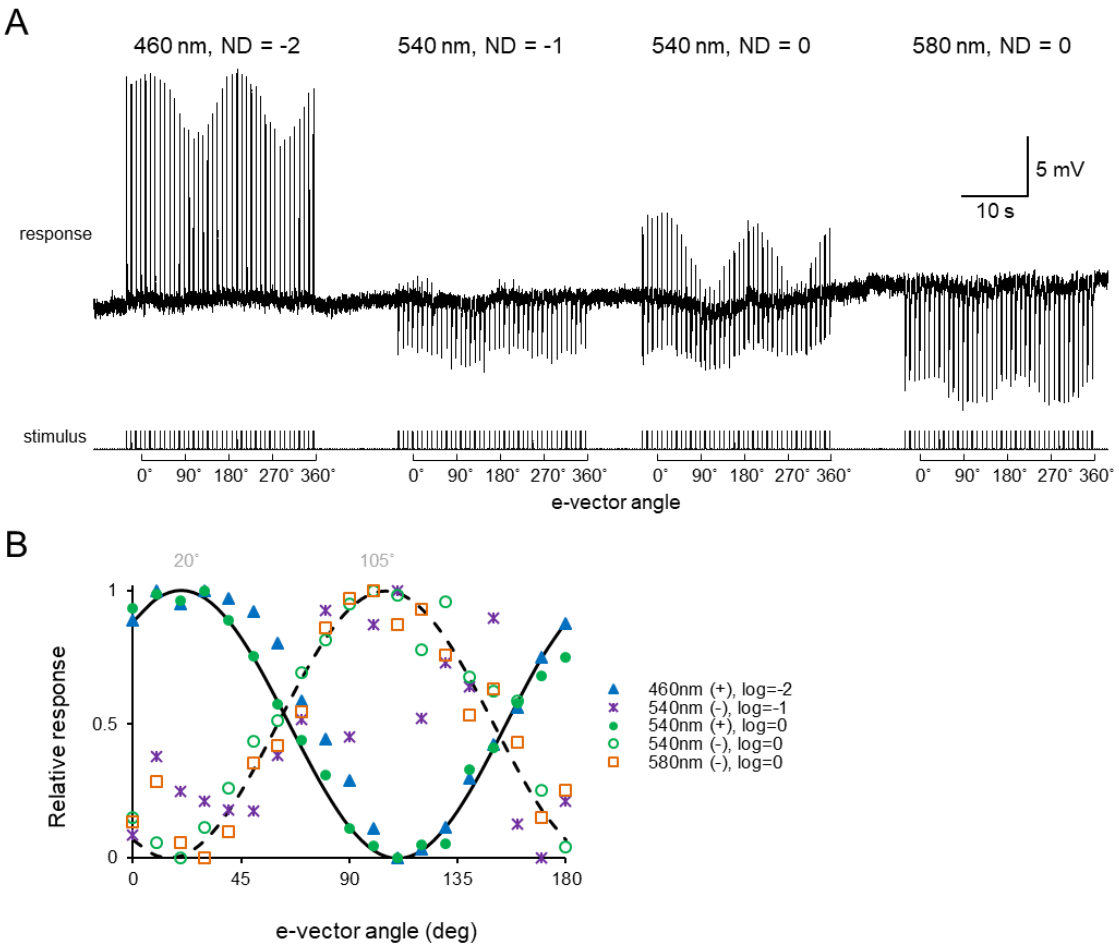


**Figure 5-11. Polarization responses of a B+/R- receptor.** (**A**) Membrane potential trace of the cell upon 30 ms pulses through a rotating polarizer with different light intensities and different color stimulation by interference filters. (**B**) Normalized polarization responses of the recording in **A**. *Solid* and *dash* lines are best-fit sinusoidal curves with the peak angle values for depolarizing (+) and hyperpolarizing (-) responses, respectively.

The polarization responses of depolarization in brighter green light (Figure 5-11A; 540 nm, ND = 0) were very similar to the one in blue (Figure 5-11A; 440 nm, ND = -2), suggesting both of them were coming from the same source which may be the blue receptor itself. Similarly, the polarization response of hyperpolarization that was obtained from the cell responding to bright green (Figure 5-11A; 540 nm, ND = 0) and red (Figure 5-11A; 580 nm, ND = 0) were rather similar. The maximal hyperpolarizing response was found near 105°; however, it might be 85° considering a 20° deviation due to the head rotation. According to the discussion in previous paragraphs, the origin of hyperpolarizing responses in the green and red wavelengths seemed to be green and red receptors in the same ommatidium. The *Papilio* red receptors are diagonally oriented photoreceptors R5–R8 which have their microvilli arranged radially (Bandai et al., 1992). Assuming R5–R8 had almost equal numbers of synaptic connections to the B+/R- opponent receptor, the recorded cell would receive weak polarization inputs from R5–R8 due to the mutual inhibition. Therefore, the polarization responses might be mainly attributed to the green receptors which peaked at 90°.

Current injection experiments have been performed in all three subclasses of blue-positive opponent receptors (Figure 5-12). When the membrane was hyperpolarized about 30 mV below its resting potential, the hyperpolarizing light-responses of a B+/R- receptor (Figure 5-12A) was either cancelled or changed in polarity in particular wavelengths, e.g. blue and red wavelengths (*asterisks*). This suggests that the antagonistic interactions were from the red receptors within the same ommatidium. The synaptic connections from the green receptors were probably far from the recording site, which resulted in unsuccessfully clamped response in the green. While B+/R- receptors most likely have the antagonistic interactions mainly with red receptors, current injection experiments indicated that B+/G-/R+ (Figure 5-12B) and B+/G- (Figure 5-12C) receptors more likely have interactions with green receptors.

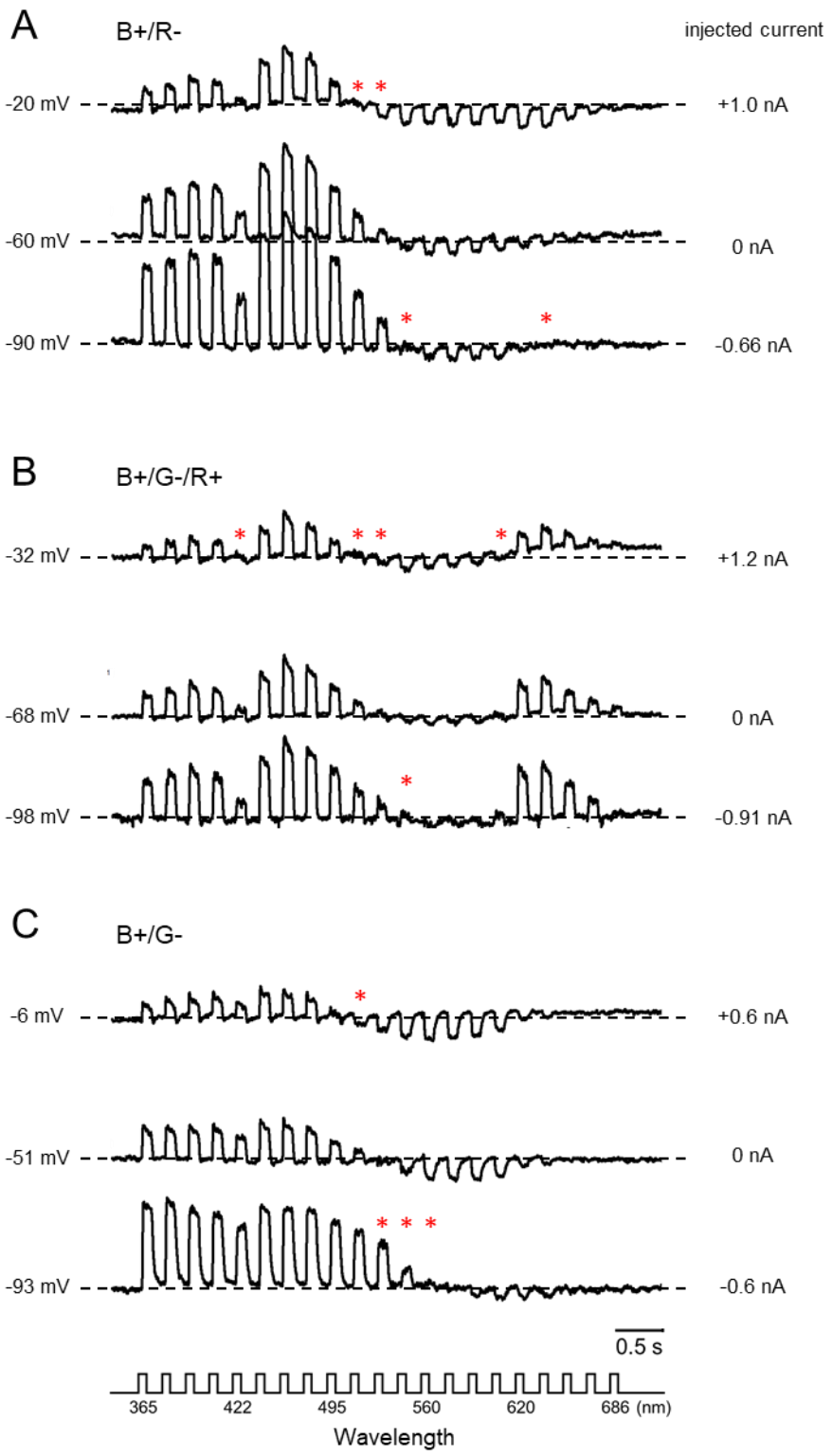


**Figure 5-12. Responses of blue-positive opponent photoreceptors to current injection.** The cells were stimulated with 100 ms isoquantal spectral pulses along with positive (top trace), none (middle trace), and negative (bottom trace) injection. *Asterisks* indicate the polarity of responses was reversed during depolarizing or hyperpolarizing current injection. (**A**) The top and bottom traces demonstrated a B+/R- receptor was depolarized with +1.0 nA and hyperpolarized with -0.66 nA, respectively. (**B**) A B+/G-/R+ receptor with +1.2 and -0.91 nA current injection. (**C**) A B+/G- receptor with +0.6 and -0.6 nA current injection.

**Green-positive opponent receptors**

Most photoreceptors encountered in the *Papilio* lamina were, similar to the case in the retina, green sensitive. However, a few of them exhibited antagonistic interactions. I grouped them into dG+/R- and UV-/sG+ receptors (Figure 5-13). I have recorded dG+/R- receptors by using the LED array (2 units; Figure 5-13B) and the IF series (1 unit; Figure 5-13C). The dG+/R- receptor has a typical spectral response profile of dual-peaked green receptors, but it shows hyperpolarization at the wavelengths beyond 650 nm (Figure 5-13B,C). The UV-/sG+ receptor has a typical spectral response profile of single-peaked green receptors, but it has hyperpolarization at the wavelengths below 380 nm (Figure 5-13E).

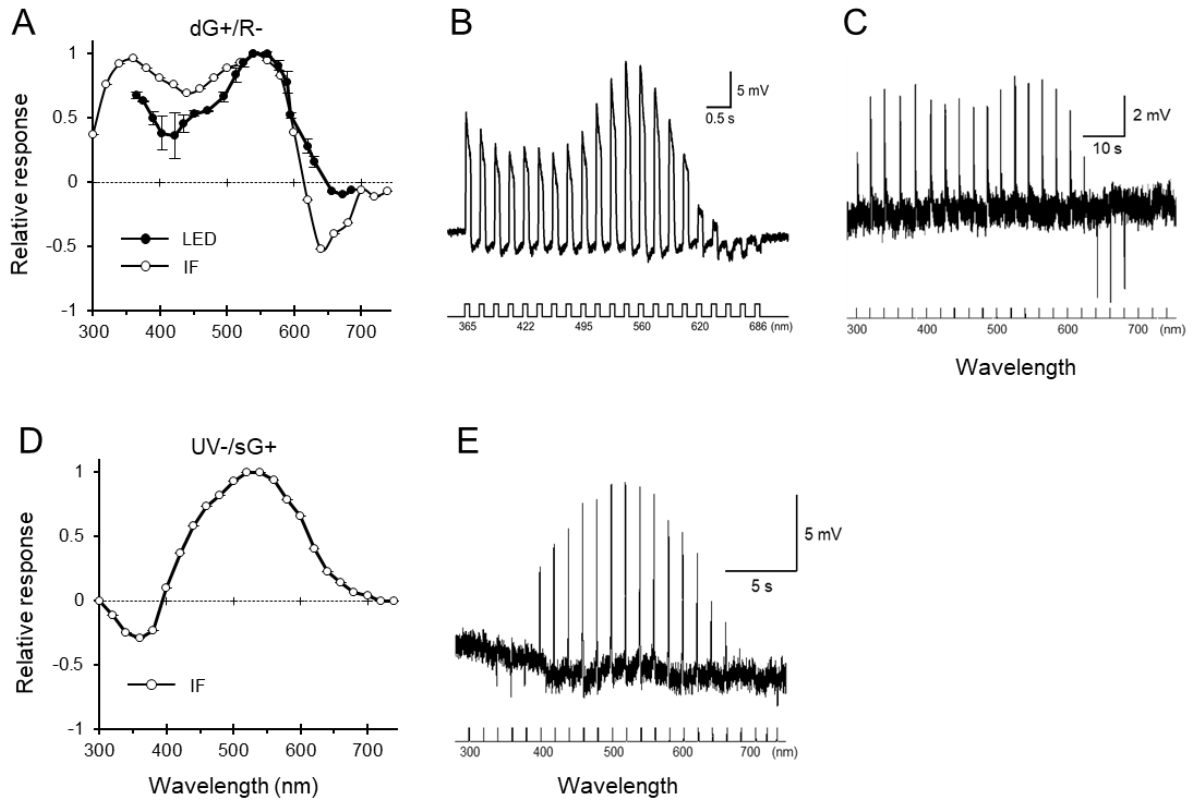


**Figure 5-13. Spectral responses of green-positive opponent photoreceptors in the lamina.** (**A**) Averaged spectral response curves (mean ± SEM) of dG+/R- receptors measured by the LED array (LED, *solid circles*; $\lambda_{max,positive}$ = 540 nm, $\lambda_{max,negative}$ = 673 nm; *N*=2) and with the IF series (IF, *open circles*; $\lambda_{max,positive}$ = 560 nm, $\lambda_{max,negative}$ = 660 nm; *N*=1). Membrane potential traces of a dG+/R- receptor upon isoquantal spectral stimulation with 100 ms pulses from the LED array (**B**) and with 30 ms pulses from the IF series (**C**). (**D**) Averaged spectral response curve of a UV-/sG+ receptor ($\lambda_{max,positive}$ = 520 nm, $\lambda_{max,negative}$ = 360 nm; *N*=1). (**E**) Membrane potential traces of a UV-/sG+ receptor upon isoquantal spectral stimulation with 30 ms pulses from the IF series.

The antagonistic interactions of dG+/R- receptors could be modulated by current injection (Figure 5-14). Injecting negative currents probably weakened the antagonistic interactions through putative PxHCLB channels, and thus resulted in break or reduction of hyperpolarization at the longer wavelengths. The peak wavelength of depolarization shifted from 560 nm towards shorter wavelength 540 nm when the membrane was hyperpolarized about 30 mV below its resting potential. The shift of peak wavelength suggests that the antagonistic interactions may not be coming only from the red receptors but also from the other short wavelength-sensitive cells such as blue and green receptors.

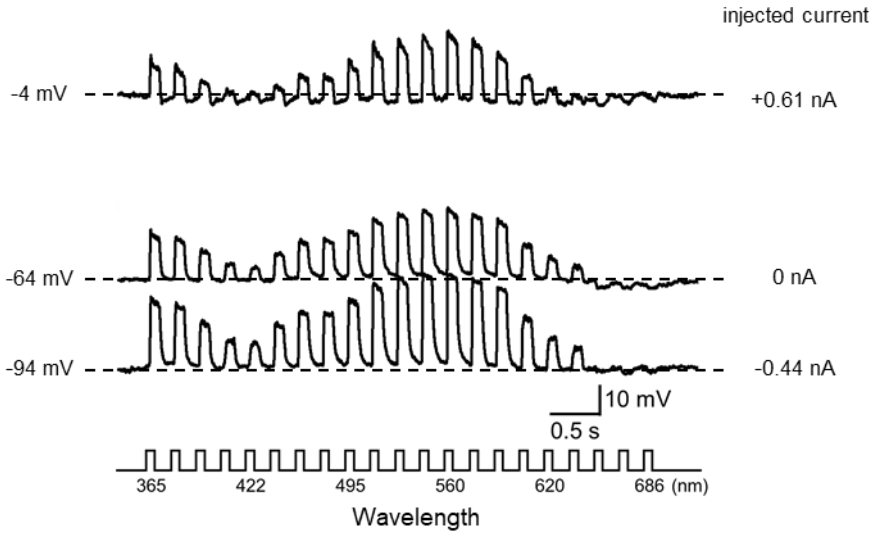


**Figure 5-14. Responses of a dG+/R- receptor to current injection.** The cell was stimulated with 100 ms isoquantal spectral pulses along with +0.61 nA (top trace), none (middle trace), and -0.44 nA (bottom trace) injection.

**Red-positive opponent receptors**

I had recorded 5 red-positive opponent receptors which contained maximal depolarization at 620 to 630 nm and maximal hyperpolarization at 420 to 450 nm. Some variations in the response polarity were observed below 390 nm (Figure 5-15): responses were either depolarizing (i.e. UV+/B-/R+; 3 units; Figure 5-15D) or hyperpolarizing (i.e. B-/R+; 3 units; Figure 5-15B,C).

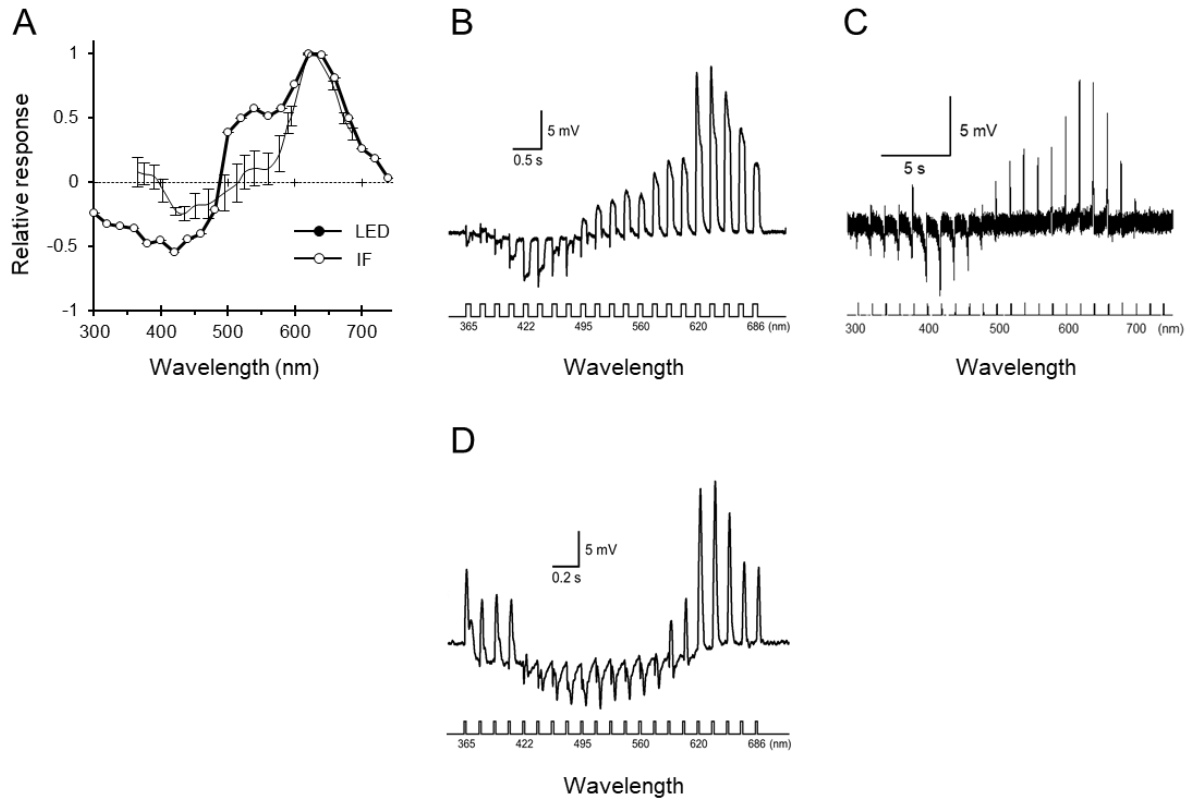


**Figure 5-15. Spectral responses of red-positive opponent photoreceptors in the lamina.** (**A**) Averaged spectral response curves (mean ± SEM) of B-/R+ receptors that measured by the LED array (LED, *solid circles*; $\lambda_{max,positive}$ = 630 nm, $\lambda_{max,negative}$ = 435 nm; *N*=5) and with the IF series (IF, *open circles*; $\lambda_{max,positive}$ = 620 nm, $\lambda_{max,negative}$ = 380 nm; *N*=1). Membrane potential traces of a B-/R+ receptor (**B**) upon isoquantal spectral stimulation with 100 ms pulses from the LED array and with 30 ms pulses from the IF series (**C**). (**D**) Membrane potential trace of a UV+/B-/R+ receptor upon isoquantal spectral stimulation with 10 ms pulses from the LED array.

I do not separate the UV+/B-/R+ and the B-/R+ receptors into different subclasses because I have recorded biphasic polarities in UV wavelength in the same cell by changing the size of light source (Figure 5-16). When a point light source was given, the cell hyperpolarized only at 422 nm, and was thereby termed as a UV+/B-/R+ receptor. The hyperpolarization is probably coming from the blue receptors in the same ommatidium. Increasing the brightness of light intensity did not change the response polarity. However, when I applied an extended source, it gave rise to an increase of antagonistic interactions in UV and blue wavelengths and resulted in a change in response polarity; the so-called UV+/B-/R+ receptor was transformed into the B-/R+ receptor. This phenomenon could be attributed to cells that have UV or blue sensitivities, e.g. UV, blue, and dual-peaked green receptors, at neighboring ommatidia. Therefore, it is most likely that the polarity variation in the UV is a result of the different degrees of interommatidial antagonistic interactions.

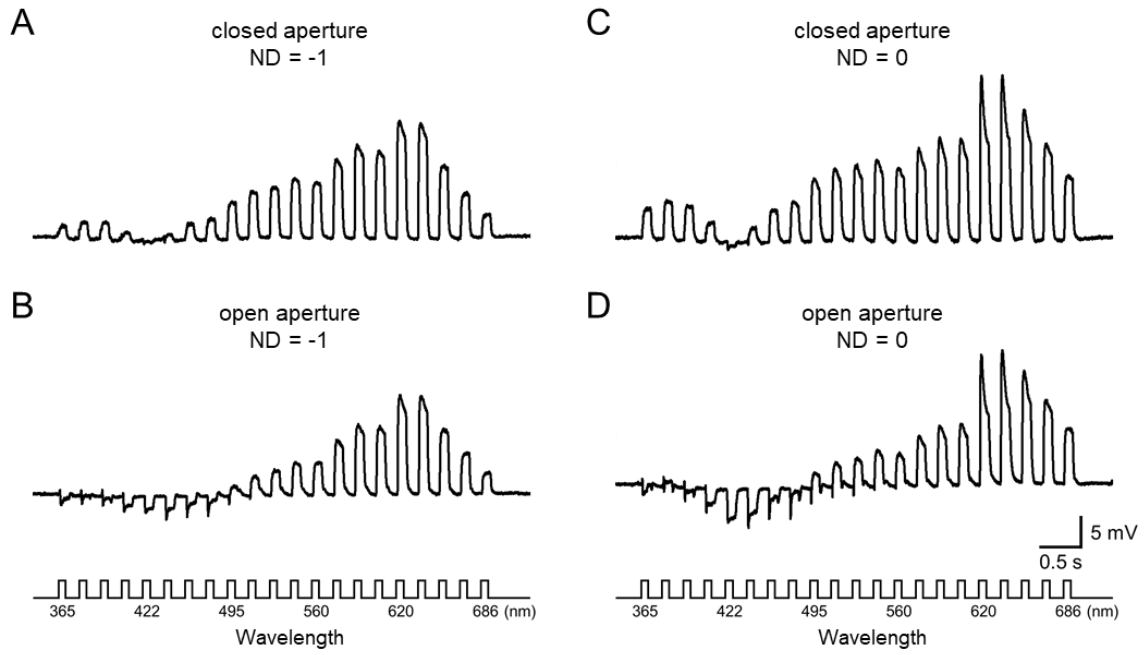


**Figure 5-16. Spectral response curves of a B-/R+ receptor at the different stimulating conditions.** Membrane potential traces upon isoquantal spectral stimulation with 100 ms pulses from the LED array. Spectral response curves of a B+/R- receptor toward a point source at lower (**A**) and higher (**C**, 10-fold brighter) light intensities as well as an extended source at lower (**B**) and higher (**D**) light intensities.

I also performed current injection in a red-positive opponent receptor. Even though some responses changed in polarity in the blue (*asterisks*) when the membrane was hyperpolarized about 25 mV below its resting potential, the fast on-set hyperpolarization was not successfully cancelled (Figure 5-17). This indicated that the antagonistic interaction is mainly from the blue receptors. However, two groups of cells might be involved in the process; those are the blue-sensitive cells within the same ommatidium and those in the neighboring ommatidia. The failure of clamping the fast on-set hyperpolarization indicates that the recording site was probably far from the synapses with blue receptors within the same ommatidium. Instead, the slow hyperpolarization, which may be a product of interommatidial interactions, was clamped successfully, indicating that the recording site might be closer to the synapses with receptors in neighboring cartridges.

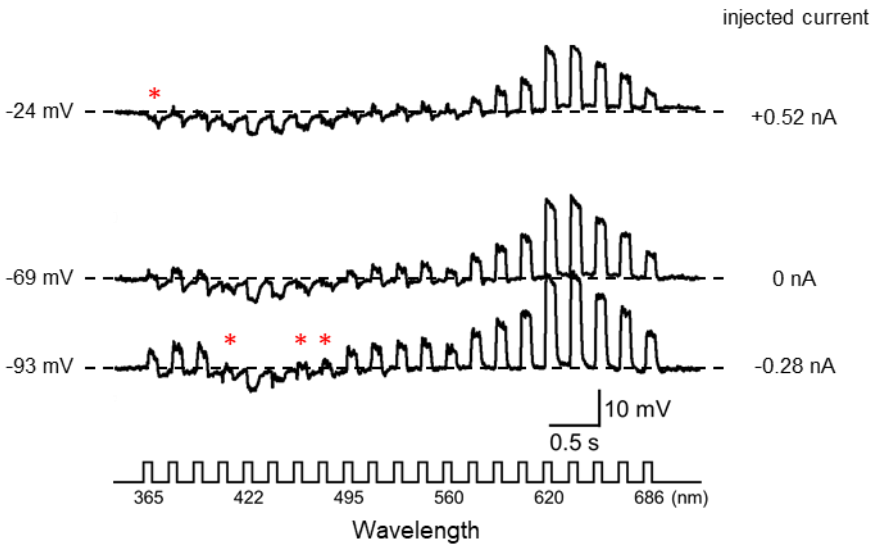


**Figure 5-17. Responses of a B-/R+ receptor to current injection.** The cell was stimulated with 100 ms isoquantal spectral pulses along with +0.52 nA (top trace), none (middle trace), and -0.28 nA (bottom trace) injection. *Asterisks* indicate the polarity of responses was reversed during depolarizing or hyperpolarizing current injection.

**Broadband-positive opponent receptors**

All cells in this spectral class (14 units) had obvious hyperpolarization below 375 nm and depolarized to a broad wavelength range with peaks in the blue (420–480 nm) and red (620–640 nm) (Figure 5-18). I have recorded UV-/BB+ receptors by using the LED array (8 units) and the IF series (5 units). The profiles of spectral responses were not significantly different between two stimulating methods.

The broad spectral response profile is similar to the *Papilio* broadband receptor, which has a spectral sensitivity covering almost the whole visible wavelength range except the UV (Arikawa, 2003). The origin of the broadband-positive opponent receptors that were recorded in the lamina is most likely the broadband receptor that has been demonstrated in type II ommatidia in the *Papilio* retina (Arikawa, 2003). The broadband receptor has features of a very broadband spectral sensitivity and virtually no sensitivity in the UV wavelength region, which are the results of coexpression of a green (PxL2) and a red (PxL3) visual pigment (Arikawa et al., 2003) and the filtering effect by the UV-absorbing fluorescent pigments in type II ommatidia (Arikawa et al., 1999b). Since the low UV sensitivity is combined with the antagonistic interactions in the lamina, the hyperpolarization in the UV is readily observed. In fact, the UV-/BB+ receptors are the second most frequently encountered class of spectrally opponent receptors during the recording.

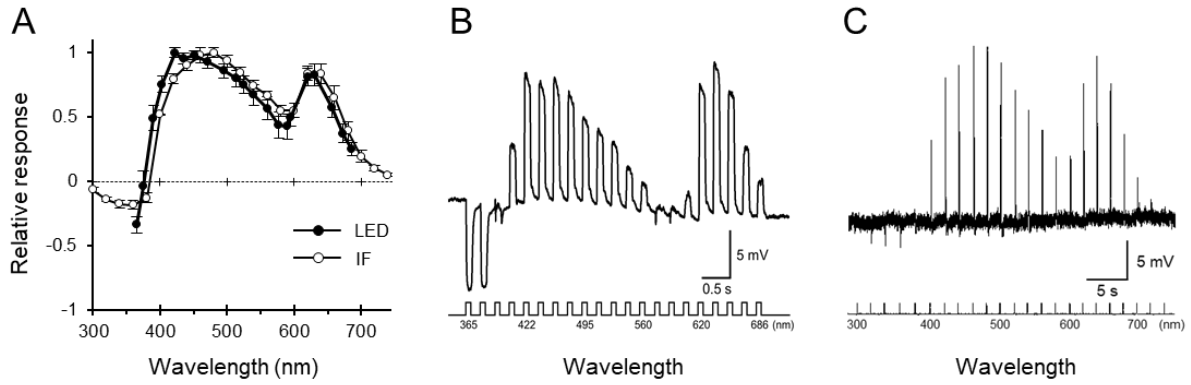


**Figure 5-18. Spectral responses of broadband-positive opponent photoreceptors in the lamina.** (**A**) Averaged spectral response curves (mean ± SEM) of UV-/BB+ receptors that measured by the LED array (LED, *solid circles*; $\lambda_{max,positive}$ = 422 nm, $\lambda_{max,negative}$ = 365 nm; *N*=8) and the IF series (IF, *open circles*; $\lambda_{max,positive}$ = 480 nm, $\lambda_{max,negative}$ = 360 nm; *N*=6). Membrane potential traces of a UV-/BB+ receptor upon isoquantal spectral stimulation with 100 ms pulses from the LED array (**B**) and with 30 ms pulses from the IF series (**C**).

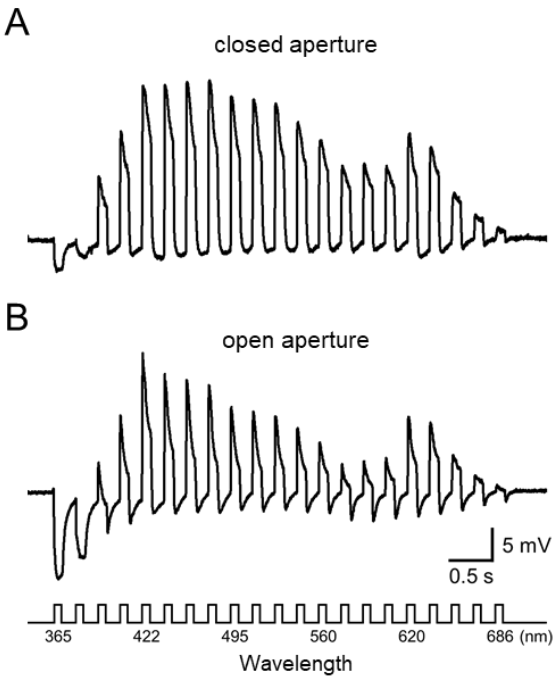


**Figure 5-19. Spectral response curves of an UV-/BB+ receptor toward a point source (A) and an extended source (B)**. Membrane potential traces upon isoquantal spectral stimulation with 100 ms pulses from the LED array.

When switching a point source to an extended stimulus, the antagonistic interactions in the UV and the slow hyperpolarizing potentials that followed depolarization at other wavelengths significantly increased (Figure 5-19). Since all photoreceptors in type II ommatidia have little sensitivity in the UV, the origin of strong UV inhibition cannot reside in the same ommatidium. Most likely, the antagonism in the UV-/BB+ receptor is due to interommatidial interactions with any kind of UV-sensitive photoreceptors, e.g. UV, blue, dual-peaked green, and red receptors, but most probably from the dual-peaked green receptors. The UV-/BB+ opponent receptor has only two main peaks at shorter (420–480 nm) and longer (620–640 nm) wavelengths, while the retinular broadband receptor has peaks at 480, 540, and 600 nm. Strong antagonism from dual-peaked green receptors can induce a suppression in the green spectrum. In fact, the 540 nm peak was suppressed, and the 480 nm and 600 nm peaks were pushed toward shorter and longer wavelength, respectively.

I have successfully performed current injection experiments in several UV-/BB+ receptors. The two cells shown in Figure 5-20 are examples of variation. By applying negative and positive currents, the depolarized responses of both cells were increased and decreased, respectively. The phenomenon might be attributed to changes in the strengths of antagonistic interactions by changing the $Cl^-$ driving force. This indicated that their synaptic connections with photoreceptors that contributed to the antagonism in the blue, green, and red wavelengths

were probably quite closer to the recording sites. Both cells had hyperpolarization in the UV, but differed in changing response amplitudes by injecting currents. The hyperpolarized light-responses of a UV-/BB+ receptor were almost canceled when the membrane was hyperpolarized about 25 mV below its original resting potential (Figure 5-20A; *asterisks* in bottom trace). This suggested that the recording site was closer to the synaptic connections with photoreceptors that have strong UV sensitivities. In contrast, another UV-/BB+ receptor did not change significantly with current injection (Figure 5-20B), indicating that the recording site of this cell was probably far from those synaptic sites for UV antagonism.

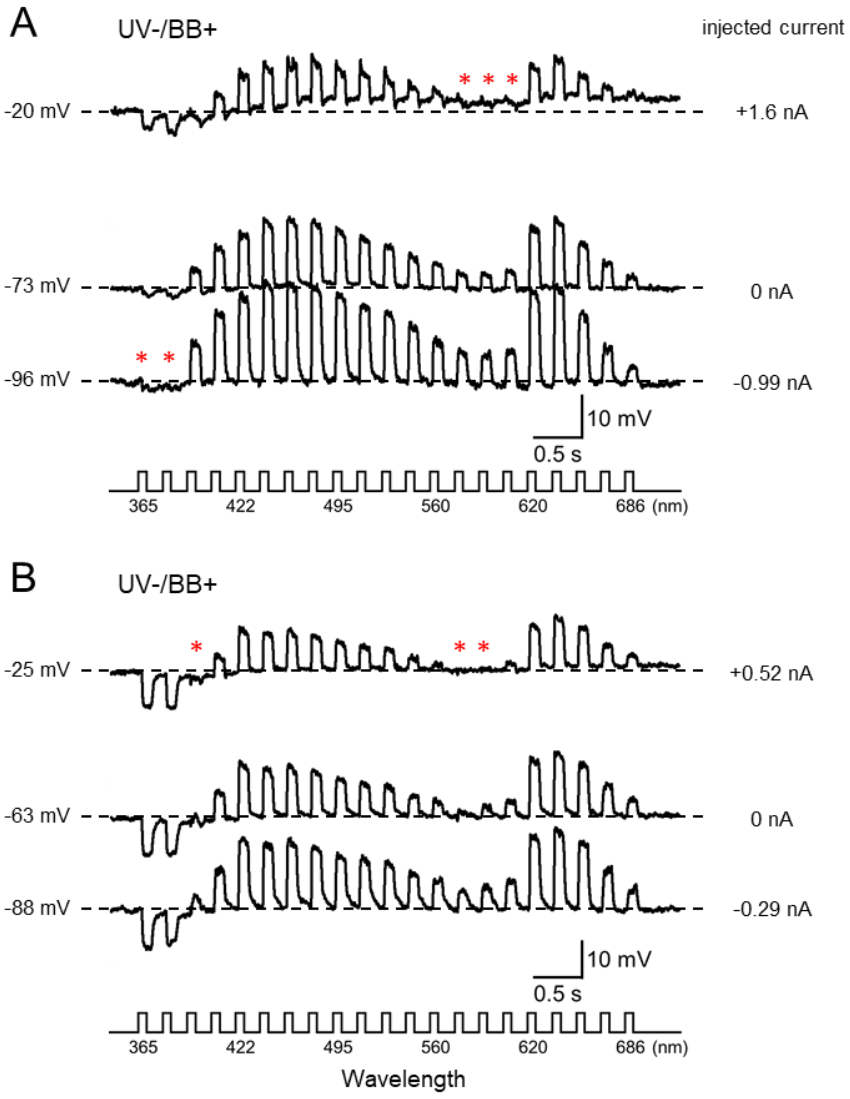


**Figure 5-20. Responses of UV-/BB+ receptors to current injection.** The cells were stimulated with 100 ms isoquantal spectral pulses along with positive (top trace), none (middle trace), and negative (bottom trace) injection. *Asterisks* indicate the polarity of responses was reversed during depolarizing or hyperpolarizing current injection. (**A**) The top and bottom traces demonstrated a UV-/BB+ receptor was depolarized with +1.6 nA and hyperpolarized with -0.99 nA, respectively. (**B**) Another UV-/BB+ receptor with +0.52 and -0.29 nA current injection.

***Modification and sharpening of photoreceptor spectral responses***

To check whether antagonistic hyperpolarization could modify and sharpen spectral responses of photoreceptors, I further compared the spectra between spectrally opponent photoreceptors and non-opponent photoreceptors (Figure 5-21). The spectral responses of non-opponent photoreceptors including eight receptor classes were obtained from 81 recordings in the retina. Their averaged spectral sensitivities (*black circles* in Supplementary Figure 5-S1) showed little variation from the published results (*white squares* in Supplementary Figure 5-S1; see also Figure 1-1A and Arikawa, 2003), suggesting the availability of recordings.

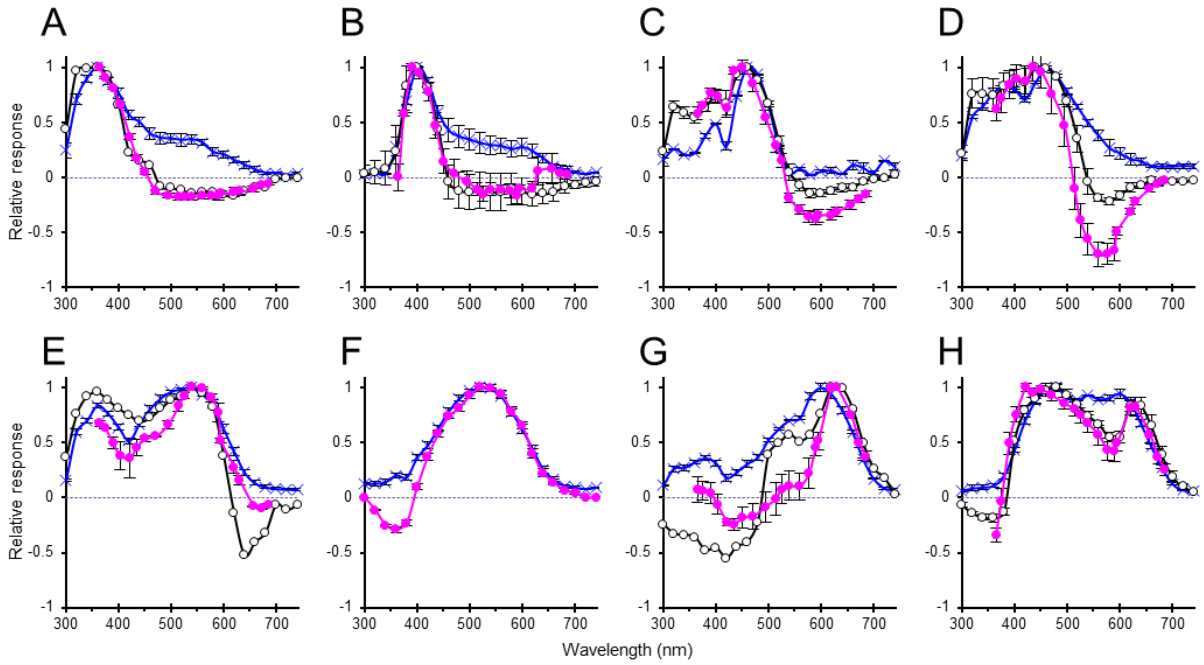


**Figure 5-21. Comparison of spectral responses between spectrally opponent and non-opponent photoreceptors.** Averaged spectral response curves (mean ± SEM) of non-opponent photoreceptors recorded by the IF series in the retina (*blue lines with crosses* (×)) as well as spectrally opponent photoreceptors recorded by the the IF series(*black lines with hollow circles* (○)) and the LED array in the lamina (*magenta lines with solid circles* (●)). (**A**) UV receptor (*N*=11) and UV+/G- receptor (*N*=6). (**B**) V receptor (*N*=6) and V+/G- receptor (*N*=4). (**C**) nB receptor (*N*=3) and B+/R- receptor (*N*=13). (**D**) wB receptor (*N*=8) and B+/G- receptor (*N*=5). (**E**) dG receptor (*N*=34) and dG+/R- receptor (*N*=2). (**F**) sG receptor (*N*=7) and UV-/sG+ receptor (*N*=1). (**G**) R receptor (*N*=11) and B-/R+ receptor (*N*=5). (**H**) BB receptor (*N*=8) and UV-/BB+ receptor (*N*=8). *wB*, wide blue; *BB*, broadband; *dG*, dual-peaked green; *nB*, narrow blue; *R*, red; *sG*, single-peaked green; *UV*, ultraviolet; *V*, violet.

In this study, I have recorded eight classes of spectrally opponent photoreceptors in the lamina. Figure 5-21 compares their spectral responses (*black and magenta lines with circles*) with the putative corresponding classes of non-opponent photoreceptors (*blue lines with crosses*). The modification and sharpening of photoreceptor spectral responses were observed.

For example, the spectral responses in the spectrally opponent photoreceptors B+/G- and B-/R+ were clearly narrower than the wide blue (wB) and red (R) receptors, respectively (Figure 5-21D,F). The original UV, violet (V) and narrow blue (nB) receptors extended a plateau shoulder at long wavelength ranges (*blue lines* in Figure 5-21A–C). Those shoulder were absent and spectral responses became negative in spectrally opponent photoreceptors (*black and magenta lines* in Figure 5-21A–C), which might enhance the contrast of spectral signals. The sharpening in the main response profiles seemed to be weaker in the dual-peaked green (dG), single-peaked green (sG) and broadband (BB) receptors (Figure 5-21E,F,H). Even though, the sharpening effect still could be observed in the long wavelength above 650 in the dG+/R- receptor (Figure 5-21E) as well as in the short wavelength below 380 nm in the UV-/BB+ receptor (Figure 5-21F) and the UV-/BB+ receptor (Figure 5-21H). Moreover, a suppression of spectral responses between 450 nm to 600 nm in the UV-/BB+ receptor (Figure 5-21H) indicated the modification effect.

***Spectrally opponent lvfs in the medulla***

I have tried to record spectrally opponent photoreceptors in the medulla. I made a hole on the cornea a little closer to the head than that for in the lamina recording. I encountered many cells that had spikes during recording, indicating that the electrode was inserted into the medulla. I specifically focused my attention to the cells showing graded depolarizing responses in response to light: these cells were assumed to be long visual fibers (lvfs). Surprisingly, spectral opponency was observed in all recorded lvfs in the medulla. Moreover, all cells depolarized at short wavelength and hyperpolarized at long wavelength. Three classes of spectrally opponent lvfs (i.e. UV, violet, and blue lvfs) have been identified based on their depolarizing peak wavelengths.

Note that the recordings of the lvfs in the medulla were near the distal layer of medulla. The recoded opponent responses were most likely derived from the lamina rather than the medulla. According to the immunolocalization of PxHCLB in the medulla, the antagonistic interaction between the photoreceptors can only happen in the medulla layer 4 where the PxHCLB channels are expressed. Therefore, although I recorded the lvfs in the medulla, the antagonistic interaction was probably performed in the lamina and passed along the axons to the medulla.

Here I briefly summarize the common features that are shared by the recorded lvfs in the medulla; in fact, many of them are quite different to the spectrally opponent receptors in the lamina. First, the depolarization followed by a slow hyperpolarized response was more clearly seen in the medulla. The evidently slow hyperpolarization indicates that these lvfs receive strong interommatidial interactions from the photoreceptors across neighboring ommatidia. Anatomical studies in inter-photoreceptor connections in the *Papilio* lamina have revealed numerous synapses between cells of different cartridges (Takemura and Arikawa, 2006). The photoreceptors R1 and R2 start receiving inputs from the other photoreceptors in the lamina and these inputs may be accumulated during the passage of R1 and R2 axons to the medulla. As a result, the slow hyperpolarization of lvfs is evident in the medulla.

Second, the amplitude of antagonistic interaction was higher in the medulla (about 50% relative to depolarization) than in the lamina (about 10-30% relative to depolarization). This could be explained by the accumulation of antagonistic interactions in the direction distal to proximal. Third, the maximal amplitudes of depolarized responses recorded in medulla lvfs were about 5 mV, which is much smaller than in the spectrally opponent photoreceptors in the

lamina. Moreover, the depolarized responses of medulla lvfs saturated at lower light intensity. Responses usually had no significant differences neither between a point source and extended stimuli nor changes in light intensities. Further details of each spectral class of lvfs are described below.

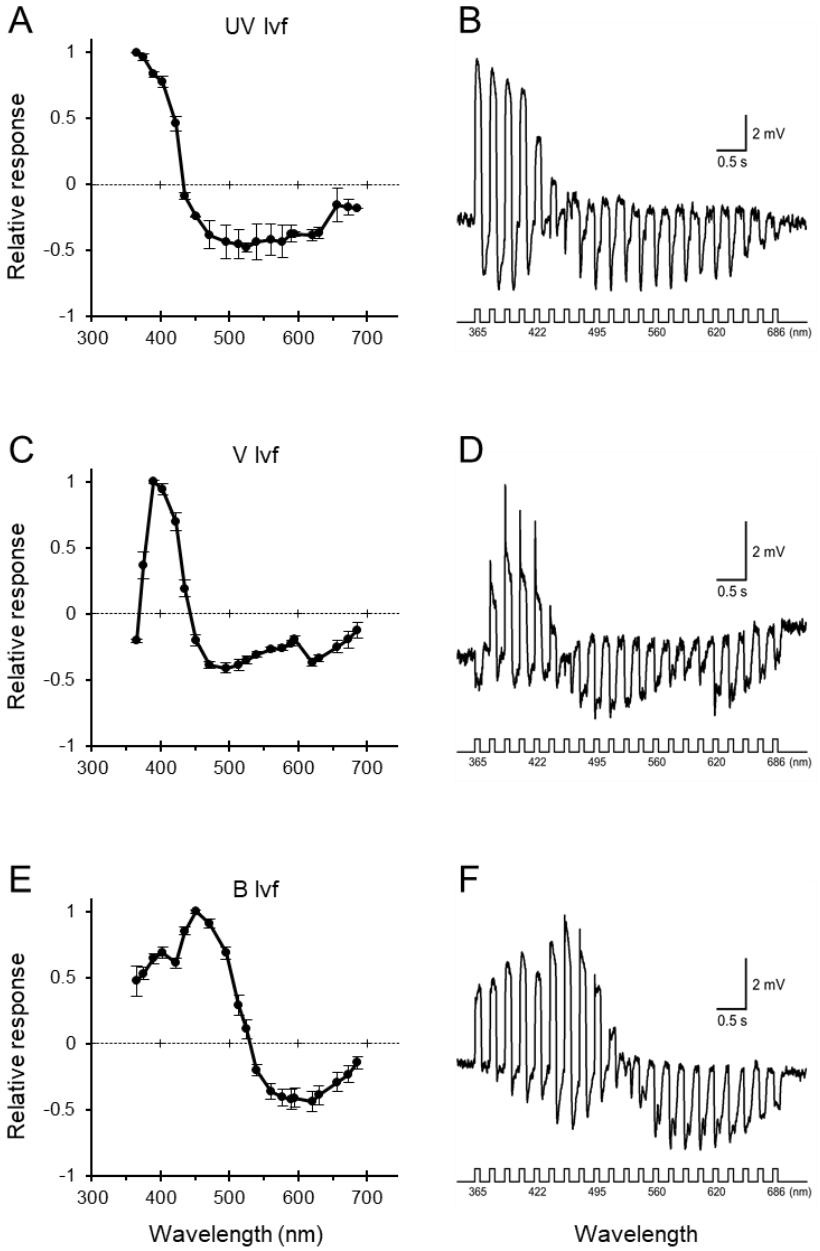


**Figure 5-22. Spectral responses of long visual fibers (lvfs) in the medulla.** Averaged spectral response curves (mean ± SEM) of UV-positive lvfs (**A**; $\lambda_{max,positive}$ = 365 nm, $\lambda_{max,negative}$ = 525 nm; *N*=2), violet-positive lvfs (**C**; $\lambda_{max,positive}$ = 390 nm, $\lambda_{max,negative}$ = 495 nm; *N*=3) and blue-positive lvfs (**E**; $\lambda_{max,positive}$ = 451 nm, $\lambda_{max,negative}$ = 620 nm; *N*=6). Membrane potential traces of an UV-positive lvf (**B**), a violet-positive lvf (**D**) and a blue-positive lvf (**F**) upon isoquantal spectral stimulation with 100 ms pulses from the LED array.

### UV-positive lvfs

The UV-positive lvfs (2 units) had maximal depolarization at 365 nm with hyperpolarization between 435 to 630 nm (Figure 5-22). The spectral response of UV lvfs recorded in the medulla showed a high similarity to that of UV+/G- receptors recorded in the lamina.

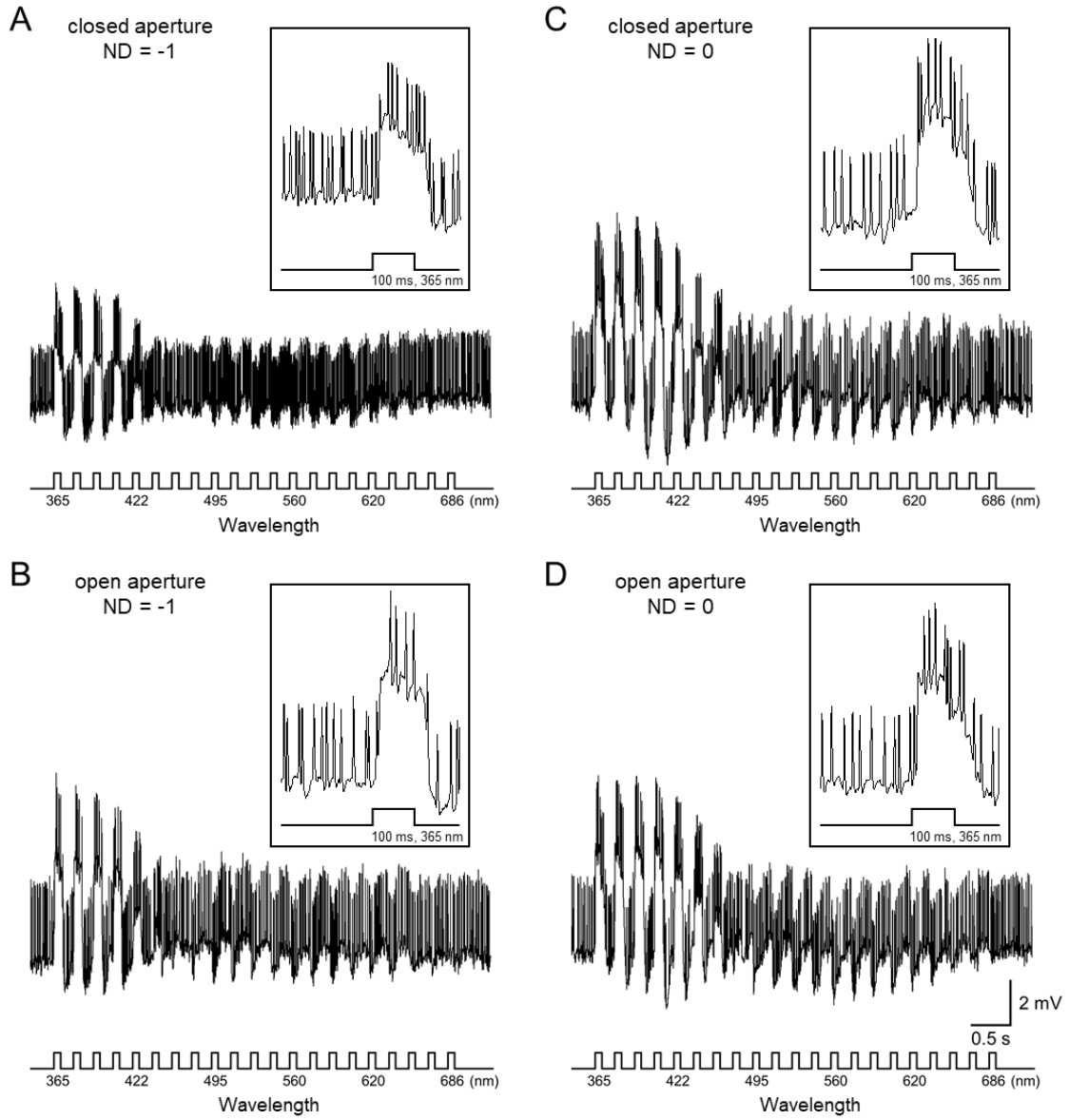


**Figure 5-23. Spectral response curves of a violet-positive lvf toward different stimulating conditions.** Membrane potential traces upon isoquantal spectral stimulation with 100 ms pulses from the LED array. Spectral response curves of a violet-positive lvf in the medulla to a point source at lower (**A**) and higher (**C**, 10-fold brighter) light intensities as well as an extended source at lower (**B**) and higher (**D**) light intensities. *Insets* in each panel illustrate an expanded time scale of the beginning of each trace including a partial resting potential and the first response to a 100 ms pulse at 365 nm.

One recorded UV lvf showed spikes superimposed on the baseline of the membrane potential (Figure 5-23), which could be seen in the medulla sometimes. Using dimmer light intensity (ND = -1), the extended stimuli brought a proportional increase in amplitudes of both depolarized and hyperpolarized responses. Another notable change is the reduction of spiking frequency. The spiking properties in lvfs were not studied further. Elucidation of the relationship between spiking frequency and light intensity in lvfs deserves further analysis.

The spectral responses were slightly modulated when stimulated with 10-fold brighter light. The depolarized responses in the blue increased at higher intensity, while the response amplitude of maximal depolarization in the UV did not increase, presumably due to saturation. On the other hand, no significant difference occurred between the extended and the point source in the spectral responses and spiking frequency.

**Violet-positive lvfs**

The violet-positive lvfs (3 units) had maximal depolarization at 390 nm with hyperpolarization below 365 nm and beyond 451 nm. The hyperpolarization in the UV resulted in a sharp cut-off at shorter wavelengths, which has also been observed in some V+/G- receptors in the lamina. Due to greater antagonistic interactions, the spectral response curves of medulla violet lvfs is much narrower compared to that of the lamina V+/G- receptors. The hyperpolarization at longer wavelength had two peaks at 495 nm and 620 nm corresponding to the broadband receptors. Both the violet receptor and the broadband receptor are identified in type II ommatidia (Arikawa, 2003), and thus the antagonism in violet lvfs from broadband receptors might happen within a single ommatidium at the lamina level. In fact, the lamina V+/G- receptors have been assumed to receive the inter-photoreceptor inputs mainly within the same ommatidium as an example given above.

One violet lvf showed unique characteristics (Figure 5-24). The cell showed a typical spectral response to a dimmer light stimulation (ND = -1) with depolarizing responses less than 6 mV. When giving stronger light intensity (ND = 0), the response amplitudes of both depolarization and hyperpolarization increased, while an action potential-like response was elicited at the peak wavelength 390 nm. The depolarizing response shot up to 18 mV, which was three times larger than the maximal depolarization at lower intensity. Such phenomenon has never been reported in any insect photoreceptor. The mechanism underlying the action

potential-like spurt is fully unknown, but is most likely mediated by voltage gated ion channel(s). The action potential-like spurt at a certain wavelength could function efficiently to sharpen the spectral sensitivity.

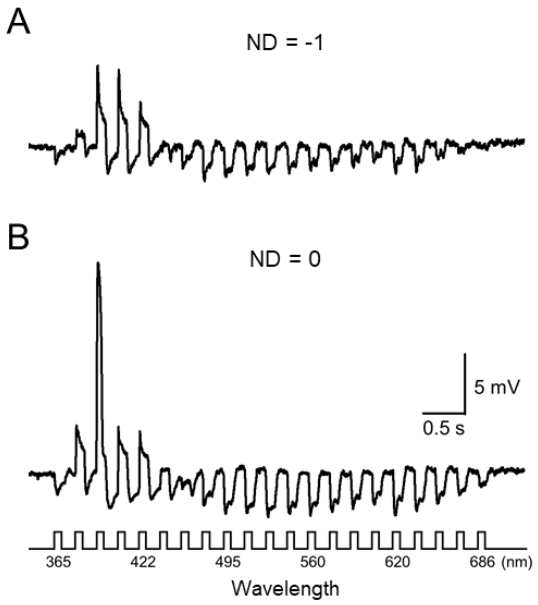


**Figure 5-24. Spectral response curves of a violet-positive lvf toward an extended source at lower (A) and higher (B, 10-fold brighter) light intensities**. Membrane potential traces upon isoquantal spectral stimulation with 100 ms pulses from the LED array. The response at 390 nm shot up when stronger light was given.

**Blue-positive lvfs**

I had recorded 6 blue-positive lvfs that had maximal depolarization at 451 nm with hyperpolarization beyond 530 nm (Figure 5-22). The blue lvf is the most frequently encountered spectral class over all spectrally opponent receptors in the *Papilio* medulla. Its spectral response highly resembles that of the B+/R- receptor, the most frequently encountered spectral class in the lamina.

An example of a V-log I function in a blue lvf is shown in Figure 5-25. Both depolarizing and hyperpolarizing responses increased their amplitudes proportionally to light intensity. The cell showed an evident spike superimposed on the rising phase of the depolarization at higher intensity. Note these initial spikes shot up to a constant potential when light intensity was above a certain level (ND > -0.9) as action potential-like responses. In fact, I have observed the action potential-like spike in many lvfs also in other spectral classes. It is probably a common feature in lvfs. However, its origin still awaits further analysis.

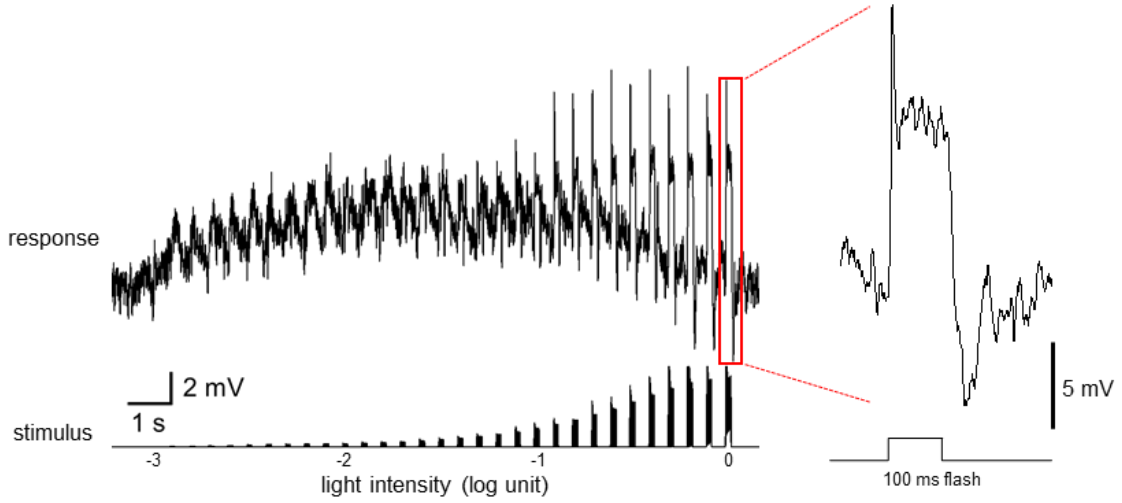


**Figure 5-25. Responses of a blue-positive lvf upon 100 ms white light pulses with a graded series (in 0.1 log intensity steps)**. *Right*, an enlarged time scale of the trace to the last stimulus.

I also tried to clamp the lvfs in the medulla and here I show an example in a blue lvf (Figure 5-26). The hyperpolarizing light-responses have never been canceled successfully in any lvfs by injecting currents. It suggests that the inter-photoreceptor synapses that contributed to antagonistic interactions were presumably in the lamina and hence too distant from the recording site in the medulla.

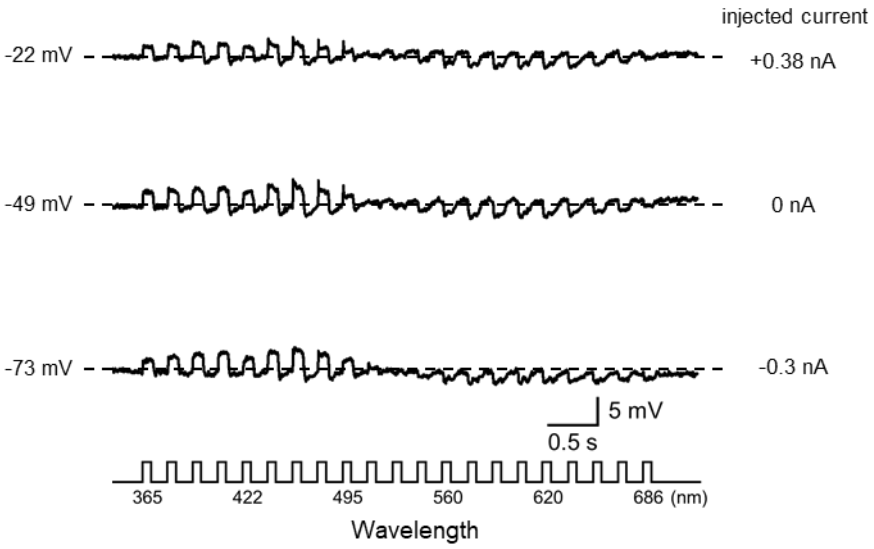


**Figure 5-26. Responses of a blue-positive lvf to current injection.** The cell was stimulated with 100 ms isoquantal spectral pulses along with +0.38 nA (top trace), none (middle trace), and -0.3 nA (bottom trace) injection.

***Comparison spectrally opponent photoreceptors with model prediction***

The antagonistic interaction between photoreceptors through histaminergic channels PxHCLB has been proposed to account for the mechanism of photoreceptor spectral opponency (Chen et al., 2019). The *Papilio* eyes bear three spectrally heterogeneous types of ommatidia each housing nine photoreceptor cells in one of three fixed combinations (Arikawa, 2003). Types I, II, and III ommatidia are furnished with four (UV, nB, dG, R), three (V, sG, BB), and two (bB, dG) receptor classes, respectively. Based on the depolarizing and hyperpolarizing peak wavelengths of spectrally opponent photoreceptors, along with the putative synaptic interactions between the spectral receptors in its ommatidium, I assumed eight classes of spectrally opponent photoreceptors are originated from the eight spectrally heterogeneous photoreceptors (Figure 5-21): UV+/G- (UV receptor), V+/G- (violet receptor), nB+/R- (narrow blue receptor), wB+/G- (wide blue receptor), dG+/R- (dual-peaked green receptor), UV-/sG+ (single-peaked green receptor), B-/R+ (red receptor), and UV-/BB+ (broadband receptor). To check the assumption, I constructed a simulation model to reproduce spectrally opponent photoreceptors. Moreover, the model may provide a hint that how many classes of spectrally opponent photoreceptors exist to make sure any possible opponent photoreceptor is missing from the present recording.

In this study, the spectral responses of spectrally opponent photoreceptors were obtained by stimulating upon a point source. Therefore, the antagonistic interaction between the spectral receptors may be limited within a single ommatidium. In the case of the origin of the antagonism is restricted to photoreceptors in its own ommatidium, the predicted spectral response of the post-synaptic photoreceptor is given as follows:

$$S_i(\lambda) = R_i(\lambda) - \sum_{j=1}^{j=8} R_j(\lambda) \times \log_{10}\left(N_{syn(i,j)} + 1\right) \times \alpha \qquad (5.1)$$

where $S_i$ is the spectral response of the post-synaptic photoreceptor *i* ($P_i$; *i*=1–8) at the terminal, i.e. lamina and medulla, after the interaction with other seven pre-synaptic photoreceptors *j* ($P_j$; *j*=1–8). The photoreceptor R9 is ignored in the present model calculations because its spectral property is uncertain. $R_i(\lambda)$ and $R_j(\lambda)$ are the original spectral response of the post-synaptic photoreceptor *i* and pre-synaptic photoreceptor *j*, respectively, in the retina. $N_{syn(i,j)}$ is the number of histaminergic synapses from pre-synaptic photoreceptor $P_j$ to post-synaptic photoreceptor $P_i$. The constant $\alpha$ indicates the gain of the antagonistic interaction from pre-

synaptic photoreceptors $P_j$ in the same ommatidium.

The averaged spectral responses of eight spectral receptors that recorded in the *Papilio* retina were used in the model calculations (Figure 5-21). To calculate the derivatives of the original photoreceptor spectral responses $R_i(\lambda)$ and $R_j(\lambda)$, the spectra were approximated as sum of Gaussian functions:

$$R_i(\lambda) = A_i exp\left(-\frac{\left(\lambda-\lambda_i^0\right)^2}{2\delta_i^2}\right) + B_i exp\left(-\frac{\left(\lambda-\lambda_i^1\right)^2}{2\sigma_i^2}\right) + C_i exp\left(-\frac{\left(\lambda-\lambda_i^2\right)^2}{2\omega_i^2}\right) \quad (5.2a)$$

and

$$R_j(\lambda) = A_j exp\left(-\frac{\left(\lambda-\lambda_j^0\right)^2}{2\delta_j^2}\right) + B_j exp\left(-\frac{\left(\lambda-\lambda_j^1\right)^2}{2\sigma_j^2}\right) + C_j exp\left(-\frac{\left(\lambda-\lambda_j^2\right)^2}{2\omega_j^2}\right) \quad (5.2b)$$

where $A_i$ $(A_j)$, $B_i$ $(B_j)$, $C_i$ $(C_j)$, $\lambda_i^0$ $(\lambda_j^0)$, $\delta_i$ $(\delta_j)$, $\lambda_i^1$ $(\lambda_j^1)$, $\sigma_i$ $(\sigma_j)$, $\lambda_i^2$ $(\lambda_j^2)$, and $\omega_i$ $(\omega_j)$ are parameters (see Supplementary Table 5-S1) whose values were adjusted to provide a best fit of measured spectral responses of photoreceptors in the retina. Supplementary Figure 5-S2 reveals that the equation (5.2) reasonably well approximates the recorded spectral responses of photoreceptors.

To make the model as simple as possible, I assumed that numbers of synapses between different spectral receptors are similar and thus $N_{syn(i,j)}$ to 20 for all photoreceptors. Under this condition, the model calculations provide the best fit to the spectral responses of most spectrally opponent photoreceptors when the constant $\alpha$ is set to 0.08 (*green dashed lines* in Figure 5-27). Based on each receptor's regionalization and specific sets of inter-photoreceptor interactions, nine and three possible results were predicted in the lamina (Figure 5-27A–I) and medulla (Figure 5-27J–L). The model prediction in generally provided reasonable fits to my recordings. Regarding simulation model in the lamina, eight possible opponent photoreceptors are supposed and one originated from the R3–R8 dG receptor in type III ommatidia do not show hyperpolarization at any wavelength (Figure 5-27I).

The model calculations successfully reproduced the response profiles of spectrally opponent photoreceptors in the medulla in particular including UV, violet and blue lvfs (Figure 5-27J–L). In comparison, in the lamina, the model prediction in the antagonistic interaction was too strong for these photoreceptor axons, i.e. UV+/G-, V+/G- and B+/G- receptors (Figure 5-27A,B,E), except for the B+/G- receptor (Figure 5-27H). It suggests that the antagonistic inputs are accumulated passing along the lvf axons toward the medulla.

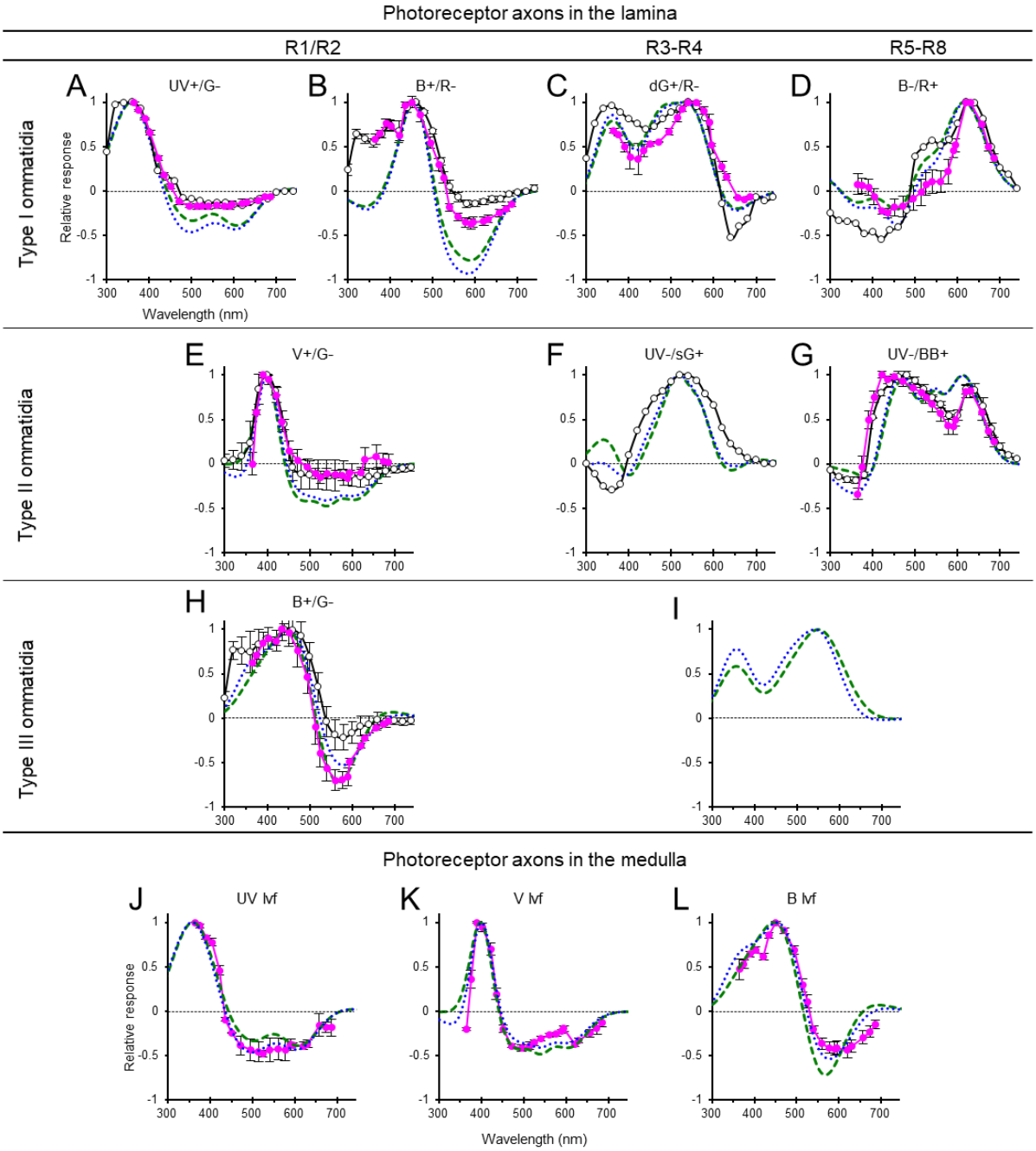


**Figure 5-27. Comparison of spectral responses of spectrally opponent photoreceptors with model predictions.** The averaged spectral response curves (mean ± SEM) of spectrally opponent photoreceptors recorded by the IF series (*black solid lines*) and the LED array (*magenta solid lines*) in the lamina (**A**–**I**) and medulla (**J**–**L**). The *green dashed lines* and *blue dotted lines* indicate model calculations that without and with the consideration of inter-cartridge interactions. (**A**) UV+/G- receptor (*N*=1 by the IF series/*N*=6 by the LDE array) and model calculations of R1/R2 UV receptors in type I ommatidia. (**B**) B+/R- receptor (*N*=4/13) and model calculations of R1/R2 narrow blue receptors in type I ommatidia. (**C**) dG+/R- receptor (*N*=1/2) and model calculations of R3–R4 dual-peaked green receptors in type I ommatidia. (**D**) B-/R+ receptor (*N*=1/5) and model calculations of R5–R8 red receptors in type I ommatidia. (**E**) V+/G- receptor (*N*=3/4) and model calculations of R1/R2 violet receptors in type II ommatidia. (**F**) UV-/sG+ receptor (*N*=1/0) and model calculations of R3–R4 single-peak green receptors in type II ommatidia. (**G**) UV-/BB+ receptor (*N*=6/8) and model calculations of R5–R8 broadband receptors in type II ommatidia. (**H**) B+/G- receptor (*N*=2/5) and model calculations of R1/R2 wide blue receptors in type III ommatidia.

(continued on the next page)

Notably, the blue lvfs had two possible origins: one is from narrow blue (nB) receptors in type I ommatidia and another one is from wide blue receptors (wB) in type III ommatidia. In other words, the averaged spectral response of the blue lvf possibly included both B+/R- and B+/G- receptors. However, I found that all blue-positive opponent photoreceptors, i.e., B+/R- and B+/G- receptors as well as blue lvfs, in fact had better fits to the model calculation for wB receptor. I therefore fit blue lvfs with the model for the wB receptor (Figure 5-27L), instead of the nB receptor. This could explain why the maximal hyperpolarization of the blue lvfs peaked at longer wavelength range than the model.

Comparing my recordings with the model, the depolarizing response profile of the B-/R+ receptor is much narrower than the prediction (Figure 5-27D). Moreover, the strong antagonistic interaction in the UV-/BB+ receptor was observed from a significant suppression of spectral responses around 600 nm (Figure 5-27G). In addition, the recording data and the model showed a poor match of the response profiles in the violet wavelength and a shift of the peak wavelength. I assumed that the proximal photoreceptors R5–R8 may receive stronger antagonistic inputs than the prediction from the present model.

The response profile of the recorded UV-/sG+ receptor is broader than the model prediction (Figure 5-27F). In addition, the model supposed that there might have hyperpolarization in the wavelength around 400 nm and 620 nm which may be attributed to the antagonistic inputs from violet (V) and broadband (BB) receptors, respectively. However, I only observed the hyperpolarized response in the UV wavelength. Regarding the model, the hyperpolarization in the red wavelength is relatively weak and only appears in small wavelength ranges. Such weak hyperpolarization probably could be observed only in photoreceptor terminals in the proximal lamina.

The model calculations could also reproduce the weak hyperpolarization in the long wavelength for dG+/R- receptors (Figure 5-27C) as well as in the UV wavelength for UV-/BB+ receptors (Figure 5-27G). However, the model calculations I applied did not reproduce hyperpolarization in the UV wavelength for V+/G- receptors (Figure 5-27E) and violet lvfs in the medulla (Figure 5-27K). Moreover, the recorded hyperpolarization in UV-/BB+ receptors was stronger than the model. It implies the model is incomplete.

(**I**) Model calculations of R3–8 dual-peak green receptors in type III ommatidia. (**J**) UV lvf (*N*=0/2) and model calculations of R1/R2 UV receptors. (**K**) Violet lvf (*N*=0/3) and model calculations of R1/R2 violet receptors. (**L**) Blue lvf (*N*=0/6) and model calculations of R1/R2 wide blue receptors.

Theoretically, the point light source that I used to record spectral responses of cells is supposed to stimulate only a single ommatidium since its angle is smaller than the acceptance angle of a single ommatidium of *Papilio xuthus* (Shibasaki et al., 2006). However, the visual fields of adjacent ommatidia overlap partially. I therefore extended the model by including a partial of antagonistic inputs through synapses between photoreceptors of different cartridges. The predicted spectral response of the post-synaptic photoreceptor is given as follows:

$$S_i(\lambda) = R_i(\lambda) - \sum_{j=1}^{j=8} R_j(\lambda) \times \log_{10}\left(N_{syn(i,j)} + 1\right) \times \alpha - \sum_{k=1}^{k=8} R_k(\lambda) \times \log_{10}\left(N_{syn(i,k)} + 1\right) \times \beta \times 3 - \sum_{l=1}^{l=8} R_l(\lambda) \times \log_{10}\left(N_{syn(i,l)} + 1\right) \times \beta \times 1.5 - \sum_{m=1}^{m=8} R_m(\lambda) \times \log_{10}\left(N_{syn(i,m)} + 1\right) \times \beta \times 1.5 \quad (5.3)$$

where $R_k(\lambda)$, $R_l(\lambda)$ and $R_m(\lambda)$ are the spectral responses of the pre-synaptic photoreceptors $k$ ($P_k$), $l$ ($P_l$) and $m$ ($P_m$) in the adjacent ommatidia types I, II and III, respectively. $N_{syn(i,k)}$, $N_{syn(i,l)}$ and $N_{syn(i,m)}$ are the numbers of histaminergic synapses from the pre-synaptic photoreceptors $P_k$, $P_l$ and $P_m$, respectively, to the post-synaptic photoreceptor $P_i$. The constant $\beta$ indicates the gain of the antagonistic interaction from pre-synaptic photoreceptors that located in the adjacent ommatidia. Supposed that the adjacent ommatidia do not receive full stimulation and thus only partial photoreceptors are active, $\beta$ is set to 0.01 which is a fifth as the gain in the central ommatidium.

The connectivity between cartridges depends on both their ommatidial types (Matsushita et al., in preparation). The inter-photoreceptor connections in neighboring cartridges of the same ommatidial type are much less than those of different ommatidial types. I thus used the following values in model calculations. Numbers of synapses between different spectral receptors are set to 20 for all photoreceptors in its own ommatidium ($N_{syn(i,j)}$) and 1 for photoreceptors in the adjacent same type of ommatidia and 5 for photoreceptors in the adjacent different types of ommatidia. On the other hand, since I used a point light as the light stimulation, here I supposed that the adjacent ommatidia only include the six immediate hexagonal neighbors that are either directly adjacent or end-to-end neighbors along the dorso-ventral axis. Based on the ratio of three ommatidial types in the *Papilio* eye (type I:II:III = 2:1:1) (Arikawa, 2003), theatrically, the numbers of ommatidial type I, II and III for the six surrounding ommatidia might be 3, 1.5 and 1.5, respectively.

In general, the new simulation model that included the partial inter-cartridge interaction (*blue dotted lines* in Figure 5-27) provide similar response profiles as the previous model that only the intra-cartridge interaction was considered (*magenta dashed curves* in Figure 5-27). The new model improved the fit slightly for the antagonistic interaction in the UV wavelengths for photoreceptors in the type II ommatidia, i.e. V+/G- receptor, UV-/BB+ receptor and violet lvfs (Figure 5-27E,G,K).

In sum, the model prediction suggests the "histamine hypothesis" that the antagonistic interaction from other spectral receptors in the same ommatidia plays a key role in photoreceptor spectral opponency (Chen et al., 2019). The assumption of the origin of these spectrally opponent photoreceptors is also supported.

## 5.5 Discussion

Previously, Takemura and Arikawa (2006) demonstrated that inter-photoreceptor contacts are in ommatidial type fixed combinations both within and between cartridges in the lamina of *Papilio xuthus*. The present electrophysiological results demonstrate that these anatomical connections are indeed functional. My intracellular recordings revealed that the *Papilio* lamina contains photoreceptors exhibiting spectral opponency of at least eight distinct spectrally opponent pathways (Figure 5-27). These can be divided into six spectral receptor classes based on the positive peak wavelengths: ultraviolet- (UV), violet- (V), blue- (B), green- (G), red- (R), and broadband- (BB) positive opponent receptors. The B and G classes each can be further divided into two subclasses according to the inhibition interaction at distinct wavelength ranges. On the other hand, all recordings in lvfs in the medulla exhibited spectral opponency which are divided into three corresponding to three spectral classes of lvfs. Figure 5-28 summarizes the modification example of the recorded spectral profiles of different spectral receptors.

***Mechanisms underlying antagonistic interactions***

The fast on-set hyperpolarization is a unique and crucial feature for the identification of opponent photoreceptors in this study (Figure 5-1). The characteristics of its time-course is shared with the on-transient hyperpolarization of the LMCs. Comparing the waveforms of the blowfly photoreceptor and LMC responses, the LMCs show a fast hyperpolarizing component upon the neurotransmitter released from the photoreceptors (Laughlin et al., 1987). The fast synaptic transmission is achieved by a histamine-gated chloride channel, HCLA, in the fly LMCs (Skingsley et al., 1995; Gengs et al., 2002; Pantazis et al., 2008; Kita et al., 2017). The opponent photoreceptors probably have a similar sign-inverting mechanism that involves direct synaptic interactions between the photoreceptors via histaminergic channels.

Using sharp microelectrode recording, I have shown that the responses of the opponent photoreceptors in the *Papilio* lamina could be reversed when the membrane potential was close to the equilibrium potential of chloride ions. Similar phenomenon has also been observed in the LMCs of the blowfly (Laughlin, 1981) and in *Papilio* as I presented in Chapter 4. The response of blowfly LMCs has a reversal potential that is about 35–40 mV negative to the resting potential, suggesting the activation of chloride conductance (Laughlin, 1981; Hardie et al., 1989). Taken together, the hyperpolarization in photoreceptors may be attributed to histaminergic chloride channels.

Recently, Schnaitmann et al. (2018) demonstrated that the terminals of lvfs mutually inhibit each other via a histamine-gated chloride channel, HCLB, leading to spectral opponency in the *Drosophila* medulla. My immunohistochemistry further provided anatomical supports that one of the *Papilio xuthus* histamine-gated chloride channels, PxHCLB, is expressed at the inter-photoreceptor synapses in the *Papilio* lamina and the medulla (Chen et al., 2019). Importantly, the immunolabeling of PxHCLB (Chen et al., 2019) along with the previously identified inter-photoreceptor connections in the *Papilio* lamina (Takemura and Arikawa, 2006) reasonably explains the recorded spectrally opponent photoreceptors, as will be discussed in detail in the section below.

***Origin of photoreceptor-level spectral opponency***

The anti-PxHCLB labeling shown in Figure 2-6C represents an inter-photoreceptor synapse between R1 and R5. *Papilio* butterflies have three types of ommatidia each comprising a different set of spectral receptors (Arikawa, 2003). Taking type I ommatidia as an example, photoreceptors R1 and R5 are respectively blue and red receptors. Let us suppose that the blue-sensitive R1 expresses PxHCLB at the synapse with the red-sensitive R5 within the same ommatidium. In this case, the blue-sensitive R1 would depolarize when the ommatidium is stimulated with 460 nm light, but when the stimulus is switched to 600 nm, the red-sensitive R5 depolarizes and releases histamine, which hyperpolarizes R1 via PxHCLB. As a result, the B+/R- opponent response is recorded from R1 blue-sensitive receptors (Figure 5-27B).

This explanation can also be applied in type I ommatidia for UV+/G- opponent receptors (Figure 5-27A), in type II ommatidia for V+/G- opponent receptors (Figure 5-27E) and in type III ommatidia for B+/G- opponent receptors (Figure 5-27H). Moreover, the anti-PxHCLB labeling was also detected on the membrane of photoreceptor R5 as shown in Figure 2-6C, suggesting that the antagonistic interaction can also act in the opposite direction. This leads to R5 receiving inhibitory inputs from R1. Under such interactions, photoreceptor R5 may be B-/R+ opponent receptors in type I ommatidia (Figure 5-27D), UV-/BB+ opponent receptors in type II ommatidia (Figure 5-27G) or B-/dG+ opponent receptors in type III ommatidia. However, I did not encounter any B-/dG+ opponent receptors during my recording, and in fact, the opponent responses seem to be absent in R3–R8 in type III ommatidia (Figure 5-27I) based on the simulation model. On the other hand, the model suggests that the R3–R4 may receive antagonistic inputs from other photoreceptors and may result in dG+/R- opponent receptors in type I ommatidia (Figure 5-27C) and UV-/sG+ in type II ommatidia (Figure 5-27F).

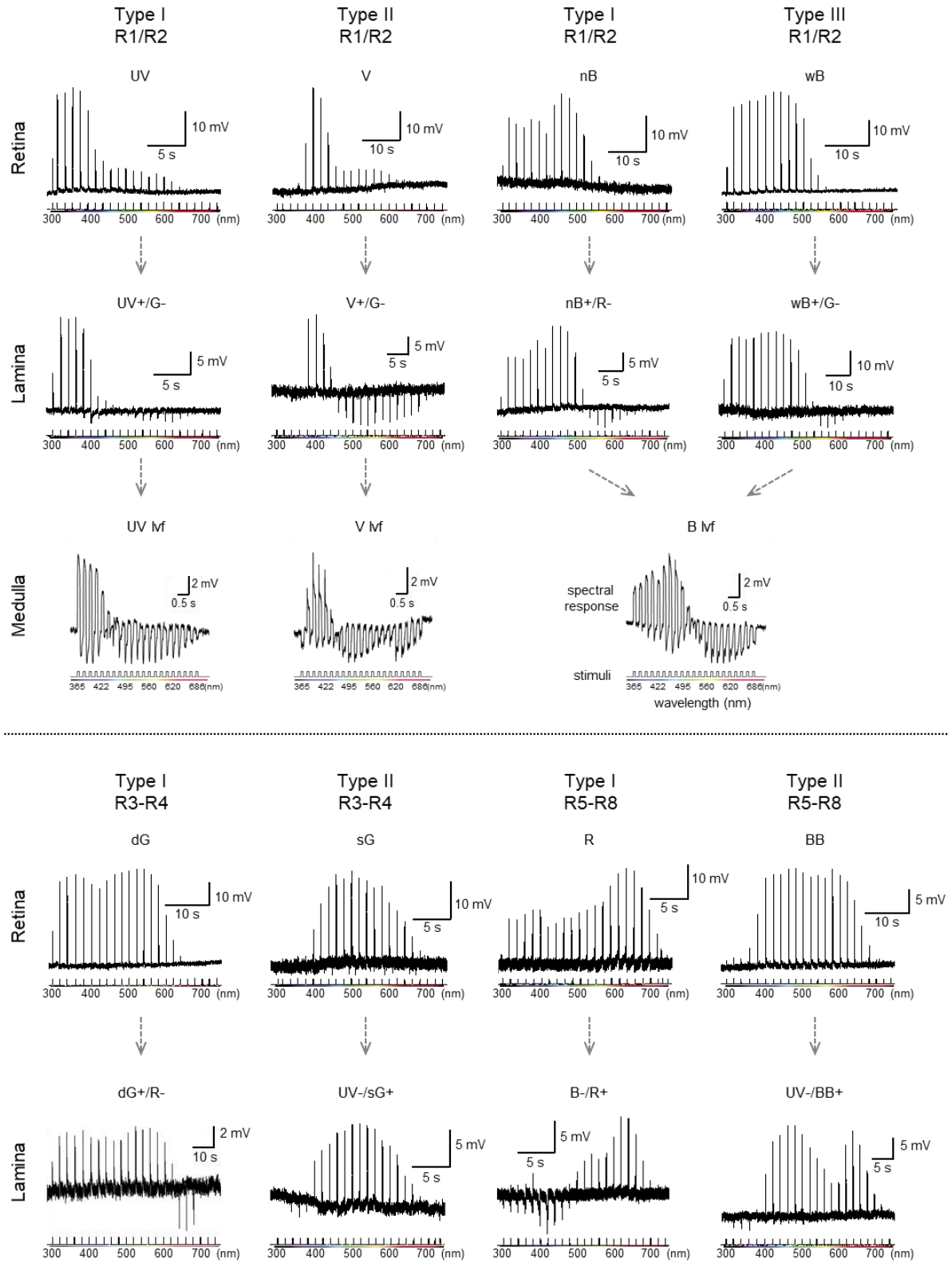


**Figure 5-28. Modification of photoreceptor spectral responses in the *Papilio* retina and optic lobe.** The top, middle and bottom rows in the upper panels are spectral responses of four lvfs recorded in the retina, lamina and medulla, respectively. The top and bottom rows in the bottom panels are spectral responses of four svfs recorded in the retina and medulla, respectively.

Regarding the simulation model, most classes of spectrally opponent receptors can be explained by the antagonistic interactions with other photoreceptors mainly within the same cartridge (*green dashed lines* in Figure 5-27). This has been suggested by the experiments (e.g. spectral scans with extended light source, comparing angular responses at positive- and negative-peak wavelengths, reversing response polarity by current injection) as I discussed in each classes of opponent receptors in the Result section. The cases of UV-/sG+ and UV-/BB+ opponent receptors (Figure 5-27F,G) indicate the simulation model was not complete: they show an example that inter-photoreceptor interaction can also happen between photoreceptors in neighboring ommatidia. Both UV-/sG+ and UV-/BB+ opponent receptors are most likely recorded from the broadband receptor in type II ommatidia. In the ventral eye, all receptors in type II ommatidia have little UV sensitivity due to the filtering effect of a UV-absorbing fluorescing pigment in the distal portion of the rhabdom (Arikawa et al., 1999b). The UV inhibition in UV-/sG+ and UV-/BB+ opponent receptors may be attributed to the inputs from receptors that contain UV sensitivity in type I and/or type III ommatidia. The simulation model considering antagonistic inputs from photoreceptors in neighboring cartridges (*blue dotted lines* in Figure 5-27) can better reproduce the hyperpolarization in the UV range for UV-/sG+ and UV-/BB+ opponent receptors. On the other hand, the current injection experiments showed difficulties in clamping membrane response in the UV range, indicating that the synaptic site was too far from the recording site, supporting the idea that the UV opponency was interommatidial. In fact, a thorough anatomy at the EM level has revealed that inter-cartridge connections are quite prominent between different ommatidial types (Matsushita et al., in preparation).

The inhibition via sign-inverting histaminergic channels between photoreceptors results in spectral opponency, which can be rather variable in terms of the amplitude and the wavelength. Anatomical analysis has revealed that inter-photoreceptor connections are abundant in the *Papilio* lamina (Takemura and Arikawa, 2006). Indeed, my electrophysiological recordings indicate that spectrally opponent photoreceptors were more frequently encountered in the lamina, where inter-photoreceptor synapses exist, than in the retina. About one quarter of photoreceptor axons in the lamina showed antagonistic hyperpolarization at specific wavelengths while the other three quarters of them were not. The variation among none, weak or strong hyperpolarizing responses implies the degree of antagonistic interactions from other photoreceptors. The antagonistic hyperpolarization seems to be cumulative, integrated on a receptor axon along its passage into the neuropils. In this sense,

the hyperpolarization may be more prominent in recording locations at the proximal lamina. This can also explain why all lvfs in the medulla showed prominent hyperpolarizing responses. The variation can also be observed in peak wavelengths. For example, some UV-/BB+ opponent receptors hyperpolarized at green wavelengths (Figures 5-18B, 5-20B) while some did not (Figures 5-18C, 5-20A). Some possible explanations are proposed as follows. First, the degree of opponency in the green could be inversely proportional to the distance between the recording electrode tip to the source of inhibition, i.e. the axonal membrane postsynaptic to the green-sensitive receptors. Second, although the interphotoreceptor contacts are mainly intraommatidial and ommatidial type-specific (Takemura and Arikawa, 2006), the number of inter-photoreceptor connections could be variable among ommatidia. Similarly, the antagonistic inhibition can be attributed to the photoreceptors from the neighboring cartridges. The number of inter-cartridge connections may differ depending on the type of surrounding ommatidia (Matsushita et al., in preparation).

***Functional implications***

Color opponency is one of the most important neural mechanisms for the processing of chromatic information (De Valois and Jacobs, 1968). The photoreceptor-level spectral opponency raises the question whether color information processing is improved by the mechanism at the initial stage in the visual system. Overlaps of the photoreceptor spectral sensitivities are important for comparison in the color opponent mechanism. In the case of spectrally opponent photoreceptors, the wavelengths where the response polarities change may be crucial for wavelength discrimination. These “border” wavelengths may be close to the regions of the spectrum where *Papilio* exhibits the highest wavelength discrimination ability: 430, 480 and 560 nm (Koshitaka et al., 2008). I thus compared the spectral responses of spectrally opponent photoreceptors with the *Papilio* wavelength discrimination function (Figure 5-29). However, I could not find any clear correlation. This suggests that the spectral opponency at the photoreceptor-level may not be the final stage of color processing in foraging *Papilio*. The spectral opponent signals may be processed and integrated in higher-order visual neurons. At the current stage, I cannot conclude how much do the spectrally opponent photoreceptors at the initial visual stage contribute to the color processing in the *Papilio* visual system.

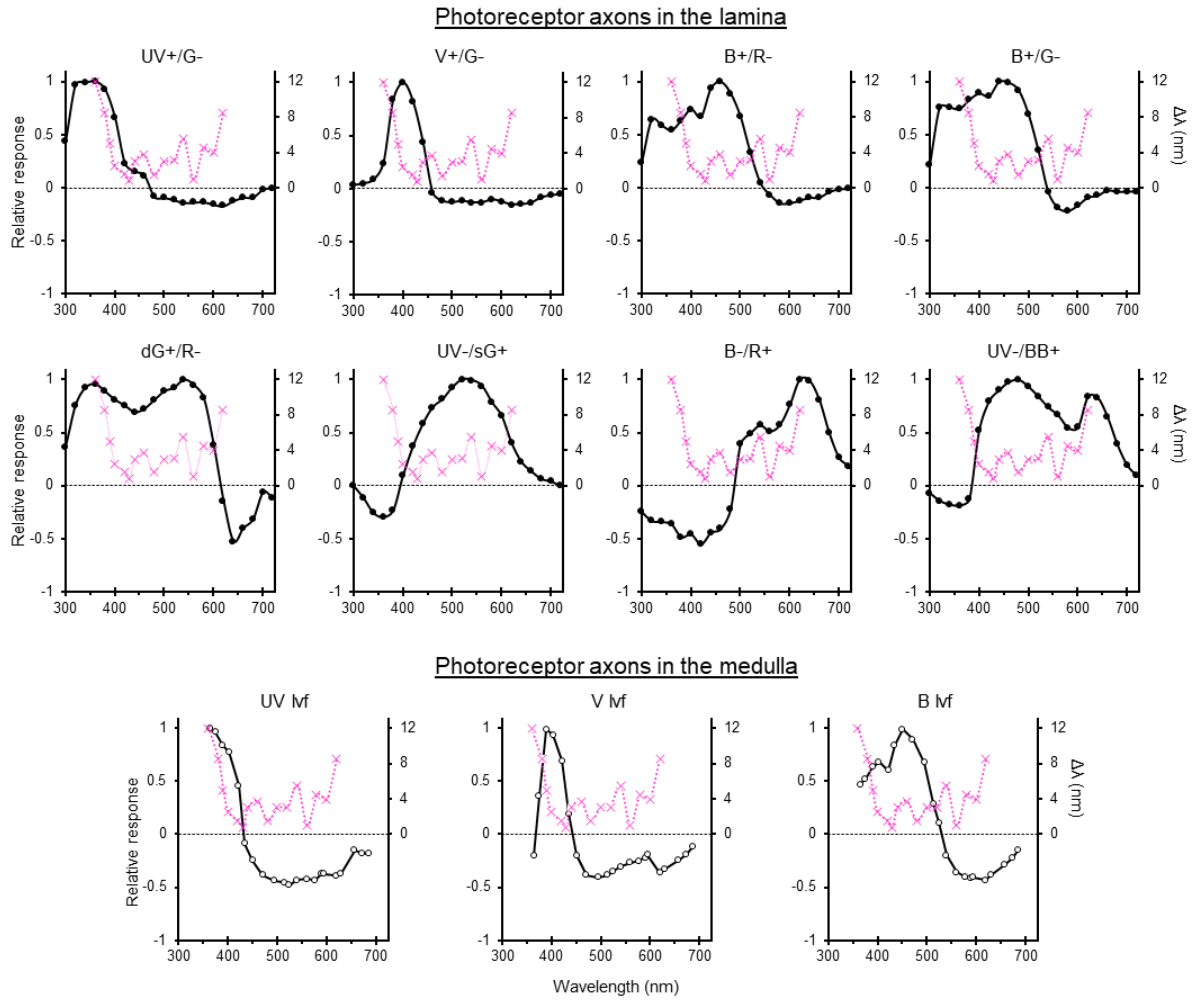


**Figure 5-29. Comparison of the present electrophysiological data in spectrally opponent photoreceptors and behavioral wavelength discrimination.** *Black solid curves* indicate the averaged spectral response curves of spectrally opponent photoreceptors upon isoquantal spectral stimulation by the IF series in the lamina and by the LED array in the medulla. *Magenta dotted curves* indicate the wavelength discrimination function of foraging *Papilio* (Koshitaka et al., 2008).

The effects of spectral opponency in photoreceptors are meaningful only if the antagonistic signals could pass into the second-order neurons in the lamina. The study of intracellular recording in the lamina of butterfly *Vanessa itea* showed that antagonistic effects of the retinal interaction could not pass into the lamina cells by synapses or by current flow (Horridge et al., 1984). Figure 5-28 demonstrates spectral responses of photoreceptors recorded in the retina, lamina and medulla. Comparing the spectral responses in the *Papilio* retina and the lamina (Figure 5-21), spectral responses are often narrower in the spectrally opponent photoreceptors recorded in the lamina compared to those in the non-opponent photoreceptors recorded in the lamina. The results are similar to my previous recordings in *Troides aeacus* (Chen et al., 2013). It is most likely that the spectral opponency in photoreceptors could function

specifically to sharpen the spectral sensitivity. Many butterflies bear screening pigments near the rhabdom boundary, which act as spectral filters (Stavenga, 2002). The antagonistic interaction between photoreceptors may further sharpen spectral responses and thus enhance contrast. This effect may result in a reduction of redundancy stemming from broadly overlapping spectral sensitivities across various spectral receptors.

I have described an example showing the modification of photoreceptor polarization sensitivities in the lamina (Figure 5-11), which can be explained by the inter-photoreceptor antagonistic interaction. Similar cases have been demonstrated in flies which show opponent polarization responses (Hardie, 1984; Weir et al., 2016). The rhabdomeres of fly inner photoreceptors R7/R8 in the dorsal rim area are untwisted along with well aligned microvilli, which provides high polarization sensitivity (Wernet et al., 2012). Weir et al. (2016) suggested that the polarization sensitivity in the terminals of R7/R8 mutually inhibit in the *Drosophila* medulla, and it is most likely resulting from local inhibitory interaction circuits via HCLB (Schnaitmann et al., 2018). The examples in flies and butterflies suggest the antagonistic interaction between photoreceptors leads to enhance contrast not only in spectral but also in polarization signals.

Taken together, the photoreceptor-level opponent mechanism can thus act as a pre-processor for LMCs, which in turn receive sharply-tuned spectral inputs from the photoreceptors whose spectral sensitivities appear much broader when measured in the retina. Also, LMCs could receive enhanced polarization sensitivities. How this mechanism contributes to shaping butterflies' sophisticated color vision is a question that must await further studies.

## 5.6 Supplementary Materials

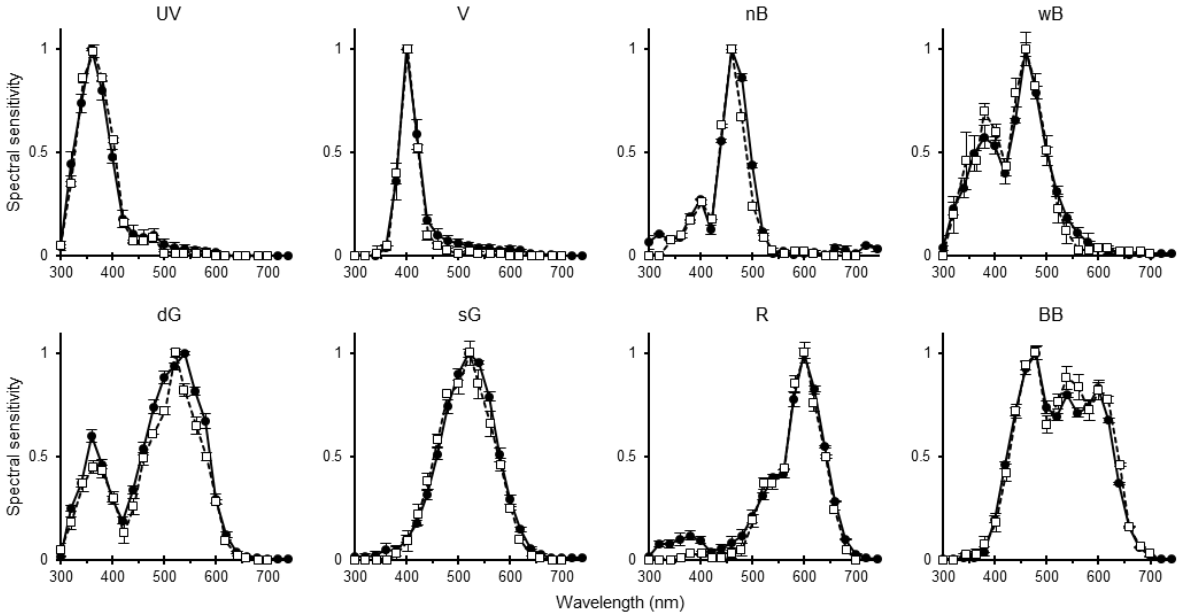


**Figure 5-S1. Comparison with published spectral sensitivities.** The averaged spectral sensitivities (mean ± standard errors) of the receptors recorded in the present study are shown as *solid lines with black circles*. The *dashed lines with white squares* reveal the previously published spectral sensitivities of *Papilio xuthus* from Arikawa (2003). UV, ultraviolet receptor. V, violet receptor. nB, narrow receptor. wB, wide receptor. dG, dual-peaked green receptor. sG, single-peaked green receptor. R, red receptor. BB, broadband receptor.

**Table 5-S1. Parameters used in the equation (5.2) to approximate spectral responses of photoreceptors**

| | UV | V | nB | wB | sG | dG | R | BB |
|---|---|---|---|---|---|---|---|---|
| $A$ | 1 | 1 | 1 | 1 | 1 | 1 | 1 | 1 |
| $\lambda^0$ | 360 | 400 | 465 | 468 | 520 | 550 | 607 | 470 |
| $\delta$ | 48 | 25 | 35 | 48 | 80 | 60 | 50 | 50 |
| $B$ | 0.35 | 0.45 | 0.50 | 0.75 | 0.10 | 0.85 | 0.40 | 0.28 |
| $\lambda^1$ | 530 | 450 | 400 | 362 | 340 | 360 | 512 | 542 |
| $\sigma$ | 80 | 60 | 70 | 40 | 30 | 40 | 30 | 20 |
| $C$ | - | 0.35 | 0.10 | 0.22 | - | 0.50 | 0.35 | 0.91 |
| $\lambda^2$ | - | 585 | 650 | 590 | - | 465 | 365 | 607 |
| $\rho$ | - | 60 | 50 | 70 | - | 40 | 80 | 45 |

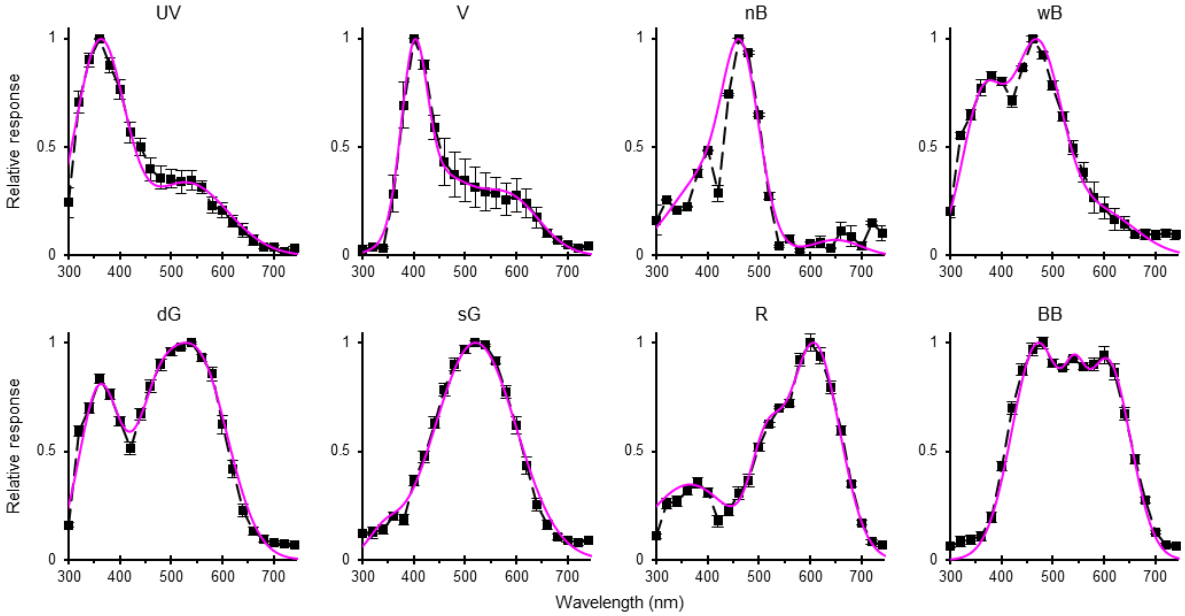


**Figure 5-S2. Comparing the derivatives of spectral response curves for the model calculations with the measured spectral responses.** The *solid lines with black circles* reveal the averaged spectral responses (mean ± standard errors) of receptors recorded in the retina of *Papilio xuthus* in this study. The *magenta curves* show the results of the derivatives of spectral response curves calculated by the equation (5.2) with the parameters shown in Supplementary Table 5-S1. UV, ultraviolet receptor. V, violet receptor. nB, narrow blue receptor. wB, wide blue receptor. dG, dual-peaked green receptor. sG, single-peaked green receptor. R, red receptor. BB, broadband receptor.

# Chapter 6

## General discussion

## 6.1 Comparison with the histaminergic channels of the fly

Generally, HCLA channels appear to be involved in the primary forward flow of visual information from the photoreceptors to higher-order neurons, while HCLB channels seem to comprise the lateral connections closely related to early spectral processing. Figure 6-1 summarizes my present results and interpretations together with what is known in *Drosophila*. R1–R6 of *Drosophila* and R3–R4 of *Papilio* (*black* in Figure 6-1) are known to be involved mainly in motion vision, while other receptors (*blue*) with variable spectral sensitivities should be responsible mainly for color vision or both color and motion vision (Stewart et al., 2015).

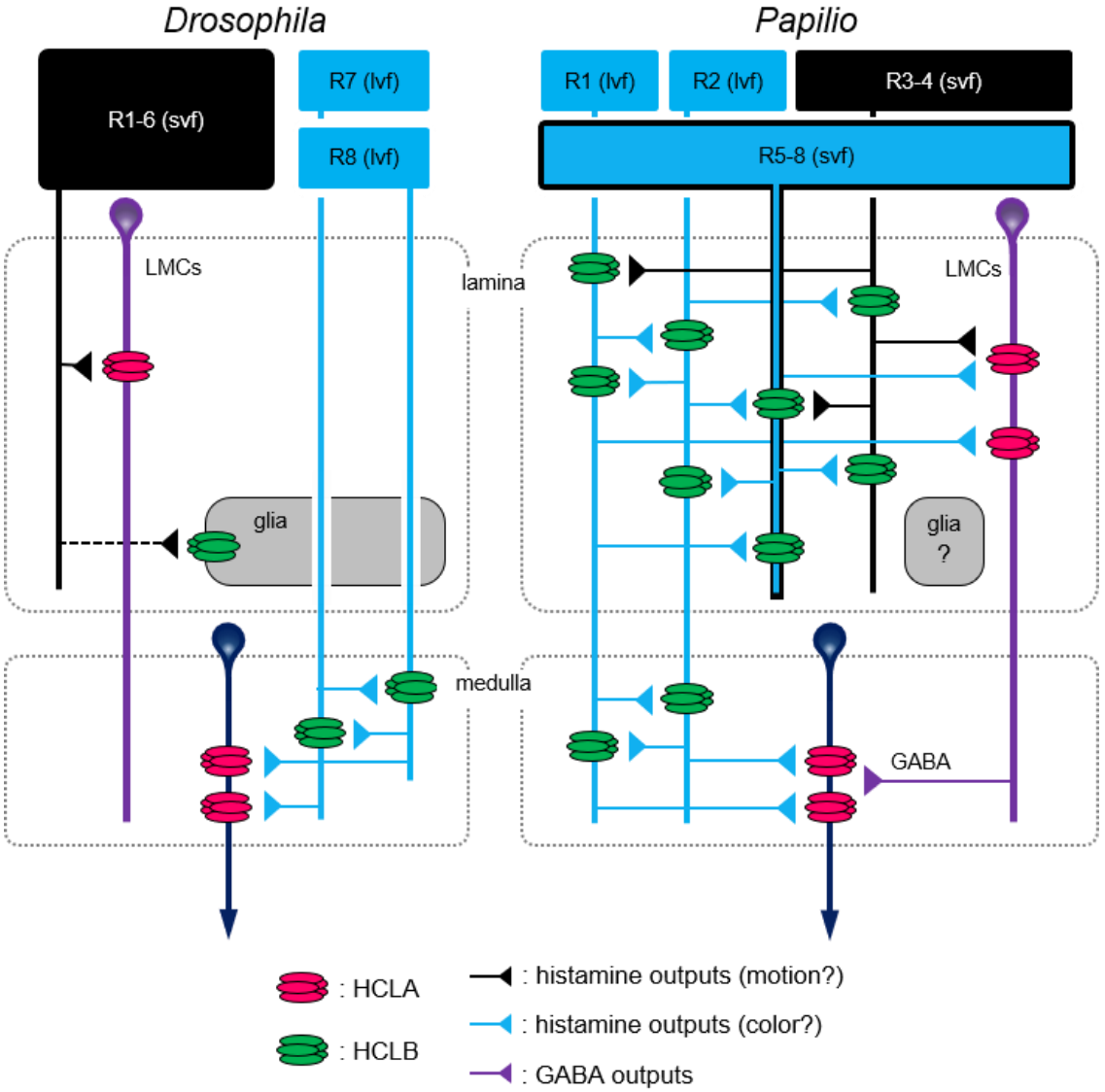


**Figure 6-1. Schematic longitudinal view of photoreceptors and neurons showing localization of histamine-gated chloride channels and putative visual circuits in the optic lobe of *Drosophila* (*left*) and *Papilio* (*right*).** The fly R1–R6 are short visual fibers (svfs) terminating in the lamina and are mainly involved in motion detection (*black*), while R7/R8 are long visual fibers (lvfs) terminating in the medulla and involved primarily in color vision (*blue*) (Morante and Desplan, 2004). (continued on the next page)

### *Spectral processing begins in the* Papilio *lamina*

Spectral processing had long been considered to start in the medulla (Kien and Menzel, 1977; Osorio, 1986; Kelly and Mote, 1990; Yang et al., 2004; Paulk et al., 2008). The *Papilio* histaminergic sign-inverting synapses between photoreceptors indicate that the neuronal circuits exist as the first visual synapses in the lamina (Chen et al., 2019), while in *Drosophila* the spectrally opponent synapses reside in the medulla (Schnaitmann et al., 2018). Accordingly, the underlying neural circuits of spectral processing do appear one-step earlier than previously hypothesized in insect visual systems.

The color vision system of *Papilio* is tetrachromatic with UV, blue, green and red channels (Koshitaka et al., 2008), and the green and red receptors are all short visual fibers (svfs) terminating in the lamina (Takemura et al., 2005). The *Drosophila* long visual fibers (lvfs) project directly to the medulla without making any synapses in the lamina, while the *Papilio* lvfs have many side branches in the lamina forming inter-photoreceptor connections with svfs (Figure 6-1). Therefore, the lamina is certainly involved in color vision in *Papilio*, and in fact, it may even be a major locus of spectral processing. Behaviorally, *Papilio* can perceive colors within a single "pixel" corresponding to an individual ommatidium (Takeuchi et al., 2006). This implies that butterflies have the basic set of mechanisms for color vision in every module making a pixel, which most likely corresponds to the lamina cartridge. Local antagonistic interactions at the level of the photoreceptors provide a basis for the discrimination of colors within single pixels.

---

The fly HCLA channels reside in the lamina, where svfs R1–R6 make histaminergic synapses to LMCs, and in the medulla, where lvfs R7/R8 connect to medullar second-order visual neurons (Gao et al., 2008). The fly HCLB is located in the glial cells in the lamina (Pantazis et al., 2008) and terminals of R7/R8 in the medulla (Schnaitmann et al., 2018). An ommatidium of *Papilio* contains nine photoreceptors R1–R9, but I ignore R9 as it was too small to be detected in the present study. The butterfly R1/R2 are lvfs homologous to *Drosophila* R7 (Friedrich et al., 2011; Perry et al., 2016) for color vision (*blue*). The butterfly R3–R8 are svfs that are homologous to *Drosophila* spectrally homogeneous R1–R6 for motion vision (*black*), while spectrally heterogeneous R5–R8 in *Papilio* are involved in both color and motion vision (*blue with black line*) (Stewart et al., 2015). Both svfs and lvfs of *Papilio* make synaptic connections to LMCs in the lamina (Takemura and Arikawa, 2006). The butterfly PxHCLA is expressed in LMCs in the lamina and is also expressed in medulla neurons facing to lvfs R1/R2. A subset of *Papilio* LMCs contain GABA (Hamanaka et al., 2012) and possibly activate the PxHCLA-expressing medulla neurons via PxHCLA, which is sensitive to GABA (Akashi et al., 2018). PxHCLB is expressed at inter-photoreceptor synapses in both the lamina and the medulla, probably mediating spectrally opponent interactions.

***Segregation of color and motion pathways***

In the *Papilio* lamina, a variety of spectral photoreceptors including the possible motion-processing R3 and R4 photoreceptors establish locally antagonistic interactions via PxHCLB (Figure 6-1). This interaction is absent in the fly lamina where all photoreceptors terminating there are spectrally identical R1–R6, which form no inter-photoreceptor connections (Rivera-Alba et al., 2011). The different distribution of HCLB channels observed between butterflies and flies presumably reflects the different degree of segregation of processing pathways for motion and color; the segregation seems more pronounced in flies.

Comparing the signal inputs via HCLA channels in visual systems of fly and butterfly, we would come to a similar conclusion. Both in fly and butterfly, the HCLA channels exist at the second-order neurons in the lamina and medulla (Figure 6-1). The HCLA channels of fly at LMCs make synapses to svfs R1–R6 (Gengs et al., 2002; Rivera-Alba et al., 2011), which are responsible for motion vision (Heisenberg and Buchner, 1977; Yamaguchi et al., 2008). In the medulla, the HCLA channels exist at medulla neurons facing to spectrally heterogeneous lvfs R7/R8 for color signals processing (Morante and Desplan, 2004). The case in the butterfly is different because the butterfly LMCs receive inputs from all receptors including the possible motion-processing photoreceptors R3/R4 and from the remaining color-processing photoreceptors via PxHCLA. In other words, the butterfly LMCs process both color and motion signals while the fly LMCs mainly process motion signals. The segregation of color and motion pathways in butterflies is not as clear as in flies in the lamina.

On the other hand, the PxHCLA of butterfly is expressed in second-order medulla neurons facing to lvfs R1/R2. Such visual circuit looks pretty similar to the fly in the medulla for color processing. However, as discussed in Chapter 3, the variability in the response to GABA between HCLA and PxHCLA may reflect differences in the underlying visual circuits between flies and butterflies. In *Papilio*, both PxHCLA and PxHCLB respond to GABA in addition to histamine (Akashi et al., 2018). A subset of *Papilio* LMCs may be GABAergic, terminating in the distal region of the medulla along with the lvfs (Hamanaka et al., 2012). The PxHCLA-expressing medulla cells could receive chromatic and motion signals from these putative GABAergic LMCs in addition to the histaminergic lvfs (Figure 6-1). In contrast, the fly HCLA is insensitive to GABA (Gisselmann et al., 2004; Kita et al., 2017), which again possibly reflects the more segregated nature of the fly motion and color pathways compared to those of butterflies.

***Early stages of spectrally opponent pathways***

The inter-photoreceptor antagonistic interactions via PxHCLB in the *Papilio* lamina result in higher variation of spectrally opponent pathways than in flies. In *Drosophila*, two lvfs in each ommatidium, i.e. R7p/R8p and R7y/R8y cells, mutually antagonize each other in the medulla and, thus, create two spectrally opponent pathways: $UV_{short}$/blue and $UV_{long}$/green, respectively (Schnaitmann et al., 2018). Inter-photoreceptor connections are more variable in the *Papilio* lamina (Takemura and Arikawa, 2006), where eight classes of spectrally heterogeneous photoreceptors are involved: the opponent pathways are much more complex in butterflies (Figure 6-1). This has been supported by my electrophysiological recordings in the *Papilio* lamina (Chapter 5). So far, eight classes of spectrally opponent photoreceptors have been recorded, including at least UV/green, UV/broadband, violet/green, blue/green, blue/red, and green/red opponent interactions (Figure 5-28).

In addition to the spectrally opponent photoreceptors, in Chapter 4, I revealed several classes of spectrally opponent LMCs. The spectrally opponent LMCs seem to be uncommon. Most LMCs are non-opponent and have similar spectral sensitivity functions (Laughlin, 1976; Laughlin and Hardie, 1978; Moring, 1978). This is not surprising because all of the inputs to LMCs in fly lamina, directly or indirectly, come from the Rl–R6 photoreceptors that constitute a single spectral class with identical broad spectral sensitivity (McCann and Arnett, 1972; Horridge and Mimura, 1975; Hardie, 1985; Rivera-Alba et al., 2011). Previously, only one spectrally opponent LMC has been reported in the worker honey bee (de Souza et al., 1992). The cell responded with a sustained depolarization in the green and blue and a phasic hyperpolarization in the UV; i.e. UV-/B+/G+. In *Papilio*, LMCs receive inputs from spectrally distinct receptors via PxHCLA (Figure 6-1) which result in several LMC spectral classes. Regarding the spectrally opponent LMCs, I have identified three main classes (Figure 4-7) that depolarized in short, middle and long wavelengths as well as five unique opponent classes (Figure 4-8) including UV+/B+/G+/R-, UV+/B+/G-/R+, UV+/B-/G+/R-, UV-/B+/G+/R+, and UV-/B+/G+/R- opponent LMCs. It again reflects a high variety of spectrally opponent pathways at the early stages of the *Papilio* visual system, which is likely important for the acute color vision of this flower forager.

## 6.2 Histaminergic signaling underlies the color vision

***Histaminergic pre-processing in the early visual system***

In Chapter 3, I presented the dose-response experiment which indicates that PxHCLB is more sensitive to histamine than PxHCLA (Akashi et al., 2018). This is consistent with the case of the lower $EC_{50}$ for histamine in the HCLB than in HCLA in *Drosophila* and house fly (Gisselmann et al., 2004; Kita et al., 2017). No study has further discussed this phenomenon and its significance. The present results provide some hints in this respect. In Chapter 2, I have detected PxHCLB at inter-photoreceptor connections in the lamina and the medulla of *Papilio* (Chen et al., 2019). The higher histamine sensitivity of HCLB would cause it to be activated more quickly than HCLA. It would allow the photoreceptors to pre-process mutual signals via PxHCLB before downstream synaptic transmission via PxHCLA. The pre-processed information is not restricted only to spectral signals. As some examples I revealed in Chapter 5, the inter-photoreceptor antagonistic interaction via PxHCLB resulted in the shaping of photoreceptor polarization sensitivities in the *Papilio* lamina (Figure 5-11). PxHCLA is presumably involved in the process at the second synapse receiving antagonistic spectral and/or polarization information from photoreceptor sets. Similar effect may also function in the *Drosophila* medulla (Weir et al., 2016; Schnaitmann et al., 2018).

.

***Spectral processing at the early visual stage of* Papilio**

The electrophysiological recordings in the *Papilio* LMCs (Chapter 4) and spectrally opponent photoreceptors (Chapter 5) suggest that the spectral processing already starts in the lamina. However, it is important to know whether the pre-processed chromatic information can be passed along to the next stage, i.e. medulla. As Figure 6-1 shown, only lvfs R1/R2 extend their axons to the medulla, while all other receptors R3-R8 are svfs that terminate in the lamina. The chromatic information is probably transmitted to the medulla through two channels, one comprising the second-order LMCs with signals derived from svfs, and the other comprising the lvfs R1/R2.

The butterfly *Papilio xuthus* shows excellent wavelength discriminability between 380 nm to 650 nm (Koshitaka et al., 2008), covering the wavelength range from UV to red. For opponent processing, the short and middle wavelength parts (380 nm to 500 nm) can be directly

achieved by the lvfs R1/R2 which are either UV, violet or blue receptors (Arikawa, 2003). The question is how do the distinct spectral channels above 500 nm reach the medulla? The LMCs are the main candidates. As I reported in Chapter 4, different spectral types of LMCs with distinct spectral sensitivities above 500 nm have been found. The non-opponent type I, II and III LMCs respectively peak at 600 nm, 560 nm and 500 nm (Figure 4-6). These LMCs reside below three distinct ommatidial types. Their signals must be subjected to lateral inter-ommatidial opponent processing at later stages to get the chromatic information.

The finding implies why is it necessary to have the retinal mosaic with three ommatidial types. Since the anatomy and electrophysiological results suggest that the LMCs receive spectral inputs only from one ommatidium, the photoreceptor array is mapped point to point onto the lamina and the retinotopical receptor mosaic is maintained at the neuropils. In order to be able to process long wavelength color using comparison among the three types, the receptor mosaic is crucial.

Signals in lvfs and LMCs are pre-processed by inter-photoreceptor opponency via PxHCLB, which sharpens up the spectral sensitivities at the inputs. My study indicates that the central processing of color is most likely in the medulla but early stages in the lamina show highly sophisticated pre-processing.

## 6.3 Summary and highlights

***Examination of the histamine hypothesis***

My study of histaminergic signaling in the *Papilio* early visual system was motivated by the observation of spectral opponency in butterfly photoreceptor. To explain its mechanism, I have proposed a "histamine hypothesis" that histaminergic sign-inverting synapses exist between different spectral receptors. Several methods from different aspects were adopted to approach the answer.

To check whether any histaminergic channels exist at the inter-photoreceptor synapses, I first carried out immunolocalization of two candidates of histamine-gated chloride channels, PxHCLA and PxHCLB, in the *Papilio* eye (Chapter 2). The double fluorescence labeling with anti-PxHCLA and anti-PxHCLB revealed that these channels do not overlap in their distribution. The PxHCLA immunoreactivity was detected at the second order neurons that are postsynaptic to photoreceptors, while the PxHCLB widely overlapped with photoreceptor axons indicating that this channel is expressed at the inter-photoreceptor synapses. The unique PxHCLB distribution provides support for the histamine hypothesis: this channel is probably involved in the photoreceptor spectral opponency.

The antibodies for immunohistochemistry were produced against the peptides of the gene products possibly encoding the histamine receptors in *Papilio* (Chapter 2). To confirm whether these molecules were really histamine-gated chloride channels, I further analyzed physiological properties of these channels by whole-cell patch-clamp using those expressed in HEK293 cells (Chapter 3). The patch-clamp experiments confirmed that both PxHCLA and PxHCLB are indeed activated by histamine and permeate chloride ions. The sensitivity to histamine and GABA was consistently higher in PxHCLB than in PxHCLA.

I found by immunohistochemistry that the *Papilio* LMCs and spectrally opponent photoreceptors expressed histaminergic channels PxHCLA and PxHCLB, respectively (Chapter 2). Using sharp microelectrode recording with current injections, I have revealed that the responses of both LMCs (Chapter 4) and spectrally opponent photoreceptors (Chapter 5) could be reversed when the membrane potential was close to the equilibrium potential of chloride. The results provide an *in vivo* electrophysiological evidence for the presence of chloride channels in these cells, which matches to my immunohistochemical localization of histamine-gated chloride channels in the *Papilio* lamina.

The combining approaches provided support for the hypothesis that spectral opponency in butterfly photoreceptors is due to direct inhibition between photoreceptors, mediated by the histaminergic chloride channel PxHCLB. The results obtained from different experiments are indispensable for conclusions, and each is strongly connected with one another.

***Histaminergic signaling in the early visual system***

To understand how the histaminergic synapses mediate chromatic processing at the level of the first synapse, I recorded spectral responses of LMCs and photoreceptor axons in the *Papilio* lamina. The recorded LMCs can be divided into non-spectral opponent and spectral opponent cells (Chapter 4). The former one includes three spectrally heterogeneous classes which are ommatidial type dependent. LMCs seem to integrate chromatic signals mainly from the photoreceptors in the same ommatidium. This suggests that PxHCLA channels most likely implement the primary visual processing from the photoreceptors to the secondary neurons (Chapter 2). Furthermore, I propose that all LMCs feed signals into motion detection circuitry and in parallel into spectral opponent circuitry. Regarding spectral sensitivities, spectrally opponent LMCs could manage opponent processing in short, middle and long wavelengths. In addition, spectral processing in the long wavelength part of the spectrum could also be mediated by comparing incoming signals from different spectral types of non-opponent LMCs.

On the other hand, I recorded eight classes of spectrally opponent photoreceptors in the *Papilio* lamina (Chapter 5). The recorded opponent responses are well explained by the ommatidial type-specific inter-photoreceptor (sign-inverting) synaptic connections via PxHCLB (Chapter 2). Moreover, all photoreceptors in the medulla exhibited spectral opponency, and could be divided into three categories corresponding to the three spectral classes of lvfs. The spectral opponent pathways between photoreceptors in *Papilio* show a high degree of variation. The antagonistic interaction between photoreceptors sharpens the spectral responses and enhances the contrast. The dominant opponent interactions at the earlier visual stage are likely important for them to have an acute color vision.

The findings in this thesis bring a closer view on the underlying histaminergic signaling and neural circuits for color vision in the *Papilio* early visual system. Our knowledge of histamine receptors in insect visual systems is based mainly on studies of flies. My results provide the first comparative anatomy (Chapter 2) and physiology (Chapter 3) of histamine-gated chloride channels in an insect visual system other than flies. My electrophysiological records in

the *Papilio* LMCs (Chapter 4) and spectrally opponent photoreceptors (Chapter 5), although somewhat preliminary, may open a new window on the study of early chromatic processing in insect visual systems.

***Summary of novel findings***

The work presented in this thesis provides new insights into the complexity of chromatic processing at the early visual stages of *Papilio*. Two different histamine-gated chloride channels, PxHCLA and PxHCLB, are involved in the extraction of spectral information at the level of the first synapses. Below, I summarize the main findings from this thesis.

- Spectral opponent processing had long been considered to start in the medulla. The expression of PxHCLB at inter-photoreceptor synapses indicates that possible neuronal circuits exist at the first visual synapses in the *Papilio* lamina (Chapter 2), while *Drosophila* has it in the medulla (Schnaitmann et al., 2018). Intracellular electrophysiology revealed a high variety of spectrally opponent pathways for both spectrally opponent photoreceptors (Chapter 5) and LMCs (Chapter 4) in the *Papilio* lamina. Accordingly, the underlying neural circuits of spectral opponent processing may appear one step earlier than previously thought in insect visual systems.

- In *Papilio*, both PxHCLA and PxHCLB respond to GABA in addition to histamine (Chapter 3) while the fly HCLA is insensitive to GABA (Gisselmann et al., 2004; Kita et al., 2017). The variability in the response to GABA between HCLA and PxHCLA, along with the differences in distribution of histaminergic channels in the visual systems of butterflies and flies (Chapter 2) suggest that in butterflies pathways for color and motion are less segregated than in flies at the early stages of visual processing.

- The dose-response experiment indicates PxHCLB is more sensitive to histamine than PxHCLA (Chapter 3), which is consistent with the case in flies (Gisselmann et al., 2004; Kita et al., 2017). Such physiological characteristics seem to be rather common across species; however, the biological function has received little attention. My intracellular electrophysiology in spectrally opponent photoreceptors suggested that spectral and/or polarization responses are shaped by the inter-photoreceptor opponent signal processing, mediated by PxHCLB (Chapter 5). Along with the localization of histaminergic channels (Chapter 2), the present results suggest that the lower $EC_{50}$ for histamine in the HCLB than in HCLA allows for higher-order neurons to receive pre-processed signals.

- The previous study in *Papilio* LMCs demonstrated that the *Papilio* LMCs as other insects appear to be exclusively important in motion detection due to broad spectral sensitivities (Rusanen et al., 2018). Findings of different spectral classes of LMCs as well as spectrally opponent LMCs (Chapter 4) provide a sign that the LMCs may have a role in the processing of chromatic information in addition to achromatic processing.

- The second-order LMCs were thought to have little polarization sensitivity due to the mutual offset after the convergence of numerous inputs from different photoreceptors. However, my intracellular electrophysiology indicated that LMCs revealed polarization sensitivities upon unsaturated illuminations (Chapter 4), suggesting the polarization information is possibly passed through LMCs to the next stage.

## 6.4 Recommendations for future directions

This study has given insights into the roles of histaminergic channels in color vision of butterflies, but as with any research it has also provided many new questions. Especially in regard to the histaminergic signaling in the early visual system there are many perspectives to investigate, with some of the main ones listed below.

***Light adaptation and panoramic stimulus***

My electrophysiological experiments, both in the photoreceptors and in the LMCs, have been performed in nearly dark-adapted state; the background light is much brighter in the nature than in my experimental preparation. However, butterflies are diurnal animals. The effects of light adaptation should be considered when studying spectral information transmission at the photoreceptor-LMC synapses. Current injection experiments have provided hints for the effects both in spectrally opponent photoreceptors and LMCs.

The steady background light leads photoreceptors to depolarize continuously. In Chapter 5, I found that when I injected positive currents into spectrally opponent photoreceptors, the inhibitory hyperpolarization became more evident. The background depolarization for photoreceptors is probably similar in light-adapted animals under bright backgrounds. This implies that the antagonistic interaction between inter-photoreceptors via PxHCLB is more pronounced when the butterfly is in its natural environment.

In turn, the background light leads LMCs to hyperpolarize continuously. The response polarity of LMCs reversed from hyperpolarization to depolarization when I injected negative currents into the cells (Figure 4-21). The spectral opponent LMCs may be much easier to be encountered in light-adapted eyes.

On the other hand, my electrophysiological results suggested the possibility of inter-cartridge interactions in both spectrally opponent photoreceptors and LMCs. In fact, I have found that some LMCs seem to have the receptive field with a center-surround configuration, as observed in vertebrates, which could be involved in refining the spatial resolution. Moreover, some LMCs even showed “double opponency” which involves spatial antagonism of spectrally opponent mechanisms. Using light-adapted eyes with an extended light source will hopefully reveal the true nature of photoreceptors and LMCs in chromatic processing in early visual systems of butterflies.

***CRISPR/Cas9 knockouts***

The contribution of LMCs and spectrally opponent photoreceptors to color vision have not been conclusively established. It is possible to make CRISPR/Cas9 mutants for histamine-gated chloride channels and perform functional analysis in *Papilio*, which actually has been planned. Using *Pxhcl* CRISPR/Cas9 knockout individuals to check wavelength discriminability behaviorally could provide conclusive evidence about the function of histaminergic channels in color processing and how histamine signaling affects the final endpoint of color vision.

On the other hand, electrophysiological recordings in *PxhclA* CRISPR/Cas9 knockout LMCs would likely be informative when it comes to investigating the origins of the LMC response components especially those depolarizing components such as the depolarizing off-transient and depolarizing plateau that I have observed in spectrally opponent LMCs. The components that are derived from PxHCLA channels should disappear in *PxhclA* CRISPR/Cas9 knockout LMCs; for instance, the fast hyperpolarizing on-transient, which has been assumed to be caused by high chloride conductance. It is very likely that the depolarizing responses would remain intact in *PxhclA* CRISPR/Cas9 knockout LMCs if they are not mediated by PxHCLA channels.

Electrophysiological recordings in *PxhclB* CRISPR/Cas9 knockout photoreceptors may provide a causal link for PxHCLB being sufficient to mediate spectral opponency in the *Papilio* photoreceptors. According to the present results, the antagonistic interaction between inter-photoreceptors would be abolished and no spectrally opponent responses could be observed in *PxhclB* CRISPR/Cas9 knockouts. The medulla might be an ideal site to perform this experiment because all photoreceptor axons recorded in medulla exhibited spectral opponency.

***Anatomy analyses***

The serial block face-scanning electron microscopy (SBF-SEM) analysis of the *Papilio* lamina at the EM level reveals that a cartridge contains four LMCs of different morphology and branching patterns (Matsushita et al., in preparation). Regarding the spiking properties, Rusanen et al. (2018) demonstrated that non-spiking LMCs are terminated in shallower medulla and thus they are most likely L1/L2, while the terminal of spiking LMCs locate in the deeper layer of the medulla and thus they are most likely L3/L4. Regarding spectral properties, I found

that LMCs can be divided into spectrally opponent and non-opponent types; furthermore, each type contains different spectral classes (Chapter 4). Whether they are belonging to different LMC morphological types remains in question. Accordingly, there are two main questions to work out for correlation spectral properties to the LMC morphological types. One is the spectral opponency and another one is the identity of the LMC spectral types.

For the former one, visualization of stained LMCs using the confocal scanning laser microscope would probably be the best technique for such an investigation, and some of this work is underway. As stained LMCs I shown in Figures 4-12 and 4-14, confocal images provide more accurate 3-D representations of neuronal fine structures and lateral processes, which are important characteristics for the identification of the LMC morphological types.

So far, I have obtained three stained LMCs which are type I (Figure 4-12) and type III (Figures 4-13.4-14) non-opponent LMCs which are belong to two distinct LMC morphological types. Based on the microscopic examinations of stained LMCs, one type I LMC (Figure 4-12) and one type III LMC (Figure 4-13) that resided in different ommatidial types had similar morphology and thus they probably belong to the same LMC morphological type. To confirm the assumption, a thorough anatomy at the EM level following confocal observation may be necessary. The SBF-SEM analysis reveals that the four morphological types of LMCs have no significant differences among three ommatidial types. Fortunately, it is still possible to identify the ommatidial types in the *Papilio* lamina by checking the lateral process patterns of photoreceptors R1 and R2, as I have discussed in Chapter 4.

The work could also be applied in spectrally opponent photoreceptors. I have summarized the possible correlation of the recorded spectral classes of the opponent photoreceptors with the ommatidia types (Figure 5-28). Although the simple model I applied could well reproduce the principal responses profiles of eight spectrally opponent photoreceptors (Figure 5-27), it would be of interest to examine the real numbers of synaptic connections with other photoreceptors. By comparing electrophysiological data to synaptic numbers, it is possible to model the weight of PxHCLB channels mediating the antagonistic interaction in spectrally opponent photoreceptors.

On the other hand, as I discussed in Chapter 4, the LMC-like unit shares some characteristics with the typical LMCs but also shares other characteristics with the extracellular potential. Intracellular recordings followed by dye injection in the LMC-like units will hopefully determine whether they are LMCs, the extracellular potential, or other interneurons.

## 6.5 Conclusion from an evolutionary view

In this thesis, I investigated the roles of histaminergic signaling underlying color processing at the early visual stages of butterflies by examining histamine-gated chloride channels and second-order neurons that post-synaptic to photoreceptors in the *Papilio* visual system. I have found several conserved characteristics that are shared with flies but also some characteristics uniquely found in *Papilio*.

In Chapter 2, I showed that while the distribution of PxHCLA channels in *Papilio* is similar to that in flies (Gengs et al., 2002), the distribution of PxHCLB channels is dissimilar in the lamina of butterflies and flies (Pantazis et al., 2008). Spectral opponent processing in *Papilio* appears earlier than in flies. In Chapter 3, I revealed that, as in flies (Gisselmann et al., 2004; Kita et al., 2017), PxHCLB is more sensitive to histamine than PxHCLA, suggesting that the physiological properties of the histaminergic channels are basically conserved among insects. However, the response to GABA differs between butterflies and flies, implying variation in early visual processing among species. In Chapter 4, my electrophysiological results suggest that *Papilio* LMCs receive inputs from numerous photoreceptors as fly LMCs (Rivera-Alba et al., 2011), but, regarding spectral sensitivities, the *Papilio* LMCs contain different spectral classes while the fly LMCs have a uniform sensitivity function. The *Papilio* LMCs most likely feed signals into achromatic circuitry and in parallel into the chromatic circuitry. In Chapter 5, I recorded eight classes of spectrally opponent photoreceptor in the *Papilio* lamina while there are two in the fly medulla (Schnaitmann et al., 2018). This suggests that the spectrally opponent pathways are much more complex in butterflies than in flies.

These differences provide evolutionary insights into the neuronal principles underlying chromatic processing between butterflies and flies. The wavelength discrimination ability of butterfly *Papilio xuthus* is twenty times better than that of *Drosophila*. The co-evolution of insects and flowering plants offers a plausible explanation. The early processing of complex chromatic information in butterflies is likely important for the acute color vision of this flower forager.

In addition to butterflies, bees are also famous pollinators that rely on color vision for survival (von Frisch, 1914; Briscoe and Chittka, 2001). The behavioral experiment also suggested that the honey bee has good color vision (von Helversen, 1972). The visual system of bees shares some features with the fly. For example, their color-processing photoreceptors, i.e. long visual fibers, pass through the lamina without forming characteristic branching patterns

and terminate in the medulla (Ribi, 1976; Rivera-Alba et al., 2011). While spectrally opponent responses at the level of photoreceptors have been recorded quite frequently in butterflies, the spectral opponency has never been reported in the lamina or retina of bees. The color processing may begin in the medulla in bees as in flies. On the other hand, bees also share some features with butterflies. For example, some of their LMCs have long lateral processes that reach neighboring cartridges in the lamina (Ribi, 1976; Greiner et al., 2004).

According to the phylogenic analysis of opsin gene expression, bees are the basal group that have the ancestral trichromatic system based on the UV-, blue-, and green-receptors (Wakakuwa et al., 2007). Other insects were losing or adding opsins during evolution (Bradley et al., 2009). In particular, butterflies show a remarkable radiation (Briscoe, 2008). Their color vision system became more complex by adding spectral receptors through opsin gene duplications in a species-specific manner. While bees as butterflies are nectar foragers and their visual systems have evolved true color vision. It would be interesting to investigate the histaminergic synapses in bees in the future. The extensive comparative studies may help us to establish general principle and broader views on the evolutionary mechanisms underly early color processing in insect visual systems.

# References


Akashi HD, Chen P-J, Akiyama T, Wakakuwa M, Takayama Y, Tominaga M, Arikawa K. 2018. Physiological responses of ionotropic histamine receptors, PxHCLA and PxHCLB, to neurotransmitter candidates in a butterfly, *Papilio xuthus*. J Exp Biol 221:jeb183129.

Altschul SF, Gish W, Miller W, Myers EW, Lipman DJ. 1990. Basic local alignment search tool. J Mol Biol 215:403-410.

Arikawa K. 2003. Spectral organization of the eye of a butterfly, *Papilio*. J Comp Physiol A 189:791-800.

Arikawa K, Stavenga DG. 1997. Random array of colour filters in the eyes of butterflies. J Exp Biol 200:2501-2506.

Arikawa K, Stavenga DG. 2014. Insect photopigments: photoreceptor spectral sensitivities and visual adaptations. Evolution of visual and non-visual pigments: Springer. p 137-162.

Arikawa K, Scholten DG, Kinoshita M, Stavenga DG. 1999a. Tuning of photoreceptor spectral sensitivities by red and yellow pigments in the butterfly *Papilio xuthus*. Zool Sci 16:17-24.

Arikawa K, Mizuno S, Kinoshita M, Stavenga DG. 2003. Coexpression of two visual pigments in a photoreceptor causes an abnormally broad spectral sensitivity in the eye of the butterfly *Papilio xuthus*. J Neurosci 23:4527-4532.

Arikawa K, Wakakuwa M, Qiu X, Kurasawa M, Stavenga DG. 2005. Sexual dimorphism of short-wavelength photoreceptors in the small white butterfly, *Pieris rapae crucivora*. J Neurosci 25:5935-5942.

Arikawa K, Mizuno S, Scholten DG, Kinoshita M, Seki T, Kitamoto J, Stavenga DG. 1999b. An ultraviolet absorbing pigment causes a narrow-band violet receptor and a single-peaked green receptor in the eye of the butterfly *Papilio*. Vision Res 39:1-8.

Asmild M, Willumsen NJ. 2000. Chloride channels in the plasma membrane of a foetal *Drosophila* cell line, S2. Pflügers Archiv 439:759-764.

Awata H, Wakakuwa M, Arikawa K. 2009. Evolution of color vision in pierid butterflies: blue opsin duplication, ommatidial heterogeneity and eye regionalization in *Colias erate*. J Comp Physiol A 195:401-408.

Awata H, Matsushita A, Wakakuwa M, Arikawa K. 2010. Eyes with basic dorsal and specific ventral regions in the glacial Apollo, *Parnassius glacialis* (Papilionidae). J Exp Biol 213:4023-4029.

Bandai K, Arikawa K, Eguchi E. 1992. Localization of spectral receptors in the ommatidium of butterfly compound eye determined by polarization sensitivity. J Comp Physiol A 171:289-297.

Belušič G, Ilić M, Meglič A, Pirih P. 2016. A fast multispectral light synthesiser based on LEDs and a diffraction grating. Scientific Reports 6:32012.

Blackiston D, Briscoe AD, Weiss MR. 2011. Color vision and learning in the monarch butterfly, *Danaus plexippus* (Nymphalidae). J Exp Biol 214:509-520.

Boschek CB. 1971. On the fine structure of the peripheral retina and lamina ganglionaris of the fly, *Musca domestica*. Z Zellforsch 118:369-409.

Bradley TJ, Briscoe AD, Brady SG, Contreras HL, Danforth BN, Dudley R, Grimaldi D, Harrison JF, Kaiser JA, Merlin C. 2009. Episodes in insect evolution. Integr Comp Biol 49:590-606.

Briscoe AD. 2000. Six opsins from the butterfly *Papilio glaucus*: molecular phylogenetic evidence for paralogous origins of red-sensitive visual pigments in insects. J Mol Evol 51:110-121.

Briscoe AD. 2008. Reconstructing the ancestral butterfly eye: focus on the opsins. J Exp Biol 211:1805-1813.

Briscoe AD, Chittka L. 2001. The evolution of color vision in insects. Annu Rev Entomol 46:471-510.

Briscoe AD, Bybee SM, Bernard GD, Yuan F, Sison-Mangus MP, Reed RD, Warren AD, Llorente-Bousquets J, Chiao CC. 2010. Positive selection of a duplicated UV-sensitive visual pigment coincides with wing pigment evolution in *Heliconius* butterflies. PNAS 107:3628-3633.

Buchsbaum G, Gottschalk A. 1983. Trichromacy, opponent colours coding and optimum colour information transmission in the retina. Proc Roy Soc B 220:89-113.

Campos-Ortega J. 1974. Autoradiographic localization of 3 H-γ-aminobutyric acid uptake in the lamina ganglionaris of *Musca* and *Drosophila*. Z Zellforsch 147:415-431.

Carlson SD, Chi C. 1979. The functional morphology of the insect photoreceptor. Annu Rev Entomol 24:379-416.

Chan J, Aoki C, Pickel VM. 1990. Optimization of differential immunogold-silver and peroxidase labeling with maintenance of ultrastructure in brain sections before plastic embedding. J Neurosci Methods 33:113-127.

Chen P-J, Arikawa K, Yang E-C. 2013. Diversity of the photoreceptors and spectral opponency in the compound eye of the Golden Birdwing, *Troides aeacus formosanus*. PloS One 8:e62240.

Chen P-J, Matsushita A, Wakakuwa M, Arikawa K. 2019. Immunolocalization suggests a role of the histamine-gated chloride channel PxHCLB in spectral opponent processing in butterfly photoreceptors. J Comp Neurol 527:753-766.

Chen P-J, Awata H, Matsushita A, Yang E-C, Arikawa K. 2016. Extreme spectral richness in the eye of the Common Bluebottle butterfly, *Graphium Sarpedon*. Front Ecol Evol 4:18.

de Souza J, Hertel H, Ventura DF, Menzel R. 1992. Response properties of stained monopolar cells in the honeybee lamina. J Comp Physiol A 170:267-274.

De Valois RL, Jacobs GH. 1968. Primate color vision. Science 162:533-540.

Demb JB, Singer JH. 2015. Functional circuitry of the retina. Annu Rev Vision Sci 1:263-289.

Dudley R, Srygley R. 1994. Flight physiology of neotropical butterflies: allometry of airspeeds during natural free flight. J Exp Biol 191:125-139.

Edwards TN, Meinertzhagen IA. 2010. The functional organisation of glia in the adult brain of *Drosophila* and other insects. Prog Neurobiol 90:471-497.

Eguchi E, Meyer-Rochow VB. 1983. Trophospongium-like structures in an insect eye: response of retinula cells of *Papilio xuthus* (Lepidoptera) to irradiation with ultraviolet light. Cell Tissue Res 231:519-526.

Elias MS, Evans PD. 1983. Histamine in the insect nervous system: distribution, synthesis and metabolism. J Neurochem 41:562-568.

Feuda R, Marletaz F, Bentley MA, Holland PW. 2016. Conservation, duplication, and divergence of five opsin genes in insect evolution. Genome Biol Evol 8:579-587.

Frentiu FD, Bernard GD, Sison-Mangus MP, Van Zandt Brower A, Briscoe AD. 2007a. Gene duplication is an evolutionary mechanism for expanding spectral diversity in the long-wavelength photopigments of butterflies. Mol Biol Evol 24:2016-2028.

Frentiu FD, Bernard GD, Cuevas CI, Sison-Mangus MP, Prudic KL, Briscoe AD. 2007b. Adaptive evolution of color vision as seen through the eyes of butterflies. PNAS 104 Suppl 1:8634-8640.

Friedrich M, Wood EJ, Wu M. 2011. Developmental evolution of the insect retina: insights from standardized numbering of homologous photoreceptors. J Exp Zool B Mol Dev Evol 316:484-499.

Futahashi R, Kawahara-Miki R, Kinoshita M, Yoshitake K, Yajima S, Arikawa K, Fukatsu T. 2015. Extraordinary diversity of visual opsin genes in dragonflies. PNAS 112:E1247-1256.

Gao S, Takemura S-Y, Ting C-Y, Huang S, Lu Z, Luan H, Rister J, Thum AS, Yang M, Hong S-T, Wang JW, Odenwald WF, White BH, Meinertzhagen IA, Lee C-H. 2008. The neural substrate of spectral preference in *Drosophila*. Neuron 60:328-342.

Gengs C, Leung H-T, Skingsley DR, Iovchev MI, Yin Z, Semenov EP, Burg MG, Hardie RC, Pak WL. 2002. The target of *Drosophila* photoreceptor synaptic transmission is a histamine-gated chloride channel encoded by *ort* (*hclA*). J Biol Chem 277:42113-42120.

Gisselmann G, Pusch H, Hovemann BT, Hatt H. 2002. Two cDNAs coding for histamine-gated ion channels in *D. melanogaster*. Nat Neurosci 5:11-12.

Gisselmann G, Plonka J, Pusch H, Hatt H. 2004. Unusual functional properties of homo-and heteromultimeric histamine-gated chloride channels of *Drosophila melanogaster*: spontaneous currents and dual gating by GABA and histamine. Neurosci Lett 372:151-156.

Greiner B, Ribi WA, Warrant EJ. 2005. A neural network to improve dim-light vision? Dendritic fields of first-order interneurons in the nocturnal bee *Megalopta genalis*. Cell Tissue Res 322:313-320.

Greiner B, Ribi WA, Wcislo WT, Warrant EJ. 2004. Neural organisation in the first optic ganglion of the nocturnal bee *Megalopta genalis*. Cell Tissue Res 318:429-437.

Gribakin F. 1988. Photoreceptor optics of the honeybee and its eye colour mutants: the effect of screening pigments on the long-wave subsystem of colour vision. J Comp Physiol A 164:123-140.

Hamanaka Y, Kinoshita M, Homberg U, Arikawa K. 2012. Immunocytochemical localization of amines and GABA in the optic lobe of the butterfly, *Papilio xuthus*. PloS One 7:e41109.

Hamanaka Y, Shibasaki H, Kinoshita M, Arikawa K. 2013. Neurons innervating the lamina in the butterfly, *Papilio xuthus*. J Comp Physiol A 199:341-351.

Hardie RC. 1984. Properties of photoreceptors R7 and R8 in dorsal marginal ommatidia in the compound eyes ofMusca andCalliphora. J Comp Physiol A 154:157-165.

Hardie RC. 1985. Functional organization of the fly retina. Progress in sensory physiology: Springer. p 1-79.

Hardie RC. 1986. The photoreceptor array of the dipteran retina. Trends Neurosci 9:419-423.

Hardie RC. 1987. Is histamine a neurotransmitter in insect photoreceptors? J Comp Physiol A 161:201-213.

Hardie RC. 1988. Effects of antagonists on putative histamine receptors in the first visual neuropile of the housefly (*Musca domestica*). J Exp Biol 138:221-241.

Hardie RC. 1989. A histamine-activated chloride channel involved in neurotransmission at a photoreceptor synapse. Nature 339:704-706.

Hardie RC, Weckström M. 1990. Three classes of potassium channels in large monopolar cells of the blowfly *Calliphora vicina*. J Comp Physiol A 167:723-736.

Hardie RC, Franze K. 2012. Photomechanical responses in *Drosophila* photoreceptors. Science 338:260-263.

Hardie RC, Laughlin SB, Osorio D. 1989. Early visual processing in the compound eye: physiology and pharmacology of the retina-lamina projection in the fly. Neurobiology of Sensory Systems: Springer. p 23-42.

Heisenberg M, Buchner E. 1977. The role of retinula cell types in visual behavior of *Drosophila melanogaster*. J Comp Physiol A 117:127-162.

Henze MJ, Oakley TH. 2015. The dynamic evolutionary history of pancrustacean eyes and opsins. Integr Comp Biol 55:830-842.

Homberg U. 2002. Neurotransmitters and neuropeptides in the brain of the locust. Microsc Res Tech 56:189-209.

Horridge GA, Mimura K. 1975. Fly photoreceptors I. Physical separation of two visual pigments in *Calliphora* retinula cells 1-6. Proc Roy Soc B 190:211-224.

Horridge GA, Marcelja L, Jahnke R. 1984. Colour vision in butterflies. J Comp Physiol A 155:529-542.

Horridge GA, Marčelja L, Jahnke R, Matić T. 1983. Single electrode studies on the retina of the butterfly *Papilio*. J Comp Physiol A 150:271-294.

Ilse D. 1928. Über den farbensinn der tagfalter. Über den Farbensinn der Tagfalter: Springer. p 658-692.

Ilse D. 1937. New observations on responses to colours in egg-laying butterflies. Nature 140:544.

Ilse D. 1941. The colour vision of insects. Proc R Philos Soc Lond 65:68-82.

Iovchev M, Boutanaev A, Ivanov I, Wolstenholme A, Nurminsky D, Semenov E. 2006. Phylogenetic shadowing of a histamine-gated chloride channel involved in insect vision. Insect Biochem Mol Biol 36:10-17.

Jagadish S, Barnea G, Clandinin TR, Axel R. 2014. Identifying functional connections of the inner photoreceptors in *Drosophila* using Tango-Trace. Neuron 83:630-644.

Järvilehto M, Zettler F. 1971. Localized intracellular potentials from pre-and postsynaptic components in the external plexiform layer of an insect retina. Zeitschrift für vergleichende Physiologie 75:422-440.

Järvilehto M, Zettler F. 1973. Electrophysiological-histological studies on some functional properties of visual cells and second order neurons of an insect retina. Z Zellforsch 136:291-306.

Juusola M, French AS, Uusitalo RO, Weckström M. 1996. Information processing by graded-potential transmission through tonically active synapses. Trends Neurosci 19:292-297.

Kelber A. 2006. Invertebrate colour vision. In: Warrant EJ, Nilsson D-E, eds. Invertebrate vision. Cambridg: Cambridge University. p 250-290.

Kelber A. 2016. Colour in the eye of the beholder: receptor sensitivities and neural circuits underlying colour opponency and colour perception. Curr Opin Neurobiol 41:106-112.

Kelber A, Pfaff M. 1999. True colour vision in the orchard butterfly, *Papilio aegeus*. Naturwissenschaften 86:221-224.

Kelber A, Vorobyev M, Osorio D. 2003. Animal colour vision--behavioural tests and physiological concepts. Biol Rev Camb Philos Soc 78:81-118.

Kelly KM, Mote MI. 1990. Electrophysiology and anatomy of medulla interneurons in the optic lobe of the cockroach, *Periplaneta americana*. J Comp Physiol A 167:745-756.

Kien J, Menzel R. 1977. Chromatic properties of interneurons in the optic lobes of the bee II Narrow band and colour opponent neurons. J Comp Physiol A 113:35-53.

Kinoshita M, Arikawa K. 2000. Colour constancy in the swallowtail butterfly *Papilio xuthus*. J Exp Biol 203:3521-3530.

Kinoshita M, Arikawa K. 2014. Color and polarization vision in foraging *Papilio*. J Comp Physiol A 200:513-526.

Kinoshita M, Shimada N, Arikawa K. 1999. Colour vision of the foraging swallowtail butterfly *Papilio xuthus*. J Exp Biol 202:95-102.

Kinoshita M, Takahashi Y, Arikawa K. 2008. Simultaneous color contrast in the foraging swallowtail butterfly, *Papilio xuthus*. J Exp Biol 211:3504-3511.

Kita T, Irie T, Nomura K, Ozoe F, Ozoe Y. 2017. Pharmacological characterization of histamine-gated chloride channels from the housefly *Musca domestica*. Neurotoxicology 60:245-253.

Kitamoto J, Ozaki K, Arikawa K. 2000. Ultraviolet and violet receptors express identical mRNA encoding an ultraviolet-absorbing opsin: identification and histological localization of two mRNAs encoding short-wavelength-absorbing opsins in the retina of the butterfly *Papilio xuthus*. J Exp Biol 203:2887-2894.

Kitamoto J, Sakamoto K, Ozaki K, Mishina Y, Arikawa K. 1998. Two visual pigments in a single photoreceptor cell: identification and histological localization of three mRNAs encoding visual pigment opsins in the retina of the butterfly *Papilio xuthus*. J Exp Biol 201:1255-1261.

Koike H, Tsuda K. 1980. Cellular synthesis and axonal transport of gamma-aminobutyric acid in a photoreceptor cell of the barnacle. J Physiol 305:125-138.

Kolodziejczyk A, Sun X, Meinertzhagen IA, Nassel DR. 2008. Glutamate, GABA and acetylcholine signaling components in the lamina of the *Drosophila* visual system. PLoS One 3:e2110.

Koshitaka H, Kinoshita M, Vorobyev M, Arikawa K. 2008. Tetrachromacy in a butterfly that has eight varieties of spectral receptors. Proc Roy Soc B 275:947-954.

Laemmli UK. 1970. Cleavage of structural proteins during the assembly of the head of bacteriophage T4. Nature 227:680.

Land MF, Nilsson D-E. 2012. Animal eyes: Oxford University Press.

Laughlin SB. 1973. Neural integration in the first optic neuropile of dragonflies. I. Signal amplification in dark-adapted second-order neurons. J Comp Physiol A 84:335-355.

Laughlin SB. 1976. Neural integration in the first optic neuropile of dragonflies. IV. Interneuron spectral sensitivity and contrast coding. J Comp Physiol A 112:199-211.

Laughlin SB. 1981. Neural principles in the peripheral visual systems of invertebrates. Handbook of sensory physiology:133-280.

Laughlin SB. 1984. The roles of parallel channels in early visual processing by the arthropod compound eye. Photoreception and vision in invertebrates: Springer. p 457-481.

Laughlin SB, Hardie RC. 1978. Common strategies for light adaptation in the peripheral visual systems of fly and dragonfly. J Comp Physiol A 128:319-340.

Laughlin SB, Howard J, Blakeslee B. 1987. Synaptic limitations to contrast coding in the retina of the blowfly *Calliphora*. Proc Roy Soc B 231:437-467.

Lin J-T. 1993. Identification of photoreceptor locations in the compound eye of *Coccinella septempunctata* Linnaeus (Coleoptera, Coccinellidae). J Insect Physiol 39:555-562.

Lind O, Henze MJ, Kelber A, Osorio D. 2017. Coevolution of coloration and colour vision? Philos Trans R Soc Lond B Biol Sci 372:20160338.

Marcos P, Corio M, Dubourg P, Covenas R, Tramu G. 1997. Double immunocytochemistry in pre-embedding electron microscopy for the detection of neurotensin and tyrosine hydroxylase in the guinea pig, using two primary antisera raised in the same species. Brain Res Protocol 2:1-8.

Matić T. 1983. Electrical inhibition in the retina of the butterfly *Papilio*. J Comp Physiol A 152:169-182.

Matsushita A, Awata H, Wakakuwa M, Takemura SY, Arikawa K. 2012. Rhabdom evolution in butterflies: insights from the uniquely tiered and heterogeneous ommatidia of the Glacial Apollo butterfly, *Parnassius glacialis*. Proc Roy Soc B 279:3482-3490.

Maxwell GD, Tait JF, Hildebrand JG. 1978. Regional synthesis of neurotransmitter candidates in the CNS of the moth *Manduca sexta*. Comp Biochem Physiol C Toxicol Pharmacol 61:109-119.

McCann GD, Arnett DW. 1972. Spectral and polarization sensitivity of the dipteran visual system. J Gen Physiol 59:534-558.

McCulloch KJ, Osorio D, Briscoe AD. 2016. Sexual dimorphism in the compound eye of *Heliconius erato*: a nymphalid butterfly with at least five spectral classes of photoreceptor. J Exp Biol:jeb136523.

Meinertzhagen IA, O'neil SD. 1991. Synaptic organization of columnar elements in the lamina of the wild type in *Drosophila melanogaster*. J Comp Neurol 305:232-263.

Meinertzhagen IA, Menzel R, Kahle G. 1983. The identification of spectral receptor types in the retina and lamina of the dragonfly *Sympetrum rubicundulum*. J Comp Physiol A 151:295-310.

Menzel R. 1974. Colour receptors in insects. Horridge GA, ed: Clarendon Press.

Menzel R. 1979. Spectral sensitivity and color vision in invertebrates. Comparative physiology and evolution of vision in invertebrates: Springer. p 503-580.

Menzel R, Blakers M. 1976. Colour receptors in the bee eye—morphology and spectral sensitivity. J Comp Physiol A 108:11-13.

Menzel R, Backhaus W. 1989. Color vision honey bees: phenomena and physiological mechanisms. Facets of vision: Springer. p 281-297.

Miyako-Shimazaki Y, Shimazaki Y, Eguchi E. 1997. Effect of formoguanamine on structure and function of the compound eye of the butterfly, *Papilio xuthus*. Zool Sci 14:29-35.

Mollon JD. 1989. "Tho' she kneel'd in that place where they grew..." The uses and origins of primate colour vision. J Exp Biol 146:21-38.

Morante J, Desplan C. 2004. Building a projection map for photoreceptor neurons in the *Drosophila* optic lobes. Semin Cell Dev Biol 15:137-143.

Morgan JR, Gebhardt KA, Stuart AE. 1999. Uptake of precursor and synthesis of transmitter in a histaminergic photoreceptor. J Neurosci 19:1217-1225.

Moring J. 1978. Spectral sensitivity of monopolar neurons in the eye of *Calliphora*. J Comp Physiol A 123:335-338.

Naka KI, Rushton WA. 1966. S-potentials from colour units in the retina of fish (Cyprinidae). J Physiol 185:536-555.

Nässel DR. 1991. Neurotransmitters and neuromodulators in the insect visual system. Prog Neurobiol 37:179-254.

Nässel DR. 1999. Histamine in the brain of insects: a review. Microsc Res Tech 44:121-136.

Neumeyer C. 1991. Evolution of colour vision. Evolution of the Eye and Visual System: Vision and Visual Dysfunction 2:284-305.

Nishikawa H, Iijima T, Kajitani R, Yamaguchi J, Ando T, Suzuki Y, Sugano S, Fujiyama A, Kosugi S, Hirakawa H. 2015. A genetic mechanism for female-limited Batesian mimicry in *Papilio* butterfly. Nat Genet 47:405.

Oertel D, Stuart AE. 1981. Transformation of signals by interneurones in the barnacle's visual pathway. J Physiol 311:127-146.

Ogawa Y, Kinoshita M, Stavenga DG, Arikawa K. 2013. Sex-specific retinal pigmentation results in sexually dimorphic long-wavelength-sensitive photoreceptors in the eastern pale clouded yellow butterfly, *Colias erate*. J Exp Biol 216:1916-1923.

Ogawa Y, Awata H, Wakakuwa M, Kinoshita M, Stavenga DG, Arikawa K. 2012. Coexpression of three middle wavelength-absorbing visual pigments in sexually dimorphic photoreceptors of the butterfly *Colias erate*. J Comp Physiol A 198:857-867.

Osorio D. 1986. Ultraviolet sensitivity and spectral opponency in the locust. J Exp Biol 122:193-208.

Osorio D, Vorobyev M. 2008. A review of the evolution of animal colour vision and visual communication signals. Vision Res 48:2042-2051.

Pantazis A, Segaran A, Liu C-H, Nikolaev A, Rister J, Thum AS, Roeder T, Semenov E, Juusola M, Hardie RC. 2008. Distinct roles for two histamine receptors (*hclA* and *hclB*) at the *Drosophila* photoreceptor synapse. J Neurosci 28:7250-7259.

Paulk AC, Phillips-Portillo J, Dacks AM, Fellous J-M, Gronenberg W. 2008. The processing of color, motion, and stimulus timing are anatomically segregated in the bumblebee brain. J Neurosci 28:6319-6332.

Peitsch D, Fietz A, Hertel H, de Souza J, Ventura DF, Menzel R. 1992. The spectral input systems of hymenopteran insects and their receptor-based colour vision. J Comp Physiol A 170:23-40.

Perry M, Kinoshita M, Saldi G, Huo L, Arikawa K, Desplan C. 2016. Molecular logic behind the three-way stochastic choices that expand butterfly colour vision. Nature 535:280.

Pirih P, Arikawa K, Stavenga DG. 2010. An expanded set of photoreceptors in the Eastern Pale Clouded Yellow butterfly, *Colias erate*. J Comp Physiol A 196:501-517.

Qiu X, Arikawa K. 2003. Polymorphism of red receptors: sensitivity spectra of proximal photoreceptors in the small white butterfly *Pieris rapae crucivora*. J Exp Biol 206:2787-2793.

Ribi WA. 1976. The first optic ganglion of the bee. II. Topographical relationships of the monopolar cells within and between cartridges. Cell Tissue Res 171:359-373.

Ribi WA. 1987. Anatomical identification of spectral receptor types in the retina and lamina of the Australian orchard butterfly, *Papilio aegeus aegeus* D. Cell Tissue Res 247:393-407.

Rister J, Pauls D, Schnell B, Ting C-Y, Lee C-H, Sinakevitch I, Morante J, Strausfeld NJ, Ito K, Heisenberg M. 2007. Dissection of the peripheral motion channel in the visual system of *Drosophila melanogaster*. Neuron 56:155-170.

Rivera-Alba M, Vitaladevuni SN, Mishchenko Y, Lu Z, Takemura S-Y, Scheffer L, Meinertzhagen IA, Chklovskii DB, de Polavieja GG. 2011. Wiring economy and volume exclusion determine neuronal placement in the *Drosophila* brain. Curr Biol 21:2000-2005.

Rusanen J, Weckström M. 2016. Frequency-selective transmission of graded signals in large monopolar neurons of blowfly *Calliphora vicina* compound eye. J Neurophysiol 115:2052-2064.

Rusanen J, Vähäkainu A, Weckström M, Arikawa K. 2017. Characterization of the first-order visual interneurons in the visual system of the bumblebee (*Bombus terrestris*). J Comp Physiol A 203:903-913.

Rusanen J, Frolov R, Weckström M, Kinoshita M, Arikawa K. 2018. Non-linear amplification of graded voltage signals in the first-order visual interneurons of the butterfly *Papilio xuthus*. J Exp Biol:jeb179085.

Saari P, Immonen E-V, French AS, Torkkeli PH, Liu H, Heimonen K, Frolov RV. 2018. Electrical interactions between photoreceptors in the compound eye of *Periplaneta americana*. J Exp Biol 221:jeb189340.

Schmid A, Becherer C. 1999. Distribution of histamine in the CNS of different spiders. Microsc Res Tech 44:81-93.

Schnaitmann C, Garbers C, Wachtler T, Tanimoto H. 2013. Color discrimination with broadband photoreceptors. Curr Biol 23:2375-2382.

Schnaitmann C, Haikala V, Abraham E, Oberhauser V, Thestrup T, Griesbeck O, Reiff DF. 2018. Color processing in the early visual system of *Drosophila*. Cell 172:318-330. e318.

Seki T, Vogt K. 1998. Evolutionary aspects of the diversity of visual pigment chromophores in the class Insecta. Comp Biochem Physiol B Biochem Mol Biol 119:53-64.

Shaw SR. 1975. Retinal resistance barriers and electrical lateral inhibition. Nature 255:480-482.

Shibasaki H, Arikawa K, Kinoshita M. 2006. Interommatidial angle, photoreceptor acceptance angle, and spatial resolution of the compound eye of the butterfly, *Papilio xuthus*. The 77th Annual Meeting of the Zoological Society of Japan, Matsue, Japan. 21-24 September.

Shichida Y, Imai H. 1998. Visual pigment: G-protein-coupled receptor for light signals. Cell Mol Life Sci 54:1299-1315.

Sinakevitch I, Strausfeld NJ. 2004. Chemical neuroanatomy of the fly's movement detection pathway. J Comp Neurol 468:6-23.

Sison-Mangus MP, Bernard GD, Lampel J, Briscoe AD. 2006. Beauty in the eye of the beholder: the two blue opsins of lycaenid butterflies and the opsin gene-driven evolution of sexually dimorphic eyes. J Exp Biol 209:3079-3090.

Skingsley DR, Laughlin SB, Hardie RC. 1995. Properties of histamine-activated chloride channels in the large monopolar cells of the dipteran compound eye: a comparative study. J Comp Physiol A 176:611-623.

Skorupski P, Chittka L. 2010. Photoreceptor spectral sensitivity in the bumblebee, *Bombus impatiens* (Hymenoptera: Apidae). PLoS One 5:e12049.

Snyder AW. 1979. Physics of vision in compound eyes. Comparative physiology and evolution of vision in invertebrates: Springer. p 225-313.

Sombke A, Harzsch S. 2015. Immunolocalization of histamine in the optic neuropils of *Scutigera coleoptrata* (Myriapoda: Chilopoda) reveals the basal organization of visual systems in Mandibulata. Neurosci Lett 594:111-116.

Stavenga DG. 1992. Eye regionalization and spectral tuning of retinal pigments in insects. Trends Neurosci 15:213-218.

Stavenga DG. 2002. Colour in the eyes of insects. J Comp Physiol A 188:337-348.

Stavenga DG, Arikawa K. 2006. Evolution of color and vision of butterflies. Arthropod Struct Dev 35:307-318.

Stavenga DG, Arikawa K. 2011. Photoreceptor spectral sensitivities of the Small White butterfly *Pieris rapae crucivora* interpreted with optical modeling. J Comp Physiol A 197:373-385.

Stavenga DG, Kinoshita M, Yang E-C, Arikawa K. 2001. Retinal regionalization and heterogeneity of butterfly eyes. Naturwissenschaften 88:477-481.

Stewart FJ, Kinoshita M, Arikawa K. 2015. The butterfly *Papilio xuthus* detects visual motion using chromatic contrast. Biol Lett 11:20150687.

Stockl AL, Ribi WA, Warrant EJ. 2016. Adaptations for nocturnal and diurnal vision in the hawkmoth lamina. J Comp Neurol 524:160-175.

Strausfeld NJ. 1971. The organization of the insect visual system (Light microscopy). Cell Tissue Res 121:377-441.

Stuart AE. 1999. From fruit flies to barnacles, histamine is the neurotransmitter of arthropod photoreceptors. Neuron 22:431-433.

Stuart AE, Borycz J, Meinertzhagen IA. 2007. The dynamics of signaling at the histaminergic photoreceptor synapse of arthropods. Prog Neurobiol 82:202-227.

Swihart CA. 1971. Colour discrimation by the butterfly, *Heliconius charitonius* Linn. Anim Behav 19:156-164.

Swihart CA, Swihart SL. 1970. Colour selection and learned feeding preferences in the butterfly, *Heliconius charitonius* Linn. Anim Behav 18:60-64.

Swihart SL. 1970. The neural basis of colour vision in the butterfly, *Papilio troilus*. J Insect Physiol 16:1623-1636.

Takayama Y, Furue H, Tominaga M. 2017. 4-isopropylcyclohexanol has potential analgesic effects through the inhibition of anoctamin 1, TRPV1 and TRPA1 channel activities. Scientific Reports 7:43132.

Takemura S-Y, Arikawa K. 2006. Ommatidial type-specific interphotoreceptor connections in the lamina of the swallowtail butterfly, *Papilio xuthus*. J Comp Physiol A 494:663-672.

Takemura S-Y, Kinoshita M, Arikawa K. 2005. Photoreceptor projection reveals heterogeneity of lamina cartridges in the visual system of the Japanese yellow swallowtail butterfly, *Papilio xuthus*. J Comp Physiol A 483:341-350.

Takemura S-Y, Bharioke A, Lu Z, Nern A, Vitaladevuni S, Rivlin PK, Katz WT, Olbris DJ, Plaza SM, Winston P. 2013. A visual motion detection circuit suggested by *Drosophila* connectomics. Nature 500:175.

Takeuchi Y, Arikawa K, Kinoshita M. 2006. Color discrimination at the spatial resolution limit in a swallowtail butterfly, *Papilio xuthus*. J Exp Biol 209:2873-2879.

Terakita A. 2005. The opsins. Genome Biol 6:213.

Thompson AJ, Lester HA, Lummis SCR. 2010. The structural basis of function in Cys-loop receptors. Q Rev Biophys 43:449-499.

Timpe LC, Stuart AE. 1984. Is γ-aminobutyric acid the neurotransmitter of barnacle photoreceptors? Brain Res 307:225-231.

Uusitalo RO, Weckström M. 2000. Potentiation in the first visual synapse of the fly compound eye. J Neurophysiol 83:2103-2112.

Uusitalo RO, Juusola M, Weckström M. 1995. Graded responses and spiking properties of identified first-order visual interneurons of the fly compound eye. J Neurophysiol 73:1782-1792.

Van Hateren J. 1987. Neural superposition and oscillations in the eye of the blowfly. J Comp Physiol A 161:849-855.

von Frisch K. 1914. Der farbensinn und formensinn der biene. Zool Jahrb Abt Allg Zool Physiol Tiere 35:1-188.

von Helversen O. 1972. Zur spektralen Unterschiedsempfindlichkeit der honigbiene. Journal of Comparative Physiology 80:439-472.

Vorobyev M, Osorio D. 1998. Receptor noise as a determinant of colour thresholds. Proc Roy Soc B 265:351-358.

Wakakuwa M, Arikawa K, Ozaki K. 2003. A novel retinol-binding protein in the retina of the swallowtail butterfly, *Papilio xuthus*. Eur J Biochem 270:2436-2445.

Wakakuwa M, Ozaki K, Arikawa K. 2004a. Immunohistochemical localization of *Papilio* RBP in the eye of butterflies. J Exp Biol 207:1479-1486.

Wakakuwa M, Stavenga DG, Arikawa K. 2007. Spectral organization of ommatidia in flower-visiting insects. Photochem Photobiol 83:27-34.

Wakakuwa M, Stavenga DG, Kurasawa M, Arikawa K. 2004b. A unique visual pigment expressed in green, red and deep-red receptors in the eye of the small white butterfly, *Pieris rapae crucivora*. J Exp Biol 207:2803-2810.

Wardill TJ, List O, Li X, Dongre S, McCulloch M, Ting C-Y, O'Kane CJ, Tang S, Lee C-H, Hardie RC. 2012. Multiple spectral inputs improve motion discrimination in the *Drosophila* visual system. Science 336:925-931.

Washizu Y, Burkhardt D, Streck P. 1964. Visual field of single retinula cells and interommatidial inclination in the compound eye of the blowfly Calliphora erythrocephala. J Comp Physiol A 48:413-428.

Weckström M, Laughlin SB. 2010. Extracellular potentials modify the transfer of information at photoreceptor output synapses in the blowfly compound eye. J Neurosci 30:9557-9566.

Weir PT, Henze MJ, Bleul C, Baumann-Klausener F, Labhart T, Dickinson MH. 2016. Anatomical reconstruction and functional imaging reveal an ordered array of skylight polarization detectors in *Drosophila*. J Neurosci 36:5397-5404.

Wernet MF, Velez MM, Clark DA, Baumann-Klausener F, Brown JR, Klovstad M, Labhart T, Clandinin TR. 2012. Genetic dissection reveals two separate retinal substrates for polarization vision in *Drosophila*. Curr Biol 22:12-20.

Witte I, Kreienkamp HJ, Gewecke M, Roeder T. 2002. Putative histamine-gated chloride channel subunits of the insect visual system and thoracic ganglion. J Neurochem 83:504-514.

Yamaguchi S, Wolf R, Desplan C, Heisenberg M. 2008. Motion vision is independent of color in *Drosophila*. PNAS 105:4910-4915.

Yang E-C, Osorio D. 1991. Spectral sensitivities of photoreceptors and lamina monopolar cells in the dragonfly, Hemicordulia tau. J Comp Physiol A 169:663-669.

Yang E-C, Lin H-C, Hung Y-S. 2004. Patterns of chromatic information processing in the lobula of the honeybee, *Apis mellifera* L. J Insect Physiol 50:913-925.

Yusein S, Wolstenholme A, Semenov E. 2010. Functional consequences of mutations in the *Drosophila* histamine receptor HCLB. J Insect Physiol 56:21-27.

Zettler F, Järvilehto M. 1971. Decrement-free conduction of graded potentials along the axon of a monopolar neuron. Zeitschrift für vergleichende Physiologie 75:402-421.

Zheng Y, Hirschberg B, Yuan J, Wang AP, Hunt DC, Ludmerer SW, Schmatz DM, Cully DF. 2002. Identification of two novel *Drosophila melanogaster* histamine-gated chloride channel subunits expressed in the eye. J Biol Chem 277:2000-2005.